

3D-deflectometry : fast nanotopography measurement for the semiconductor industry

Citation for published version (APA):

Szwedowicz, K. K. (2006). *3D-deflectometry : fast nanotopography measurement for the semiconductor industry*. [Phd Thesis 1 (Research TU/e / Graduation TU/e), Applied Physics and Science Education]. Technische Universiteit Eindhoven. <https://doi.org/10.6100/IR609510>

DOI:

[10.6100/IR609510](https://doi.org/10.6100/IR609510)

Document status and date:

Published: 01/01/2006

Document Version:

Publisher's PDF, also known as Version of Record (includes final page, issue and volume numbers)

Please check the document version of this publication:

- A submitted manuscript is the version of the article upon submission and before peer-review. There can be important differences between the submitted version and the official published version of record. People interested in the research are advised to contact the author for the final version of the publication, or visit the DOI to the publisher's website.
- The final author version and the galley proof are versions of the publication after peer review.
- The final published version features the final layout of the paper including the volume, issue and page numbers.

[Link to publication](#)

General rights

Copyright and moral rights for the publications made accessible in the public portal are retained by the authors and/or other copyright owners and it is a condition of accessing publications that users recognise and abide by the legal requirements associated with these rights.

- Users may download and print one copy of any publication from the public portal for the purpose of private study or research.
- You may not further distribute the material or use it for any profit-making activity or commercial gain
- You may freely distribute the URL identifying the publication in the public portal.

If the publication is distributed under the terms of Article 25fa of the Dutch Copyright Act, indicated by the "Taverne" license above, please follow below link for the End User Agreement:

www.tue.nl/taverne

Take down policy

If you believe that this document breaches copyright please contact us at:

openaccess@tue.nl

providing details and we will investigate your claim.

3D-deflectometry

Fast nanotopography measurement for the semiconductor industry

Proefontwerp

ter verkrijging van de graad van doctor aan de
Technische Universiteit Eindhoven, op gezag van de
Rector Magnificus, prof.dr.ir. C.J. van Duijn, voor een
commissie aangewezen door het College voor
Promoties in het openbaar te verdedigen
op woensdag 8 november 2006 om 16.00 uur

door

Konrad Krzysztof Szwedowicz

geboren te Warschau, Polen

De documentatie van het proefontwerp is goedgekeurd door de promotoren:

prof.dr. H.C.W. Beijerinck

en

prof.dr. A.G. Tjihuis

Copromotor:

dr. S.M.B. Bäumer

CIP-DATA LIBRARY TECHNISCHE UNIVERSITEIT EINDHOVEN

Szwedowicz, Konrad Krzysztof

3D-deflectometry: fast nanotopography measurement for the semiconductor industry /

by Konrad Krzysztof Szwedowicz. - Eindhoven : Technische Universiteit Eindhoven, 2006

Proefontwerp.

ISBN 90-386-0679-6

ISBN 978-90-386-0679-8

NUR 926

Keywords: Deflectometry, Surface metrology, Nanotopography, Semiconductors

Cover: 3D image of a topography artifact on a bare silicone wafer, measured with a 3D-deflectometer (vertical scale less than 70 nm)

Summary

The goal of this project was to investigate the possibilities and limitations of 3D-deflectometry, and to design an instrument – 3D-deflectometer – based on requirements for the semiconductor industry. These requirements are an inspection area the size of a 12'' wafer, a lateral resolution of 100 micron, a height resolution of 5 nm, and a maximum value of the total measuring time of only 60 s. Conventional metrology tools do not meet these demands. We investigate a new surface metrology technique – 3D deflectometry - based on an optical measurement of the slope of the surface. The principle of operation is that a focused laser beam scans the surface-under-test. During the scan, the local slope vector of the surface is measured by an autocollimator-like sensor. Hence, after the measurement a complete slope map of the surface is available. To reconstruct the topography of the surface-under-test, we process the slope data by means of a numerical surface-integration procedure.

A major advantage of this method is that by using a combination of a mechanical and optical scan, and a fast slope sensor, large surfaces – like Ø300 mm wafers – can be measured with high lateral resolution and short measurement time. Furthermore, very high height resolution can be achieved easily just by using a long focal length of the objective of the slope sensor. Finally, the measurement is insensitive for height errors due to vertical vibration and drift of the surface-under-test, which are the primary error sources for any direct height measurement at nanometre scale.

In order to introduce an optimum design of the instrument, we derived a basic theoretical model of optical slope measurement and of the surface reconstruction. The latter shows that by applying an advanced surface integration algorithm we can provide a strong correction for random errors in the measurement. The understanding of this unique feature of 3D-deflectometry was essential, since it allows a more relaxed design of the system components, while still leading to very high height resolution (better than 1 nm).

To overcome theoretical limits for the lateral resolution of the slope measurement, we investigated an innovative approach for slope detection, so-called Large Beam Detection (LBD) mode. We concluded that by applying this method, we can increase the lateral resolution of the system by at least a factor of two, without degrading performance of other parameters, such as the sampling rate or the slope range. Furthermore, the LBD mode does not require any physical modifications to the slope sensor but only correction in software.

The set-up presented in this thesis is based on a modified Fast Optical Scanner (FOS) from Philips Applied Technologies and it is capable of measuring the topography of flat or slightly curved surfaces, with the lateral dimensions up to 110 x 500 mm². The maximum number of measurement points is about 6.5 millions. By applying the LBD mode we achieved a lateral resolution of 200 µm and a measurement time of approximately 60 s for a 100 x 100 mm² area. This prototype does not meet the demands of the semiconductor industry, but allows the development and experimental verification of rigid calibration procedures as essential for a new metrology tool.

We developed a set of calibration procedures for the system, including a calibration of the slope sensor and of the mapping of the lateral position. Moreover, to increase the long-range accuracy of the measurement, we developed and applied a method for characterizing and correcting systematic errors in deflectometers. These errors, which are mostly due to the optical aberrations

and the mechanical deviations, are calibrated by using an optical flat as an external reference surface.

To prove the performance of the deflectometer as a metrology tool, we did an extended verification of the system by comparing the results from the 3D-deflectometer to measurements by external reference devices, like various monochromatic- and white-light interferometers and a stylus. Based on these measurements, we claim a height accuracy of our instrument of better than 5 nm in the nanotopography region (spatial wavelengths in the range from ~100 micron to ~20 mm) and of at least 35 nm in the global shape (110x110 mm² area).

Finally, we show that a careful upgrade of the prototype of the 3D deflectometer described in this thesis can readily meet the demands of the semiconductor industry as given above.

Table of contents

Summary.....	i
Table of contents.....	iii
1. Introduction.....	1
1.1. How flat is flat?	1
1.2. Why slope measurement?.....	3
1.3. Principle of 3D-deflectometry.....	5
1.4. Surface reconstruction from a slope measurement.....	9
1.5. Design limits.....	13
1.6. Contents of this thesis.....	18
1.7. References.....	18
2. Modern surface metrology.....	21
2.1. General remarks on surface description.....	21
2.2. Surface metrology for wafers inspection.....	23
2.3. Surface metrology techniques.....	26
2.3.1. Introduction to surface metrology.....	26
2.3.2. Stylus profilers.....	28
2.3.3. Scanning Probe Microscopes.....	29
2.3.4. Optical Focus Sensors.....	29
2.3.5. Interferometers.....	30
2.3.6. Topography by Optical Slope Measurement.....	33
2.4. Concluding remarks on surface metrology.....	34
2.5. References.....	34
3. Feasibility study of 3D-deflectometry.....	37
3.1. Implementation of Fast Optical Scanning.....	37
3.2. 3D-deflectometry test-bed.....	39
3.3. Main system errors.....	41
3.4. Comparison with a white light interferometer.....	47
3.5. Concluding remarks on the feasibility study.....	48
3.6. References.....	50

4.	Design of the 3D-deflectometer.....	51
4.1.	User requirements.....	51
4.2.	Design process.....	51
4.3.	Boundary conditions.....	52
4.3.1.	General scan strategy.....	52
4.3.2.	Lateral resolution.....	53
4.3.3.	Height resolution.....	57
4.3.4.	Scanning.....	59
4.3.5.	Measurement time.....	63
4.4.	Choices.....	63
4.5.	Technology tuning.....	66
4.5.1.	Large beam detection.....	66
4.5.2.	Sampling.....	68
4.5.3.	Slope stitching.....	69
4.5.4.	Effective gain in performance.....	69
4.6.	References.....	69
5.	Architecture of the new system.....	71
5.1.	General remarks.....	71
5.2.	Hardware.....	71
5.3.	Data flow and scan synchronization.....	79
5.4.	Software program.....	79
5.5.	References.....	81
6.	Calibrations of the 3D deflectometer.....	83
6.1.	Introduction to calibration.....	83
6.2.	Scan position mapping: systematic errors.....	86
6.3.	Scan position mapping: (pseudo)random errors.....	90
6.4.	Detector alignment.....	95
6.5.	Slope response.....	98
6.6.	System signature.....	101
6.7.	Optical flat reconstruction.....	103
6.8.	Surface reconstruction errors.....	106
6.9.	Calibration procedure.....	108
6.10.	References.....	109
7.	Validation by industrial applications.....	111
7.1.	Introduction.....	111

7.2.	Flatness of a 4" wafer.....	112
7.3.	Epi-pinmark profile.....	114
7.4.	Polishing control.....	115
7.5.	Patterned wafer: LCoS panels.....	119
7.6.	Long aluminium mirror.....	122
7.7.	Final estimation of the performance for the 3D-deflectometer.....	125
8.	Concluding remarks.....	127

Appendixes

	Introduction to appendixes.....	131
A1	Definitions of the Gaussian beam size.....	132
C1	Position Sensitive Diode.....	134
C2	Parabolic approximation of a sphere.....	137
C3	Estimation of the lens quality from its high frequency aberrations.....	138
D1	General consideration on the surface scan strategy.....	140
D2	Model of the surface response for an optical slope measurement.....	143
D3	Surface finish considerations for deflectometry.....	145
D4	Derivation of the basic scan requirement formula.....	148
D5	Translation speed of the 3D-deflectometer.....	150
D6	Measurement time of the 3D-deflectometer.....	151
D7	Model of the large-beam detection.....	153
D8	Experimental set-up for investigation of the large-beam detection (LBD).....	156
D9	Experimental evaluation of the displacement response for LBD.....	158
D10	Experimental evaluation of the displacement resolution for LBD.....	160
D11	Derivation of the deflectometer resolution formula.....	162
D12	Derivation of the formula for the resolution of the slope measurement.....	163
F1	Calibration report of the reference flat.....	164
F2	Calibration of the scan non-linearity.....	165
F3	Measurement report of the yaw of the translation stage.....	168
F4	Calibration of the slope response.....	170
F5	Calibration of the system signature.....	175
F6	Measurement report of the reference flat.....	179
G1	Measurement report of 100mm silicon wafer substrate (3D-deflectometer).....	183
G2a	Measurement report of epi-pinmark on a wafer substrate (3D-deflectometer).....	186
G2b	Measurement report of epi-pinmark on a wafer substrate (white light interfer.).....	188
G3a	Measurement report of patterned test-wafer (3D-deflectometer).....	190
G3b	Measurement report of patterned test-wafer (Stylus).....	199
G4a	Measurement report of patterned wafer for LCoS panels (3D-deflectometer).....	202
G4b	Measurement report of patterned wafer for LCoS panels (white light interfer.).....	205
G5a	Measurement report of long aluminium mirror (3D-deflectometer).....	207

G5b Measurement report of long aluminium mirror (4" phase-shift interferometer).....211

Samenvatting..... 213

Acknowledgments..... 215

Biography..... 217

Chapter 1

Introduction

In this chapter we describe the motivation for this thesis. In section 1.1 we give a general background for the present research in surface metrology, particularly for nearly-flat surfaces such as silicon wafers used in the semiconductor industry. In section 1.2, we explain the benefits of measuring topography in the slope domain. The principle of Optical Slope Measurement as well as basic 3D deflectometry description is given in section 1.3. Next, in section 1.4, we discuss the mathematical background of reconstructing topography from slope measurements, and the main limitations of such a reconstruction. The design limits of deflectometry are discussed in section 1.5. The chapter ends with an outline of this thesis.

1.1. How flat is flat?

Technological progress in integrated circuits (IC) industry entails that the number of transistors in state-of-the-art produced on silicon doubles roughly every 18 months. Higher density of transistors enables producing more powerful and cost-effective semiconductor devices. This continuous trend is described by Moore's law. Technologically, it implies that finer and finer structures are being imprinted on silicon wafers by optical projection lithography. Consequently, surface metrology is important because only the surface which can be measured precisely can be made precisely. The IC structures are imprinted on the photoresist layer by an optical beam focused on the wafer. In order to follow fine features the spot size of this beam must be small. Following diffraction theory, the spot size is coupled to the so-called depth of focus (*DoF*) of the beam, which is the vertical range for which the processed surface is in-focus. For example, the *DoF* for a Gaussian beam is defined often by:

$$DoF = 2z_R = \frac{\pi d_0^2}{2\lambda} \quad (\text{eq. 1.1})$$

with z_R the Rayleigh range, d_0 the FWe²M spot size of a Gaussian beam¹, and λ the wavelength. Within the Rayleigh range the beam size increases by no more than $\sqrt{2}$ of the spot size. Other definitions of *DoF* focus are possible; generally speaking, a *DoF* criterion depends on the application, and is defined by the maximum increase of the beam size allowed by the particular process.

¹ For the beam/spot size notation followed in this thesis see appendix A1

When a surface under lithographic exposure is outside the *DoF* range, the feature being imprinted has larger (incorrect) lateral size and/or has insufficient depth (due to insufficient local energy concentration of the beam). As a consequence, continuous decrease of the IC feature size requires higher flatness of wafer substrates. Presently, state-of-the-art 90 nm optical lithography process ($\lambda = 193$ nm) requires flatness of the wafer substrates of 50 nm. The flatness requirements are given typically “per die”, since those structures corresponding to a single microprocessor are exposed at the same time in the lithography process. The dimensions of a die vary with the customer, but are typically on the order of 2×2 mm² to 25×25 mm² [1,2]. Between the dies the beam can be re-focused.

To produce the required flatness during the wafer manufacturing process, wafer substrates must be polished. This is done by chemical-mechanical polishing (CMP). The polishing, though very accurate, needs a feedback by means of an in-line flatness-testing instrument. Furthermore, for the final classification and certification, each product must be measured again. Presently, wafer manufacturers face a situation where a large part of the flatness tolerance comes from the measuring technique itself, which leads to many false rejects of their products. To guarantee correct product specification, the accuracy of the flatness inspection must be on the order of a few nm.

The lack of an adequate metrology tool raises a problem not only for the wafer manufacturers, but also for the IC manufacturers. After completion of each functional layer on a silicon wafer, the layer is passivated with a thick SiO₂ film. Before the next functional layer is produced via metallization, lithography, implant and etching processes, the flatness of the wafer must be restored. This is done using again CMP. Inaccuracies of the measurement and several-hours-long measurement time result in an increase of the production costs.

High-end requirements in the semiconductor industry introduce a challenge for metrology of flat surfaces. This includes not only a high accuracy of height measurement, but also large dimensions of the inspection area. Recently, $\varnothing 300$ mm wafers have been introduced to state-of-the-art integrated circuits fabrication plants, replacing the $\varnothing 200$ mm technology. In the future, $\varnothing 450$ mm wafers or even larger are expected. Using larger silicon wafers, more dies can be produced on a single wafer, which decreases the cost of production significantly. One can imagine, however, that if a 300 mm wafer is measured with spatial resolution of 0.1 mm, which is reasonable for that kind of measurements (see chapter 2.1), about ten million data points must be taken and processed in a short time.

The problem of flatness inspection of large objects has never been fully solved in the industrial world, although different techniques have been proposed over the years. They can be separated into two categories. First, when the measurement is inherently two-dimensional and fast – represented by interferometry; second, when the measurement is sequential and consequently slower – this is represented by various scanning methods. The lack of success in the development of topography measurement methods is related mainly to several error sources, such as calibration accuracy and references in interferometry, angular and positional deviations of mechanical elements in scanning methods, and in general whole-body movement in direct height measurements. Also, the speed of scanning methods is usually unsatisfactory. As a result, instruments used presently are a compromise between accuracy, spatial resolution and throughput. Often on-line surface measurement is skipped, paying the price of a lower yield. Thus, part of the production is wasted because of lack of satisfactory metrology systems.

In conclusion, the flatness requirements for industrial surfaces changes rapidly with progress in technology. Just a few years ago, micro-technology was state-of-the-art, and nowadays nano-technology is commonly used. This indicates a completely new interest in description of a surface and introduces new challenges for surface metrology. In this thesis we present a new solution for fast metrology for nearly-flat surfaces. The method is called 3D-deflectometry and it is based on optical slope measurement.

1.2. Why slope measurement?

The phrase 3D-deflectometry is used for a surface metrology method where a surface is measured optically in the slope domain and the topography is reconstructed from the slope data. Such an approach has several advantages over a direct height measurement.

First, the measurement itself is insensitive to the vertical displacement of the surface. Therefore, the measurement accuracy is not influenced by the vibration or drift of the surface during the measurement. This is due to the fact that the slope does not contain absolute height information - explained schematically in figure 1.1.

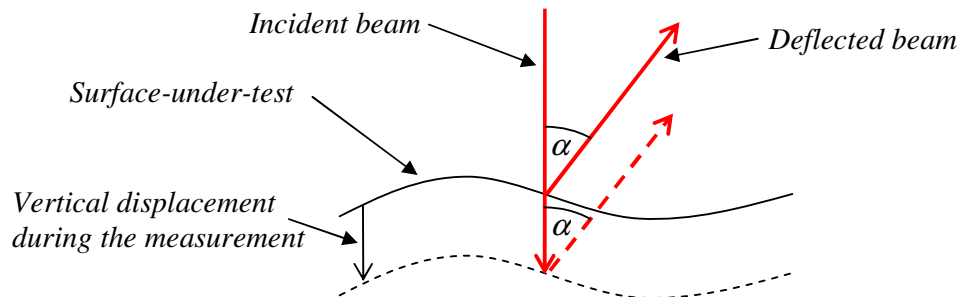


Figure 1.1. Slope measurement of a surface, where α is the measured slope angle. The vertical displacement of the surface during the measurement (e.g. as a result of unwanted mechanical vibration) does not affect the measurement.

This feature is very important in industrial applications, particularly when the accuracy of the height measurement must be on the order of nanometres: the height stability at this scale is almost impossible to achieve. The drawback, however, is that the measurement is insensitive to step-like surface features, where the slope practically cannot be measured because the measurement does not contain information on the height difference between the surfaces separated by the step.

Second, the slope measurement can easily reach extremely high height-sensitivity for small surface features. We explain it schematically in figure 1.2. In this simple geometrical figure the height of the surface feature is given against spatial wavelength (feature size) with a constant slope across that area. One can notice that the height sensitivity of a slope-measuring device will change linearly with the lateral resolution. In other words, using a very fine probing beam, very small height deviations can be resolved. For example, when the slope measuring device is capable of resolving 1 μ rad over a 10 mm-large area (possible with a standard autocollimator), a height difference of 10 nm over that area could be measured; using the same slope resolution of 1 μ rad, but decreasing the probing beam size such that

spatial wavelengths of 100 μm can be resolved, the height deviation of 0.1 nm over that area could be measured!

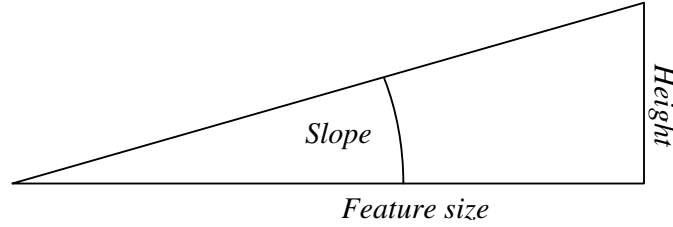


Figure 1.2. Relation between the height deviation reconstructed from a measured surface slope, and the lateral size of the measured feature.

This magnification feature of the slope measurement becomes apparent in the Fourier domain, where a surface is represented by the Fourier transform of its height amplitude Σ :

$$\hat{\Sigma}(k) = F[\Sigma(x)] = \int_{-\infty}^{\infty} \Sigma(x) e^{j2\pi kx} dx \quad (\text{eq. 1.2})$$

In practice, the integration boundaries are limited by the object size. Following the basic properties of Fourier transforms, the derivative $\hat{\sigma}$ of a surface is represented in Fourier space by a product of the surface $\hat{\Sigma}(k)$ and the corresponding spatial frequency k :

$$F\left[\frac{d\Sigma(x)}{dx}\right] = 2\pi k \hat{\Sigma}(k) \quad (\text{eq. 1.3})$$

As one can notice that the differentiation acts indeed as an amplitude magnifier for increasing spatial frequency, which means that the small height deviations are easier to detect for increasing k -value of a spatial frequency components. Since an optical slope measurement with sub-millimetre lateral resolution can be easily done, such metrological tools have enormous potential in resolving small height deviations - a much more complicated task to be accomplished when measuring directly in the height domain.

The property expressed by equation 1.3 has another significant consequence for measuring a surface in the slope domain. Namely, a typical surface has a height variation spectrum where the amplitude for small values of k (long spatial wavelengths) is much larger than that of the features characterized by large k values. In general, such a spectrum is typical for most polished surfaces [3]: one can imagine, for example, that while polishing a surface it is easy to produce high flatness quality over a small area, but the absolute flatness will degrade with increasing area size. Such a hypothetical surface is presented in figure 1.3, where a steep spectral density in height leads to a flat slope spectrum due to the k magnification.

A consequence of this property for practical applications is that different kind of objects can be measured easily using the same slope sensitivity. A single instrument without any modifications could measure large, strongly deformed objects, as well as small surface features with height deviations on the nanometre scale. In other words, that feature guarantees high flexibility as well as the high dynamic range of the slope-based metrology. One must be aware, however, that the total slope range from a surface is the integral of all the slope components; therefore, the dynamic range will be smaller if the surface consists of many different surface structures superimposed on each other.

The measurement of topography in the slope domain has another strong benefit. As we will explain later in this thesis, topography is reconstructed from a slope measurement by integrating the slope. Although the surface reconstruction requires additional processing time, it can improve the measurement accuracy dramatically, since many measurement errors can be corrected during such computation. This is possible by using redundant information, which is naturally acquired by deflectometers. This topic is discussed in more detail in chapter 1.4.

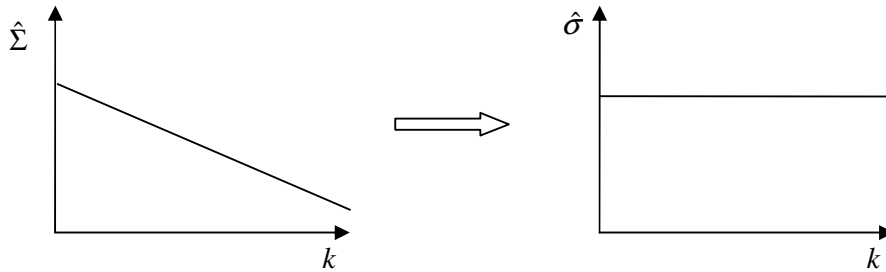


Figure 1.3. A typical height amplitude spectrum $\hat{\Sigma}(k)$ of a polished surface [3] and the corresponding slope amplitude spectrum $\hat{\sigma}(k)$.

1.3. Principle of 3D-deflectometry

Optical Slope Measurement

Optical Slope Measurement (OSM) describes a group of methods for measuring a surface slope by means of an optical beam which is deflected by the surface. In these methods, the slope vector is measured by applying the law of reflection (figure 1.4). The law of reflection is based on two facts:

- The angle of incidence (angle between an incident beam and the surface normal at the incidence point) is equal to the reflection angle (angle between the normal and the reflected beam).
- The incident beam, the surface normal and the deflected beam lie in a common plane, called the plane-of-incidence.

This is called specular reflection, and it holds for most of well-polished surfaces. Hence, by measuring the deflection angle, the local slope vector can be determined.

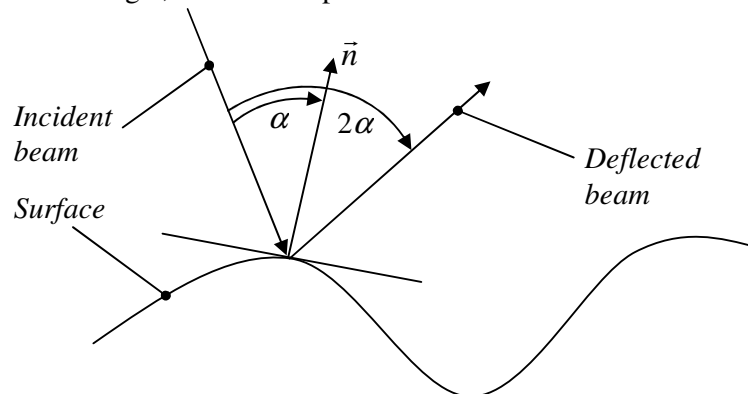


Figure 1.4. Relation between the surface normal \vec{n} (slope vector) and angles of an incidence and deflection of an optical beam (α and 2α , respectively).

In practice, all OSM methods are based on a common principle: the angle of the deflected beam is measured from its displacement in the focal plane of a lens. We explain that principle using the example of an autocollimator (ACT), which in many aspects resembles the deflectometry concept. An autocollimator is a pure slope-measuring device, in the sense that it measures very small angular changes of a surface, independently of distance. The basic layout of a modern autocollimator is depicted and explained in figure 1.5.

Using the fundamental property of the focusing lenses, the angle of the deflected beam can be measured from displacement in the detection plane. Applying the small angle approximation, mechanical tilt of the mirror σ can be calculated from a linear relation:

$$\sigma = \frac{\Delta\xi}{2f} \quad (\text{eq.1.4})$$

where $\Delta\xi$ is the image displacement at the detection plane and f the focal length of the objective. Equation 1.4 will be called the autocollimator formula, and it is fundamental to all OSM methods. It is essential to realize that the primary property being measured is the beam displacement $\Delta\xi$. This implies that one of the basic components of any OSM device is a position sensitive detector. The scaling parameter is the focal length f of the objective. The objective serves as a magnifier, influencing the slope sensitivity of the device. Thus, to reach high slope sensitivity, either a high-resolution position sensitive detector or a long focal length objective must be used. For the first autocollimators f used to be the essential parameter, since the beam displacement used to be measured by an eye-piece with a grid scale located in the detection plane. In modern ACTs, accurate position-sensitive detectors are used, which enable to reach very high sensitivity using a relatively small f . Typical angular resolution for a standard ACT is 0.02 μrad with a range of 10 mrad [6,7].

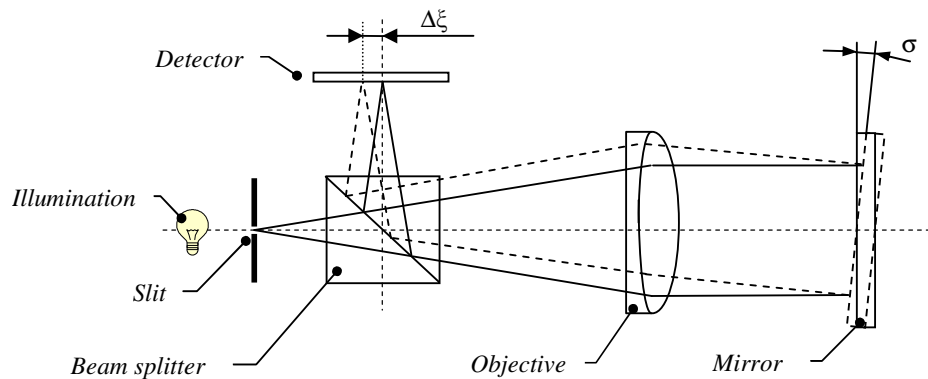


Figure 1.5. Optical layout of an autocollimator. The image of a pinhole or a slit, located at the rear focal plane of an objective, is projected to infinity and reflected back by a mirror. The reflected beam is re-imaged in the focal plane of the objective (detection plane). A tilt (slope) of the mirror σ is transformed into displacement $\Delta\xi$ of the reflected image at the position sensitive detector, which is located in the detection plane. The light source and the detector are separated by a beam splitter [4,5].

Fast Optical Scanning

The term “Fast Optical Scanning” describes the first slope measurement method based on the deflectometry principle [1]. In the past, “Fast Optical Scanning” (FOS) and “Deflectometry”

were used synonymously. Nowadays, more and more often deflectometry describes a group of slope measurement techniques [10-15] and the original FOS concept is often called scanning- or laser deflectometry.

Fast Optical Scanning is a fast, line-scanning technique, and measures the local slope vector of a surface across the scan line. We will explain the FOS principle using the example of an instrument built at Philips Applied Technologies for testing long, flat mirrors [9]. The basic layout of a FOS deflectometer is depicted in figure 1.6. Inside the instrument, a laser beam falls on an optical deflector (typically an oscillating mirror), where it is transformed into a flat scanning fan of beams. The deflector is located at the rear focal plane of a large scan lens. Thus, when the scanning beam passes the lens, the angular scan is converted into a telecentric lateral scan of a reflective surface-under-test (SUT). The telecentric fan of beams, reflected back by the object, is focused onto a two-dimensional position-sensitive detector located at the rear focal plane of the same scan lens. To separate the location of the deflector and the detector, both are used slightly off-axis relative to the scan lens. Such a design avoids using a beam splitter which could introduce false reflections on the detector – usually difficult to eliminate. Since the folding angle is small, a slight dependence between a lateral position of the probing beam and surface height variation can usually be neglected.

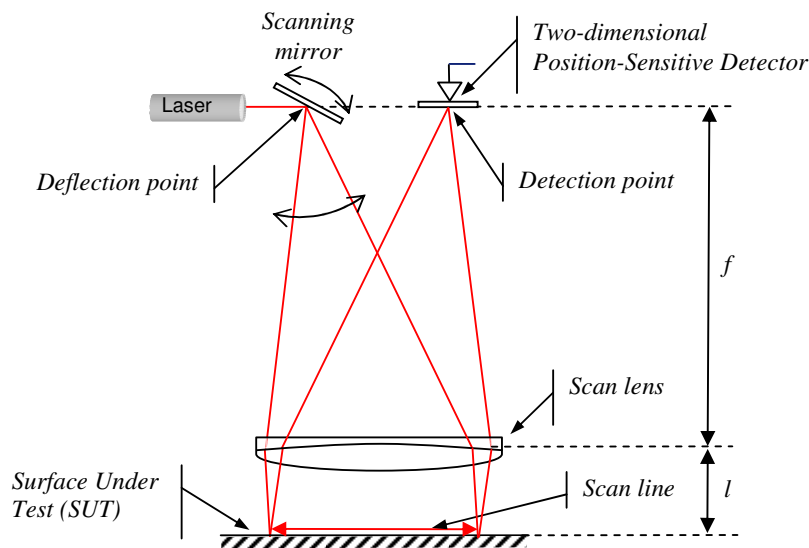


Figure 1.6. Basic layout of the Fast Optical Scanning deflectometer. An oscillating mirror at the focal plane of the scanning lens results in a telecentric scan of the surface. An angular variation of the scanning beam, reflected by the object, indicates the local slope vector of the surface. The beam angle is measured by the two-dimensional Position-Sensitive Detector at the rear focal plane of the scan lens.

One can imagine that the FOS setup is an autocollimator-like instrument, in which a single beam projected to infinity by the objective is replaced by a telecentric fan of beams. However, using FOS, we are able to measure with high lateral resolution the surface slope along the scan line, instead of only a mean slope vector, as with the ACT. For each position along the scan line, the OSM principle applies, and the local slope can be quantified using equation 1.6. Since the slope sensing is achieved by a two-dimensional position-sensitive detector, both coordinates of the local slope vector are measured simultaneously. Figure 1.7

presents an example of slope signals produced by the deflectometer. Since FOS is a typical scanning system, the slope coordinate measured in the direction of scanning is usually called the scan slope, and the perpendicular coordinate is called the cross-scan slope. The scan slope indicates an optical differentiation along the scan line (slope profile); the cross-scan slope indicates torsion or warpage across the scan line.

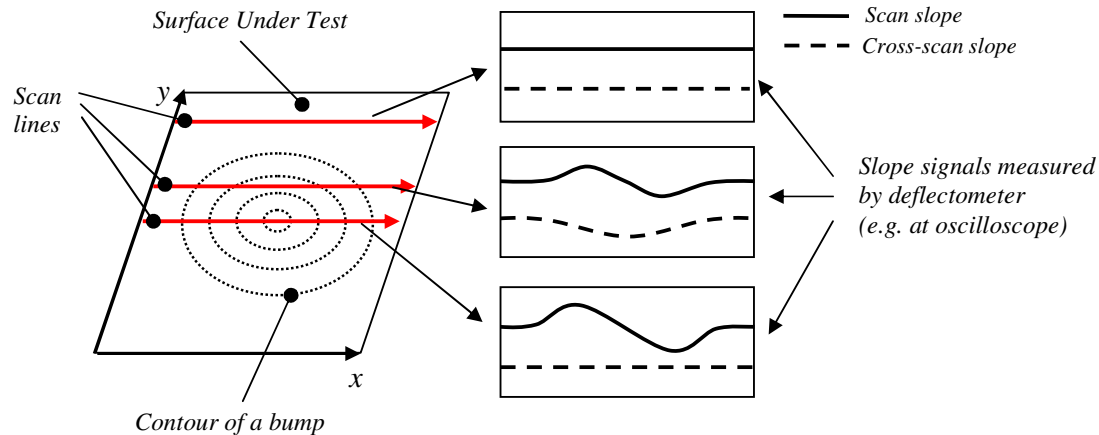


Figure 1.7. Example of the response of a slope measurement by FOS to a bump on a surface. The scan slope represents the slope component measured in the direction of scanning; the cross-scan slope represents the component perpendicular the scan direction. The three scan lines represent separate measurements.

3D-deflectometry

3D-deflectometry is a surface scan technique where an optical line scan is combined with a mechanical translation [27]. The optical scan is performed by a FOS deflectometer. During the scan, the object is translated in the cross-scan direction, so line after line, a complete surface is scanned. The cross-scan translation is performed by a linear translation stage (figure 1.8).

During this two-dimensional scan, the local slope is being measured in the scan- and in cross-scan directions. Therefore, after a single translation, a complete map of local slope vectors of the surface is achieved. The vector map is given by two Cartesian arrays, each representing one slope component. The scan strategy for 3D-deflectometry is explained schematically in figure 1.9². Between subsequent line-scans, the scanning beam retraces to the start-of-scan position. Since the optical scan is very fast, in practice the object is translated continuously and the scan lines are at a slight angle with respect to the scan-slope axis.

Using the proposed scan strategy, the complete two-dimensional map of the local slope vectors is acquired after a single translation. As we will explain in the next section, such a scan leads to double redundancy in the slope data without losing throughput. The redundant information can be used to improve accuracy of surface reconstruction algorithms.

² Typically for scanning systems, a 3D deflectometer performs a top-down scan, which might lead to some confusion concerning the Cartesian coordinate system (as depicted in figure 1.8). In fact, the scan is based on matrix geometry, where the scan is represented by an array with the first pixel in the upper, left corner of the measurement area.

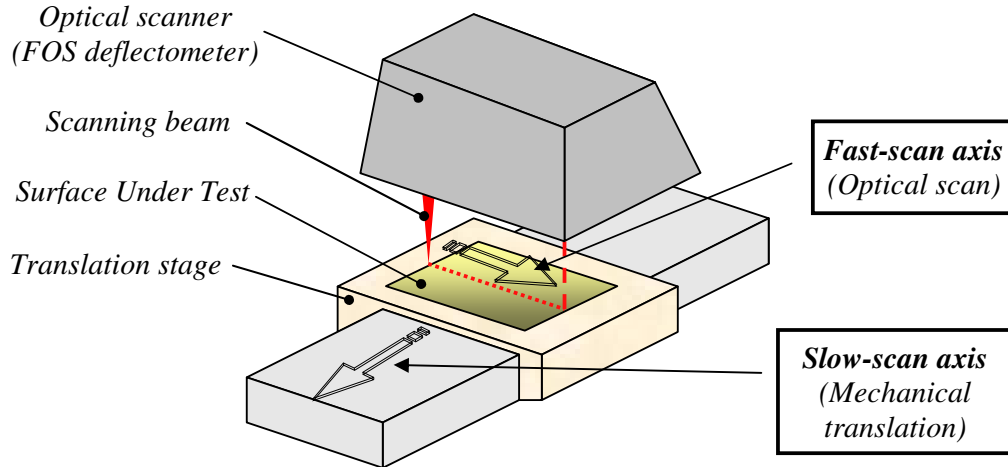


Figure 1.8. Basic lay-out of a 3D-deflectometer.

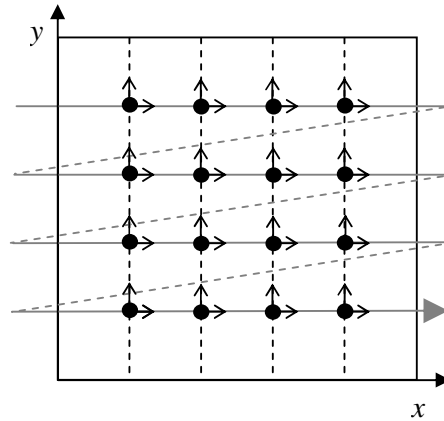


Fig 1.9. Scan strategy for 3D-deflectometry, with x the fast scan axis (optical scan) and y the cross-scan axis (mechanical translation). Solid lines: optical scan, dashed lines: scan retrace, dots: sampling points, arrows: slope ordinates being measured.

1.4. Surface reconstruction from a slope measurement

Basic definitions

We define a surface by the height coordinate $\Sigma(x,y)$ and the lateral coordinates (x,y) . For the sake of simplicity, we assume a Cartesian coordinate system (although it is not a necessity for slope measurements and the subsequent surface reconstruction). A local slope vector is defined as:

$$\vec{\sigma} = (\sigma_x, \sigma_y) = [\partial\Sigma/\partial x, \partial\Sigma/\partial y] \quad (\text{eq. 1.5})$$

To introduce the reconstruction procedure of height information from slopes, we consider the simplest example, where a single height profile is reconstructed from a line-measurement. The profile reconstruction requires information of only a single slope component, measured in the profile direction. For the sake of simplicity again, we assume that the measurement path is a straight line parallel to the x -axis of the object. Since the slope measurement represents differentiation of the surface, the height information can be retrieved from the

integral of the measurement data. The height profile is reconstructed by the linear integration of the measured slope component:

$$\Sigma(x, y_0) = \int_0^x \sigma_x(x', y_0) dx' + C \quad (\text{eq.1.6})$$

with x' the running variable and $C = \Sigma(x'=0)$ the integration constant, which introduces an arbitrary height offset to the reconstructed height profile (therefore the absolute height information cannot be retrieved from a slope measurement).

Simple surface integration

An example of a direct application of the linear integration for a surface reconstruction is given in figure 1.10. In this simplest integration routine, the three-dimensional surface information is obtained by combining many line profiles Σ_x reconstructed from σ_x slope component and placing them next to each other. However, the surface cannot be reconstructed from the Σ_x profiles alone. This is due to presence of the integration constant C that introduces an unknown offset between the profiles. Therefore, at least one additional profile Σ_y is needed in the algorithm to provide information about the relative offsets.

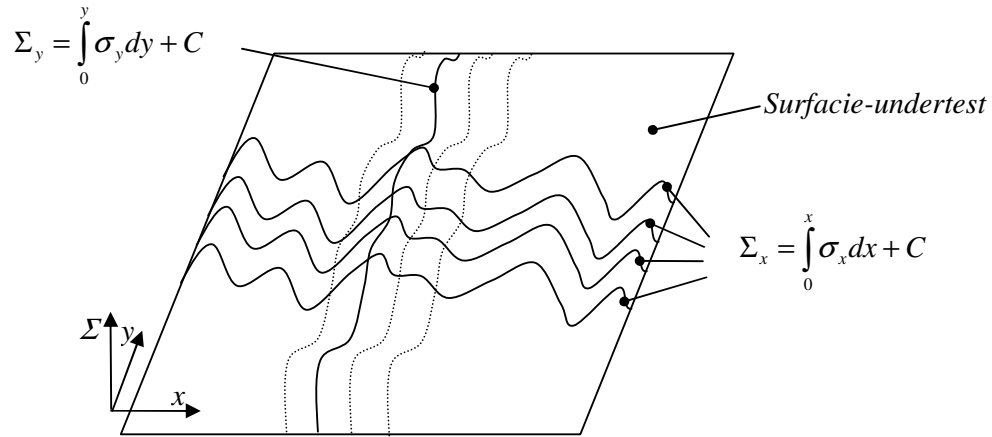


Figure 1.10. Basic surface reconstruction from slope measurements. The surface is reproduced by many height profiles Σ_x reconstructed in the x -direction. A single Σ_y profile, reconstructed in y -direction is used to determine the height offset between the Σ_x profiles.

Reconstruction errors

In figure 1.11 we show that different integration paths can be chosen to reconstruct the height difference between points p_0 and p . Since at the macroscopic scale a surface can be treated as continuous, theoretically all those paths should lead to the same result. In practice differences in height values will occur. The measured field is no longer conservative because of integration and measurement errors. We will discuss the main sources of those errors.

First, any optical slope measurement uses an optical beam with finite lateral dimension on the surface. The beam averages the slope information over a certain area. Therefore the measured slope information is not an exact derivative of the surface, but the result of a weighted average over the beam cross-section. Thus, we define a new parameter that we call the measured slope. By analogy to the real slope vector, the measured slope is given by two

components $\tilde{\sigma}_x$ and $\tilde{\sigma}_y$ (the tilde symbol indicates convolution with an optical beam). The optical convolution acts as a low-pass filter, precluding the exact reconstruction of the surface; for the measured slope, the amplitude of short spatial wavelengths (in particular those close shorter than the beam size) is attenuated.

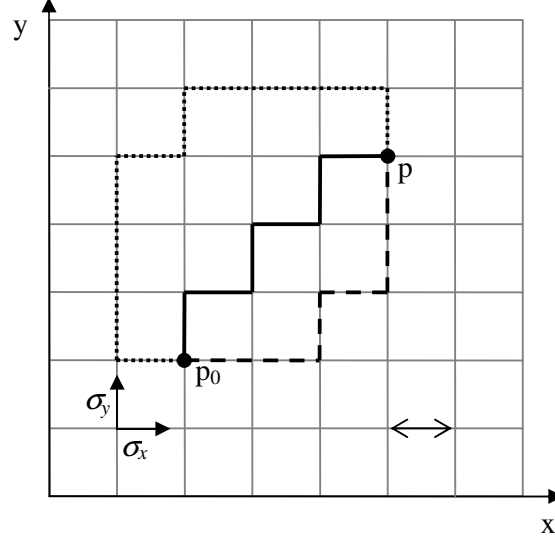


Figure 1.11. Multiple integration paths for reconstructing the height difference between points p_0 and p . The grid represents a Cartesian array of the measured slopes.

The second source of errors is that the slope is measured at discrete points. Therefore, the integral in the surface reconstruction must be substituted by the corresponding sum, calculated by numerical means, such as for instance:

$$\tilde{\Sigma}(x, y_0) = \sum_{L=0}^{N=x/\Delta x} \tilde{\sigma}_x(x_L, y_0) \Delta x + C \quad (\text{eq. 1.7})$$

with $\tilde{\Sigma}$ a profile reconstructed from the measured slope by means of a numerical integration. Sampling of the slope information provides discontinuity of the surface, which leads to a discretization error in the topography reconstruction. The discretization error can be reduced by using a more advanced numerical integration method such as the Simpson rule, the trapezoidal rule, instead of the simple summation of slopes.

Finally, any measurement includes some uncertainty level. Therefore, disregarding the numerical integration errors, the measured accuracy suffers from systematic and random measurement errors, inherent to any metrology system. In general, the reconstructed profile can be represented as:

$$\tilde{\Sigma} = \Sigma + \delta\Sigma_R + \delta\Sigma_S \quad (\text{eq. 1.8})$$

where $\delta\Sigma_R$ and $\delta\Sigma_S$ are the systematic and the random error components, respectively.

The systematic errors can be eliminated by calibration. The random errors (like noise due to airflow or the ground vibrations) cannot be corrected by definition. When a linear integration is applied to retrieve the height information, the measurement uncertainty (RMS) due to the random errors will propagate along the measurement path:

$$\delta\Sigma_R = \sqrt{N} \delta\sigma * \Delta x \quad (\text{eq. 1.9})$$

where N is the number of samples along the integration path.

One can see that the measurement problems mentioned above are inherent to any surface measuring system. Finite probe dimension (whether of an optical wavefront or of a mechanical device), space-separation of the measurement points, and the measurement inaccuracy set natural limits in metrology. Due to measurement errors, the measurement field is not conservative. The main difference between a slope measurement and a direct height measurement is the integration of the measured data which leads to error propagation during the topography reconstruction. The error will increase with the area size and/or with higher lateral resolution (since in both cases the number of the integrated samples increases). Therefore, the surface integration algorithm presented in figure 1.11, has very limited usability. Although computing time for such a method is small, the algorithm is very sensitive to measurement errors and not accurate enough for most real measurements.

Advanced surface integration

The accuracy of the reconstructed surface profile from measured slopes can be increased if the measurement is repeated and the resulting height reconstructions averaged. In this case, the measurement uncertainty due to random slope errors would be:

$$\delta\Sigma_R = \frac{\sqrt{N}}{\sqrt{n}} \delta\sigma * \Delta x \quad (\text{eq. 1.10})$$

where n is the number of averages.

Such a multiple measurement is introduced virtually when a surface map of slopes is measured. Referring to figure 1.11, it is apparent that there are many independent integration paths that could be chosen to reconstruct the height difference between the points p_0 and p . If the result of the calculated height values is averaged, the measurement error is reduced following equation 1.10. The question is how many independent paths exist for such a reconstruction method.

Using figure 1.11 as the most general example and assuming the array size $N \times N$ samples (thus $2N^2$ slope ordinates) and the length of the integration path N , one could find that as a zero-order estimate, the number of independent integration paths is:

$$n = \frac{2N^2}{N} = 2N \quad (\text{eq. 1.11})$$

Hence, the reconstruction inaccuracy due to random errors is:

$$\delta\Sigma_R = \frac{\sqrt{2}}{2} \delta\sigma * \Delta x \approx 0.7 \delta\sigma * \Delta x \quad (\text{eq. 1.12})$$

We can see that the error propagation problem is eliminated by using the large redundancy in the measurement data, when both the slope components across a surface are measured simultaneously and an advanced integration procedure is used for the surface reconstruction.

A long-known measurement strategy using redundancy of the slope measurement for surface reconstruction consists of multiple perpendicular and diagonal line measurements (figure 1.12) [26]. The method is used for measuring large flats (e.g., a-few-square-meter-large granite tables), when the flatness is reconstructed from discrete slope measurement (e.g. using an autocollimator or a liquid- or a gravity lever sensor). Because of the similarity of the scan path to the pattern on the British national flag, the method is called occasionally the “Union Jack method” [26]. The drawback of the “Union Jack” is the lower throughput, since

the surface is measured more than once. This is not a problem in 3D-deflectometry since the complete set of slopes is obtained after a single measurement.

Recently, many other advanced mathematical algorithms are being developed for the problem of surface reconstruction from slopes [17-23]. They usually are based on iterations or least-square solutions for the error reduction. By using the enormous information redundancy, they exhibit the “self-healing” property, leading to strong reduction of the influence of noise and local measurement errors. Thus, although optical slope measurement methods require additional post-processing, the measurement accuracy can be increased using information redundancy – which is simply not present in a direct height measurement.

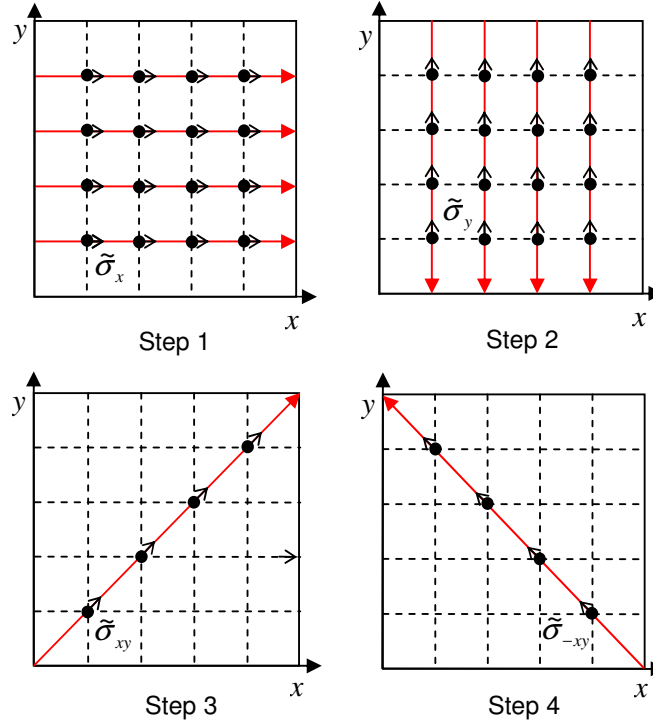


Fig 1.12. “Union Jack” measurement strategy, used for measuring of large flats. The scan is based on a rectangular grid, with additional diagonal scans [26].

1.5 Design limits

The need in the integrated circuit industry is to have a compact instrument that characterizes with high accuracy large-area wafers in a short time with high spatial resolution and large dynamic range. It is clear that all these conditions cannot be met in a single Optical Slope Measuring instrument. As we will explain, the ultimate limiting factor is the diffractive angular spread inherent to any laser beam. For the sake of simplicity, we will limit our discussion to a laser beam with a Gaussian intensity profile, although this consideration could be extended for any spot shape.

From diffraction theory, the spot size at the waist of a laser beam is inherently limited to its full divergence angle θ_0 by the relation:

$$d_0 = \frac{4\lambda}{\pi\theta_0} \quad (\text{eq. 1.13})$$

The smaller the spot size d_0 , the more the laser beam diverges in the far field. Along the propagation axis z , the diameter d_z of the Gaussian beam evolves as:

$$d_z = d_0 \sqrt{1 + (z/z_R)^2} \quad (\text{eq. 1.14})$$

where z_R is the Rayleigh range:

$$z_R = \frac{\pi d_0^2}{4\lambda} \quad (\text{eq. 1.15})$$

The beam divergence and the focal length define the beam size d_f in the focal plane of the scan lens is:

$$d_f = \theta_0 f \quad (\text{eq. 1.16})$$

The interpretation of this equation for deflectometry is straightforward: when the spot size d_0 on the surface-under-test decreases, the beam size at the detector increases proportionally to d_0^{-1} . In the following example we will show the implications of this fundamental property for the design of a deflectometer.

Slope resolution

First, the diffractive spread introduces a limit to the accuracy of a slope measurement. The absolute accuracy in determining the beam position on the detector is fundamentally limited by experimental conditions such as shot-noise of the detector, airborne noise such as turbulence and lens aberrations. As a consequence, the beam position uncertainty is fraction of the beam size itself. Therefore, following 1.16, the more precisely we locate the measured slope using a finer spot size (thus larger θ_0), the less accurate the measurement itself will be (due to increased d_f). This feature does not depend on the specific optical system used. Hence, we can define the slope resolution limit as:

$$\delta\sigma \geq \frac{\theta_0}{2 \cdot 10^n} \quad (\text{eq. 1.17})$$

where, by rule of thumb, n ranges from 1 to 3 depending on the measurement conditions. The factor two in the denominator takes into account the fact that the measured deflection of the reflected beam equals twice the slope of the surface.

In practice, when the lateral resolution of the measurement is relatively low, the influence of the beam divergence on the slope resolution can be neglected, e.g. when $d_0 = 5$ mm, $\lambda = 633$ nm and $n = 3$, the divergence is $\theta_0 = 161$ μ rad and the slope resolution limit is $\delta\sigma = 0.08$ μ rad only. This estimation is relevant for autocollimators – in this case, the slope resolution is defined rather by the detector resolution than by the optical limit. On the other hand, for systems like a deflectometer, where the lateral resolution is much higher, the divergence can become a dominant factor, defining a resolution limit in the slope measurement (figure 1.13). For example, it is practically impossible to reach a slope resolution of 1 μ rad with with a spot size $d_0 < 300$ μ m (using a red laser).

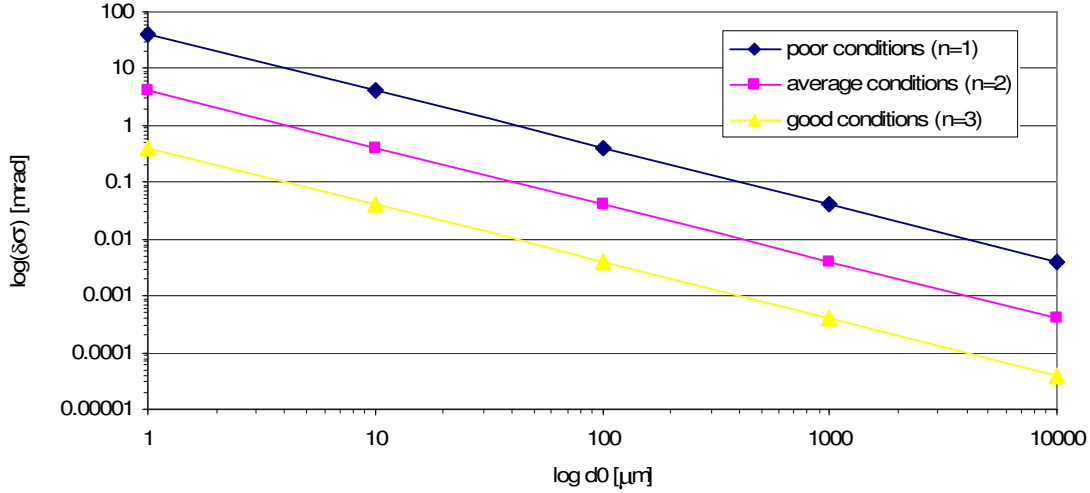


Figure 1.13. The fundamental limit of the slope resolution of an optical slope measurement using a red laser ($\lambda = 633 \text{ nm}$), as a function of the lateral resolution of the system and the measurement conditions.

Dynamic range

Another wish for measurement systems is a large dynamic range of the measured property. In case of OSM systems, the dynamic range can be increased by using a larger detector. Furthermore, a larger detector makes the measurement more accurate since the beam is not truncated by the detector; otherwise the beam displacement measurement is affected by a convolution of the detector area with the beam profile. Therefore, to reach a large dynamic range and high linearity of the detector response, OSM systems are usually designed such that the detector size meets the condition that $D_{\text{det}} \gg d_f$.

On the other hand, in order to reach high displacement resolution and short response time of a position-sensitive detector like a PSD or a CCD, its aperture should be as small as possible. Again these demands are contradictory, especially for high-lateral-resolution systems, where the beam size on the detector is large. As a first approximation, we can assume that the limiting case for the slope measurement with a high lateral resolution is when $D_{\text{det}} \geq 2d_f$. Converting this requirement into the slope range:

$$\sigma_{\text{max}} = \frac{\theta_0}{4} \quad (\text{eq. 1.18})$$

where σ_{mac} is the maximum amplitude of the slope detection. One consequence of this approach is that for a certain detector size (e.g. limited by a maximum allowed bandwidth) the slope range defines the maximum lateral resolution of the system. By combining equations 1.17 and 1.18, one can find the limit of the dynamic range of this “optimum” design:

$$\frac{\delta\sigma}{2\sigma_{\text{max}}} \geq 1:1000 \quad (\text{eq. 1.19})$$

where we assume $n = 3$. This is not a fundamental limit of FOS – a higher dynamic range can be reached, but only by sacrificing either the measurement time (by choosing a larger detector), or by decreasing the lateral resolution.

Measurement time

Following the above discussion one can expect another important design limit in FOS – the minimum measurement time, as a function of its lateral resolution. Neglecting the duty cycle of the scanning system, we can estimate the total measurement time for FOS as:

$$T = N^2 \tau \quad (\text{eq. 1.20})$$

where N^2 is the number of samples for a $N \times N$ sampling grid and τ is the response time of the detector due to its bandwidth limit. The number of samples is related directly to the lateral resolution of the system: the higher the resolution, the more samples need to be acquired. In optical scanning, the lateral resolution can be associated with the spot size on the object d_0 . For our consideration we assume the step size $\Delta x = 0.5d_0$ (figure 1.14), corresponding to a two fold over-sampling. Hence, we can define the number of samples for a two-dimensional scan:

$$N^2 = 4A / d_0^2 \quad (\text{eq. 1.21})$$

where A is the inspection area. Assuming the use of a Position-Sensitive Diode (PSD) for slope sensing, the response time is limited by its sheet resistance and the junction capacitance (Appendix C1). Since the later is proportional to the detector area, we can define the PSD response time approximately as:

$$\tau = \Xi A_{\text{det}} \quad (\text{eq. 1.22})$$

where Ξ is the response time per unit area and A_{det} is the detector area.

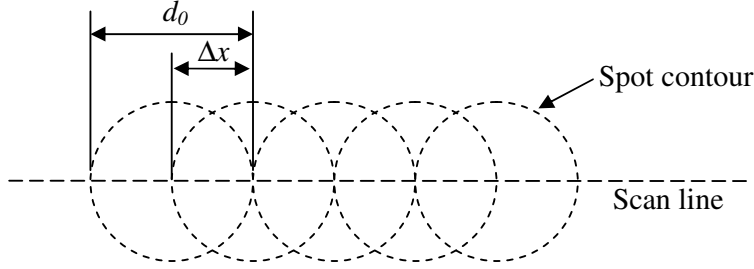


Figure 1.14 Location of the sampled spots for twofold over-sampling.

The detector size is defined by a beam size in the focal plane and by the slope range. By using equations 1.13 and 1.16 one could find that:

$$A_{\text{det}} = (d_f + 2\xi_{\text{max}})^2 = \left(\frac{4\lambda f}{\pi d_0} + 4f\sigma_{\text{max}} \right)^2 = 16f^2 \left(\frac{\lambda}{\pi d_0} + \sigma_{\text{max}} \right)^2 \quad (\text{eq. 1.23})$$

Substituting equations 1.21-1.23 into equation 1.20, we obtain a design formula for the measurement time:

$$T = 64 \frac{A}{d_0^2} \left(\frac{\lambda}{\pi d_0} + \sigma_{\text{max}} \right)^2 \Xi f^2 \quad (\text{eq. 1.24})$$

In practice, one finds that in most applications $\theta_0 \ll \sigma_{\text{max}}$ and the influence of the beam divergence can be neglected. In result equation 1.24 simplifies to:

$$T = 64 \frac{A}{d_0^2} \sigma_{\text{max}}^2 \Xi f^2 \quad (\text{eq. 1.25})$$

On the other hand, one could think of an application with a very high lateral resolution, where the relation $\theta_0 \gg \sigma_{\max}$ holds. In this case, equation 1.24 can be approximated by:

$$T = \frac{64}{\pi^2} \frac{A}{d_0^4} \Xi \lambda^2 f^2 \quad (\text{eq 1.26})$$

As one can expect, a consequence of increasing the lateral resolution (smaller d_0) is a longer measurement time. This relation is strongly enhanced for a high resolution system, where the beam divergence results in $T \sim 1/d_0^4$.

In table 1.1 we summarize our discussion on the design limits by giving a numerical example for the performance of a typical FOS system as a function of its lateral resolution (represented by the spot size).

Table 1.1. Influence of the lateral resolution – as represented by the spot size - on the performance of a typical 3D-deflectometer. System parameters: $A = 0.3 \times 0.3 \text{ m}^2$ (e.g. a 300 mm silicon wafer), $\sigma_{\max} = 10 \text{ mrad}$, $\Xi = 6 \cdot 10^{-3} \text{ s/m}^2$, $\lambda = 633 \text{ nm}$, $f = 1000 \text{ mm}$ and $n = 3$. In FOS configurations with low lateral resolutions, the slope resolution and the dynamic range are limited mainly by resolution of the position-sensitive element itself.

System mode	Spot size (mm)	Slope resolution (mrad)	Dynamic range	Measurement time ³
Autocollimator	10	0.001	1:10000	< 1 s
Standard	1	0.001	1:10000	3.6 s
High-resolution	0.1	0.01	1:2000	8 min
Ultra-high resolution	0.01	0.1	1:200	4 days
Diffraction limit	0.001	1	1:20	49 years

Following table 1.1, the spot size of any FOS system will be always much larger than the theoretical diffraction limit, which is on the order of the wavelength of the light source used. Ultra-high resolution deflectometers with a spot size less than 100 μm already require a major trade-off in their critical performance parameters - slope resolution, dynamic range, or measurement time - that is unacceptable for many practical applications. In this thesis we limit ourselves to the design of high resolution deflectometers, using the available knowledge on standard deflectometers as a starting point.

We can summarize that, as any other metrology method, deflectometry cannot bring an ultimate solution for a customer. The performance limitations are due to the fundamental properties of light, i.e., the diffractive divergence of a laser beam. Specification of a system can be improved by using light with a shorter wavelength, but in general, the design of a deflectometer always requires a careful trade-off between the system parameters and the user requirements.

³ This estimation is valid for optical measurement systems like FOS, where the beam displacement is measured in the focal plane of the objective. One must be aware, that other systems exist, like e.g. retro-scanners, where the reflected beam passes through the deflector, and an optical magnification can be applied. In this case, however, a similar relation could be derived where the speed-limiting factor would be the bandwidth of a deflector.

1.6 Contents of this thesis

This thesis describes the design of a 3D-deflectometry system and some basic research on deflectometry. The author tried to find a proper balance between self-explanation of the chapters, and a storyline throughout the complete thesis. To make the text easier to read, major calculations and some topics which are beyond the main storyline are covered in appendixes.

In chapter 1 a general introduction is given, explaining basic industrial motivation for the research, as well as introducing the reader to the 3D-deflectometry concept. This includes optical scanning, surface reconstruction from slope measurements and the major design limitations of the method. Chapter 2 gives more details on the background of this research. The metrology problems in the semiconductor industry are discussed and a brief review of modern surface metrology is given. An important conclusion of this chapter is a specification for a new flatness-testing instrument. In chapter 3, we explain in detail the implementation of a Fast Optical Scanning measurement, the basis for a 3D-deflectometry system. In this chapter we also describe the first feasibility tests for the new system using a test-bed instrument. We also present the first-ever topography results by a 3D-deflectometry (verified by an independent measurement). The actual design of the new 3D-deflectometer is described in chapter 4. This chapter presents the detailed boundary conditions for the design and the optimum choice of the system components. In addition, we introduce some suggestions for improving the performance by accepting extra restrictions in applicability or demanding a larger calibration effort. We call this technology tuning, distinguishing it from the more fundamental design effort. In chapter 5 we describe the 3D-deflectometer, the final result of this project. As the reader will notice, the system specifications differ from the optimum design. This is due to limitations in the project's budget, the manpower available, and the internal project goals. Chapter 6 considers the calibration of the system, including analysis of the measurement uncertainties. The analysis and experiments lead to the final specification of the instrument. Chapter 7 is dedicated to the readers interested in real industrial applications. Therefore, several examples of measurements of industrial objects, mostly patterned wafers and substrates, are presented. Lastly, the system's performance is verified and compared with other surface measurement methods. In chapter 8, we summarize this project and we give concluding remarks on the research and the design presented in this thesis. The author tries to give a fair analysis of major achievements and emerging opportunities for the 3D-deflectometry.

1.7. References

- [1] F. Lo, M. Shell, *Intel passes milestones toward production-level EUV Lithography*, Technology Intel Magazine, 1-5 (September 2004)
- [2] Dr. Peter Wagner, Siltronic – private communication
- [3] J.M. Bennett, L. Mattsson, *Introduction to surface roughness and scattering*, Optical Society of America (1989),
- [4] D.F. Home, *Optical instruments and their applications*, Adam Hilger Bristol (1980)
- [5] R.S. Siroki, M. P. Kothiyal, *Optical components, systems, and measurement techniques*, Marcel Dekker, New York (1991)
- [6] Möeller-Wedel GmbH, Web site: www.moeller-wedel-optical.com

- [7] TriOptics GmbH, Web site: www.trioptics.com
- [8] W.D. van Amstel, S.M. Bäumer, J.L. Horijon, *Optical figure testing by scanning deflectometry*, Proc. SPIE **3739**, 283-290 (1999)
- [9] R. Boerhof, J.C.J. van Vliet, *Deflectometer voor vlakheidmeting van optische spiegels*, graduation report, Hogeschool van Utrecht (1998)
- [10] K. Kreske, E. Keren, O. Kafri, *Insights on Moire deflectometry*, Laser & Optronics, 63-66 (October 1988)
- [11] N. Fournier, M. Grédiac, P. A. Paris, Y. Surrel, *Shape measurement of vibrating composite plates by deflectometry*,
- [12] Y. Surrel N. Fournier, M. Grédiac, P. A. Paris, *Phase-Stepped Deflectometry Applied to Shape Measurement of Bent Plates*, Experimental Mechanics **39**, 66-70 (1999)
- [13] C. Horneber, M. Knauer, G. Häusler, *Phase Measuring Deflectometry – a new method to measure reflective surfaces*, Annual Report, university of Erlangen-Nuremberg, Optics department (2000)
- [14] R.D. Geckeler, I. Weingärtner, *Sub-nm topography measurement by deflectometry: flatness standard and wafer nanotopography*, Proc. SPIE **4779**, 1-12 (2002)
- [15] M. Rosete-Aguilar, R. Diaz-Uribe, *Profile testing of spherical surfaces by laser deflectometry*, Applied Optics, **32** (1993)
- [16] K. Szwedowicz, *3D-deflectometry platform for inspection of 110mm silicon wafers*, Stan Ackermans Instituut, Eindhoven (2003)
- [17] C. Elster, I. Weingärtner, *High-accuracy reconstruction of a function $f(x)$ when only $df(x)/dx$ is known at discrete measurement points*, poster at SPIE Annual Meeting in Seattle (Juli 2002)
- [18] W. Zou, Z. Zhang, *Generalized wave-front reconstruction algorithms applied in a Shack-Hartmann test*, Applied Optics **39**, 250-268, (2000)
- [19] W.H. Southwell, *Wave-front estimation from wave-front slope measurements*, J. Opt. Soc. Am. **70**, 998-1006 (1980)
- [20] L.P. Yaroslavsky, J. Campos, A. Moreno, M.J. Yzuel, *Comparison of three methods of integration to obtain the profile from its slope*, Proc. SPIE **4829**, 902-904 (2003)
- [21] I. Weingärtner, P. Thomsen-Schmidt, M. Schultz, *Methods, errors influences and limits for the ultra-precise measurement of slope and figure for large, slightly non-flat or steep complex surfaces*
- [22] M. Grédiac, *Method for surface reconstruction from slope of curvature measurements of rectangular areas*, Applied Optics, **36**, 4823-4829 (1997)
- [23] J. Campos, L. P. Yaroslavsky, A. Moreno, M. J. Yzuel, *Integration in the Fourier domain for restoration of a function from its slope: comparison of four methods*, Optical Letters, **27**, 1986-1988 (2002)
- [24] J.G. Skinner, *Comment on light beam deflectors*, Appl. Opt. **3**, 1504 (1964)
- [25] L. Beiser, *Laser scanning systems in Laser Applications*, M. Ross, Academic press, 53-159, New York (1974)
- [26] L. Beiser, *Fundamental architecture of optical scanning systems*, Applied Optics, **34**, 7307-7317 (1995)
- [27] W. van Amstel, *Design considerations and first global design for fast optical scanning deflectometry*, Philips internal report, CTB556-02-5088, (2002)

Chapter 2

Modern surface metrology

In this chapter we present the industrial requirements for inspection of silicon wafers. We start with a general description of surface characterization. Then, in section 2.2, we describe metrology problems in the semiconductor industry for different steps of wafer manufacturing/processing, and give a specification for a new nanopography inspection tool. In section 2.3 we present a brief review of modern surface metrology. Finally, we give concluding remarks for this chapter in section 2.4.

2.1. General remarks on surface characterization

Surface metrology characterizes the height profile $\Sigma(x)$ and its deviations from the desired surface form. This characterization can be done in the spatial domain or in the spatial frequency domain. The most intuitive description is in the spatial domain, since it refers to the usual way in which we experience three dimensional space. In this case, the surface is represented usually as a graph of height versus position. Alternatively, we can describe a surface in the spatial frequency domain, using the spatial frequency $k = \Lambda^{-1}$ [m^{-1}] as variable, with Λ the spatial wavelength of the surface feature. By applying Fourier analysis to $\Sigma(x)$ we can determine the amplitude spectrum $\hat{\Sigma}(k)$ of the surface. In this case, the surface is represented by the power spectrum. A major benefit of using the frequency transform for surface description is that various surface wavelengths can be easily extracted. Consequently, metrology equipment can be more easily assessed using the instrumental response function. In this thesis we will use both ways of surface description, choosing one or the other, depending on which one is more suitable for the particular discussion.

The most common classification of industrial surfaces splits topography into three spatial regions, namely: form, waviness and roughness [1-8]. Form, called also geometry or figure, refers to a general, macroscopic shape, characterized by spatial wavelengths $\Lambda \geq 1$ mm. A form of optical components is obtained usually by grinding or lapping, which ensures that errors in form are microscopic laterally (greater than 1 mm extent) and vertically (less than 500 nm). Form deviations can be the result of many factors, such as bending, low frequency deviations of machining tool, or stress patterns in the component.

The final stage of surface generation usually involves the polishing removal of surface irregularities left over by the process of lapping. These may occur as random or periodic height variations, called roughness and waviness, respectively. They extend over the whole surface where they are collectively termed surface texture or localized imperfections. These

remaining microscopic defects of texture and imperfections are collectively referred to as the finish of the surface. Waviness consists of Mid Spatial Frequency (MSFR) components, corresponding to wavelengths of $20 \mu\text{m} \leq \Lambda \leq 1 \text{ mm}$. It is usually caused by instabilities in the machining process, such as imbalances in a grinding wheel, or by deliberate actions in the machining process. Roughness contains the shortest wavelength, called High Spatial Frequencies (HSFR), which are defined by $\Lambda \leq 20 \mu\text{m}$. Roughness is usually introduced by the action of the cutting tool or by the machining process, but may include other factors such as the structure of the material. Roughness, waviness or form is rarely found in isolation. Most surfaces are a combination of all three and it is customary to assess them separately by various spatial-filtering techniques. The filters are described by the cut-off wavelengths Λ_{\min} and Λ_{\max} or by the corresponding spatial bandwidth k_{\max} and k_{\min} .

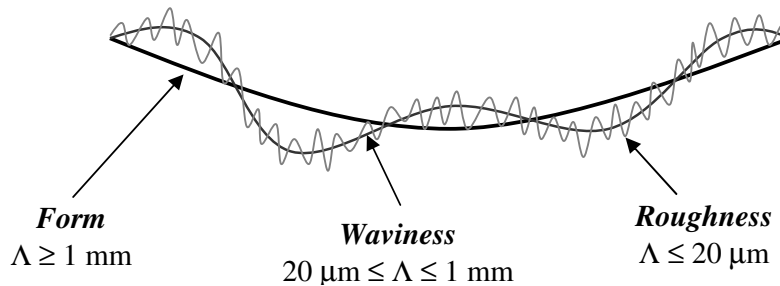


Figure 2.1 Surface height parameters described in spatial wavelength Λ .

The wavelength ranges given above are indicative only. There is no single definition of a surface description; the wavelength where the roughness becomes the waviness, or the waviness turns into form depends on the application – for example, the waviness element on an optical lens may be considered as roughness on an automotive part [1]. Nevertheless, by following these general rules for surface description, one can distinguish metrology tasks related to figure testing from those for the roughness measurement.

The semiconductor industry introduced its own standards for surface description [5] as follows:

- Geometry, characterized by $\Lambda \geq 1 \text{ mm}$
- Nanotopography, with $20 \text{ mm} \leq \Lambda \leq 0.2 \text{ mm}$
- Roughness, with $\Lambda \leq 0.5 \text{ mm}$

The regions are separated by applying spatial filtering – typically using Gaussian, Double Gaussian or 5-th order Butterworth filters. The general filter requirements are described in reference [6]. An example of a typical surface spectrum for a 300 mm silicon wafer is shown schematically in figure 2.2 (adopted from [9]).

The slope spectrum is of basic interest for the deflectometry design presented in this thesis. To convert the height information into the slope domain, we will describe the surface by a Fourier series. This way, the slope information can be obtained easily by multiplying the height amplitude $\hat{\Sigma}(k)$ by the corresponding spatial frequency k (eq. 1.3). The result of such an analysis is given in table 2.1.

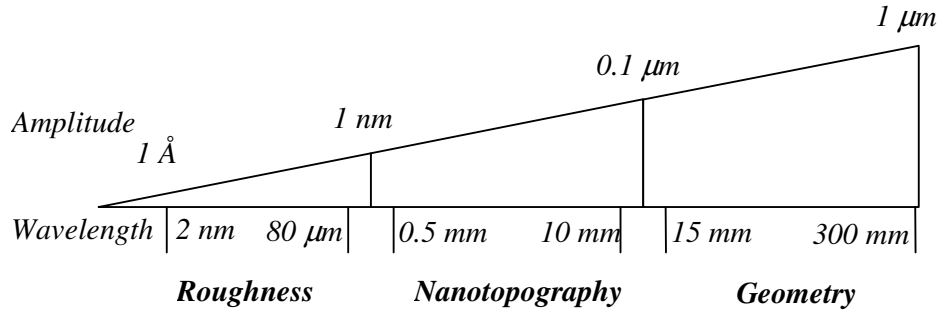


Figure 2.2. Typical characteristic of surface height deviation in the spatial domain of a silicon wafer [9].

Table 2.1. Characteristic values of the spatial frequency k and corresponding height amplitude $\hat{\Sigma}(k)$ of commercially available silicon wafers. The last entry line “Gravity” indicates the deviation of the geometry due to bending by gravity for an edge-supported 12” wafer.

Range	k (m^{-1})	$\hat{\Sigma}(k)$ (m)	$2\pi k\hat{\Sigma}(k)$	σ (mrad)
Atomic scale	10^{10}	10^{-10}	6.3	1500
Roughness	$5 \cdot 10^8 - 10^4$	$10^{-10} - 10^{-9}$	$6 \cdot 10^{-5} - 3 \cdot 10^{-1}$	0.06 – 300
Nanotopography	$2 \cdot 10^3 - 10^3$	$10^{-8} - 10^{-7}$	$10^{-4} - 6 \cdot 10^{-4}$	0.1 – 0.6
Geometry	70 – 1.7	$10^{-7} - 2 \cdot 10^{-6}$	$2 \cdot 10^{-5} - 4 \cdot 10^{-5}$	0.02 – 0.04
Gravity	1.7	$150 \cdot 10^{-6}$	-	2

The lowest spatial frequency in the height spectrum in figure 2.2 is due to the wafer geometry on a flat support. However, during the measurement, the wafers are supported often by a ring carried at the outer edge of a wafer. The ring carrier causes bending due to gravity, with sag of about 150 μm for a 300 mm wafer. Since the bending is parabolic in first approximation, in table 2.1 we used the parabolic approximation to find the corresponding slope range. This method gives more accurate results than the Fourier series analysis. One can see that the bending gives the major contribution to the slope range for a typical silicon wafer (besides of the slope on atomic-scale, which cannot be detected with a deflectometer).

2.2. Surface metrology for wafer inspection

Wafer manufacturing

Silicon wafers are manufactured from single mono-crystals. Single silicon crystal ingots are produced by Czochralski (CZ) or Magnetic Field Applied (MCZ) methods [10]. In the CZ method (used for ICs), highly pure silicon - only a few ppm impurities - is melted in a quartz crucible with dopants. Then, a thin silicon seed is dipped into the melt in the desired crystal orientation and slowly pulled out such that silicon from the melt solidifies on it to create a single crystal. Once the crystal has been made, it is sliced into single wafers. This is done by an inner-diameter saw (ID) or, by a more modern, multi-wire sawing method (MWS). The wire saws are more efficient because an entire ingot can be sliced at once. Next, newly sliced

wafers have to be machined to reach smooth, flat and plane-parallel surface. This is done by grinding with fine diamond grinding wheels, by lapping with special suspensions, or by a combination of both processes. Although these processes help achieve a highly flat surface, mechanical interference damages the crystal structure to a depth of several micrometers. This surface layer of the damaged structure is removed by an etching process prior to the chemical mechanical polishing (CMP). The CMP process applies two kinds of polishing pads – the soft pads and the stiff pads. Depending on the stiffness, the polishing pads are able to adjust to flatness deviations. The pads size defines the planarization length (PL), which extends from 2 mm (soft pads) to 10 mm (stiff pads). One can see that the size and stiffness of the pads affect the interaction with the polished surface. For example, one main concern is the interaction of the nanotopography wavelength Λ with the planarization length. Through the polishing quality, this can lead to yield concerns in shallow trench isolation process (STI) or lithography [6, 9-12]. This is explained schematically in figure 2.3 (adopted from [13]). As presented in the figure, in the case of using long and stiff pads, the polishing can lead to non-uniform film thinning, which is a main concern in the STI process, where the nitride film thinning can be critical in determining device yield. Using soft pads, the uniform film thickness is conserved, but high flatness deviations of short wavelengths remain a serious concern for the lithography process.

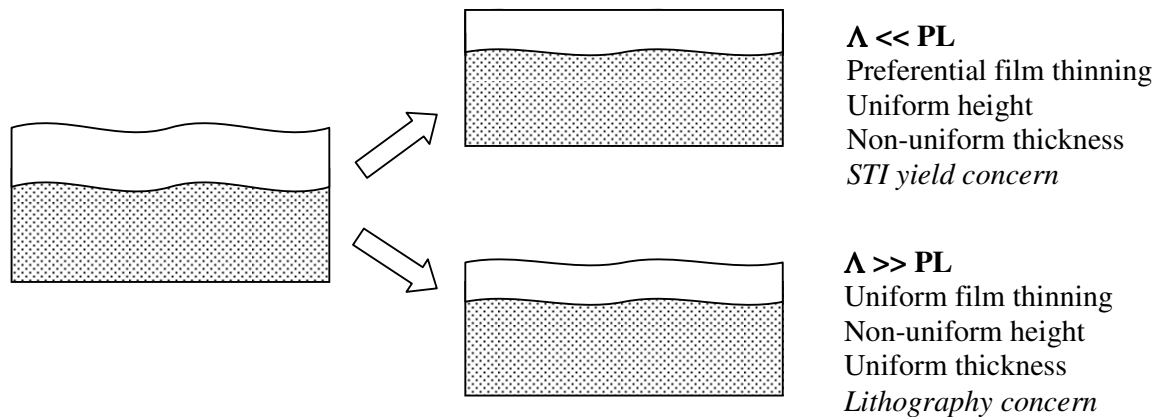


Figure 2.3. The importance of relative length scales in nanotopography and CMP [13], with PL the planarization length of the polishing process.

The interaction between topography and the CMP process, which is crucial for the final flatness specification of the substrate, is not yet fully understood. So far, the process is studied carefully by using special test wafers with various polishing parameters. Therefore, the availability of proper metrology tools is essential for both the process control in the factory and for understanding and modelling the CMP process.

The nanotopography spatial range is essential for a quantitative description of the polishing, (see section 2.1). Requirements for the lateral resolution for a nanotopography inspection tool are given by the Semi M49 standard [2]. The document specifies the spatial bandwidth of the response function of the instrument, expressed by spatial cut-off frequencies $k_{\min} = 0.05 \text{ mm}^{-1}$

and $k_{\max} = 2.5 \text{ mm}^{-1}$ (corresponding to $\Lambda_{\max} = 20 \text{ mm}$ and $\Lambda_{\min} = 0.4 \text{ mm}$, respectively). The cut-offs correspond to an attenuation of 0.5 (-6 dB) for the amplitude of a sinusoidal surface. The required vertical accuracy of the inspection is related to the depth of focus (DoF) for the lithographic system. In general, local planarity in a die-size area must be better than this DoF. Currently, IC industry requires local planarity $\leq 50 \text{ nm}$ for each $10 \times 10 \text{ mm}^2$ area on a wafer substrate. In order to reach such high accuracy, about 30 times finer measurement resolution in height is required [17] – this brings the requirement for RMS height resolution to 1.7 nm per $10 \times 10 \text{ mm}^2$ area.

Another requirement is that the measurement should also be fast, with the measurement rate for $\varnothing 300 \text{ mm}$ wafers of 40 wafers per hour, which, together with wafer handling gives a measurement time requirement of $T = 1 \text{ min/wafer}$ [6].

Wafer processing

During complete IC processing many functional layers are produced on a single wafer. Each functional layer is passivated with a dielectric film, and, before a new IC structure is produced on top of the previous one, the surface flatness must be restored to meet the initial lithography requirements again. Therefore, the wafer metrology demands for the IC industry are similar to those for wafer manufacturing. As we explained in chapter 1.1, the reason for high flatness requirements for a wafer surface is the limited depth of focus of litho-machines during the IC production. An example of the polishing problem for IC structure is explained schematically in figure 2.4. In the example the problem is caused by an under-exposed via (contact connecting two metallization levels).

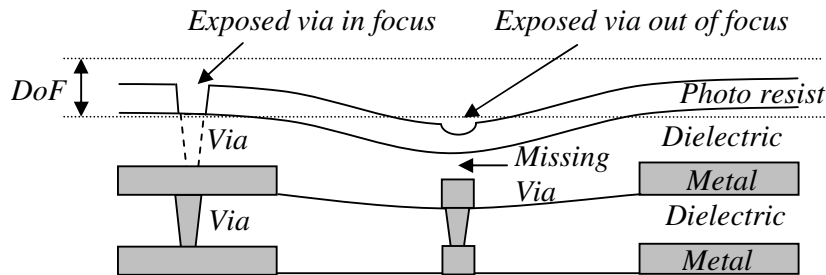


Figure 2.4. Defective exposure of inter-metallic connections (via) during IC manufacturing by optical projection lithography.

The flatness is restored again by the CMP process. One key metric for CMP performance is the global planarity, which is a measure of the lithographical depth-of-focus budget that has been consumed by the polishing process. The global planarization is characterized by spatial bandwidth $k_{\min} = 3.3 \cdot 10^{-3} \text{ mm}^{-1}$ and $k_{\max} = 10 \text{ mm}^{-1}$. The vertical resolution is $\delta\Sigma = 10 \text{ nm}$ per die, with typical die size extending from $2 \times 2 \text{ mm}^2$ to $25 \times 25 \text{ mm}^2$. The wafers are measured on a flat vacuum chuck, and the vertical range is $\Delta\Sigma \leq 2 \mu\text{m}$. The measurement can be done per dye or across the whole wafer.

CMP control affects also the local planarization, which, however, is of less interest for deflectometry as it is related to inspection with a high lateral resolution of about $0.1 \mu\text{m}$ [18].

In table 2.2 we summarize the user requirements for a nanotopography inspection tool for silicon wafers, for wafer manufacturers and users.

Table 2.2. Summary of user requirements for nanotopography inspection of silicon wafers

parameter	Wafer manufacturing	IC industry
$k_{\min} (\Lambda_{\max})$	0.05 mm ⁻¹ (20 mm)	0.05 mm ⁻¹ (20 mm)
$k_{\max} (\Lambda_{\min})$	2.5 mm ⁻¹ (0.4 mm)	10 mm ⁻¹ (0.1 mm)
$\Delta\Sigma$	150 μm/300 mm wafer	2 μm
$\delta\Sigma$	1.7 nm/10x10 mm ²	10 nm / 2x2 - 25x25 mm ²
T	60 s/wafer	60 s/wafer

2.3. Surface metrology techniques

2.3.1. Introduction to surface metrology

There are several ways of classifying surface metrology systems [19-22]. Generally, the instruments can be split into figure-testing and profilers, depending on their lateral resolution and the measurement area. Figure-testing instruments are characterized by larger measurement area but usually lower lateral resolution. They are represented mostly by large interferometers. Profilers are used to measure surface finish, surface roughness and geometry of small features on the object [21,22]. Typically, the inspection area of profilers is limited to tens of millimetres, but the minimum field of view can be as small as a few nanometres. Some interferometers, however, can be used for both profiling and figure testing (i.e., by replacing the objective or by lateral stitching).

Another classification splits measurements into contact and non-contact types. The major type of contact measurements is represented by stylus probes, which perform mechanical scans across a surface, looking at the height variation of the probe. The non-contact measurements are performed by optical methods like interferometry and focus sensors, or by capacity measurements.

The measurement strategy splits the surface metrology instruments into single-point measurements, line measurements and surface-mapping devices. The main difference among these categories is the way in which a 3D-image of the surface topography is produced. Surface mappers, like interferometers or wave-front sensors, take a 2D-measurement in a single step. Single-point instruments (e.g. the Atomic Force Microscopes and the Focus Sensors) and line measuring instruments (e.g. some Styli and scanning autocollimators) are scanning devices. These need an additional mechanical translation of the surface-under-test for the instrument to compile many profiles into a full surface scan.

Recently, another division of surface metrology has become common: direct height measurements and slope measurements. In the last few years, various surface-slope measurements have been used for topography measurements. One of the reasons is that a slope measurement is in principle independent on height variation (see section 1.2), which is a fundamental problem for any direct height measurement. Another reason is the availability of fast computers that decrease drastically the calculation time necessary for topography

reconstruction. Slope measurements are performed by differential and shearing interferometers, wavefront sensors and deflectometers (including scanning autocollimators). An elegant and powerful method for comparing performance of various surface-measuring instruments is the Stedman diagram [50-52]. The performance of instruments is tested by their response to sinusoidal profiles and compared by mapping their limits in the amplitude-wavelength (AW) space. Using sinusoidal waves is mathematically and practically convenient, since they are widely used to model surface perturbation. Moreover, any finite profile may be resolved into sinusoidal components by Fourier analysis. Mapping in AW space allows the relation between different limits to be seen, and the instrument performance to be compared. Four topographical parameters of the specific instrument can be easily visualized: height, lateral wavelength, slope and curvature. Since a wide range of A- and W-values is used, the AW space is plotted on logarithmic scales. A general example of the Stedman diagram is shown in figure 2.5.

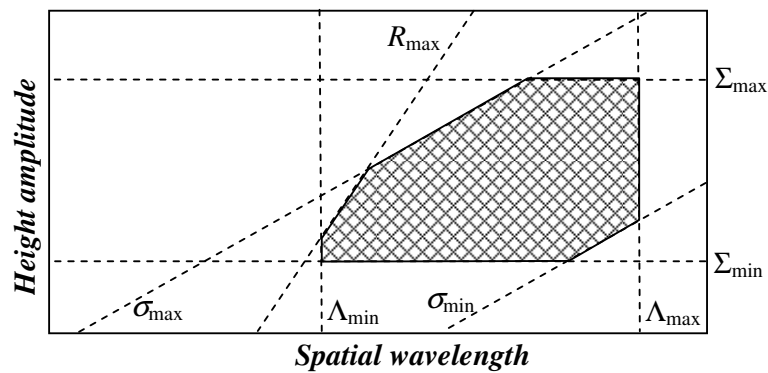


Figure 2.5. Stedman diagram: parametric limits in AW space. The height amplitude and the spatial wavelength scales are logarithmic. The limiting parameters in the figure correspond to: Σ_{\max} largest height difference, Σ_{\min} smallest height difference, Λ_{\max} longest wavelength, Λ_{\min} shortest wavelength, σ_{\max} steepest slope, σ_{\min} max slope error, R_{\max} sharpest curvature.

The diagram contains a series of lines, each corresponding to a specific parameter. Collectively, they intersect to define a polygonal zone that represents the effective working range of the instrument. This way, the general system performance can be studied easily by decoupling limiting factors and considering them separately. The characteristic of the instrument is limited by the vertical and horizontal boundaries, which are related to the vertical and lateral resolution and range of the device. Together, they define a rectangular operational window of the instrument. The boundaries at an angle to the sides of this window are introduced by the limits in surface slope and/or curvature. These are limited by the instrument features like the probe geometry.

The size and shape of the polygonal working zone of an instrument gives a “footprint” that is valuable for both the user and the designer interested in improving the performance. The height of the figure gives the amplitude to resolution ratio, the width of the figure corresponds to the bandwidth capability for responding to surface wavelengths, and the area gives a measure of instrument versatility. Each edge of the polygon is associated with a particular component or parameter. The length of any side is an indication of how critical that

component is in determining the performance of the instrument. These guidelines are summarized in figure 2.6.

As a final remark on the Stedman diagram, one could see that it does not give complete information for the system performance. An important parameter that is not taken into account is the measurement time. Thus, two instruments may have a similar working range in AW-space, though a very different performance due to the measurement time (and price!).

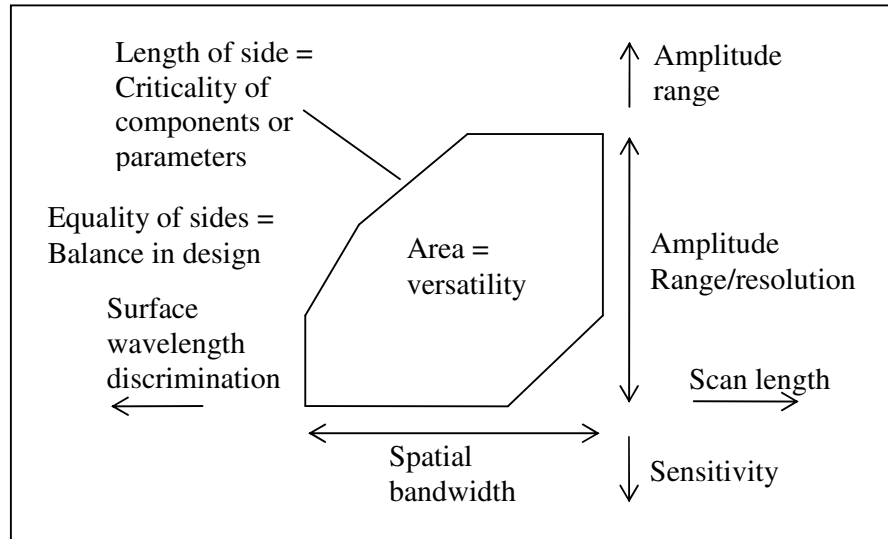


Figure 2.6. Instrument performance window (Stedman diagram) in AW-space.

2.3.2. Stylus profilers

The stylus represents the most common group of contact surface profilers [1, 21-26]. A height profile is determined by moving a small-tipped probe across the surface and sensing the height variations of the tip. Styli can determine a surface roughness with RMS height resolution down to 5 nm and lateral resolution of 0.1 to 0.2 μm .

The lateral resolution of the probe is limited by the shape and dimensions of the stylus tip. The output of the measurement is a convolution of the surface and the tip. When the tip is smaller and sharper, the surface can be followed better. However, if the tip becomes too sharp, the local force on the surface under the tip can cause a deformation that leads to inaccurate height measurement or even damage of the surface. Therefore, for high lateral resolution, the load is decreased and the measurement speed significantly reduced. The most sensitive styli use tip radii of tenths of micrometer and tip loading of a few milligrams. In this case, measurement of a few thousand points takes many minutes.

To increase the accuracy of the measurement, a vibration isolation system must be applied. Furthermore, most stylus profilers use a reference datum. Usually, the reference is a skid that is moved across the surface with the stylus, or is scanned by a second, large radius probe in a fixed relationship to the measuring stylus.

Styli are so popular for surface profilers because of their high accuracy and high lateral resolution. The disadvantages, however, are that they are contact measurements, the measurement area is small and the measurement time is long. In figure 2.7 we present a Stedman diagram for a Stylus instrument.

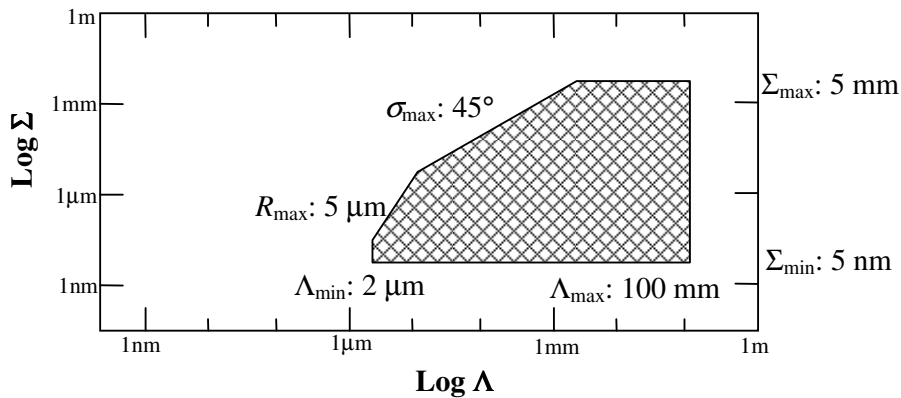


Figure 2.7. Stedman diagram for a stylus instrument [52]

2.3.3 Scanning Probe Microscopes

Scanning probe microscopes (SPM's) resemble a stylus instrument in the sense that a fine tip is used to scan a surface. SPM's, however, are designed to measure a surface for atomic-resolution applications, thus they apply different measuring methods than Styli. From many different SPM methods, two are the most popular, namely: the Scanning Tunnelling Microscopy (STM) and the Atomic Force Microscopy (AFM) [1, 21, 25, 26].

In the STM, a tunnelling current is measured by a tip, which is moved toward the surface. To measure the tunnelling current, a voltage is applied between the tip and the surface. This requirement limits the application to conductive materials. Materials such as glass or conductors with dielectric layer cannot be measured. STM is a non-contact measurement method, but the tunnelling current can be sensed when the tip is no further than 1 nm from the surface.

In contrast to the STM, the AFM can measure any kind of surface. An AFM works in two modes, with either a repulsive or an attractive atomic force being measured. In the repulsive mode, the scanning tip is in a cantilever position, making contact with the surface, and its deflection is measured.

In the attractive mode, no contact is made to the surface, and the tip must be kept 2-20 nm above the surface. The high-frequency vibration of the tip caused by the attractive atomic force is measured. In this mode the vertical resolution is somewhat lower than in repulsive mode.

Scanning Probe Microscopes are calibrated against a traceable standard of approximately the same height range as the measured surface, in order to determine the scale factor.

Scanning Probe Microscopes give high resolution, but they can be applied only to specific applications, since the measurement area is small (only fraction of square mm) and the measurement time long, on the order of a few minutes.

2.3.4. Optical Focus Sensors

Optical Focus Sensors perform a non-contact roughness measurement of finely machined surfaces [21, 27-29]. The functioning of Optical Focus Sensors resembles that of an actuator in a CD player – an optical beam with a large numerical aperture is adjusted so it is being kept focused on the surface. The height of the scanned profile is measured by the actuator

displacement. The 3D-topography can be measured by scanning the surface across both lateral axes. The lateral resolution is limited to about 2 μm by the spot size on the surface. The height can be measured with resolution down to 20 nm. The measurement area is limited only by the number of points and the sampling distance.

Since an optical focus sensor is a null device, the measurement is in principle slow because at each measurement point the focus must be adjusted. If large heights are being measured, the focusing resolution must be coarser to maintain the same measurement speed. If finer focusing is used for wide height ranges, the measurement time increases considerably.

A more modern type of an Optical Focus Sensors is a chromatic probe [29], which can reach a vertical resolution of 10 nm. The measurement principle is similar to other optical focusing sensors, but instead of mechanical focusing, the chromatic aberration of the objective lens is measured. Each wavelength of the white light is focused at different vertical position. By using the confocal principle and a spectroscope, height can be measured without mechanical focusing, thus much faster than for an actuator-based instrument.

2.3.5. Interferometers

One of the most important techniques in metrology is interferometry [19-22]. Fields of applications and possible interferometric configurations are enormous, and even a brief review is beyond the scope of this thesis. Therefore we will focus on the most important and industrially accepted applications for surface metrology.

Interferometry represents an accurate, fast, and non-contact optical method for surface testing and precise displacement measurement. The advantage of interferometry is that the unit of measured height is the wavelength of light, so the measurement resolution is very high. The method is based on measuring the optical path difference (OPD) between two wavefronts. The OPD can be produced by displacement of the object or deviation from the reference wavefront. The phase difference introduced by the OPD results in the interference pattern, which can be recorded by the human eye or a detector. For typical surface testing, the OPD between the object and a reference surface is reconstructed from the interferometric fringes – contours of equal phase. The fringes are predominantly sinusoidal and separated by $\lambda/2$. Typical pattern detection of static fringes introduces the measurement uncertainty of $\lambda/10$. An example of the basic interferometer is the Fizeau interferometer [21] depicted in figure 2.8.

Basic interferometer set-ups, like Newton or Fizeau, even though trivial, are so powerful that they are often used for optical testing without any technologically advanced equipment. Present surface technology, however, requires height resolution better than is guaranteed by traditional interferometers. Therefore, new interferometric techniques have been developed using computers and digital data processing, like heterodyne interferometry [19, 21, 30, 31] and Phase Shifting Interferometry (PSI) [19, 21, 26, 31]. These techniques have several advantages: the accuracy is high, the measurements are done rapidly without slowly varying influences, low-contrast fringes can be used without sacrificing accuracy, intensity variations across the interference pattern do not influence the result, and the measurements are carried out at fixed points in a grid.

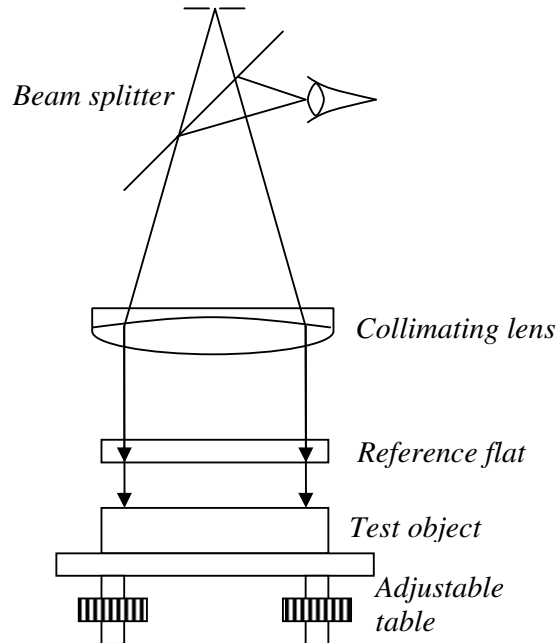


Figure 2.8. Basic layout of the Fizeau interferometer. A beam, collimated by the lens, is reflected by the lower surface of the reference flat, and the upper surface of the test object. The reflected beam is focused onto the eye pupil. The test surface is placed on an adjustable table, so the width of the fringes can be adjusted by changing the angle between test and reference wavefront.

An important drawback of interferometers is that the lateral resolution is limited by the resolution of CCD detectors, commonly used for detection of the fringe pattern. Therefore, only general figure can be measured using traditional and large interferometers. For surface profiling interferometric microscopes are used. They use a standard microscope where the objective is replaced with an interferometric objective based on traditional interferometers, like Michelson, Mirau, Linnik and Fizeau [21, 31].

The most important group of interferometric microscopes is the White Light Interferometer (WLI), known also as low coherence interferometer – shown in figure 2.9. WLI's are often preferred for industrial applications for their combination of repeatable 3D-measurements, high speed and sub-nanometre height resolution. This method can measure average roughness down to 0.1 nm, peak-to-valley height up to several millimetres, with repeatability of 0.1 nm or better [31]. A White Light Interferometer uses a white light source, like a halogen lamp, and is based on the detection of the coherence peak created by two interfering, polychromatic wavefronts. Interferograms obtained with white light sources show fringes of good modulation only when the OPD between two beams is small. This characteristic becomes important when trying to determine large discontinuities in phase, where temporal phase-shifting interferometry is unable to assign the correct order of fringes. In other words, intensity modulation of fringes carries additional information on the OPD. Therefore, WLI allows for the easy identification of the fringe with the best visibility because the contrast falls off so quickly.

As we explained so far, interferometers can be used either with low lateral resolution for inspection of large areas, or with high lateral resolution for small areas. Thus, they fail to provide measurement data of large areas with high resolution, which is required for many applications. This problem is solved by stitching together multiple high-spatial-resolution measurements of adjacent areas on a measured surface. The measurement can be fit together in a global sense or by matching the piston and tilt over the overlap areas. Together with WLI, the stitching procedure introduces probably the most universal interferometric metrology tool. Stitching techniques have also same drawbacks – most importantly, long measurement times. In general, the measurement time increases because of the demand of large field overlap to obtain sufficient accuracy in matching the surface profiles. As shown in [35], about 20 percent overlap is needed for a good trade-off between acceptable repeatability and a minimum number of data sets for stitching. Stitching can be applied in lateral direction, in vertical direction, or in both. Stitching along the vertical axis is used to increase the range of height of the measurement.

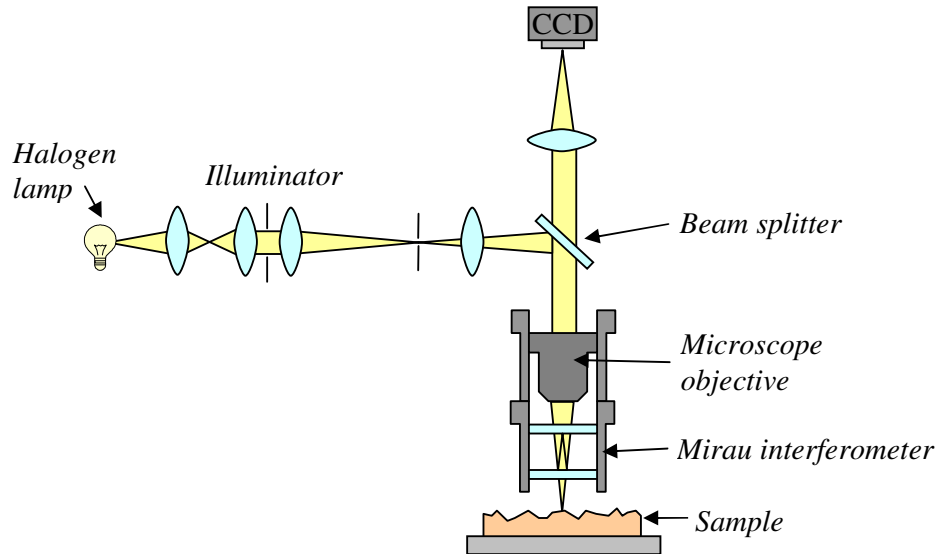


Figure 2.9. Schematic of a white light interferometric microscope

Another category of interferometric profilers use single point devices, where the probing beam is focussed on a single spot on the surface. The surface profile is measured by scanning the surface – similar to the stylus systems, but without physical contact. Although the scanning interferometers can solve the problem of low throughput of stitching interferometers [36], so far they are used rather seldom in industrial metrology.

An interesting evolution of single point interferometers is the differential interferometer [19]. The differential profiling interferometer uses two beams on the surface: one producing the reference wavefront, the other being the actual probing beam. The gradient of the path function is measured instead of a single height value. The differential configuration makes the instruments insensitive to rigid-body motion because this affects both beams in a similar way. Therefore, these instruments have the property of self-reference. In fact, a differential interferometer makes a slope measurement rather than a height measurement. The height is reconstructed by integrating the slope data. Differential interferometric profilers are very accurate and can measure relatively long profiles, since accuracy is in first order independent

on translation quality. The Sommargen's instrument, based on differential principles, provides a measurement with less than 0.1 nm RMS precision [21]. A Long Trance Profiler [38, 39], based on a pencil beam interferometer [37], measures 1500 mm long profiles with height resolution of about 1 nm and accuracy better than 50 nm.

Lateral shearing interferometers [25] also have a differential configuration. The method is based on lateral shearing of the wavefront and obtaining the interference pattern between the original and the displaced wavefronts. Similarly to differential profilers, shearing interferometry is considered a slope-measuring method, and thus topographical reconstruction requires additional data processing. Shearing interferometers are also rarely encountered in industry.

2.3.6. Topography by Optical Slope Measurement

Another class of instruments in surface metrology is represented by methods based on Optical Slope Measurement (OSM). A characteristic for OSM is that the surface slope is measured not from an interference pattern, like in shearing interferometers, but from the displacement in the focal plane of a lens of a reflected probing beam.

A very popular method for measuring topography of long profiles involves an autocollimator (ACT). The straightness or flatness of a profile is obtained by integrating the measured slope. The measurement principle is explained schematically in figure 2.10.

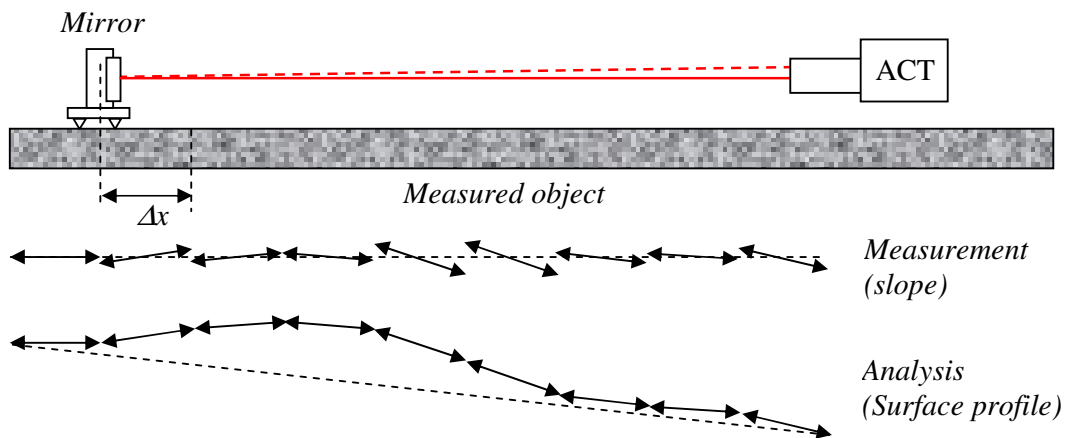


Fig. 2.10. Basic set-up and data analysis for the straightness measurement of long profiles with a slope-measuring device. The slope is measured at discrete points along the profile. To determine the straightness, slope data are numerically integrated.

For reflective surfaces, an ACT itself can become a scanning device. The accuracy of slope measurement is increased if a penta-prism is used for scanning. Using a penta-prism in the way depicted in figure 2.11 results in making the slope measurement independent on the pitch error in the scan direction.

An example of combining an ACT with a scanning penta-prism is the flatness measurement proposed by the National Physical Laboratory [40-43]. The profiler can reproduce a 3D surface topography by combining line measurement with extra translation or rotation of the object. The drawback of the penta-prism method is that the measurement is slow due to the mechanical translation.

The accuracy of scanning autocollimators can be increased further by applying a shearing configuration. An example is an ultra-precise topography measurement by Extended Shear Angle Difference (ESAD) at the ‘‘Physikalisch-Technische Bundesanstalt Braunschweig und Berlin’’ [44-46], which claims reproducibility of a height measurement of 0.15 nm [39].

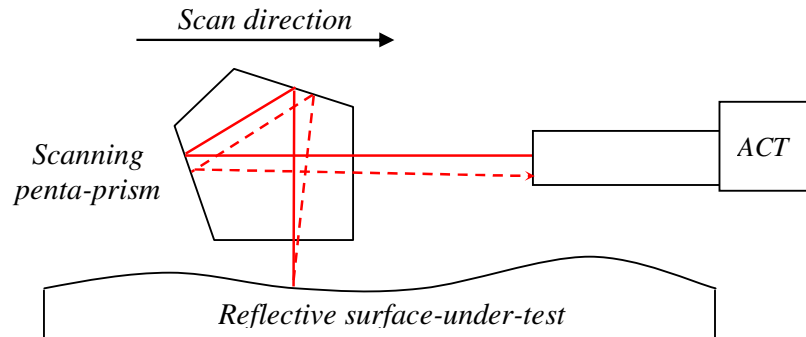


Fig. 2.11. Slope-measuring set-up, used for scanning of self-reflecting surfaces. The penta-prism is used to fold the measuring beam. Scanning of the profile is achieved by translating the penta-prism along the profile.

So far we have described the surface slope measurements based on lateral scanning. The slope measurement can be extended to two-dimensions as well. Two-dimensional slope measurements are represented by the Shack-Hartmann wave-front sensor (SH) [47-49]. The sensor utilizes an array of micro-lenses and an array detector, so that a 2D slope deviation across the incident optical wavefront can be measured. Recently SH sensors have been applied also for 3D-topography measurement [49].

2.4. Concluding remarks on modern surface metrology

Various surface measuring techniques are offered commercially. Since there is no ultimate method, the choice of a measuring device must consider the needs of the specific application, including properties of the surface, lateral and vertical measurement range, resolution and accuracy, measurement time, calibration means, and cost. The most used method is the Stylus-type, unless mechanical contact is undesired. Roughness can be measured using the focus sensor. Reflective and well-polished surfaces are measurable with interferometric profilers. For the highest lateral resolution Scanning Probe Microscopes can be used – but they are slow. Interferometers are well suited for fast and accurate figure measurement of large objects, as well as for fast testing of optical components. For straightness measurements of long profiles, Optical Slope Measurements are best suited. Besides of the measurement parameter, the final choice is often a compromise between cost and measurement specification (e.g., accuracy vs. measurement time).

2.5. References

- [1] Taylor Hobson Company. Web site: www.taylor-hobson.com
- [2] ISO 4287
- [3] ISO 11562 (1996) 2.6, 3.2
- [4] ISO 3274 (1996) 4.4

- [5] SEMI M43 – *Guide for reporting wafer nanotopography*
- [6] SEMI M49 – *Guide for specifying measuring equipment for silicon wafers for 130nm technology generation.*
- [7] L.R. Baker, *Surface metrology of optical components*, course notes, SPIE's 44th Annual Meeting (1999)
- [8] I. Weingärtner, M. Schultz, *High-accuracy interferometric measurement of aspheres*, Proc. SPIE **4778**, 105-118 (2002)
- [9] MEMC Electronic Materials, Inc., *Wafer nanotopography*, Application Note AE-008, (August 2001), www.memc.com
- [10] S. Wolf, R.N. Tauber, *Silicon processing for the VLSI Era: volume 1 – process technology*, Lattice Press, California (1986),
- [11] MEMC Electronic Materials, Inc., Web site: www.memc.com
- [12] B. Lee, D. Boning, W. Baylies, N. Poduje, P. Hester, Y. Xie, J. Valley, C. Koliopoulos, D. Herherington, H. Sun, M. Lacy, *Wafer nanotopography effects on CMP: Experimental validation of modelling Methods*, Materials Research Society (MRS) Spring Meeting, San Francisco, CA (April 2001)
- [13] D. Boning, B. Lee, W. Baylies, N. Poduje, P. Hester, J. Valley, C. Koliopoulos, D. Herherington, *Characterization and modelling of nanotopography effects on CMP*, International CMP symposium, Tokyo (December 2000)
- [14] J.Schlueter, *Trench Wavefare: CMP and Shallow Trench Isolation*, Semiconductor International (October 1999)
- [15] B. Lee, D. Boning, W. Baylies, N. Poduje, J. Valley, *Modeling and mapping of nanotopography interactions with CMP*, Materials Research Society (MRS) Spring Meeting, San Francisco, (April 2002)
- [16] A.C. Diebold, *Handbook of silicon semiconductor metrology*, Marcel Dekker, New York (2001)
- [17] Dr. Peter Wagner, Siltronic AG – *private communication*
- [18] Dr. Erik Jan Lous, Philips Semiconductors – *private communication*
- [19] R.S. Siroki, M. P. Kothiyal, *Optical components, systems, and measurement techniques*, Marcel Dekker, New York (1991)
- [20] D.F. Horne, *Optical production technology*, Adam Hilger, London and Crane Russak, New York (1972)
- [21] D. Malacara, *Optical Shop Testing*, John Wiley & Sons, New York (1992)
- [22] D.J. Whitehouse, *Handbook of surface and nanometrology*, Institute of Physics Publishing (2003)
- [23] J.M. Bennett, *Comparison of instruments for measuring step heights and surface profiles*, Applied Optics, **24**, 3766-3772 (1985)
- [24] J.F. Song, T. V. Vorburger, *Stylus profiling at high resolution and low force*, Applied Optics, **30**, 42-50 (1991)
- [25] KLA-Tencor Company, Web site: www.kla-tencor.com
- [26] Veeco instruments, Inc, Web site: www.veeco.com
- [27] T. Kohno, N. Ozawa, K. Miyamoto, T. Musha, *High precision optical surface sensor*, Applied Optics, **27**, 103-108 (1988)
- [28] Solarius company, Web site: www.solarius-inc.com
- [29] Precitec Optronik Company, Web site: <http://www.precitec-optronik.de/>

- [30] G.E. Sommargeren, *Optical Heterodyne Profilometry*, Applied Optics, **20**, 610-618 (1981)
- [31] A. Olszak, J. Schmit, M. Heaton, *Interferometry: Technology and Applications*, Application Note AN47, Veeco Instruments, Inc, Web site: www.veeco.com
- [32] Zygo Company, Web site: www.zygo.com
- [33] ADE Corporation, Web site: www.ade.com
- [34] Fisba Optik, Web site: www.fisba.ch
- [35] J. Schmit, J. Wyant, *Large field of view, high spatial resolution surface measurement*, Application Note AN504, Veeco Instruments, Inc, www.veeco.com
- [36] M. Zecchino, A. Olszak, *High speed surface measurement with lateral scanning white light interferometry*, Application Note AN502, Veeco Instruments, Inc, www.veeco.com
- [37] K. von Bieren, *Pencil beam interferometer for spherical optical surfaces*, Laser Diagnostic, Proc. SPIE **343**, 101-108 (1982)
- [38] P.Z. Takacs, S. Quia, J. Colbert, *Design of a long trace surface profiler*, Proc. SPIE **749**, 59-64 (1987)
- [39] S. Qian, G. Sostero, P.Z. Takacs, *Precision calibration and systematic error reduction in the long trace profiler*, Optical Engineering, **39**, 304-310 (2000)
- [40] Z. Zhou, T. Zhang, W. Zhou, *Laser profiling for on-line measurement of superfine surfaces*, Applied Optics, **41**, 125-129 (2002)
- [41] A.E. Ennos, M.S. Virdee, *High accuracy profile measurement of quasi-conical mirror surfaces by laser autocollimation*, Precision Engineering, **4**, 5-8 (1982)
- [42] M.S. Virdee, *Nanometrology of optical flats by laser autocollimation*, Surface Topography **1**, 415-425 (1988)
- [43] M.S. Virdee, *A new approach for establishing a reference plane for absolute measurement of shape and flatness with nanometer precision*, National Physical Laboratory report, MOM 114 (1993)
- [44] I. Weingärtner, M. Schultz, C. Elster, *Novel scanning technique for ultra precise measurement of topography*, Proc SPIE **3782**, 306-317 (1999)
- [45] I. Weingärtner, M. Schultz, *Novel scanning technique for ultraprecise measurement of slope and topography of flats, aspheres, and complex surfaces*, Proc. SPIE **3739**, 274-282 (1999)
- [46] R.D. Geckeler, I. Weingärtner, *Sub-nm topography measurement by deflectometry: flatness standard and wafer nanotopography*, Proc. SPIE **4779**, 1-12 (2002)
- [47] L. E. Schmutz, M. Levine, *Hartman sensors detect optical fabrication errors*, Laser Focus World, 111-117, (April 1996)
- [48] J. Ares, T. Mancebo, S. Bara, *Position and displacement sensing with Shack-Hartman wave front sensors*, Applied Optics, **39**, 1511-1520 (2000)
- [49] Wavefront Sciences Company, Web site: www.wavefrontsciences.com
- [50] M. Stedman, *Mapping the performance of surface measuring instruments*, SPIE **803**, 138-142 (1987)
- [51] A. Franks, B. Gale, M. Stedman, *Grazing incidence optics, amplitude-wavelength mapping as unified approach to specification, theory, and metrology*, Appl. Opt., **27**, 1508-1517 (1988)
- [52] G. T. Smith, *Industrial metrology: surface roughness and roundness*, Springer, London, (2002)

Chapter 3

Feasibility study of 3D-deflectometry

In this chapter we present the first test on 3D-deflectometry performed on a test-bed set-up. In section 3.1 we discuss in more detail the basic implementation of a 3D-deflectometer. In section 3.2 we present the test-bed. Next, in section 3.3 we address the main limits in the accuracy of the slope measurement and propose a method for increasing the measurement accuracy by calibrating the instrument with a reference surface. Finally, in section 3.4, we present the first-ever topography results from the test-bed, which are compared with an independent reference measurement by a White Light Interferometer.

3.1. Implementation of Fast Optical Scanning

We will describe a FOS implementation using the example of the instrument built at Philips Applied Technologies for testing of long mirrors (section 1.3) [1,2]. From the design point of view the FOS deflectometer consists of two separate sub-systems: an optical scanner and a slope-measuring device. This approach for describing the FOS system is shown in figure 3.1. Both sub-systems contain a common lens, which serves as scan lens for the scanner, and as objective for the slope measurement. Of course, the scan could also be performed in a different way, for instance, by mechanical translation. However, optical scanning makes FOS fast and less sensitive to the drift and deviations of the mechanical elements.

The scanning sub-system is a flat-field, low inertia galvanometric scanner, having a galvanometric mirror as the active scanning device. The design of the scanner aims at producing a telecentric linear scan, with the waist of the scanning beam located on the surface-under-test (SUT). Since the scan lens has a relatively large focal length (for high sensitivity of the slope detection system), the Free Working Distance (FWD - the distance between the lens and the object) is much shorter than the focal length f of the lens. This relatively short FWD limits the influence of the airborne measurement noise and of the beam position error due to aberrations of the scan lens. In result, the scan lens functions as a telecentric field flattener, and only partially serves for beam focusing. The latter is mainly performed by additional beam shaping optics, located between the light source and the scanning mirror; the beam is already converging toward the lens. Such a configuration classifies the FOS as a combination of a pre-objective- and a post-objective scanner [3-5].

Similar as for autocollimators (ACT's), the deflectometer is in first approximation insensitive to small vertical positioning errors of the surface-under-test (e.g. due to drift, unflatness of the translation axis, or ground vibrations). In contrast to ACT's, the vertical position of the surface-under-test might be limited by the short Rayleigh range z_R of the scanning beam, since the beam is focused on the surface. One can notice, however, that even for spot sizes as

small as $d_0 = 100 \mu\text{m}$, the corresponding Rayleigh range is $z_R = 12 \text{ mm}$ (for $\lambda = 633 \text{ nm}$), which makes negligible any vertical positioning error that may occur during the measurement.

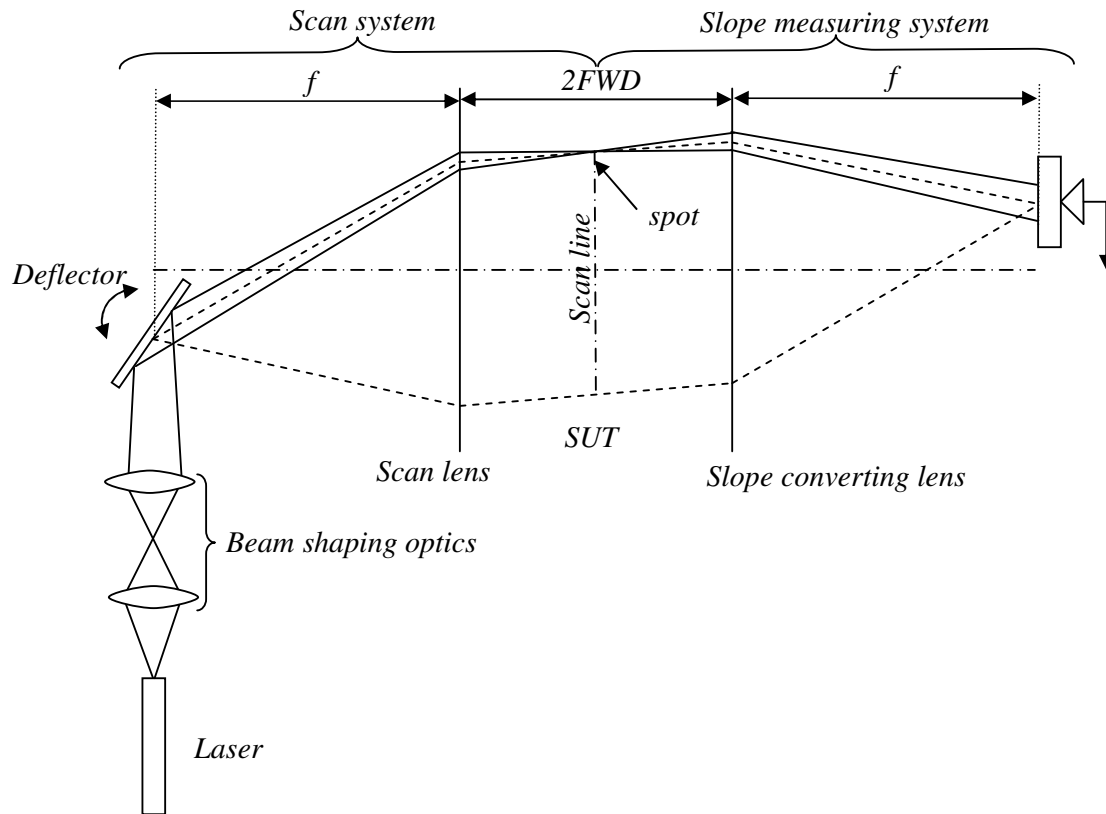


Fig. 3.1. Unfolded layout of the Fast Optical Scanner at Philips Applied Technologies, which virtually separates the deflectometer into two independent systems. The left part of the figure represents the scan system, consisting of a beam deflector and a scan lens. The right part shows the slope measuring system with a large lens that converts deflection of the beam into position on the detector.

The beam displacement is measured by a two-dimensional position-sensitive diode – 2D PSD (Appendix C1). This is a very fast and an accurate detector, thus well suited for FOS. The PSD detection unit (the detector and dedicated preamplifier) produces three analog voltage signals. Two signals, S_ξ and S_η , are related to the beam position on the detector’s surface. They indicate the centre of gravity of the incident light, measured separately along two perpendicular PSD axes: ξ and η . The third signal, S_I , is related to the light intensity on the detector. During the measurement, the PSD signals are sampled and digitised by a data acquisition system. By calibrating the slope detector, the voltage values S_ξ and S_η are converted to the measured slope components $\tilde{\sigma}_x$ and $\tilde{\sigma}_y$, respectively. Typical for scanning techniques, the lateral coordinate in the scan direction is called the “scan axis”, and the coordinate perpendicular the scan axis is called the “cross-scan axis”. Consequently, $\tilde{\sigma}_x$ is called the “scan slope component” and $\tilde{\sigma}_y$ is called the “cross-scan slope component”.

Since the optical system in FOS resembles an ACT, in the first order design, the slope response for both slope components can be calculated from the autocollimator formula (eq. 1.2):

$$\tilde{\sigma}_x = \xi/2f \text{ and } \tilde{\sigma}_y = \eta/2f \quad (\text{eq. 3.1})$$

where ξ and η are the beam displacement on the detector in the x - and y -direction, respectively, and f is the focal length of the objective lens.

3.2. 3D-deflectometry test-bed

To obtain insight in the feasibility of the 3D-deflectometer concept, we have built a test-bed instrument, a 3D-deflectometry platform [6]. This is the hardware and software platform on which the construction of the final instrument (chapter 5) has been based. Using the test-bed, we had the opportunity to test for the first time integration algorithms on real measurement data acquired by a 3D FOS deflectometer. The test bed is composed of a FOS deflectometer (described in sections 1.2 and 3.1) and a Linear Manipulator Module System (LIMMS), which is a translation system from Philips Applied Technologies. The basic specification of the deflectometer is given in table 3.1 and a picture of the instrument is shown in figure 3.2.

Table 3.1. Hardware specification of the FOS Deflectometer for testing of flat mirrors (Philips Applied Technologies).

Element	Specification	Supplier
Light source	Laser diode, 5 mW, $\lambda = 670$ nm	Power Technologies
Optical Deflector	7×7 mm ² galvanometric mirror for bar-code scanners	Philips
Scan lens	$f = 800$ mm, $\varnothing = 150$ mm, standard doublet	Linos
Detector	4×4 mm ² PSD/dedicated electronics	Sitek/Philips
Data acquisition	1.25 MHz 12 bits, model PCI-MIO-16E	National Instruments
Translation stage	LIMMS, cross-roller bearing, 350 mm stroke	Philips

The maximum width of the measured object is limited by the optical scan line to about 110 mm. The optical scan is controlled by an external function generator that operates in a sinusoidal mode, resulting in oscillations of the scanning mirror. To obtain an acceptable linearity of the scan speed, only half of the scan amplitude is effectively used for scanning the object. The data acquisition (DAQ) is performed by a DAQ card from National Instrument and a standard PC. DAQ is synchronized to the optical scan via a TTL signal from the function generator. The data acquisition and processing program is created in LabView. The translation stage is driven by an external controller, independent from the DAQ. The position signal produced by the stage controller is used for synchronization of the DAQ to the translation axis. Although the stage had been designed originally for high-performance operation concerning velocity and positioning, the first tests with an autocollimator indicated a relatively large pitch of $320 \mu\text{rad} / 200$ mm. Such a large deviation is unacceptable for accurate slope measurements as it corresponds to about $8 \mu\text{m}$ of the parabolic bend-error

introduced to the measured surface. If not corrected, this effect results in a large systematic error in the surface topography reconstructed from the slope measurements. The final specification of the 3D-deflectometry platform is given in table 3.2.

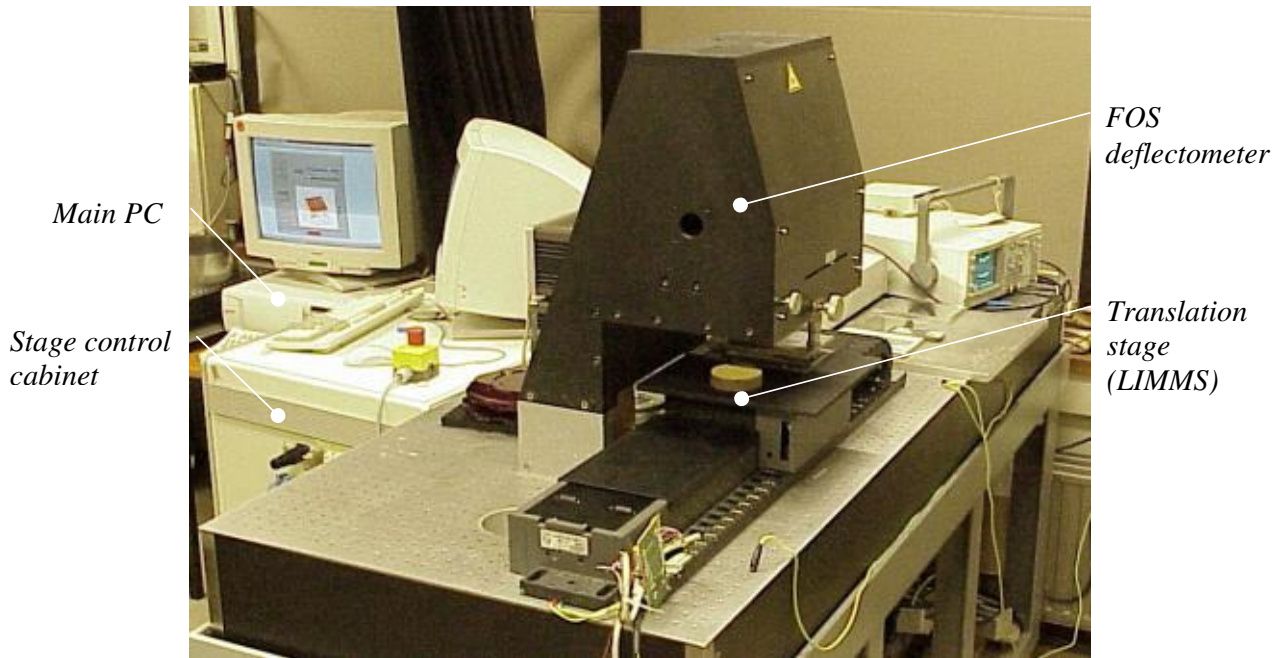


Figure 3.2. A picture of the 3D-deflectometry platform.

Table 3.2. Specification of the 3D-deflectometry platform

Parameter	Specification
Spot size on the object	1.6 mm FWe ⁻² M
Sampling distance	200±20 μm
Slope detection bandwidth	100 kHz
Sampling speed	66 ksamples/s
Measurement speed	20 lines/s
Translation speed	4 mm/s
Slope resolution	<1 μrad
Slope range (object)	~2 mrad
Max scan width (optical)	110 mm
Max scan length (mechanical)	350 mm

Calibration

The basic calibration of the deflectometer consists of a slope sensor calibration and a pixel size calibration. The slope sensor was calibrated using an autocollimator. The calibration set-up is presented schematically in figure 3.3. A flat mirror is placed on a tilting table and scanned by the deflectometer. When the tilt of the mirror is changed, a PSD voltage signal S is measured and compared to the angle α measured by the autocollimator. The voltage value is taken from the average of all samples along the scan line. The calibration is performed separately for both PSD axes.

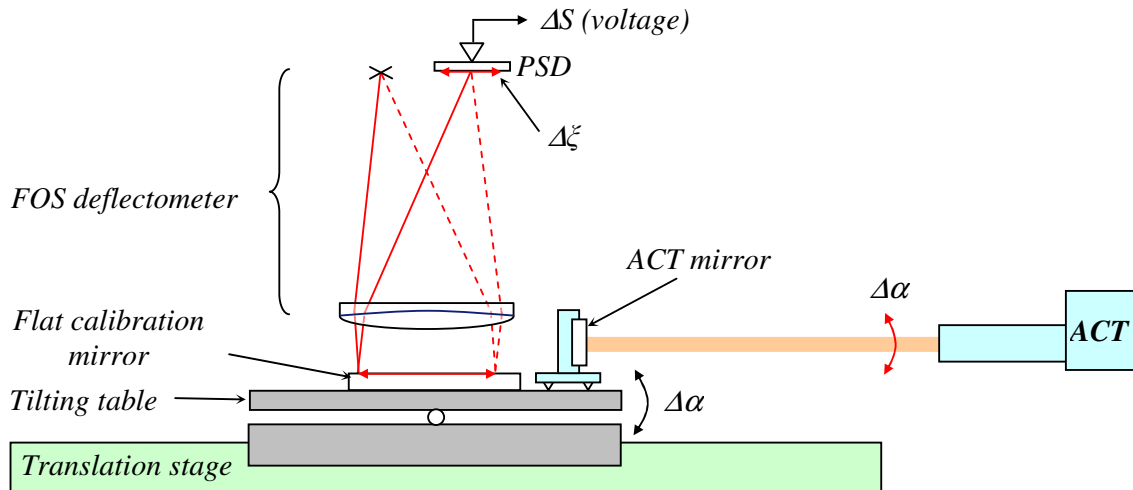


Figure 3.3 Calibration of the slope sensor for the 3D-deflectometry test-bed. The calibrated slope response equals $dS/d\alpha$.

The pixel size is calibrated by measuring a sharp-edged mirror of a known size and dividing its size by the number of samples acquired across the mirror. Additionally, we checked the linearity of the scan using an equidistant grid with a 10 mm pitch (an interval of about 10 % of the optical scan length). The grid was printed on a transparent foil and fixed on a flat mirror. The scan linearity was checked by comparing the number of pixels measured between the different grid lines along the scan line. The measurement indicated about $\pm 10\%$ deviation of the scan speed from the mean value, which will introduce error in the pixel size of $\pm 10\%$. This high pixel-size error that is introduced by the sinusoidal variation of the scan speed, is neglected for the test-bed.

3.3. Main system errors

It is well known that any metrology system has characteristic deviations and aberrations that introduce a certain level of uncertainty into the measurement. In 3D-deflectometry the limiting factor is related to the errors in the slope measurement. There are two major error sources that can be easily pointed out. First, there are aberrations of the optical elements, particularly of the large scan lens. Any lens based on spherical design has a certain level of spherical aberrations [9]. Due to the high slope sensitivity of the deflectometer, the spherical aberrations may introduce a significant error into the measured slope, even though the doublet design of the scan lens significantly reduces its magnitude. The spherical aberration of a doublet produces a low spatial-frequency slope offset, with a characteristic 3rd-order-polynomial shape. In addition to these low-frequency components, one can also expect high spatial-frequency deviations of the measured slope. These are related to local imperfections of the lens, introduced by:

- Manufacturing errors, like unwanted waviness and roughness of the lens surface left after polishing
- Material imperfection,
- Environmental influence, like dirt or dust particles on the lens surface.

Second, slope errors will be introduced by mechanical deviations of the translation device. Therefore performance of the translation axis is crucial for a 3D-deflectometer. Figure 3.5 shows the possible angular deviation of a translation stage. Again, due to high slope sensitivity, the influence of the angular deviation of the stage cannot be completely eliminated.

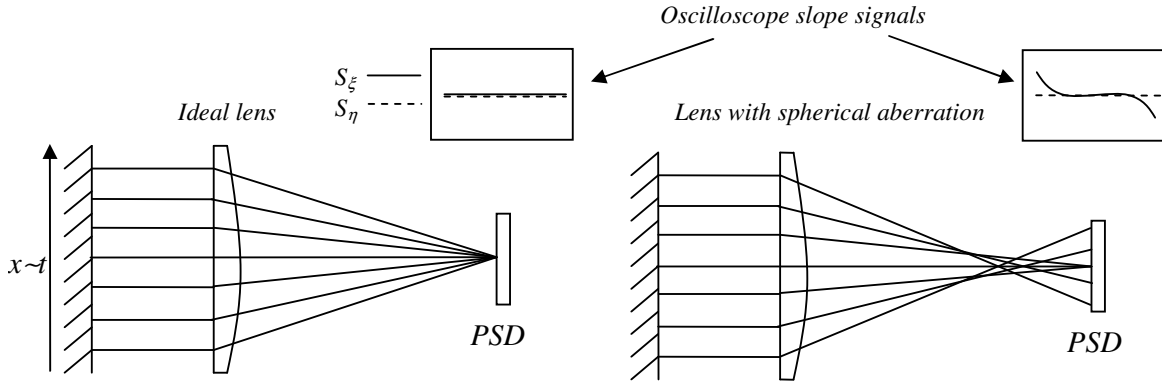


Figure 3.4. Influence of the spherical aberration of the scan lens on the slope signal (for an ideal flat surface-under-test).

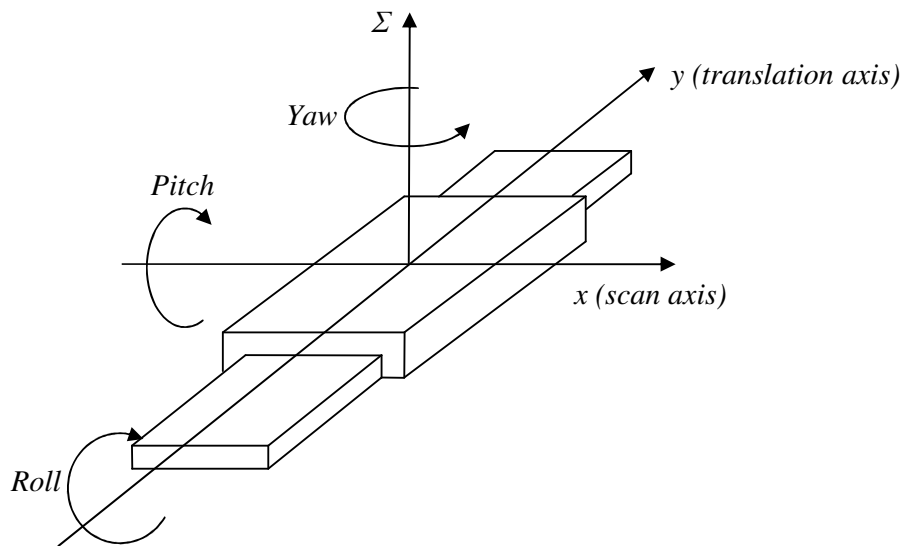


Figure 3.5. Angular deviations of a translation stage

Using the platform and a flat reference these main errors can be measured. When measuring a perfectly flat surface, the deflectometer measures the quality of its components rather than the surface itself. Although, in reality an ideal surface does not exist, using averaging procedures even a non-ideal surface can be used for investigating small system deviations. For example, by measuring many different profiles on a flat surface and averaging the result, a systematic component related to system deviations should become dominant upon the varying amplitude of the measured profiles. This procedure is similar to the noise reduction in a signal and is explained in more detail next.

For the first test of the system aberrations we used a $\lambda/10$ -flat mirror as a reference surface ($\varnothing 80\text{mm}$) and compared the result with the predicted values of the slope deviation. To estimate the expected slope deviation of our test device we assumed the lowest order of surface deformation: a parabolic bending (or sag), typical for optical flats. To calculate the slope deviation, we follow the sag formula in the parabolic approximation (Appendix C2):

$$\Delta\Sigma = \frac{(L/2)^2}{2R} \quad (\text{eq. 3.2})$$

where $\Delta\Sigma$ is the sag, L the length of the surface, and R the radius of curvature (figure 3.6)

The slope modulation range for edge-to-edge $\Delta\sigma$ (across length L) then simply equals:

$$\Delta\sigma = \frac{L}{R} \quad (\text{eq. 3.3})$$

Combining both equations:

$$\Delta\sigma = 8 \frac{\Delta\Sigma}{L} \quad (\text{eq. 3.4})$$

Since the expected sag of the $\lambda/10$ mirror is $\Delta\Sigma_{\lambda/10} \leq 63 \text{ nm}$, the predicted slope modulation is $\Delta\sigma_{\lambda/10} \leq 6.3 \mu\text{rad}$, which could easily be measured by the deflectometer.

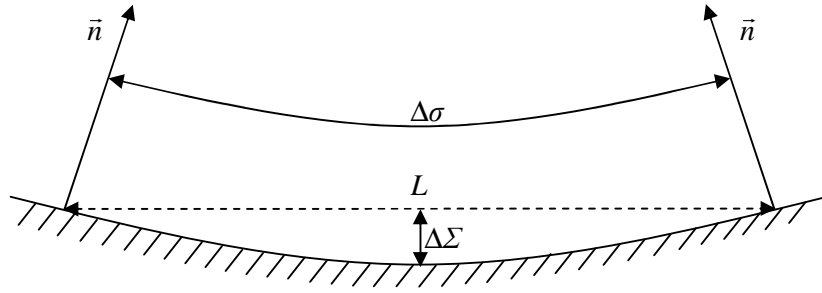


Figure 3.6. The relation between the parabolic sag $\Delta\Sigma$ and the slope modulation $\Delta\sigma$ across the width L .

The actual measurement results are given in figure 3.7. The measured peak-to-valley (PV) slopes of $\Delta\sigma_x \leq 13 \mu\text{rad}$ $\Delta\sigma_y \leq 60 \mu\text{rad}$ are about an order of magnitude higher than expected. Furthermore, the slope images show a surface far different from a smooth and flat surface that one expects from an optical flat. This suggests that at that level of slope resolution the main components of the measured slope are due to system deviations rather than to surface topology. In addition, one notices that for both slope components the main contributions to the deviation are highly systematic along the translation direction, suggesting thus that they might be introduced by the pitch and roll of the translation stage. The order of magnitude in the deviation of the cross-scan slope is consistent with the pitch of the stage, as measured earlier with an autocollimator (see section 3.2). Looking at shorter spatial wavelengths in figure 3.7b, a characteristic waviness with a period of about 12 mm can be distinguished. This period is consistent with the distance between the magnets of the linear drive – which might locally influence the pitch performance. Finally, we also recognize a smaller ripple with a period of about 2 mm, which might be caused by vibrations of the motor. This problem has been recognized earlier and occurs for low translation speeds of LIMMS. It is

caused by the stage controller which is normally tuned for very high translation speed with high acceleration.

A systematic deviation along the scan line can also be seen. This deviation, however, is much weaker, on the order of only a few μrad . We suspect that it is introduced by the lens aberration. Although the scan distance is probably too short to show the third order spherical aberration of the lens, the high frequency ripple due to local lens imperfections should be distinguishable. This is in agreement with earlier measurements of aberrations of that particular lens, performed during the original design of the FOS measuring head [2].

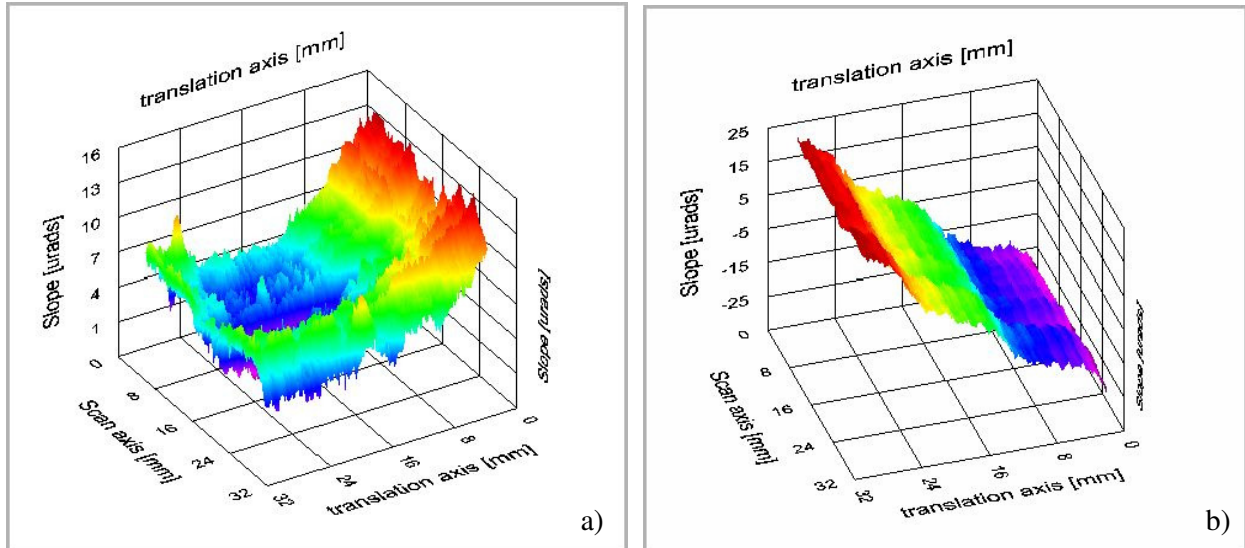


Figure 3.7. Raw slope images of the $\lambda/10$ mirror, obtained with the 3D-deflectometry platform. Left image: the scan slope; right image: the cross-scan slope.

As we mentioned earlier, since both kinds of deviations seem to be systematic, we can extract them from the actual measurement and use them as a virtual reference surface. The subtraction can be done simply by averaging the slopes along the axis for which the aberration repeats. Thus, to extract the stage deviation, both slope components measured for a reference surface must be averaged across the scan axis. By analogy, to extract the lens aberration we must average the slope components along the translation axis.

Since the extracted deviations and aberrations are characteristic for the specific components, we will call them the stage signature and the lens signature. The result of the signature extraction (done separately for each slope component) is shown in figures 3.8 and 3.9.

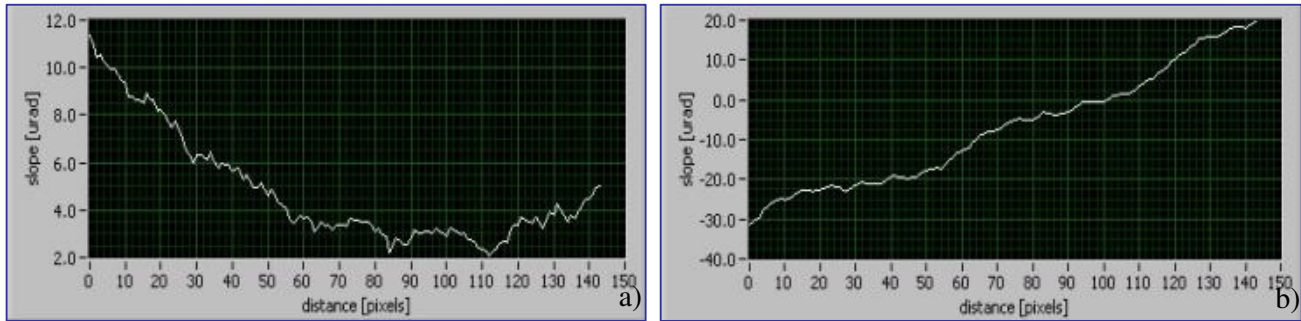


Figure 3.8 Stage signature measured using a $\lambda/10$ mirror as a reference: a) the scan signature due to the roll of the translation stage; b) the cross-scan slope signature due to the pitch of the stage. Horizontal axis scale: 0.2 mm/pixel

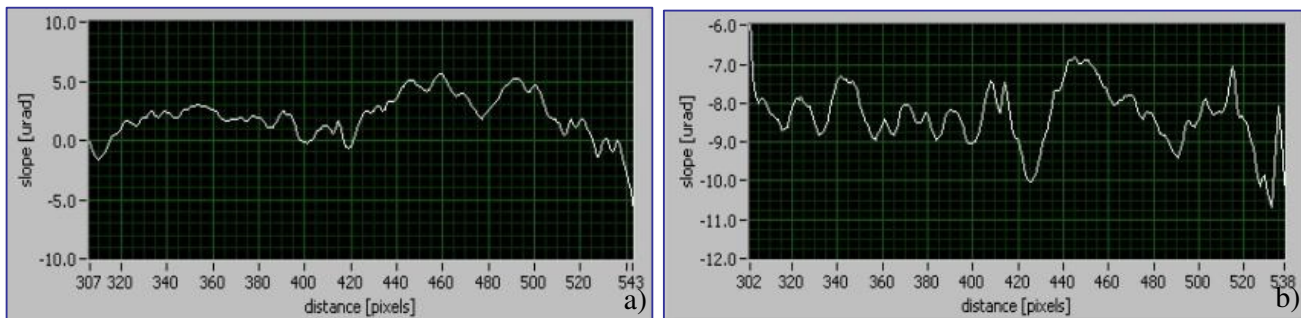


Figure 3.9 Lens signature measured using a $\lambda/10$ mirror as a reference: a) the scan signature; b) the cross-scan slope signature. Horizontal axis scale 0.2 mm/pixel

The interpretation of the stage signature is straightforward, since it is related directly to the mechanical deviations that have been measured earlier with an ACT. To understand the meaning of the lens signature we refer to the Snell's law of refraction. We make a simple calculation assuming that the slope deviations are caused by imperfections in a single glass-to-air interface (as presented schematically in Appendix C3). This is an approximation, since in reality the scan lens is a doublet, the deflectometer is a double-pass system, and thus the laser beam crosses in total eight lens surfaces responsible for the high-frequency slope aberrations. By analyzing the lens signature in figure 3.9, we recognize three main slope components σ with corresponding spatial wavelength Λ : $\sigma_1 = 5 \mu\text{rad}$ and $\Lambda_1 = 20 \text{ mm}$; $\sigma_2 = 2 \mu\text{rad}$ and $\Lambda_2 = 4 \text{ mm}$; and $\sigma_3 = 1 \mu\text{rad}$ and $\Lambda_3 = 1 \text{ mm}$. From these values we calculate the amplitude A_i of the waviness on the lens surface with spatial frequency $k_i = 1/\Lambda_i$. From Appendix C3 we conclude that the measured lens signature indicates lens imperfections on the order of:

$$A_1 = 66 \text{ nm}, A_2 = 5 \text{ nm}, A_3 = 1.5 \text{ nm} .$$

This simple analysis shows a surprisingly high quality of the scan lens: the waviness on the lens surface is on order of nanometres only. This, however, has a negative implication for the deflectometer, since it indicates that slope errors are difficult to eliminate by better polishing of the lens. Therefore, we need to find a different approach to increasing the measurement accuracy. For example, one could imagine that the measured signatures define a virtual reference surface and we can subtract the signatures from the measurement data.

For the first test of the signature subtraction, we used the same flat mirror as for the reference measurement. Between the reference measurement and the actual measurement, the mirror was rotated by 90° . The measurement data are in the form of rectangular arrays, where the columns represent the translation axes and the rows represent the scan axis. To correct the measurement for the stage signature we subtract the stage signature from each column of the slope array. To correct the measurement for the lens signature we subtract the lens signature from each row. Both corrections must be done separately and for each slope component. Figure 3.10 shows slope images corrected for the stage signature, which is the major slope deviation.

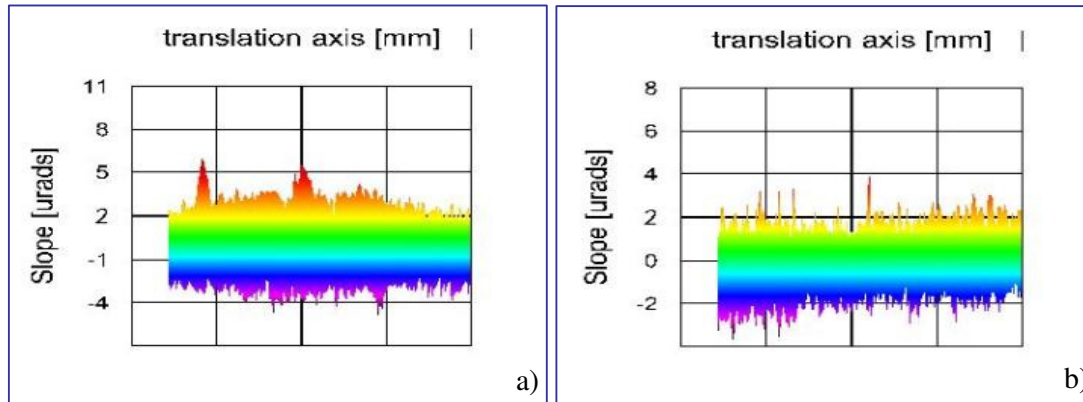


Fig. 3.10 Slope images of a $\lambda/10$ mirror corrected for the stage signature. Picture a) represents the scan slope; b) is the cross-scan slope. Horizontal scale: 8 mm / division.

By comparing the result to the raw data in figure 3.7, one notices that the slopes are distributed much more uniformly after the subtraction, and that the peak-to-valley values are strongly reduced to $\leq 8 \mu\text{rad}$, and $\leq 6 \mu\text{rad}$, for the scan slope and the cross-scan slope respectively. The surface also consists of some peaks which could be local surface imperfections that were averaged out in the signature.

Finally, we subtract the lens signature from the data corrected previously for the stage signature. The result is shown in figure 3.11.

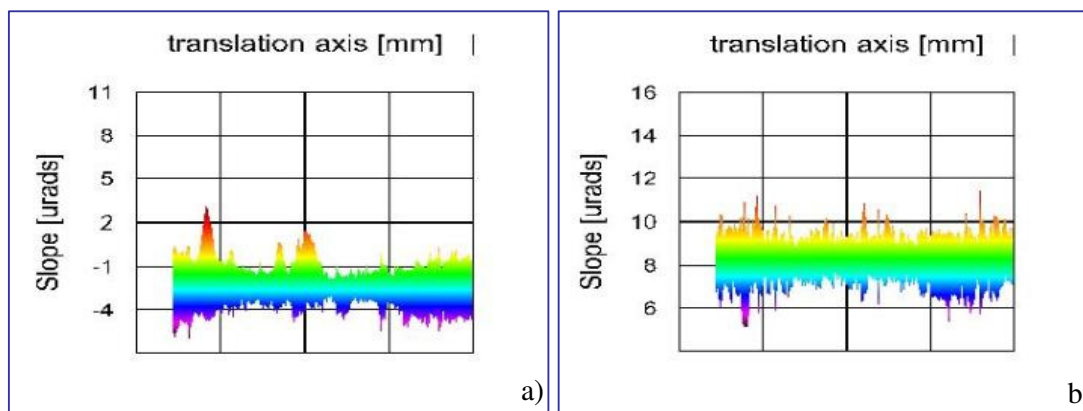


Fig. 3.11. Slope images of a $\lambda/10$ mirror, corrected for the stage and lens signature. Picture a) represents the scan slope; b) is the cross-scan slope. Horizontal scale: 8 mm / division.

The subtraction of both signatures leads to slope values of $\Delta\sigma_x \leq 6 \mu\text{rad}$ and $\Delta\sigma_y \leq 4 \mu\text{rad}$ (PV), which implies high sensitivity of the deflectometry test-bed. The measurement also suggests that the reference mirror has a better quality than specified by $\lambda/10$. This conclusion is based on the fact that the measured slope with PV of about $6 \mu\text{rad}$ exhibits a noisy but flat image, although at the predicted order of magnitude. This suggests that the topography contains mostly small local imperfections and the assumed sag of the mirror is much smaller than the predicted one. This effect, however, can be explained easily. First, we use only part of the mirror's surface ($30 \times 30 \text{ mm}^2$), which has higher absolute flatness than the whole mirror. Second, we use the same mirror for the reference measurement – therefore, if the major “unflatness component” of the mirror is indeed parabolic, it is rotationally symmetric, and will be cancelled in first order after subtracting the lens signature. This holds even if the surface is rotated between the reference and the actual measurement.

The remaining noise-like slope variation is most likely introduced by non-systematic error sources, like the measurement noise (air turbulence, vibrations), inaccuracy of the scan synchronization (jitter) and finally the surface itself (including imperfections and dust on the surface). To get an impression about the background noise characteristics of our laboratory room, we did a simple experiment with an autocollimator. We placed the autocollimator on the lab table and we placed a mirror just in front of the objective. The autocollimator collected the slope data for a couple of hours. We found that the slope noise in our laboratory is between 3 and 5 μrad , depending on the part of the day and the activities in the building. This shows that by a simple calibration with a flat reference we reached the local measurement sensitivity on the order of the natural limit for our laboratory environment.

3.4. Comparison with a White Light interferometer

The first verification of the deflectometry test-bed was done using a “glued mirror” as an optical test device. The mirror was manufactured by vacuum-sucking and gluing of a 0.8 mm thick mirror to a 10 mm machine-shop quality metal plate. The surface was distorted within a few μm due to the process, and therefore, the topography structure of the surface should be easily recognizable.

For a simple verification we measured the surface with the deflectometer and integrated the slope data using two different integration algorithms. One was a simple algorithm based on linear integration, and the other a more advanced one called the soap film method. The latter is an error-minimizing based on surface integration [10]. The instrument signatures were removed from the slope data before integration, using a $\lambda/4$ mirror as reference. The obtained topography was verified by an independent measurement using a Zygo White-Light interferometer.

The topographical images obtained by both instruments are presented in figure 3.12. The similarity of the surface images is striking. Quantitatively, the height range of all images differs by about 1 μm only (PV range: about 14 μm). There is an apparent difference between the ‘soap film method’ image (figure 3.13c) and the other two images. This is due to the fact that the latter image has been created using different software, and thus the colour coding is not the same. In addition, the surface measured with the interferometer (figure 3.13a) is slightly rotated with respect to the surface measured with the deflectometer (figure 3.13b,c). Finally, some tilt difference between the images is present.

A complete numerical comparison between the measurements requires a six-degrees-of-freedom software correction to take into account the relative displacements and rotations of the measured data arrays. Furthermore, the data must be re-sampled due to different lateral resolutions. Therefore, due to time limitations, the first verification was done by comparing only the scale range and the general figure of the surface, without full numerical comparison.

3.5. Concluding remarks on the feasibility study

The first tests with the 3D-deflectometry test bed show that the quality of the components has a strong effect on the measurement accuracy. We found that mechanical deviations and optical aberrations, inherent to our system, limit the absolute accuracy of the measurement to a level at least one order of magnitude higher than expected at design. There are two solutions to this problem.

In one approach, the accuracy could be increased by using components of higher quality, like a high-end, air-bearing translation stage, or an objective with a few extra polished lenses. As we concluded, however, the lens quality probably could not be improved significantly since the lens used in the current set-up already was of high quality. Furthermore, using high-end components is very expensive. For example a high-end translation stage can cost at least 20.000 €, and a high quality objective with a few extra-polished lenses another few thousands euros, with the price increasing strongly with the aperture.

Another approach, shown during our first feasibility study, is to increase the accuracy at much lower cost, by applying a simple calibration with a flat reference surface. This way, even our test-bed can reach extremely high, environment-limited, measurement resolution. Of course, the accuracy of instrument is limited by the flatness specification of the reference. Nevertheless, small surface features can be measured with accuracy much better than the global flatness specification of the reference. Finally, we showed that by decomposing the measurement into two scan axes, the signature calibrations can be done using a relatively small reference surface instead of expensive, full-inspection-area-size optical flats, since a narrow strip mirror can be used for calibration of both the axes.

As a final test, we proved that the test-bed can be used for accurate topography measurements. By verification with an independent reference measurement by a white light interferometer, we showed that the accuracy of the figure measurement of a highly distorted mirror is better one μm . Such accuracy can be achieved even using simple integration routines. The first topography result was stimulating and provided a strong motivation for further research.

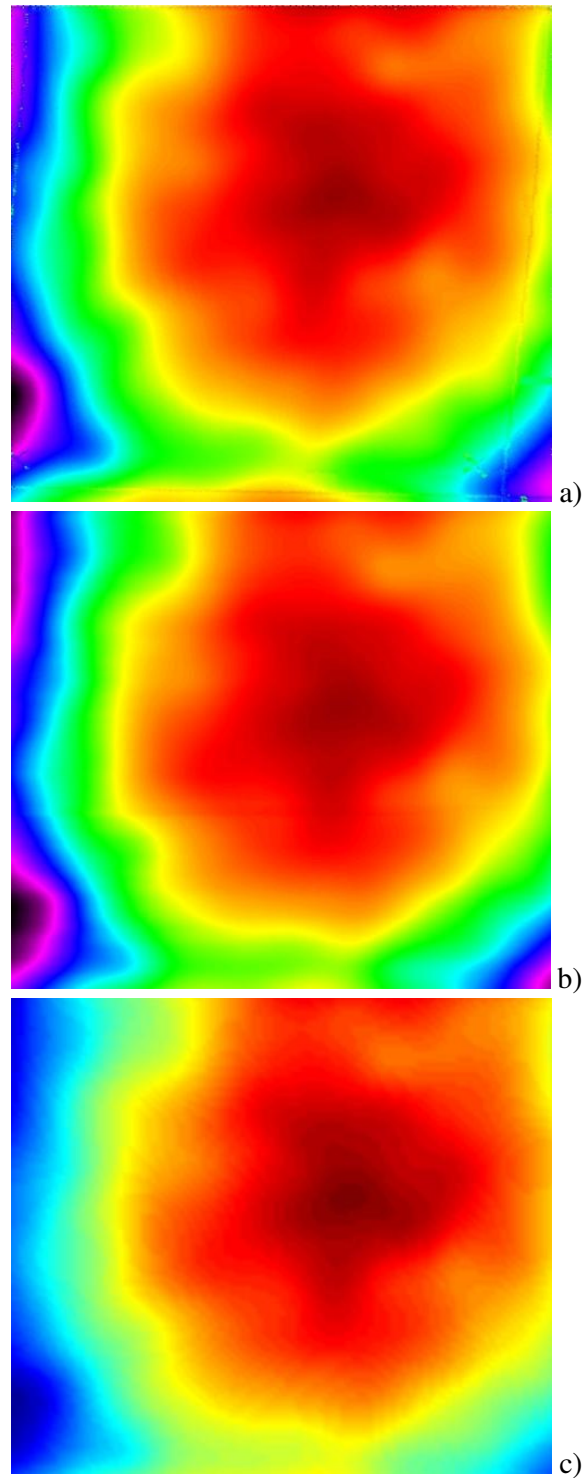


Fig. 3.12. Topography images of the “glued mirror”: (a) the topography measured by the white light interferometer; (b) topography measured by the 3D-deflectometry platform and linear integration; (c) topography measured by the 3D-deflectometry platform and the “soap film” integration method. The “soap film method” image has been created with MatLab, while the other two have been created using LabView. The measured area is about 80 x 80 mm. The vertical scale range for all images is $14\pm 1\ \mu\text{m}$.

3.6. References

- [1] W.D. van Amstel, S.M. Bäumer, J.L. Horijon, *Optical figure testing by scanning deflectometry*, Proc. SPIE **3739**, 283-290 (1999)
- [2] R.Boerhof, J.C.J.van Vliet, *Deflectometer voor vlakheidmeting van optische spiegels*, graduation report, Hogeschool van Utrecht (1998)
- [3] L. Beiser, *Laser scanning systems in Laser Applications*, M. Ross, Academic press, 53-159, New York (1974)
- [4] L. Beiser, *Fundamental architecture of optical scanning systems*, Applied Optics, **34**, 7307-7317 (1995)
- [5] G. Marshall, *Laser Beam Scanning: opto-mechanical devices, systems, and data storage optics*, Marcel Dekker, New York (1985)
- [6] K. Szwedowicz, *3D deflectometry platform for inspection of 110mm silicon wafers*, Stan Ackermans Instituut, Eindhoven (2003)
- [7] Aerotech, Inc., Web site: www.aerotech.com
- [8] Anorad, Web site: www.anorad.com
- [9] E. Hecht, *Optics*, Addison Wesley; 4th edition (2001)
- [10] W.Poetze, *Method to reconstruct surface topography from measured slopes*, Philips Applied Technologies internal report (2002)

Chapter 4

Design of the 3D deflectometer

In this chapter we present the design of the 3D-deflectometer. First, in section 4.1, we give the final specification for the new instrument based on the industrial requirements presented in chapter 2. In section 4.2 we introduce the design process by defining a conceptual space for the 3D-deflectometer. In the following section, 4.3, the design boundary conditions are addressed, from which the optimum design choice is made (section 4.4). Finally, in section 4.5 we discuss the “technology tuning” that could enable overcoming some design limitations.

4.1. User requirements

In chapter 2.2 we presented the user requirement specification for the semiconductor industry. As shown in table 2.1, these are slightly different for wafer manufacturers and users. Therefore, the final requirement specification for a new deflectometer must be a compromise between these. The difference concerns mostly the height range and lateral resolution of the measurement. To achieve high flexibility, we decided to design for large dynamic range in height due to the non-flat wafer support, and high lateral resolution of 0.1 mm. The final user requirement specification for the new system is given in table 4.1.

Table 4.1. Basic user requirements specification for a 3D-deflectometer for nanotopography inspection of 300 mm silicon wafers.

Parameter	Value
Height resolution/Scan area	$\delta\Sigma \leq 1.7 \text{ nm}/10 \times 10 \text{ mm}^2 \text{ area}$
Height range/Spatial range	$\Delta\Sigma/L_{\text{wafer}} = 150 \text{ }\mu\text{m}/300 \text{ mm}$ (parabolic bending) (Slope range $\sigma_{\text{max}} = \pm 2 \text{ mrad}$)
Lateral resolution	$\Lambda_{\text{min}} = 0.1 \text{ mm}$
Measurement time	$T = 60 \text{ s}$

4.2. Design process

The design of a surface metrology system is always a compromise between the key performance parameters. In the design of a 3D-deflectometer for application in the semiconductor industry, the main trade-off is among the lateral resolution Λ_{min} , the height resolution $\delta\Sigma$, the height range Σ_{max} and the total measurement time T for a test-surface of

area A . In the current system the lateral range plays a minor role, since we are talking about a scanning system. Constraints in that area are covert within the measurement time budget.

Next to these constraints, which are basically given by the user requirement specification, there is a set of parameters, which the designer can use to design a system of optimum performance. For the deflectometer these are laser wavelength λ , spot size d_0 , focal length of the system f , detector response time per unit area Ξ .

The design process basically consists of maximizing the area in the Stedman diagram with major constraint measurement time. However, in order to do so, the theoretical connection between the different parameters should be found. Only if these are know, the designer can work and predict the result of his design. It also helps him to balance between the various, often contradicting demands. As an example the derivation of the formula for measurement time can be taken (eq. 1.24). Here the relation between measuring time, wavelength, spot size, focal length, measurement area, and detector response is put together. Using this equation, some basic trade-offs can be studied. As for measurement time, similar connections can be derived for resolution and range in both the lateral and the slope domain.

For the current FOS system an additional requirement is to match the scanning system with the detection system. As explained in chapter 3, the FOS system consists of a scanning system and a slope detection system, folded into each other. The challenge for this particular system is to find a balance between these two sub-systems. The approach in this thesis is to take a close look at the design parameter time. For the scanning system the limiting factor for time is the deflector speed. For a detection system – at a specified range and resolution – the time limiting factor is the detector response time. That is why in the following both systems and their parameters are discussed. A well balanced system is one, where detector response and scan frequency are in good balance.

The last, but not least important constraint for the design is cost. At a certain point in the design process one has to take a look at the estimated price / performance ratio as well.

4.3. Boundary conditions

4.3.1. General scan strategy

In this section we present a brief analysis of a few possible concepts for the design of a scan system for a 3D-deflectometer. In principle, the complete 2D scan could be performed optically. Such a system, however, would require much more complicated scanning optics and would consist of the fast- and the slow scan axis anyway. Since the scan along the slow axis would be thousands times slower than along the fast axis, it is much easier to perform the slow scan mechanically. Thus, we restrict our considerations to scanning systems where scanning is done by combination of an optical line-scan and a mechanical translation of the object.

In appendix D1 we discuss three different scan strategies: a single-stroke Cartesian mode, a multiple-strokes Cartesian mode with stitching, and a polar mode. In the single-stroke Cartesian and the polar modes the wafer area is scanned in a single measurement. In the multi-stroke mode, the reconstruction of the full area is realized by stitching the measured

sub-files. In table 4.2 we give a summary of the scanning strategies and the advantages and disadvantages of each one with respect to performance and design complexity.

Each considered system is attractive for certain aspects. The single stroke Cartesian system is the most efficient and should be considered when the number of samples for post-processing is the major issue. The stitching system leads to the shortest measurement time but the system is more complex and the footprint large. The polar scanning system has the smallest footprint and relatively simple system design but it leads to problems in the surface reconstruction (due to polar coordinates) and the largest number of samples (because of the lowest scan efficiency).

Table 4.2. Comparison of various scanning strategies for 3D-deflectometry.

System type	For	Against
Single-stroke Cartesian	<ul style="list-style-type: none"> • Highest scan efficiency • Simple system design 	<ul style="list-style-type: none"> • Expensive (because of large scan lens) • Longest measurement time
Multiple-stroke Cartesian	<ul style="list-style-type: none"> • Shortest measurement time • Simpler scanner design (smaller slope range) 	<ul style="list-style-type: none"> • Complex system design • Expensive (because of additional translation axis) • Additional post-processing needed (for stitching) • Large footprint
Polar	<ul style="list-style-type: none"> • Simple system design • Small footprint (area under the instrument) 	<ul style="list-style-type: none"> • Lowest efficiency • More complex and less accurate surface reconstruction algorithm (because of the polar coordinates)

4.3.2. Lateral resolution

Spot size

The lateral resolution of an optical scanning system is limited by the system response at high spatial frequencies. Referring to Fast Optical Scanning, one can imagine that when scanning a surface with an optical beam and measuring the angle of the reflected beam, the beam will follow well the long slope wavelengths, while its slope response to shorter structures will be attenuated. The level of attenuation will increase gradually with k -value until $k = k_{\max}$ is reached. The value of k_{\max} describes the spatial frequency where the instrument response drops down to the minimum value allowed by the requirements. The semiconductor standards [1] define k_{\max} for a wafer inspection instruments as the frequency which corresponds to 50 % response (-6 dB) of the system response function. This criterion will be used for our system to describe its lateral resolution.

The relation between the spot size of the scanning beam and response attenuation is given by a transfer function of the slope measurement. In appendix D2 we propose a first-approximation model of the optical slope response, from which the transfer function of the

deflectometer is derived. From that model, the spatial frequency transfer function $H(x)$ can be represented by the Fourier transform of the beam profile:

$$H(k) = F[G(x)] \quad (\text{eq. 4.1})$$

where $G(x)$ is the Gaussian distribution of the irradiation amplitude of the scanning beam on the surface under test.

The system response was solved numerically and in figure 4.1 we show the normalized frequency transfer function of a deflectometer based on our model. The vertical axis represents the system response to the exact surface slope; the horizontal axis represents the spatial frequency normalized to the spot size d_0 of the probing beam.

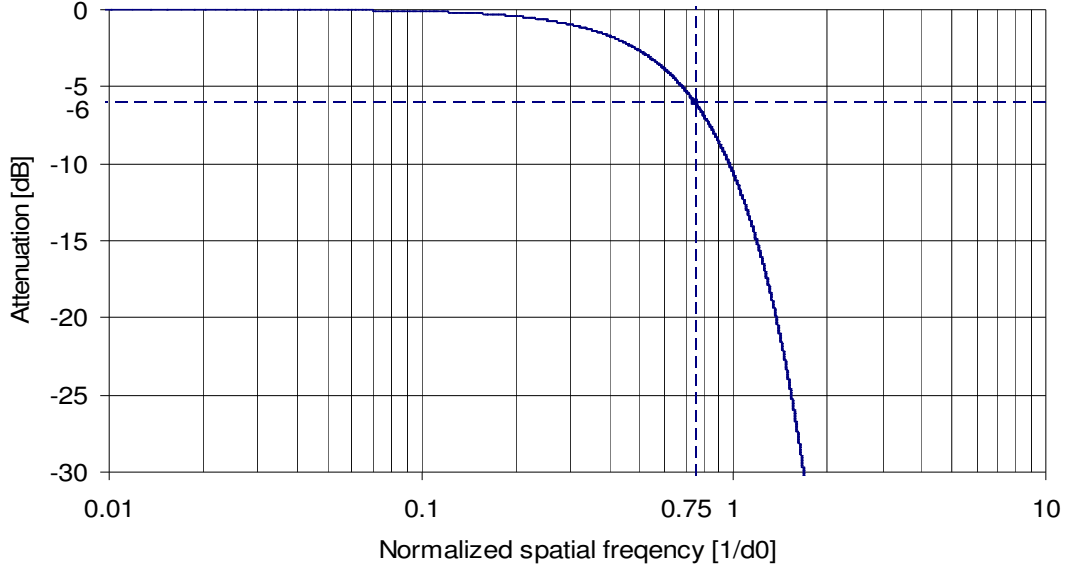


Figure 4.1. Simulated transfer function of the optical slope measurement with a Gaussian beam. The spatial frequency is normalized to the $FWe^{-2}M$ size of the probing beam. The curve represents the attenuation of the exact surface derivative. The spatial frequency corresponding to the -6 dB lateral resolution is marked with the dashed line.

Following the figure, the -6 dB lateral resolution of a deflectometer corresponds to the normalized spatial frequency of:

$$k_{\max} = 0.75 / d_0 \quad (\text{eq. 4.2})$$

or to the spatial wavelength:

$$\Lambda_{\min} = 1.33d_0 \quad (\text{eq. 4.3})$$

Sampling distance

The sampling distance for an optical slope measurement can be derived using signal theory [2,3,4] applied to the spatial domain with spatial frequency k . Following the Nyquist theorem, the minimum sampling frequency $1/\Delta x$ is defined as:

$$1/\Delta x > 2k_M \quad (\text{eq. 4.4})$$

where k_M is the spatial cut-off frequency. The $2k_M$ frequency is commonly referred to as the Nyquist rate. The cut-off frequency implies a bandwidth limit in the signal. As we showed in previous section, the spatial-bandwidth limit of an optical scanner is introduced initially by

the optical surface filtering with the scanning beam. Such filtering, however, is non-ideal (it has no sharp cut-off). Therefore, frequencies $k > k_M$ are also measured, though attenuated (see figure 4.2). This leads to aliasing: high-frequency components with $k > 1/\Delta x$ are effectively translated to frequencies with $k < 1/\Delta x$ by the sampling process, resulting in erroneous signals. The required accuracy determines a maximum signal error that can be tolerated. Together with the expected accuracy of the A/D conversion and the transfer function of the spot, this determines the minimum allowed value of $1/\Delta x$.

The value of k_M also depends on the signal itself, and thus the proper choice of sampling distance requires preliminary knowledge of the slope content of the surface-under-test. In our considerations, we will assume a typical slope spectrum of a silicon wafer on a non-flat support (table 2.1), where the amplitude of the high spatial frequencies is roughly 100 times (20 dB) smaller than the full-scale signal. In figure 4.2 we present the spectrum of the slope signal (normalized to the full-scale signal) derived by a numerical simulation, where we indicate the Nyquist and the sampling frequencies for the deflectometer. The simulation is based on the deflectometer's transfer function (see previous sub-section) and the assumed slope spectrum. In table 4.3 we present the sampling distance at the Nyquist rates estimated for various resolutions of the A/D conversion (maximum allowed level of the aliasing error) derived from figure 4.2.

Using the information in section 2.1, we can estimate that the resolution of the deflectometer's A/D converter will not exceed 10-12 bits. Therefore we choose for a fixed ratio between sampling distance and spot size, as given by:

$$\Delta x = d_0 / 4 = \Lambda_{\min} / 5.5 \quad (\text{eq. 4.5})$$

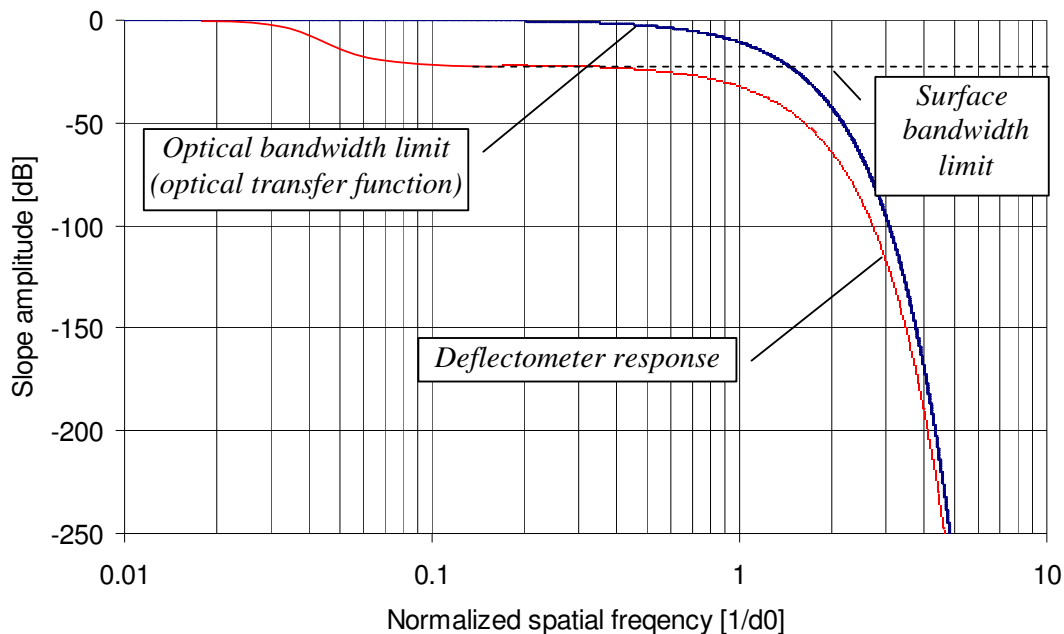


Figure 4.2. Theoretical wafer slope-signal spectrum measured with a deflectometer. The signal amplitude is normalized to the maximum slope; the spatial frequency is normalized to the spot size of the scanning beam. The spatial frequency, where the slope amplitude (surface bandwidth limit) drops down by 22 dB, is included as well.

Table 4.3. Requirement for the sampling (spatial) frequency of the deflectometer as a function of the resolution of the A/D converter. The sampling spatial frequency is normalized to the spot size.

ADC resolution (bits)	Corresponding aliasing error (dB)	Spatial frequency $d_0/\Delta x$
8	-48	3.2
10	-60	3.8
12	-72	4.2
14	-84	4.8
16	-96	5.2

All the following formulas are based on this choice for a fixed ratio between spot size and sampling distance. Fine tuning of the design of the deflectometer can be done by reconsidering this choice, as discussed in section 4.5.2.

Slope detection bandwidth

The detector bandwidth limit will result in attenuation of the slope signal similar to the one due to the optical bandwidth limit k_{max} . A rule of thumb for a well designed system is that the cut-off frequency (defined usually by -3 dB signal attenuation) should be at a higher frequency than k_{max} . Otherwise, the PSD response will reduce the optical response of the system, which in turn would lead to significant reduction of the lateral resolution in the scan direction (the -6 dB signal attenuation would be shifted to lower spatial frequencies). To compare the detector and the optical responses, we will convert the system slope response from the spatial frequency domain to time frequency domain. This can be done by multiplying the spatial frequency by the velocity of the scanning beam:

$$(1/\tau)_{-3dB} \geq k_{max} V_{scan} \quad (\text{eq.4.6})$$

where $(1/\tau)_{-3dB}$ is the -3 dB bandwidth limit of the detector. This relation is explained schematically in figure 4.3.

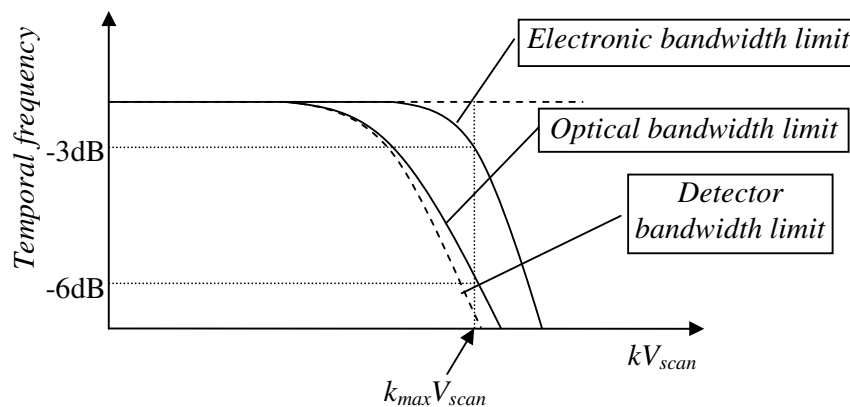


Figure 4.3. Detector bandwidth requirement for a deflectometer. The vertical axis shows the slope signal attenuation and the horizontal axis the time frequency.

4.3.3. Height resolution

Noise level in the slope signal

Height resolution in deflectometry is related to the uncertainty of the topography reconstruction from the slope. In chapter 1.4 we showed that by using an advanced surface reconstruction algorithms this uncertainty can be approximated by:

$$\delta\Sigma \cong 0.7\delta\sigma * \Delta x \quad (\text{eq. 4.7})$$

where $\delta\Sigma$ is the RMS topography reconstruction error due to measurement noise.

Hence, for a height resolution of $\delta\Sigma = 1.7 \text{ nm}$, the requirement for the minimum noise level in the slope signal is:

$$\delta\sigma \leq \frac{1.7 * 10^{-9} \text{ m}}{0.7\Delta x} \approx \frac{2.43 * 10^{-9} \text{ m}}{\Delta x} \quad (\text{eq. 4.8})$$

Following this estimation, we can derive a relation between $\delta\sigma$ and the lateral resolution of the measurement Λ_{\min} (linked to Δx by equation 4.5). In table 4.4 we present the results.

Table 4.4. Requirement on slope uncertainty for 1.7 nm height accuracy, for different lateral resolutions Λ_{\min} , assuming 5.5-fold over-sampling upon the lateral resolution Λ_{\min} (see equation 4.5).

Λ_{\min} (mm)	$\delta\sigma$ (μrad)
0.1	133
0.2	66
0.3	44
0.4	34
0.5	26

Clearly, smaller lateral resolutions have lower demands on the noise level of the slope measurement. Uncertainty levels of a few μrad can be easily reached with an optical slope measurement (section 3.4), and thus the noise requirement is not a problem for a deflectometer.

Dynamic range of the detector

Resolution of a PSD is defined by its dynamic range, expressed as the signal-to-noise (S/N) ratio. Expressing the PSD dynamic range in the slope domain, the S/N is defined by the ratio between the slope uncertainty $\delta\sigma$ and the full-scale slope signal σ_{\max} . The required noise level was derived in the previous section and the result is given in table 4.4. The full-scale slope can be derived from a typical topography presented in table 2.2., where we showed that for a non-flat support, the slope range is mainly due to the general wafer geometry and it is about 2 mrad (amplitude) for a 300 mm wafer. It makes sense to increase the slope range by another 1 mrad to compensate for contribution to the slope of smaller surface features and for the tilt adjustment of the specimen. In general, some additional detection range, typically about 20 %, should be included because of the effective detector range (due to the beam size on the detector and to the detector linearity). This first order estimation leads to a required slope

range in the object domain of $\sigma_{\max} = \pm 3$ mrad. The required PSD resolution based on our estimations is given in table 4.5.

Table 4.5. Requirement for the PSD dynamic range for different lateral resolutions Λ_{\min} of a deflectometer.

Λ_{\min} (mm)	S/N (dB)
0.1	33
0.2	39
0.3	42
0.4	44
0.5	47

Quantization error

Quantization error is introduced by the analog-to-digital (A/D) signal conversion of the data acquisition system. The relevant quantity in this process is the slope step $\Delta\sigma_{ADC}$, corresponding to the step size of the last significant bit in the A/D conversion. Translating the separation level into an effective RMS error, $\Delta\sigma_{ADC}$ results in [3]:

$$\delta\sigma = \frac{\Delta\sigma_{ADC}}{\sqrt{12}} \quad (\text{eq. 4.9})$$

This is the boundary condition for the deflectometry slope resolution due to the A/D conversion. In practice, it is always safe to use ADC resolution of 2-4 bit below the noise limit, unless it leads to significant increase in the measuring time or in the cost of the DAQ system. In this case, a trade-off between acceptable price, measurement time and measurement accuracy must be made.

Surface finish

Another factor affecting uncertainty is the surface itself. The surface preparation can not only introduce additional uncertainty, but even disable completely a deflectometric measurement. In principle, deflectometry is used for inspection of specular surfaces for which the law of reflection holds (section 1.3). In general, a specular reflection is obtained for well-polished surfaces, when roughness amplitude is small compared with the incident wavelength [3,5,6]. Otherwise, a diffuse reflection takes place and the angle of deflection cannot be measured. Both types of the surface preparation are present at various steps of wafer manufacturing. In general, post-CMP surfaces exhibit specular reflection, while post-grinded (often at the back side of wafers) produce scatter (figure 4.4). As a consequence, only post-CMP wafers can be inspected with deflectometry.

A special case of surface reflection from a smooth surface is when the surface consists of a periodic structure and a diffraction pattern is observed in the reflected beam. Sharp, step-like surface features will introduce distortion of the beam's shape due to diffraction from the truncated beam. In both cases the measurement uncertainty will be strongly increased, resulting often in the disabling of the optical slope measurement. As we show in appendix D3, some general rules can be given for the allowed surface structure for the deflectometric measurement. However, the limiting conditions depend on the particular deflectometry system.



Figure 4.4. A silicon wafer with a rough, grinded surface (left) and with a specular, CMP-polished surface (right).

Another factor in uncertainty introduced has to do with the layered structure of the surface. Layered structures are common in IC manufacturing and one must be careful which layer is actually being measured. In general deflectometry should be applied only to mirror-like surfaces where the top layer is fully reflective for the wavelength used. Otherwise, the measurement can be distorted by additional reflections or interference between layers.

Thus, surface finish has a great influence on the limitations of the use of deflectometry, and needs to be taken into account. The method is best suited for reflective and smooth surfaces. Under some conditions, however, measurement of diffractive structures is possible. In general, the surface structure should be considered carefully, taking into account reflectivity, structure periodicity and layer composition.

4.3.4. Scanning

Basic scan relation

One of the key elements for wafer inspection is the measurement time. In a FOS deflectometer the measurement time is limited by the response time of the slope detection or by the maximum scan frequency. In our design we assume that the measurement time is limited by the detector speed only, thus the optical scan system should be at least as “fast” at the slope detection. Therefore, we can define a general criterion for the scan system design (appendix D4):

$$\pi v_{\max} \theta_{scan} f \geq 1.4 d_0 / \tau \quad (\text{eq. 4.10})$$

The left side of the formula represents the maximum speed of the scanning beam, where v_{\max} is the maximum scan frequency of the deflector, θ_{scan} the full scan angle, and f the focal length of the scan lens. The speed of optical scanning is limited by the resonant frequency of the scanning mirror together with its suspension. The right side represents the maximum scan speed due to the slope detection system.

Duty cycle

An important parameter for the design of an optical scanner is the duty cycle of the deflector, a measure of the scanner efficiency. The duty cycle is the ratio between the full scan cycle T_{scan} and the effective time used for the scan T_{eff} :

$$\chi = \frac{T_{eff}}{T_{scan}} \quad (\text{eq. 4.11})$$

The value of χ depends on the particular system and can be up to unity for an ideal deflector. In low-inertia scanners with an oscillating mirror, the duty cycle is decreased by the retrace time and/or linearity demand for the scan.

First, the data are usually not acquired during the retrace of the mirror. This is due to the difficult matching of the scan grid when data are acquired in both scan directions of the optical scan.

Second, in order to achieve the highest scan frequency, the oscillating mirror must work near its resonant frequency. As a result, the mirror performs a harmonic scan with the beam velocity on the surface described by a sine function. As the sampling clock of a DAQ system is usually fixed, such non-linear scan introduces a strong variation of the step size between the pixels. Though this variation can be corrected by software during post-processing, a reasonably small pixel size deviation should be maintained. To provide a first order correction for the scan a-linearity, only part of the scanning amplitude (typically about half) is used effectively; this leads to pixel size deviation of about $\pm 10\%$ from the mean value.

As a consequence, the duty cycle in the harmonic mode is about 0.17. A higher duty cycle is possible when the required scan frequency is well below the resonant frequency of the mirror. In this case, a triangular or a saw-tooth scan can be performed, and the duty cycle above 0.5 can be reached. In deflectometry, a lower duty cycle shifts the design space towards longer measurement times or higher requirements for the detector's response time.

Lens quality

As we pointed out in chapter 3, the slope accuracy of a deflectometer is influenced by the optical aberrations of the scan lens. The aberrations introduce a systematic error into the measured slope. The strongest influence is due to spherical aberration, which, in first approximation, is proportional to the L/f ratio of a deflectometer's scan system. Therefore, a longer focal length of the scan lens is always advantageous for the accuracy of the measurement. The influence of the spherical aberrations can be reduced by using a more complex lens system, like a doublet, a triplet, etc. Of course, more complex lens systems are also more expensive. As we demonstrated in section 3.4, the measurement error due to spherical aberrations can be corrected in deflectometry by a proper calibration. In result, demands for the quality and price of deflectometer's scan lens can be strongly reduced. We estimate that a correction of the spherical aberrations to at least 10 % of the nominal value can be done, with even higher correction in some cases.

Another source of error is introduced by local imperfections on the scan lens surface, mainly caused by small scratches left after polishing. Such imperfections result in high spatial frequency ripple present in both the slope components. The ripple is much more difficult to remove by calibration, but it can be reduced by a better polished lens (which leads to additional costs, as well).

Although the multiple-lens system reduces the spherical aberration, it will increase the high frequency aberrations by $\sqrt{4n}$, with n the number of lenses (each lens has two surfaces and it is passed twice by the scanning beam). Therefore, the choice of the lens system is a trade-off between the quality (high/low frequency aberrations) and price.

Translation system

The main parameter characterizing the translation stage for a deflectometer is translation velocity V . For a single-stroke scan, the full length of the surface-under-test is scanned only once; therefore, the maximum translation velocity for a 300 mm wafer is $V = 300 \text{ mm} / 60 \text{ s} = 5 \text{ mm/s}$, where 60 s is the total measurement time. For a multi-stroke scan, the translation velocity is $V = 5n \text{ mm/s}$ with n the number of strokes. Even for large number of strokes an acceptable translation velocity can be obtained with most commercially available translation stages. For a particular deflectometry system, the translation velocity can be calculated by using basic parameters (Appendix D5):

$$V = \frac{0.34 \chi d_0^2}{L \tau} \quad (\text{eq. 4.12})$$

The translation system for a 3D-deflectometer should be chosen carefully in order to lead to an acceptable level of the errors introduced by mechanical deviations. The main parameters are the straightness and the angular deviations, which introduce the pixel position error and the slope measurement error, respectively. The flatness of the stage is of no concern since a deflectometer is insensitive to the vertical position error (section 1.2).

The pixel-position errors are caused by un-straightness, velocity deviations and yaw of the stage. As a rule of thumb, their contributions should not exceed 1 % of the pixel size. The corresponding requirements for the lateral performance of the stage are given in table 4.6.

Table 4.6. Translation stage parameters that introduce a pixel position error in the 3D-deflectometer.

Error	Criteria
Un-straightness	$\delta x \leq 0.01 \Delta x$
Velocity error	$\delta V \leq 0.01 V$
Yaw ⁴	$\varphi_{yaw} \leq 0.02 \Delta x / L$

Other angular deviations of the translation axis, the pitch and the roll, introduce measurement errors in cross-scan and scan slope, respectively. These errors consist of systematic and random components. As we showed in section 3.3, the systematic components can be corrected to at least 10 % of the nominal value by a proper calibration. The maximum acceptable pitch/roll can be calculated using the parabolic approximation formula (eq. 3.6) and the height accuracy requirement:

$$\theta_{pitch/roll} \leq 80 \frac{\delta \Sigma}{L} \quad (\text{eq. 4.13})$$

⁴ In the table we used the following approximation for the maximum pixel-position error due to yaw: $\delta x = R \sin(\varphi_{yaw}) \approx L/2 * \varphi_{yaw}$, where $R=L/2$ is the radius of the SUT. Note that the corresponding pixel position error increases with the distance from the wafer's origin

The random errors, which by definition cannot be corrected by calibration, have lower influence on the system performance since they are reduced during the surface integration procedure. As a rule of thumb, the random error in pitch/roll should not exceed 1% of the acceptable noise level in the slope signal.

Free working distance

Another parameter that must be considered is the beam size on the scan lens. Imperfections of the scan lens (like scratches, intrusions, variations of the refractive index or dust on its surface), distort the beam quality and introduce inaccuracy into the slope measurement. These problems can be solved partly by using the instrument in a clean environment, and partly by using a high quality lens. However, even a high quality lens will exhibit some degree of high spatial frequency ripple that originates from the polishing process. Those local imperfections are optically filtered out by the scanning beam passing the lens. The filtering effect is stronger when the size of the beam on the scan lens, d_{lens} , is larger. For typical commercially available doublets, $d_{\text{lens}} = 1$ mm results in a peak-to-valley slope error of $\Delta\sigma = 1\text{-}10$ μrad , depending of the specific lens [7]. Furthermore, $\delta\sigma$ is proportional to d_{lens}^{-1} . Therefore, as a rule of thumb, when using a well-polished scan lens a beam size of at least 1mm should be used in deflectometry.

Figure 4.5 shows the size of a Gaussian beam ($\lambda = 633$ nm) as a function of a distance from the waist. Following the graph, one can notice that due to the diffractive beam divergence, a small spot of the scanning beam is advantageous in FOS. This is because a short free working distance can be used and is beneficial for the airborne measurement noise. For larger spot sizes, say $d_0 > 150$ μm , the free working distance is a trade-off between measurement uncertainty due to environmental influences and that due to lens quality. As a side note, the lens quality influence becomes more significant for shorter laser wavelengths, since the beam divergence and d_{lens} are smaller (for the same FWD).

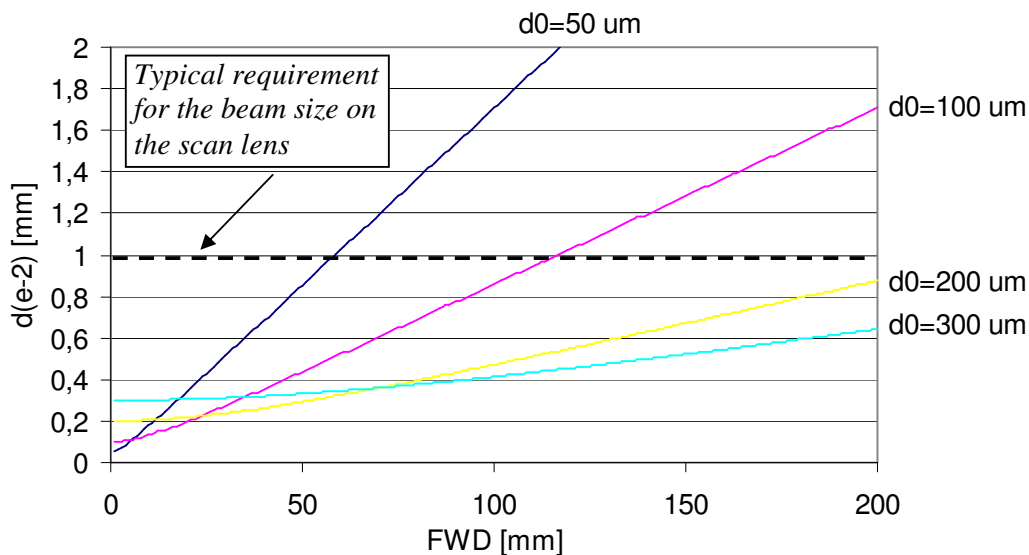


Figure 4.5. Design plot for the deflectometer's free working distance FWD.

4.3.5. Measurement time

In general, the measurement time T of a 3D-deflectometer is limited by the number of samples N^2 , by the sampling speed τ_{ADC} of the A/D converter and the duty cycle of the scanning system χ :

$$T = \frac{1}{\chi} N^2 \tau_{ADC} \quad (\text{eq. 4.14})$$

Following the general sampling rule for the 3D-deflectometer (equation 4.5), one can derive a more elegant form of this equation, linking the measurement time to basic parameters like the spot size and the detector response time:

$$T = 2.9 \frac{1}{\chi} \frac{A}{d_0^2} \tau \quad (\text{eq.4.15})$$

PSD response time

Typically, FOS deflectometry uses a Position-Sensitive Diode for slope sensing. The response time of such a detector is limited by its junction capacitance and the sheet resistance. Since the junction capacitance is roughly proportional to the detector area A_{PSD} , the response time is also proportional to A_{PSD} . In practice, the response time is limited also by the PSD preamplifier quality. Including that factor, the response time of the complete PSD detection unit can be defined as (Appendix C1):

$$\tau = \gamma \Xi A_{PSD} \quad (\text{eq. 4.16})$$

where $\gamma \geq 1$ is the preamplifier quality factor and Ξ [s/m²] the PSD response per unit area (which depends on the specific type of PSD).

Image Reconstruction Time

At the moment, one of the greatest challenges in 3D-deflectometry is the processing time required for topography reconstruction. The advanced integration algorithms using a large number of samples require a lot of memory and processing power. The largest slope array that can be integrated using the reconstruction algorithm used at Philips [8] using a standard PC (Pentium 4 2.0 GHz processor and 2 Gbyte RAM memory) is about 2500 x 2500. The corresponding processing time is about 40 min. Thus, in order to integrate the complete 300 x 300 mm² area, the sampling distance cannot exceed 120 μm . In conclusion, to utilize capabilities of high resolution deflectometry for a real industrial application, a much faster algorithm or an industrial computer is required. The processing time is considered to be beyond the scope of this thesis and will not be discussed further.

4.4. Choices

Scanning strategy

From considerations presented above, we conclude that the optimum scan choice for the 3D-deflectometer is a multiple stroke system. This leads to the shortest measuring time (section 4.3.1). Another advantage of such a system is that the required slope range can be decreased and the object's tilt can be readjusted between the stroke-measurements (it is always possible to readjust it during translation). In this case, the slope range of the deflectometer is decreased by factor of s , with s being the number of strokes. Also, a much cheaper lens can

be used for the optical scan; this, however, is compensated by the cost of the additional translation axis.

For a 300 mm wafer, a three-stroke system would be a good choice; the larger number of strokes would increase the measurement time significantly as a consequence of long total time for the stroke-to-stroke translations. For such a system, the required slope range can be decreased to about $\sigma_{\max} = \pm 1$ mrad of the object's slope.

Scan lens

The first choice for a 3D-deflectometer's scan lens, looking at the price-to-quality ratio, is an extra-polished doublet lens with diameter of 130-150 mm and an effective aperture of $L = 110$ mm (10 % for stitching). The optimum choice for the focal length would be $f \approx 500$ mm. We can estimate a slope error due to spherical aberrations to be about 40-50 $\mu\text{rad} / 110$ mm for such a lens. This could be easily decreased to a negligible level by the lens signature calibration. At the same time, four well-polished surfaces should lead to an acceptable level of the high frequency signature.

In the end, a 500 mm focal length lens for a 3-stroke stitching system offers a reasonable displacement range of 2 mm in the focal plane (see equation 3.1). Therefore, the detector will be limited by the beam size in the focal plane, rather than by the displacement range.

Wavelength

The most obvious choice for the new deflectometer is a short wavelength laser. As we showed in chapter 1.5, a shorter wavelength enables a shorter measurement time and a higher slope resolution of the system. Even more important is the effect of this choice is the decrease of the beam size at the scanning device, which increases the operating frequency the scanning device.

Red lasers are the most common solution for optical scanners, since they are cheap, durable and available at various optical powers. A typical wavelength used often as a reference is $\lambda = 633$ nm (a Ne-He laser). A better choice for deflectometry would be a blue laser, which is still in the visible range, but has shorter wavelength. The laser used in the DVD successor developed by Philips – the Blu-Ray system – has a wavelength $\lambda = 405$ nm and an optical power up to 15 mW. This would be a logical choice for our deflectometer.

Scanning device

The scanning device of choice for a 3D-deflectometer is a galvanometric mirror. These devices are best suited for the chosen aperture and focal length of the scan lens, which lead to scan angle $\theta_{\text{scan}} = 22^\circ$, where we assume a twice over-scan of the scan lens due to the required correction for the scan a-linearity. In addition, such mirrors can reach relatively high resonance-limited frequencies of a few hundred Hz for a few mm scan aperture. If we cannot meet the demands of a 750 Hz scan frequency with this type of system, we can use the available technology of polygon deflectors.

Free Working Distance

A free working distance of 100-150 mm is a good choice, leading to acceptable measurement errors due to airborne noise and lens quality.

Data acquisition

The optimum choice for data acquisition is a 12 bit ADC. The corresponding S/N ratio of about 74 dB for such a system offers safe quantization error levels for the deflectometer, particularly when the maximum slope deviation is decreased due to stitching. Furthermore, commercial 12 bit DAQ systems can reach very high sampling speeds (up to 10^7 samples/s [9]) and usually are attractively priced.

Translation stage

Given the major requirements for the translation axis of $V_{\max} = 15$ mm/s and $\theta_{\text{pitch/roll}} \leq 14$ μrad per 10 mm (section 4.3.4), the optimum translation system for a 3D-deflectometer is an air-bearing or a high quality crossed-roller-bearing translation stage. Even higher performance could be achieved by a stage with a hydrostatic or magnetic-levitation bearings but the price of such an advanced system is much higher.

Measurement time

In appendix D6a we derive the final measurement time formula for our deflectometer:

$$T = 46 \frac{A}{d_0^2} \left(\frac{\lambda}{\pi d_0} + \sigma_{\max} \right)^2 \frac{\gamma}{\chi} \Xi f^2 \quad (\text{eq. 4.17})$$

Following this equation, the inspection of a 300 mm wafer with lateral resolution of 0.1 mm and ideal scanning ($\chi = 1$) and slope detection ($\gamma \neq 1$) could be accomplished in 8 s (appendix D5)! Of course, the actual quality of the components (e.g., $\chi = 0.17$ and $\gamma = 2$) will decrease the system performance roughly by factor of 10 and eventually one finds that in order to meet the initial $T = 60$ s, the lateral resolution needs to be decreased to $\Lambda_{\min} \approx 0.110$ mm. This causes a design conflict and requires a trade-off between measurement time and lateral resolution. For an in-line inspection, this slightly lower lateral resolution could be easily accepted in order to achieve the highest throughput possible. For a laboratory inspection outside the production line, longer measurement time could be more appropriate in order to get higher lateral resolution.

In table 4.7 we present the optimum hardware configuration for such a system, while in table 4.8 we give the detailed specification of its performance. In both tables we concentrate on a system configuration to reach the initial $T = 60$ s requirement.

Table 4.7. Major components of a 3D-deflectometer designed for in-line inspection of 300 mm silicon wafers.

Element	Type	Parameters
Light source	Solid state laser	$\lambda = 405$ nm
Active scan element	Galvanometric mirror	$A_{\text{mirror}} = 4 \times 4$ mm ² , $v_{\text{scan}} = 750$ Hz (harmonic), $\theta_{\text{scan}} = 24^\circ$
Passive scan element/objective	Doublet lens, fine polished	$f = 500$ mm, clear aperture 110 mm
Mechanical scan	Linear translation stage	Air-bearings or crossed-roller bearings
Detector	Position sensitive diode	$A_{\text{PSD}} = 3 \times 3$ mm, $\gamma = 2$
Data acquisition	PC data acquisition card	$\Delta_{\text{ADC}} = 12$ bit, $1/\tau_{\text{ADC}} = 2.3 \cdot 10^7$ samples/s

Table 4.8. Specification of a 3D-deflectometer designed for the in-line inspection of 300 mm silicon wafers.

Parameter	Value
Height resolution (RMS)	$\delta\Sigma = 1.7 \text{ nm}$
Height range/ Spatial range	$\Delta\Sigma / L_{\text{wafer}} = 150 \text{ }\mu\text{m} / 300 \text{ mm}$ (parabolic bending)
Slope range	$\sigma_{\text{max}} = \pm 3 \text{ mrad}$ (by 3-stroke stitching)
Lateral resolution (-6dB)	$A_{\text{min}} = 0.11 \text{ mm}$
Measurement time ⁵	$T = 60 \text{ s}$
Spot size	$d_0 = 82 \text{ }\mu\text{m}$
Sampling distance	$\Delta x = 20 \text{ }\mu\text{m}$
Number of samples	$N^2 = 2.25 \cdot 10^8$
Scan frequency	$\nu = 750 \text{ Hz}$

4.5. Technology tuning

As we concluded in section 4.4, a 3D-deflectometer system can be designed to reach current user specification from the semiconductor industry. However, one could think of a number of technologies, which enable reaching even better specification and therefore future technology development process. These are presented in this sub-section.

4.5.1. Large beam detection

In chapter 1.5 we explained that one of the basic design limitations when measuring the slope with a Position Sensitive Diode concerns the lateral resolution and its influence on the measurement time. In a classical design, in order to achieve high accuracy, the detector is much larger than the incident beam. Otherwise, the measurement would be affected by fluctuations in beam shape and would be inaccurate. A consequence of large dimensions of the detector is its low response time, and thus a long measurement time. If the detector-to-beam size (D/B) ratio decreases, the measurement is faster but less accurate. Thus, looking for the optimum design for a deflectometer, one is looking at a trade-off between measurement uncertainty and measurement time.

One could think of consequences of choosing a PSD detector with a size roughly equal to the beam size (D/B = 1). In this section we will consider such a configuration for which we will use a term the Large Beam Detection (LBD) mode. Analogically, we will call the traditional beam detection configuration the Small Beam Detection (SBD) mode.

The PSD signal carries information about the location of the beam centroid even when the detector aperture is of the same order of magnitude as the beam size. In this case the response of the PSD to the beam displacement is no longer linear since a PSD measures the centre of gravity for only a fraction of the beam. The location of the beam centroid can be derived by a calibration. With this configuration, the gain in the range of detection significant, since

⁵ Processing time excluded

theoretically the beam position could be measured even when the central point of the beam is beyond the edge of the detector!

To investigate the LBD mode, we modelled the detector response (Appendix D7) assuming an undisturbed Gaussian beam. Figure 4.6 shows the results of a simulation of the PSD response for various ratios $D/B = D_{\text{det}}/d_{\text{det}}$, where D_{det} is the detector size and d_{det} the beam size on the detector. The horizontal axis in the graph indicates the position $\xi_c/(D_{\text{det}})$ of the beam centroid; the vertical axis shows the corresponding PSD signal ξ , which indicates the centre of gravity of light on the detector. The detector area is limited by $\langle -1, 1 \rangle$ ordinates on both axes. The SBD modes are represented by $D/B = 100$, $D/B = 10$ and $D/B = 2$; the LBD mode is represented by $D/B = 1$, $D/B = 0.5887$ ($D_{\text{det}} = d_{\text{det}}$ (FWHM)) and $D/B = 0.5$.

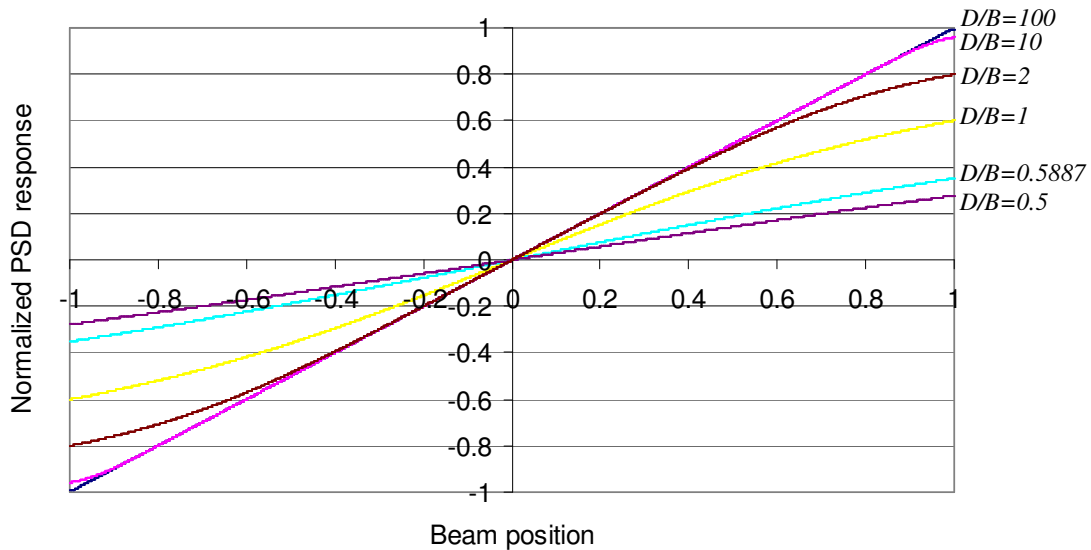


Figure 4.6. Calculated PSD response for various detector-to-beam-size ratios D/B , as a function of the normalized position $\xi_c/(D_{\text{det}})$ on the detector. The detector size corresponds to $\langle -1, 1 \rangle$ range on both axes.

As we show in our model, the sensitivity of the PSD response decreases with larger D/B ratio. However, due to very high resolution of the PSD itself, the detection resolution in the LBD mode is still high. As we prove in the appendix D10, even with the $D_{\text{det}} = d_{\text{det}}$ (FWHM), measurement resolution better than 12 bit has been achieved.

We also proved (appendix D9) that the effective displacement range of the beam detection in the LBD mode is much higher when compared to the traditional SBD. Although the deflections in the LBD mode are limited by decreasing sensitivity and a low irradiance when the beam centroid moves off the detector, the beam position can be measured even when the beam centroid is well outside the detector aperture.

As we mentioned earlier, one could predict that the position of the beam centroid measured in the LBD mode will be influenced strongly by deviations of the beam shape and size – the first caused e.g. by airflow and diffraction/truncation effects on the surface, the latter caused by a variation of the local curvature of the measured surface. Both these factors will increase the uncertainty of detection, and as a result degrade measurement accuracy as compared to

the SBD mode. On the other hand, LBD mode is much less sensitive to a stray light, diffraction from scratches and ghost spots on the PSD surface. Since these effects are probably the most significant factors influencing measurement uncertainty in the SBD mode, we can expect that in practice the measurement uncertainty of the LBD mode can be comparable to the SBD mode.

Furthermore, the LBD mode requires, polynomial fitting of the calibration data since the PSD response is not linear. Such a calibration will introduce additional errors, but as we proved in the appendix D9, even a simple correction with a third order curve gives only a small error in describing the data.

In conclusion, the Large Beam Detection concept seems to be very promising for High-Resolution deflectometry. Although the LBD mode requires a larger calibration effort, due to the non-linear response, it enables a significant reduction of the measurement time due to using a smaller, thus faster, PSD. A somewhat lower resolution and accuracy due to diffraction and environmental influence of the measurement are acceptable. since those measurement errors (random) are averaged out during the numerical integration procedure (chapter 1.4).

4.5.2. Sampling

The measurement time, the total number of samples, and the required ADC speed can be slightly improved by filtering the slope signal in the DAQ system. As we showed in section 4.3.2, the slope signal measured with a Gaussian beam requires high over-sampling. By applying a low-pass filter to the slope signal to attenuate frequencies $k > k_{\max}$, the sampling distance Δx in the scan direction can be increased without decreasing the measurement quality. With an ideal filter, the sampling spatial frequency could be decreased to $1/\Delta x = 2k_{\max}$. We estimate that by using a real filter (which is always non-ideal) a sampling of $1/\Delta x = 3k_{\max}$ ($\Delta x \approx 2.3d_0$) could be achieved.

The “frequency approach” presented above aims in reconstructing the slope data “as accurate as possible”. Since the final aim for 3D deflectometry is to measure topography, one could think of another, more efficient approach for sampling a slope signal. The new strategy would aim at such a sampling strategy that leads to the smallest topography error after integrating the sampled slopes. An example is a sampling strategy that resembles a discrete linear interpolation of the slope signal. For example, for an ideally square beam irradiance profile (instead of a Gaussian), the samples should be taken exactly one next to another, without any over-/under-sampling. Although information about spatial frequencies on the order of the beam size is lost (due to an averaging effect), after integration, the height change should be recovered accurately. For a beam with a different profile, e.g. a Gaussian beam, the sampling distance should be chosen such that the integrated irradiance on the measured area is uniform. For a Gaussian beam, this recipe results in taking samples at distance approximately equal to the FWHM of the beam.

Due to time limitations in the project, this approach has not been further investigated and tested. It seems, however, very attractive for deflectometry since it leads a few times higher throughput and much lower requirements for DAQ system.

4.5.3. Slope stitching

The image of the complete area of the surface-under-test is obtained by stitching the measured sub-fields during post-processing. Stitching of topographic images is a well known technique and is widely used in interferometry, where to reach high lateral resolution the field of view is often much smaller than the area of interest. The stitching is done by fitting the sub-fields together in a global sense, or by matching the piston and tilt over the overlap region [10]. The drawback of topography stitching is the error propagation introduced by the procedure. A relatively large overlap is needed to minimize the stitching error. Therefore, the stitching in the height domain is always a trade-off between throughput and accuracy of the measurement.

The stitching procedure can be improved significantly when the surface-under-test is measured in the slope domain, where the stitching is done directly on the slope data [11]. In this case, the stitching procedure is easier since the measured slope arrays do not require correction for tilt but only for piston. This is because the absolute height information is not present in the slope data (see figure 1.1), and therefore the height difference between the adjacent fields does not require correction. Furthermore, the difference of tilt between the sub-field produces only an offset in the slope data. The offset correction is a simple mathematical operation and can be done precisely even when only a small overlap is present between the fields. Finally, the remaining errors will be corrected during surface reconstruction.

Thanks to the stitching in the slope domain, the decrease of throughput and accuracy of the deflectometer becomes negligible. This feature shows again the advantage of measuring surface topography in the slope domain.

4.5.4. Effective gain in performance

In appendix D5b we derive the expression for the new measurement time T' that includes the technology tuning factors. In the case of LBD, the detector size is determined mainly by the slope range σ_{\max} and not in first order by the beam size. Including a smaller detector size and a larger sampling distance in the scan-direction, we find:

$$T' = 37 \frac{A}{d_0^2} \sigma_{\max}^2 \frac{\gamma}{\chi} f^2 \Xi \quad (\text{eq. 4.18})$$

One can notice that the effective gain in measurement time due to technology tuning is simply:

$$T / T' \approx 5 \quad (\text{eq. 4.19})$$

We can see that by taking the risk of lower measurement accuracy in the LBD mode, we can provide a major improvement to the system by decreasing the measurement time by as much as a factor of five. This is a perfect example of how the theoretical system limitations can be overcome by “non-standard” design concepts.

4.6. References

- [1] SEMI M43 standard – *Guide for reporting wafer nanotopography*
- [2] A.V. Oppenheim, A.S. Willsky, N.S. Hamid, *Signals and Systems*, Prentice Hall (1996)
- [3] D.J. Whitehouse, *Handbook of surface and nanometrology*, Institute of Physics Publishing (2003)
- [4] J.W. Goodman, *Introduction to Fourier Optics*, Mc-Graw-Hill, 3rd edition (2004)

- [5] E. Hecht, *Optics*, Addison Wesley; 4th edition (2001)
- [6] J.C. Stover, *Optical scattering: measurement and analysis*, SPIE; 2nd edition (1995)
- [7] J.A.P. Snijders, *Evaluation of strip-lens manufacturing-technique for deflectometry*, TUE, internship report AQT 04-02 (June 2004)
- [8] J. Campos, L.P. Yaroslavsky, A. Moreno, M.J. Yzuel, *Integration in the Fourier domain for restoration a function from its slope: comparison of four methods*, *Optics Letters*, **27**, 1986 (2002)
- [9] National Instruments Inc., Web site: www.ni.com
- [10] J. Schmit, J. Wyant, *Large field of view, high spatial resolution surface measurement*, Application Note AN504, Veeco Instruments, Inc, www.veeco.com
- [11] W.van Amstel, K. Szwedowicz, *Slope stitching*, patent application PH000521EP1

Chapter 5

The architecture of the new system

In this chapter we will present the detailed architecture and components of the High Resolution 3D-deflectometer built at Philips Applied Technologies. In the first section we give some general remarks about the system, explaining the motivation for the final choice of components. Further on, in sections 5.2, 5.3 and 5.4 we explain the hardware architecture, the data flow and software program for the system, respectively.

5.1. General remarks

Two determining factors for the final system construction were the limited project time and budget, both in capital for new equipment and in outsourcing work within Philips Applied Technologies. With these limitations, it was impossible to build the optimum design described in chapter 4. Therefore, the new system that has been built during this project is based on the existing FOS deflectometer with a 100 mm optical scan width, which, by coincidence, corresponds to the optimum scan width. With this system, only a single-stroke Cartesian scan is possible. To upgrade the current system to a sufficiently convincing beta-prototype for testing by a customer, e.g., Philips Semiconductors in Nijmegen, several essential steps still need to be taken. First, there is the need to add a new xy -translation table and a stitching software to upgrade the system to a multi-stroke Cartesian that allows the inspection of 300 mm wafers. Second, we have to improve both: the PSD electronics and deflection system such that higher scan/acquisition rates could be achieved.

5.2. Hardware

The complete 3D-deflectometry system consists of three main elements: the FOS head, the translation stage and the control PC. A picture of the system is shown in figure 5.1

The Fast Optical Scanner

Figure 5.2 presents a schematic drawing of the FOS deflectometer used in our system. The telecentric scan is done by a doublet lens with diameter of 150 mm (effective aperture $L = 110$ mm) and focal length $f = 800$ mm produced by Linos. To avoid the impractically large dimensions of the instrument, two mirrors are added to fold the optical path inside the deflectometer. The deflector and detector are located about 5 cm from each other, resulting in about 4° angular shift from the optical axis of the scan lens.

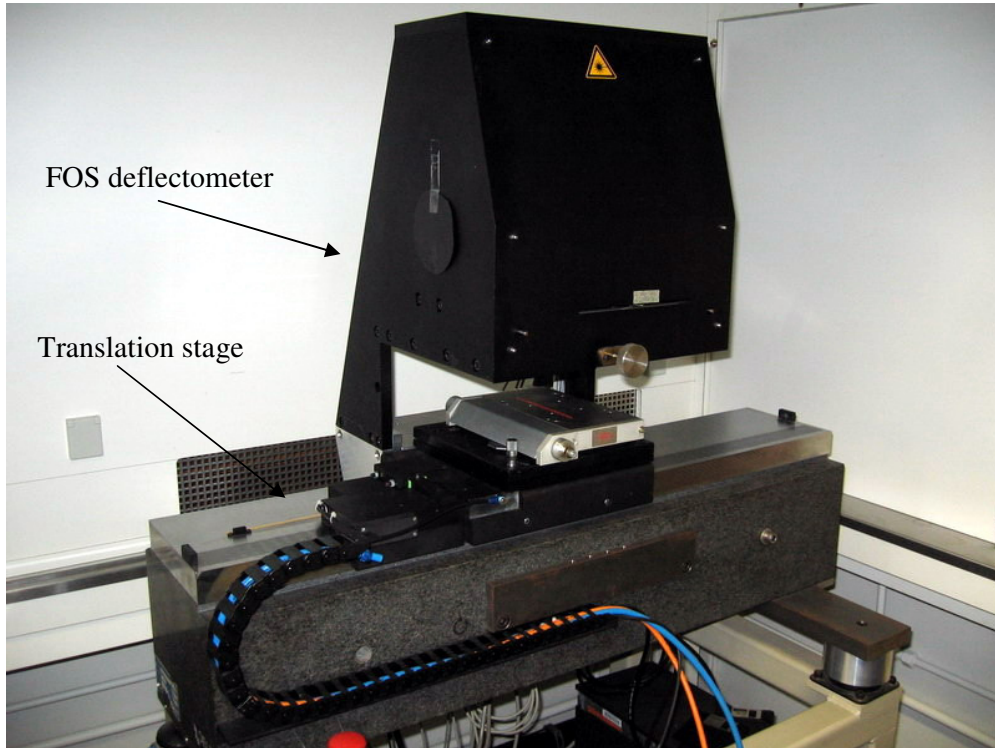


Figure 5.1. The general overview of the 3D-Deflectometer at Philips Applied Technologies.

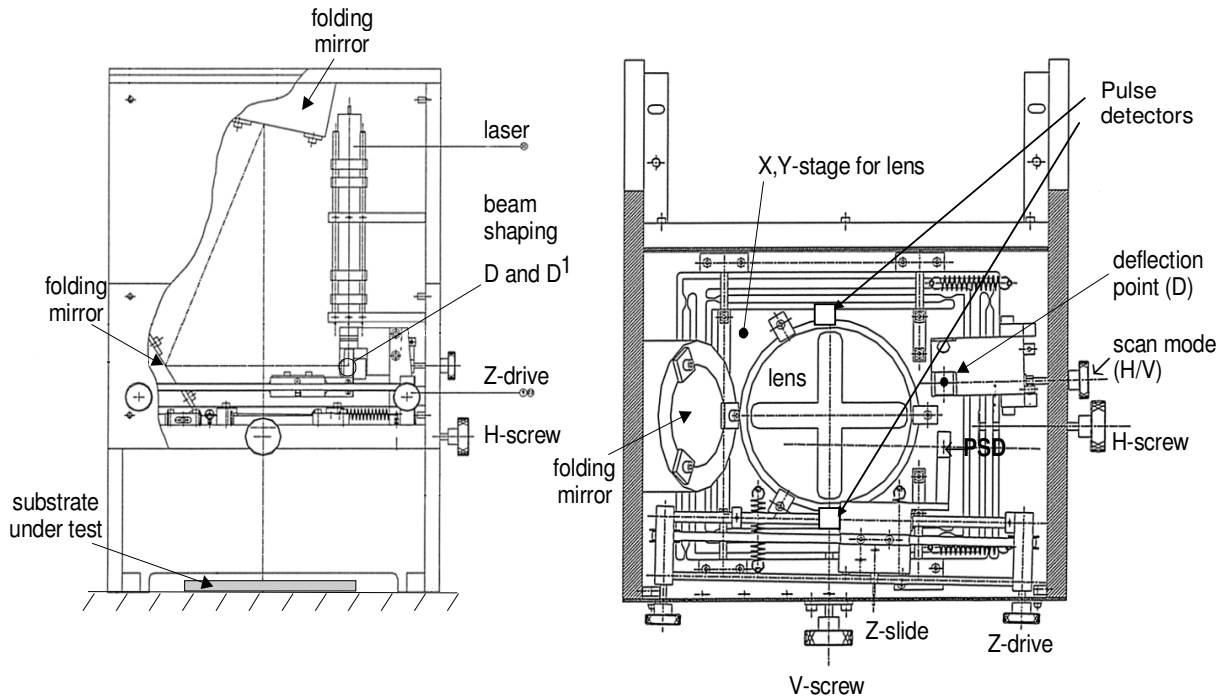


Fig. 5.2. Schematic drawing of the 110 mm deflectometer [1]. The left image shows a side view and the right image shows a top view. Although the deflection point D and the detector D¹ are virtually located 800 mm above the scanning lens, two folding mirrors help compact the instrument.

The horizontal position of the scan lens can be adjusted using the V and the H screws, which thus adjust the (ξ, η) position of the focal point at the detector, providing a virtual tilt correction of the scanned surface.

Using the Z-drive we can operate the z-slide with the PSD and shift the detector along the optical axis of the scan. We use this degree of freedom to focus the fan of reflected beams on the detector. This feature can be used to extend the slope range of the deflectometer to a surface-under-test with concave or convex form. The surface then effectively acts as an extra optical element that shifts the focal plane of the fan of reflected beams out of focus. If we shift the detector towards this new effective focal plane, we focus the reflected telecentric beams on the detector again. This way we lose the information on the general curvature, but we can measure a local curvature of the surface with higher slope range (in the scan direction). Of course, this “power correction” requires re-calibrating the slope sensor.

The ‘scan mode’ screw, shown at the right picture of figure 5.2, has been originally used for changing the horizontal orientation of the deflectometer’s scan – perpendicular or parallel to the front view of the deflectometer. For the 3D-deflectometry platform we do not use this option anymore, and the scan is fixed in the ‘perpendicular’ configuration only.

The light source and beam shaping

The goal of the design of the optical system is to achieve a waist of the laser beam on the surface-under-test of $d_0 = 150 \mu\text{m}$. The lay-out and the complete optical configuration of the beam shaping module are presented in figures 5.3 and 5.4, respectively. The light source is a 5 mW diode laser with wavelength of 670 nm. As we mentioned in chapter 3.2.1, FOS uses a beam-shaping module to produce the desired spot size on the object. The first three elements to the right of the laser in figure 5.4 form the beam-shaping module. The module consists of two lenses and an additional pinhole between the beam shaping lenses, which improves the beam quality by filtering the stray light. The beam shaping produces a close to ideal Gaussian spot on the surface.

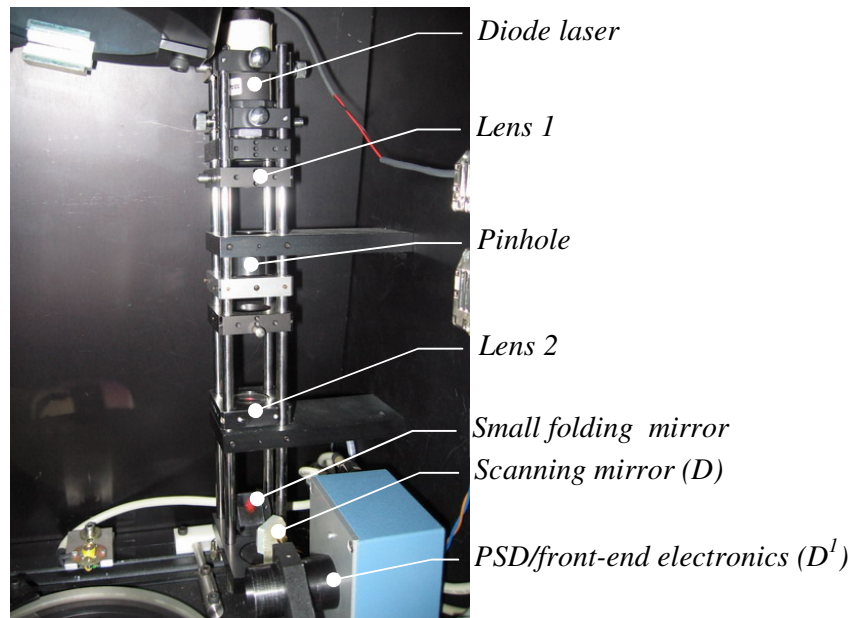


Figure 5.3. Beam shaping module assembled inside the 3D-deflectometer.

The optical design has been verified using a beam profiler (figure 5.5). The measurement indicates a spot size of about $d_0 = 150\text{-}170\ \mu\text{m}$. The beam exhibits astigmatism, typical for diode lasers. Nevertheless, assuming the SUT position between 1 and 10 mm above the support surface, the spot size variation between the two axes is less than 10 %.

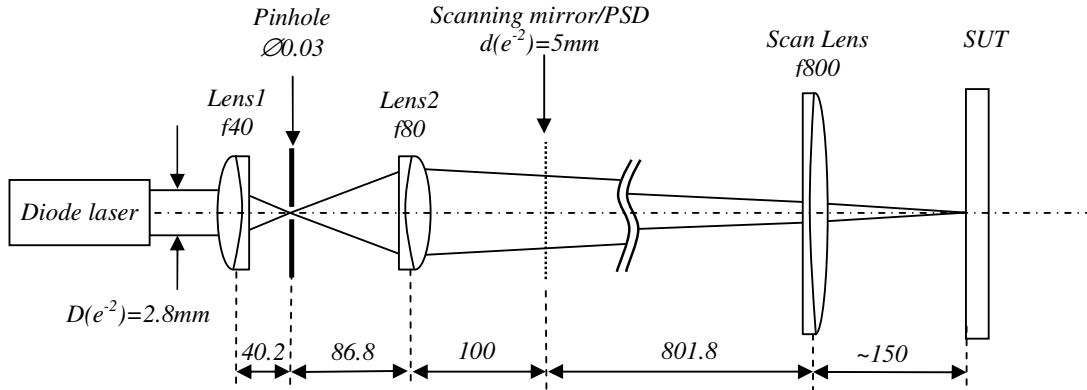


Fig. 5.4. Optical configuration of the high-resolution deflectometer.

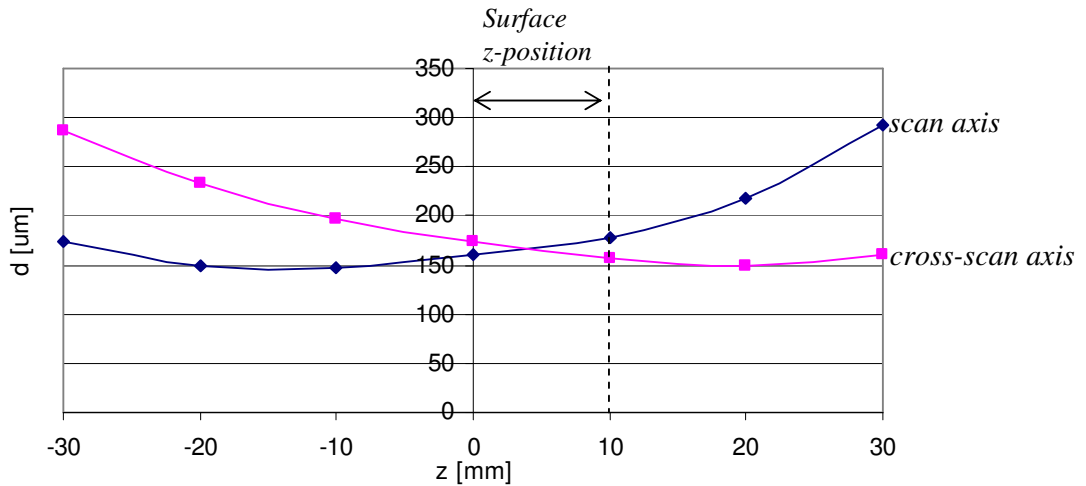


Fig. 5.5. Beam size d of the probing beam as function of the vertical position z at the surface-under-test. The z -axis is centred at the support of the surface-under-test.

The scanning mirror

The angular scan is performed by a 10 x 15 mm galvanometric mirror. The mirror has been made at Philips Applied Technologies, for Video Long Play systems (VLPs). It has a nominal tilt range of about 30° and resonant frequency of 50 Hz. The mirror is show in figure 5.6. The mirror is controlled by a National Instrument analog output card; the signal is amplified by a dedicated amplifier.



Figure 5.6. VLP scanning mirror used in the high-resolution deflectometer. The scanning aperture is 10 x 15 mm and the resonant frequency 50 Hz.

The detection and the Data Acquisition system (DAQ)

The slope sensing is performed by a 4 x 4 mm PSD from Sitek. The DAQ system is a research model developed specifically for the deflectometer at Philips Applied Technologies. The system consists of three parts: an analog front end, an analog-to-digital converter (ADC), and a digital DAQ PCI card. The front-end electronics produces three analog signals: two differential position-related signals (not normalized to intensity), and an intensity signal. For the sake of low noise, the front-end unit is attached directly to the PSD. The analog signals are acquired by digital electronics consisting of three fast ADCs. Before the A/D conversion, each of the three signals is processed by anti-aliasing filters. The digital signals are acquired by the digital DAQ. The complete system is controlled by LabView software installed on the main PC. The specifications of the data acquisition components are given in table 5.1.

Table 5.1. Components of the deflectometer’s detection and data acquisition system.

Element	Parameters	Manufacturer/model
PSD	4x4 mm ²	Sitek, 2L4
Analogue front-end	Bandwidth: 300 kHz SN ratio: ≤ 100 dB	Philips Applied Technologies
ADC	Simultaneous sampling Sampling speed: 1.2 MHz Resolution: 16 bits	Philips Applied Technologies
Digital DAQ card	Resolution: 16 bits	National Instrument, NI 6552

The translation stage

For mechanical translation we applied an air-bearing translation stage from PASIM GmbH. The stage has a good price-to-performance ratio. The stage consists of a 500 mm-long sliding axis and a motor. The axis is fixed to a flat granite block, which increases the flatness of the axis and provides vibration isolation for the deflectometer. To decrease the influence of the motor vibrations on the object stability, the object is not supported directly by the motor. Instead, we use an additional support, a passive carriage dragged by the motor. The carriage is equipped with air bearings, and it is connected to the motor by a flexible coupling to minimize the influence of the motor vibrations on the surface-under-test. The motor and the passive carriage are shown in figure 5.7. The stage is controlled by an EcoStep200 controller from Jenaer Antriebstechnik GmbH, which interfaces to the main PC via an RS 232 port.

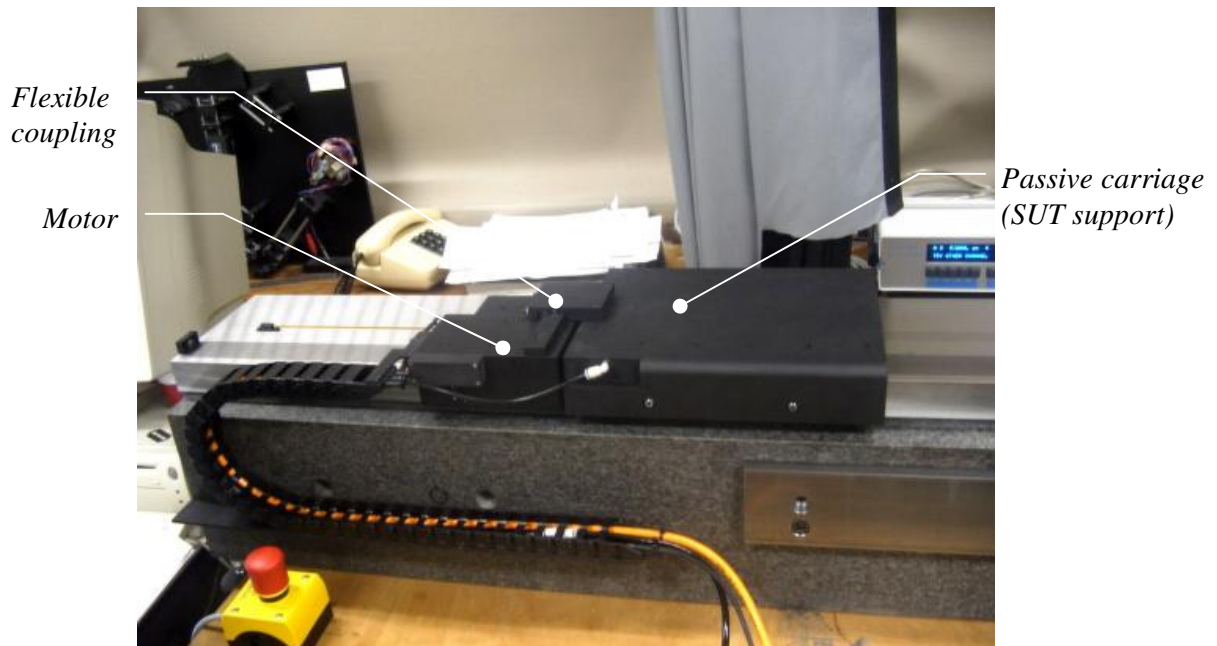


Figure 5.7. A 500 mm long, air-bearing translation stage from Pasim GmbH. A passive carriage is connected to the motor by a flexible coupling. This way motor vibration does not influence the object on the passive carriage.

Summary of the 3D-deflectometer's hardware

The summary of the hardware components and corresponding system performance for our 3D-deflectometry system are given in tables 5.2 and 5.3, respectively.

Table 5.2. Summary of hardware components for the High Resolution 3D-deflectometer.

	Element	Type	Manufacturer
Optical and scanning system	Scan lens	$f800, 150 \text{ mm}$	Linos
	Beam shaping	L1: $f40$, L2: $f80$, pinhole: $50 \mu\text{m}$	Linos
	Scanning mirror	$10 \times 15 \times 2 \text{ mm}$, galvanometric (VLP)	Philips Applied Technologies
	Scan control	Analog-output card NI PCI-6711	National Instruments
Detector and DAQ	Detector	PSD, $4 \times 4 \text{ mm}^2$, model 2L4	Sitek
	Front-end	Analogue, 300 kHz	Philips Applied Technologies
	ADC	$3 \times 1.2 \text{ Msample/s}$, 16 bits	Philips Applied Technologies
	DAQ	NI PCI-6552	National Instruments
Translation axis	Translation stage	Airbearing, 500 mm	Pasim
	Controler	Ecostep 200 via RS 232	Jenaer Antriebstechnik
Main control	Desktop PC	P4 2GHz, 2 GB RAM, Windows XP	Compaq

Table 5.3. Performance parameters of the 3D-deflectometer

Parameter	Value
Spatial range	optical $L = 110 \text{ mm}$
	translation $L_y = 500 \text{ mm}$
Slope range	$\sigma_{\max} = \pm 1.25 \text{ mrad}$
Height resolution	$\delta\Sigma = 1 \text{ nm}$
Spot size	$d_0 = 170 \mu\text{m}$
Sampling distance	$\Delta x = 30 \mu\text{m}$
Sampling speed	$1/\tau_{\text{ADC}} = 1.2 \text{ Msample/s}$
Maximum number of samples	$N^2 = 10^7$
Scan frequency	$\nu = 50 \text{ Hz}$
Measurement time	$T = 73 \text{ s} / 110 \times 110 \text{ mm}^2$

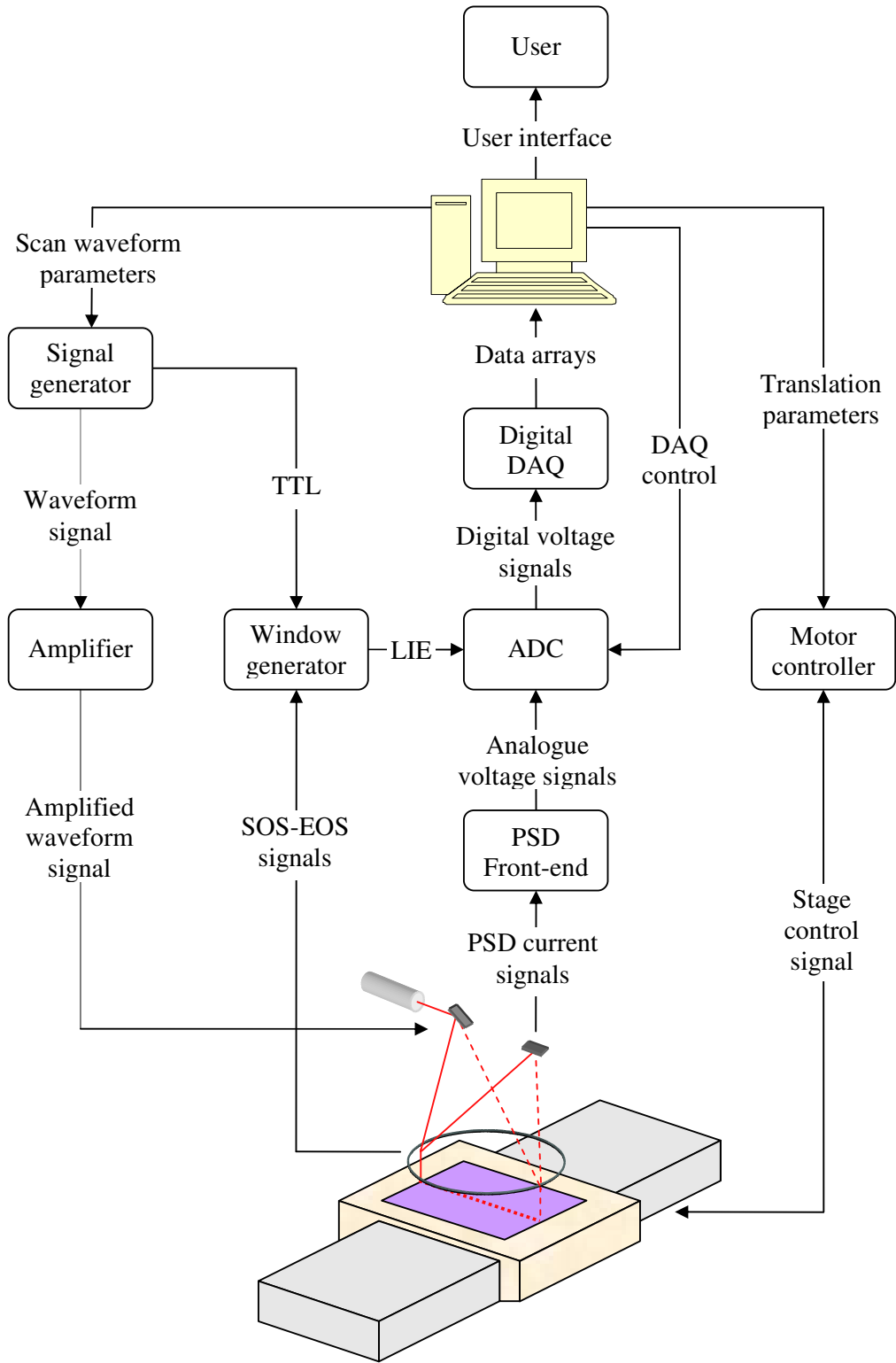


Figure 5.9. General system architecture of the 3D-deflectometer

5.3. Data flow and scan synchronization

The data flow in the 3D-deflectometer is presented schematically in figure 5.9. One of the key parameters in the scanning system is synchronization of the scan to the DAQ system. The most efficient way to achieve scan synchronisation is to use optical pulse detectors that indicate precisely the moment when the optical beam physically crosses a fixed position on the scan line. This way the scan synchronization is independent on the delays in the operation system.

The detectors are photodiodes assembled at the beginning and at the end of the optical scan line. When the scanning beam passes the detectors, it produces electrical pulses called ‘Start of Scan’ (SOS) and ‘End of Scan’ (EOS). These pulses are combined electronically with the TTL signal from the sinusoidal wave generator by a window generator, resulting in a digital ‘Line Enabled’ signal (LIE). The LIE signal is used further for the synchronization of the DAQ with the position of the scanning beam. The SOS-EOS and the TTL signals are combined such that the LIE signal is high only for one direction of the scan, and thus data are not acquired during the retrace. This is shown schematically in figure 5.10.

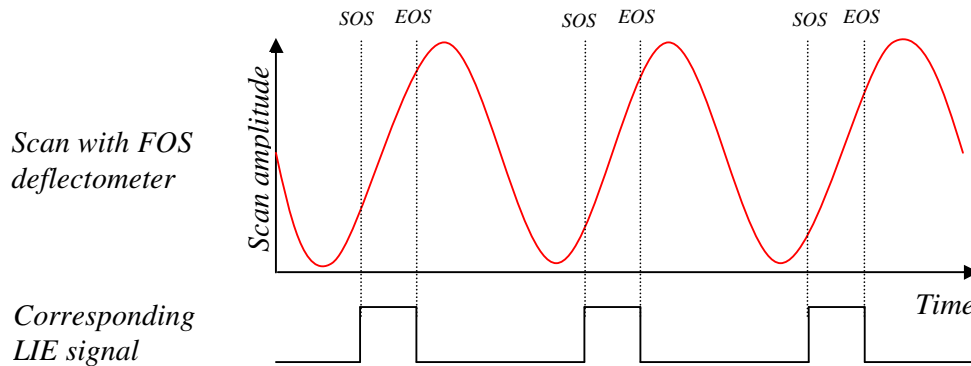


Fig. 5.10. Relation between the location of the scanning beam along the scan line, positions of the SOS-EOS detectors and the LIE signal.

5.4. The software program

The complete software program for the 3D-deflectometry system has been written in LabView. The program consists of several modules, which are described below.

Hardware control

This most essential part of the program consists of the:

- Data acquisition (DAQ) control
- Translation stage control
- Scanning mirror control

The DAQ control gives the parameters and commands for acquisition and collecting the data from the A/D converter. The program converts the digital data from ADC into three two-dimensional arrays corresponding to the scan- and cross-scan slope signals, and the intensity signal.

The translation stage control communicates (via RS 232) to the stage controller to send translation parameters and commands (start, stop, etc...). It also reads the actual position of the stage.

The scanning mirror control sends the scan waveform parameters to the analogue-output (AO) card that controls the scanning mirror. This information consists of the shape of the waveform, the amplitude and the scan frequency. Another channel of the AO card is programmed to produce a TTL signal for synchronisation of the data acquisition to the optical scan (see section 5.1 “SOS-EOS detectors”)

The basic post-processing

The basic post processing consists of:

- normalization
- signal to slope conversion

The analog front-end of the PSD produces slope-related signals that are dependent not only on the beam location, but also on the total light intensity on the PSD. Therefore, those signals must be normalized to the corresponding intensity (which is the third signal acquired from the PSD). Since this feature is not supported by our front-end preamplifier, it is done digitally during post-processing.

The digital values of the normalized signal have no physical meaning. Therefore, the digital signal is converted into slopes by applying a polynomial evaluation. The polynomial is determined from the slope calibration curve (see the following paragraph).

The calibration

The calibration program consists of:

- Slope calibration
- Pixel size calibration
- Signature removal

The slope calibration is used to determine a relation between the normalized slope-related signals for the detector/DAQ and the slope. Pixel size calibration is used to determine the spatial distance between the samples. Signature removal is used to increase the measurement accuracy by determining and removing optical aberrations of the scan lens and mechanical deviations of the mechanical translation. The calibration procedures are described in detail in chapter 6.

Advanced post-processing

The advanced post-processing provides several options, increasing the functionality of the system. Thus, this module consists of:

- Graphical display
- Basic surface-reconstruction
- Down-sampling
- Choosing an area of interest
- Intensity threshold
- Polynomial shape removal

The graphical display is used to show an image of the measured surface. The display includes a 2D view (xy projection), a 3D-view and chosen profiles in x - and y - directions. The program can display signal intensity, slopes or a topography image.

The basic surface-reconstruction module is used to produce topography from the measured slope data. It applies a simple double linear integration, which has been explained in chapter 1.4 (figure 1.11). Since this surface reconstruction algorithm is sensitive to measurement noise and errors, it can be used only for a smooth surfaces or for a quick check of the measurement results. For accurate surface reconstruction an external application is used, based on the Iterative Fourier Integration developed by Universitat Autònoma de Barcelona (a partner in the European “3D-deflectometry” project) [2].

Down-sampling is used to virtually increase the sampling distance. This is done by re-sampling the original slope data by aid of a spline interpolation on the original data. This option is used whenever the number of samples exceeds capabilities of the surface-reconstructing program.

The area-of-interest option is used to extract a chosen sub-field from the measured slope or topography arrays.

The intensity-threshold option is used to subtract a low-reflectance area from the slope or the topography array. This option is useful to remove non-relevant areas of the measurement field, for example when a circular object (e.g. a wafer) must be located within a rectangular measurement field.

Polynomial shape removal is used mainly to correct the topography for tilt and piston. It can be used also to remove a parabolic bend or higher-order polynomial form deviations.

5.5. References

- [1] R. Boerhof, J.C.J. van Vliet, *Deflectometer voor vlakheidmeting van optische spiegels*, graduation report, Hogeschool van Utrecht (1998)
- [2] J. Campos, L.P. Yaroslavsky, A. Moreno, M.J. Yzuel, *Integration in the Fourier domain for restoration a function from its slope: comparison of four methods*, *Optics Letters*, **27**, 1986 (2002)

Chapter 6

Calibration of the 3D-deflectometer

Calibration of the 3D-deflectometer has to do with defining, and if possible, correcting for the measurement errors which influence the vertical and lateral accuracy in the measured topography. In this chapter we present the estimation of error sources in the system and the corresponding correction procedure. In section 6.1 we give a general introduction to the calibration of the deflectometer. In sections 6.2 and 6.3 we discuss the calibration of the systematic and random errors of the scan grid, respectively. In section 6.4 we consider the alignment of the detector (the slope sensor). In section 6.5 the calibration of the slope sensor is described. In section 6.6 we describe the calibration of the system signatures (systematic errors in measured slope). In section 6.7 we give the estimation of the surface reconstruction errors. Finally, in section 6.8 we summarize the calibration procedure applied for the 3D-deflectometer.

6.1. Introduction to calibration

Boundary conditions for calibration

The integration procedure for the reconstruction of the surface is a least-squares-type optimization that has the advantage of being robust and forgiving in error propagation. This is because of its multiple-path nature, as discussed in chapter 1.4. In chapter 7 we show that this is an essential condition for the application of deflectometry as a metrology tool. Even for the current size of data arrays, assuming an equidistant array of data points, the calculation time is already a major limiting factor on the performance of our deflectometer. For a data set with varying grid size and non Cartesian grid points, the software calculations would become even more complex and inefficient, resulting in unacceptable calculation times. For this reason we calibrate our 3D-deflectometer in such way that the grid entering the calculation is equidistant and perfectly Cartesian.

An even more fundamental reason for establishing a perfect Cartesian grid stems from the direct nature of deflectometry. Systematic errors in grid position and spacing do not only result in an erroneous location of the surface, but also result in an error in the reconstructed surface height Σ . This is due to the underlying integration process: systematic errors in the grid spacing directly translate into systematic errors in surface height (figure 6.1) that will propagate along the grid. Systematic errors in grid point position just result in an erroneous location, as is the case for most other metrology tools. Random errors in the grid position and spacing have a much smaller effect, because the integration procedure applied is very forgiving and avoids random error propagation [1].

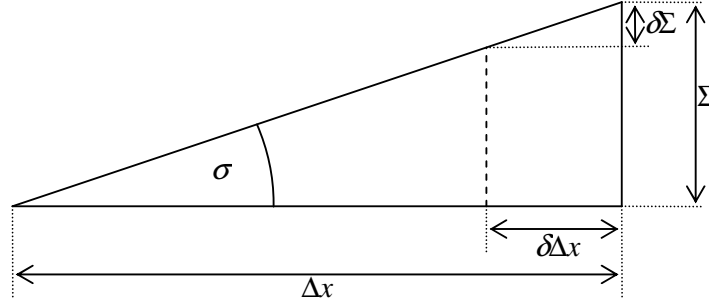


Figure 6.1. Reconstruction of height Σ from measured surface slope σ over a spatial distance Δx . Height error $\delta\Sigma$ is introduced as a result of error $\delta\Delta x$ in the estimated spatial distance. In the 3D-deflectometer the error can result from incorrect pixel size assumed for the surface reconstruction.

The scanning system

The experimental data output is an array of slope data $\bar{\sigma}_{ij}$ with pixel index (i, j) measured at absolute position (x_i, y_j) as input. The reconstructed values are $(\tilde{x}_i, \tilde{y}_j)$ that differ from absolute position as:

$$(\tilde{x}_i, \tilde{y}_j) = (x_i, y_j) + (\delta^R x_i, \delta^R y_j) + (\delta^S x_i, \delta^S y_j) \quad (\text{eq. 6.1})$$

with random errors δ^R and systematic errors δ^S . The task is to find the function $f(i, j) = \tilde{x}_i$ and $g(i, j) = \tilde{y}_j$. In first order approximation we assume that the functions are uncoupled and obey:

$$\frac{df(i, j)}{dj} = \frac{dg(i, j)}{di} = 0 \quad (\text{eq. 6.2})$$

The approach of our calibration procedure is to map a well defined and highly accurate Cartesian grid with the grid points (x_N, y_M) onto the measurement grid (i, j) of the deflectometer. Characteristic features of this calibration device can then help us define the calibration functions f and g and show us where errors are introduced by the malfunctioning of the 3D-deflectometer. An example of the latter, one can think of jitter in the triggering system of the data acquisition device.

The slope measuring system

In the 3D-deflectometer the signals S_{ij} are collected as a measure for the components of the slope vector $\bar{\sigma}_{ij}$ in the direction of the coordinate system of the surface-under-test at the positions (x_i, y_j) . For a perfectly aligned detector system, the transformation between the signals S and the slopes σ is simply given by $\bar{\sigma} = A_{CAL} \bar{S}$ with the matrix:

$$A_{CAL} = \begin{bmatrix} C_x & 0 \\ 0 & C_y \end{bmatrix} \quad (\text{eq. 6.3})$$

with C_x and C_y the geometry factors for the scan and the cross-scan slope, respectively, derived from calibration (e.g., with an autocollimator setup – figure 3.3). Mechanical

misalignment of the PSD will result in errors in this transformation. For example, a rotation of the detector over a small angle φ requires a transformation matrix:

$$A_{\text{det}} = \begin{bmatrix} \cos \varphi & \sin \varphi \\ -\sin \varphi & \cos \varphi \end{bmatrix} \quad (\text{eq. 6.4})$$

Mechanical misalignment along the optical axis, leaving the PSD out of focus, results in an offset in the detector response that depends on the position x_i on the scan line. Finally, deviations of the detector response from a linear behaviour require a more complicated function such as:

$$\sigma_x = C_x S_\xi + P_n(S_\xi) \quad (\text{eq. 6.5})$$

with P_n a polynomial that takes into account the non-linear behaviour. This is the case when we use a PSD in the Large Beam Detection mode.

Approach

For most error-correction procedures we can think of two approaches. First, we try to eliminate the errors by careful alignment of the mechanical and optical system of the 3D-deflectometer – the hardware approach. Of course, this requires procedures and recipes that are reliable and repeatable, that can be done by an experienced operator.

Second, we can measure the transfer function such as f and g for the grid correction and P_n for the PSD non-linearity and apply these to the data arrays before performing the surface reconstruction – the software approach. Both the hardware and the software approaches will be discussed in this chapter, together with recipes for the hardware alignment and the measurement of the transfer function for the software approach.

Calibration tools

For the measurement of the transfer function we will use three essential calibration tools, carefully selected (purchased or manufactured) and calibrated by other metrology tools. First, we have manufactured on a 3 mm thick glass substrate an accurate reference grid of chromium lines with a line-width of 1 μm , a pitch of 5 mm, and the coordinates of the line edges with accuracy better than 2 μm . An intensity image of this grid – just using the total PSD intensity signal S_I – is an ideal input for determining the f and g functions.

Second, we use a ‘zerodur’ optical flat with a diameter of 300 mm, thickness of 50 mm and flatness of about $\lambda/10$ (PV $\delta\Sigma \leq 63$ nm) over the complete area (calibration report in Appendix F1). This reference flat is used for measuring the response of the deflectometer as a function of x_i and y_j , and to determine with a high accuracy the signature of both the lens and the translation stage. Also, the optical flat is an essential tool for aligning the system in the hardware approach.

Finally, we use an autocollimator set-up as described in chapter 3.2 to measure the transfer functions C and P_n . As reference device we use the Elcomat 2000 autocollimator from Moeller-Wedel GmbH with a nominal accuracy of 0.5 μrad .

6.2. Scan position mapping: systematic errors

To get a first impression of the deviation of the measured pixels grid as compared to the nominal Cartesian grid, we scanned a rectangular area of about $110 \times 110 \text{ mm}^2$ of the reference grid. During the measurement the grid orientation was aligned precisely so that the grid lines are oriented in the nominal scan and translation directions. The alignment was done by measuring and re-aligning the plate several times until the desired orientation was achieved. By this procedure we are able to align the grid with accuracy of 1 pixel/complete translation length, which translates into misalignment error of 0.3 mrad. From the obtained intensity image in (i, j) coordinates, the major deviations of the scan accuracy can be identified. The intensity image of the grid is given in figure 6.2.

There are three major position errors that can be recognized from the image. First, there is a compression of the grid in the middle of the image along the scan axis – the distance between the y -lines (the lines parallel to the nominal cross-scan axis) is smaller in the middle and larger at the edges. Second, a general skewness of the measured grid is apparent in the cross-scan direction – the x -lines (the lines parallel to the nominal scan axis) are at an angle with respect to the nominal scan axis. Finally, there is jitter in the y -lines – the edges of the lines are not sharp. The source of those errors and the corresponding calibration procedures are explained in the following part of this section.

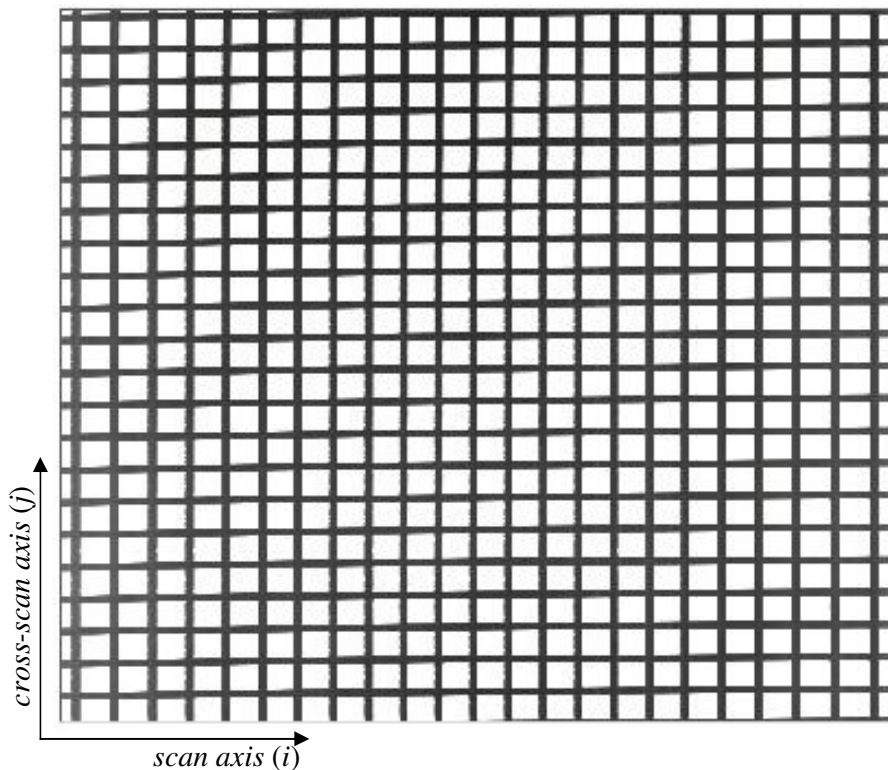


Figure 6.2. An intensity image of the reference grid measured with the 3D-deflectometer after a careful initial alignment of the grid with the translation axis with an accuracy of about 0.3 mrad (about one pixel per the complete length of the grid). The image is given in the pixel coordinates (i, j) .

Grid compression

The most critical feature of the lateral scan is related to the non-linearity of the optical scan. To obtain high scan velocity, the scanning mirror runs in the harmonic mode, characterized by a sinusoidal variation of the scan velocity on the surface-under-test (chapter 4.3). Since the data acquisition system has a fixed sampling clock, this variation of the scanning velocity results in a significant pixel size error along the scan line; the step size will be larger in the middle of the scan line, where the scan velocity has its maximum, and smaller at the edges of the scan line, where the scan is slower. As a consequence, the surface features in the (i, j) coordinate system at the edges will appear larger than those in the middle, since more samples will be acquired within the same length unit.

Pixel size error

Calibration of the pixel grid in the scan direction aims in assigning a correct position (x_i) to the corresponding pixel i . This is done by using an algorithm:

$$\tilde{x}_{i+1} = \tilde{x}_i + f(i)\Delta x \quad (\text{eq. 6.6})$$

where Δx is the mean step size between the pixels along the scan line and $f(i)$ is the function describing deviation of the pixel size along the scan line, normalized to the mean pixel size.

Both the value of Δx and the $f(i)$ -function can be estimated by scanning the reference grid and using the intensity signal. The exact calibration procedure is described in appendix F1. The applied procedure enables measurement at only discrete values of the $f(i)$ -function along the scan line; to obtain an analytical function, which is required in the equation 6.6, the function is approximated by a polynomial fit. For example, for the zeroth-order calibration, the grid is assumed to be linear; therefore that kind of calibration indicates directly the scan non-linearity. Higher order calibrations are done using even-power polynomials, due to axis-symmetry of the $f(i)$ curve introduced by the sinusoidal scan.

To estimate the pixel size error $\delta\Delta x_i$ along the scan line we calculate a residue of the polynomial fit of the $f(i)$ function, defined as:

$$\frac{\delta\Delta x_i}{\Delta x} = f(i) - \frac{x_{i+1} - x_i}{\Delta x} \quad (\text{eq. 6.7})$$

The result is shown in figure 6.3, where the pixel deviation is plotted against the position x . In table 6.1 we present the quantified values of the pixel size error calculated for different calibration orders.

We conclude that at least a 4th order approximation of the $f(i)$ function should be used for calibration of the 3D-deflectometry, since it provides a major correction of the pixel size error.

Table 6.1. The measured pixel size error for different calibration procedure.

Calibration type (polynomial order)	$\delta\Delta x$ (%)	
	max/min deviation	RMS
0	+9.48/-4.56	4.32
2	+0.45/-0.41	0.19
4	+0.17/-0.15	0.10
6	+0.17/-0.17	0.09
8	+0.19/-0.15	0.09

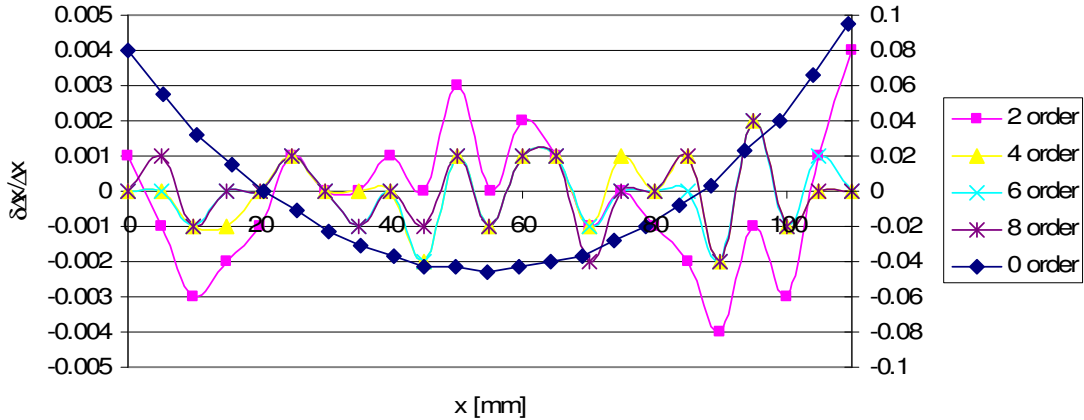


Figure 6.3. The relative deviation $\delta\Delta x_i/\Delta x$ of the pixel size after correction with n -th order polynomial, with Δx the average pixel size (left vertical scale). The right vertical axis gives the scale of the zero-order approximation, which clearly shows the sinusoidal nature of the scan velocity: velocity: fast in the middle (i.e. large pixel size) and slow at the edges (i.e. small pixel size).

Absolute position error

To verify the accuracy of our method, we scanned the calibration grid again and estimated the error in the measured positions of the grid bars as compared to the nominal positions. The result of the experiment is given in figure 6.4. From the graph we can clearly state that a polynomial calibration of the pixel grid is a must for the 3D-deflectometer, since the linear calibration results in a very large error of the pixel position. To give a numerical comparison of the considered calibration orders we estimate the corresponding PV and RMS position errors. The result is given in table 6.2.

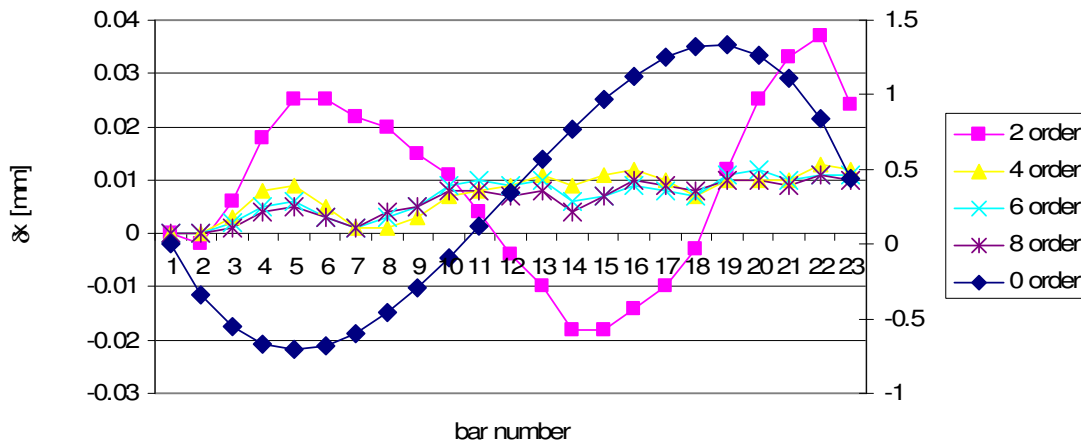


Figure 6.4. Position error $\delta\tilde{x}_i = \tilde{x}_i - x$ along the scan line estimated from the reference grid for different calibration orders. Values of the “linear” plot refer to the secondary vertical axis.

Table 6.2. Pixel position error calculated for different orders of the calibration.

Calibration type (polynomial order)	δx_i (μm)	
	PV	RMS
0	1331	749.9
2	37	16.6
4	13	4.1
6	11	3.8
8	11	3.5

As we conclude from the table, by using a 4th order polynomial approximation of the $f(i)$ function we provide a major correction of the pixel position error due to the scan non-linearity; the pixel position error is corrected by roughly 99.5 %, to only 4 μm for the complete scan length.

The residue for the 2nd to 8th order approximation of $f(i)$ shows a systematic deviation that is proportional to the bar number N . This is the result of a systematic discretization error in defining the input values $f(i_N)$ for the curve fit (Appendix F2). The software of the calibration procedure of the deflectometer still has to be corrected for this minor error of 10 μm over the full width of the scan.

Skewness of the grid

Pixel position error will be introduced when there is a misalignment between the scan lens and the scanning mirror (i.e., between the optical axis of the lens and the optical scan plane). As a consequence, the scan line on the surface-under-test will be at an angle with respect to the nominal scan axis, and/or the scan line will be un-straight (bow-like). In both cases a position error δy_i is introduced, which appears as skewness and/or bending of the pixel grid. The bow can be introduced also by distortions of the lens manufacturing. Since the error has no significant influence on the step size between the pixels, in first approximation it will not lead to errors in the reconstructed height, but will produce a significant lateral distortion of the measured surface features.

In figure 6.5 we have zoomed-in on the data in figure 6.2, showing the full length of a single 1 mm-wide x -bar of the grid in (i,j) coordinates. The measured bar exhibits a strong skewness of 12 pixels ($\Delta y = 100 \mu\text{m}$), corresponding to an angle $\varphi_{\text{skew}} = 1.2 \text{ mm} / 110 \text{ mm} \approx 11 \text{ mrad}$. This indicates poor alignment of the scanning mirror with respect to its optical axis. Also, we see a slight curvature of x -bar. With the current set-up of the mechanical mount of the scanning mirror this error cannot be corrected in hardware. We estimate that with a better mechanical assembly, the un-straightness could be reduced to 100 μm or less.

If necessary, further correction could be done in software. We first assign a correct y -position to each measured pixel. This can be done by using the algorithm:

$$\tilde{y}_{ij} = \tilde{y}_{0j} + h(i)\Delta y \quad (\text{eq.6.8})$$

where, $y_{0j} = j * \Delta y$ and $h(i)$ is a polynomial correction-function measured by aid of the calibration grid.

Next we resample the slope arrays to new positions on an equidistant grid in the y -direction to generate the desired input for the reconstruction process. In this case, we can estimate the final reduction of the y -position error for the complete scan line to be 10 μm or better.

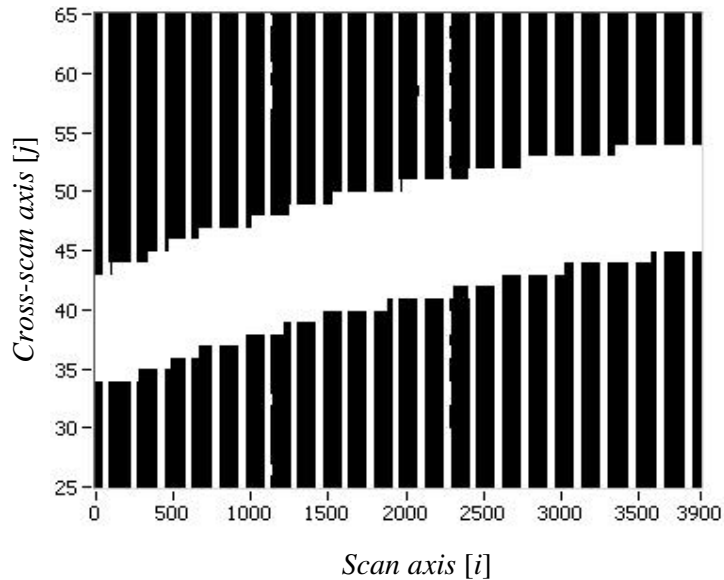


Figure 6.5. An intensity image of a single x -line of the reference grid, as measured by the 3D-deflectometer. The line is aligned perpendicularly to the translation axis, i.e. parallel to the nominal scan axis. The tilt and un-straightness of the line measured in (i,j) -coordinates indicate the misalignment error of the scan line.

6.3. Scan position mapping: (pseudo)random errors

Scan jitter

One of the typical errors for optical scanners is the scan jitter. The jitter is a relative offset in x_i pixel position between the adjacent scan lines. Typically, the jitter is a result of inaccurate synchronization of the DAQ clock to the start-of-scan signal (chapter 5.3), which leads to varying delay of the sampling trigger for each scanned line. As a consequence, the complete pixel grid in the scan direction senses a lateral shift from line to line. For a well-designed DAQ system, this start-of-scan jitter is only a small fraction of a pixel size, usually negligible (say, in order of 1 % of Δx). The jitter can also appear in the middle or at the end of the scan line, as a result of the non-repeatability of the deflector's amplitude (caused by instability of the driving amplifier).

The jitter of the 3D-deflectometer was verified by measuring a y -line of the reference grid and observing variation of x_i -position from the line edges. The result of this experiment is shown in figure 6.6, essentially a zoom-in of figure 6.2. The scan starts at $j = 1100$, showing a drift of the triggering of about 2 - 4 pixels (corresponding to an x -shift of 60 to 120 μm) in the first 350 lines. For lines $j < 750$ we observe a jitter of the triggering with a peak-to-valley value of a single pixel. This relates to a RMS error $\delta x < 0.3\Delta x = 9 \mu\text{m}$.

We conclude that we have a serious performance problem related to the triggering of the A/D-converter. A software correction does not seem appropriate. This is a pure hardware problem that should be fixed by a redesign of the data acquisition system. Due to the manpower and budget limitation this has not been fixed as yet.

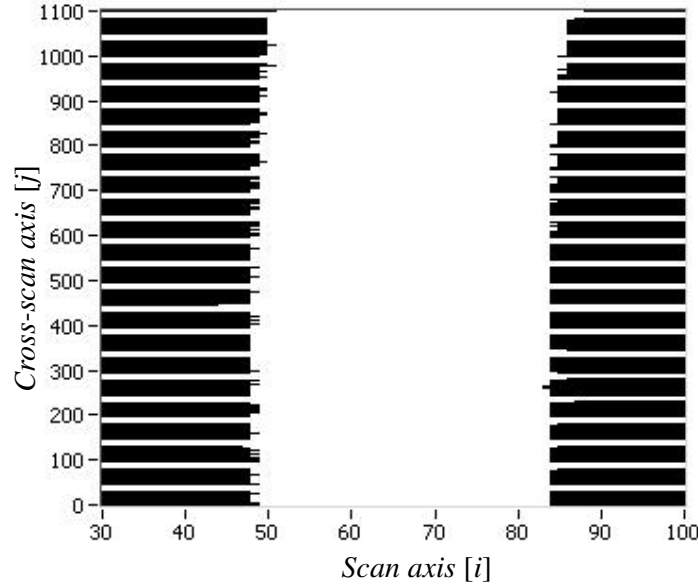


Figure 6.6. An intensity image of a single y -line of the reference grid, measured with the 3D-deflectometer. The surface is scanned top-down, thus the first scanned line is $j = 1100$. The un-straightness or high frequency distortion of the bar is the result of jitter in the scan line triggering.

Continuous translation

The 3D-deflectometer operates in a continuous translation mode. Therefore, the beam position in the cross-direction depends on the beam displacement in the scan direction. As a result, the pixel grid senses a slight skewness, as explained schematically in figure 6.7.

The position error $y_j - y_0$ due to the continuous translation in the cross-scan direction is equal to:

$$\tilde{y}_{ij} - \tilde{y}_{i0} = -\chi \Delta y \frac{x_{ij}}{L} \quad (\text{eq. 6.9})$$

where χ is the duty cycle of the optical scanning. The resulting RMS error introduced in the y -direction is equal to:

$$\delta y = 0.3 \chi \Delta y \quad (\text{eq. 6.10})$$

Inserting $\chi = 1/6$ and $\Delta y = 30 \mu\text{m}$, we find $\delta y = 1.5 \mu\text{m}$, a much smaller value than observed in the current setup (figure 6.5).

This effective rotation of the scan grid is indistinguishable from the rotation of the scanning grid by a misalignment of the scanning mirror: both result in a skewness of scan from the reference grid. Therefore, correction for the continuous translation error is already present in the correction procedure for the scanning mirror misalignment (eq. 6.7).

The grid skewness can be corrected in hardware by changing the orientation of the optical scan axis with respect to the translation axis. In this case, the PSD orientation should be changed correspondingly.

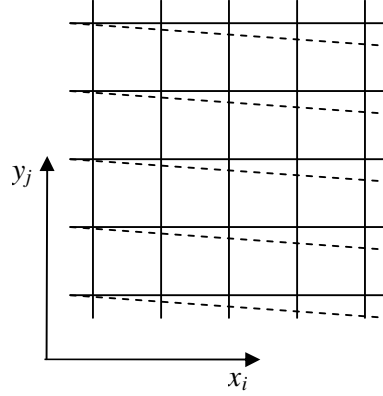


Figure 6.7. Schematic diagram of the pixel grid distortion due to misalignment between the optical and mechanical scan axes. The solid lines represent the nominal scan grid; the dashed lines represent the optical scan when the surface-under-test moves in the positive y -direction.

Translation axis

Un-straightness of the translation has a direct influence on the pixels position error in the scan direction. Following the information from the manufacturer, we estimate that error is roughly $\delta\Delta x = 1 \mu\text{m}$.

Yaw

The yaw of the translation stage will introduce position errors in both the x - and y -direction. These are proportional to the distance from the centre of rotation of the surface-under-test to its edges at distance $L/2$ and $L_y/2$. The peak-to-valley range is equal to $L\sin\varphi_{yaw}$ and $L_y\sin\varphi_{yaw}$, respectively, which results in RMS errors given by:

$$\delta x = 0.15L_y \sin \varphi_{yaw} \quad (\text{eq. 6.11a})$$

$$\delta y = 0.15L \sin \varphi_{yaw} \quad (\text{eq. 6.11b})$$

We have measured the yaw of our translation stage by using an autocollimator. The result is given in figure 6.8, showing a PV range of the yaw equal to $\Delta\varphi_{yaw} = 15.5 \mu\text{rad}$.

In appendix F3 we discuss the nature of the systematic and random components in φ_{yaw} . Using $L = 110 \text{ mm}$ and $L_y = 300 \text{ mm}$, the systematic components correspond to RMS position errors of $\delta x = 0.5 \mu\text{m}$ and $\delta y = 0.2 \mu\text{m}$. The random component $\delta\varphi_{yaw}^R = 1.17 \mu\text{rad}$ introduces a negligible level of position uncertainty, less than $\delta x, \delta y \leq 0.05 \mu\text{m}$.

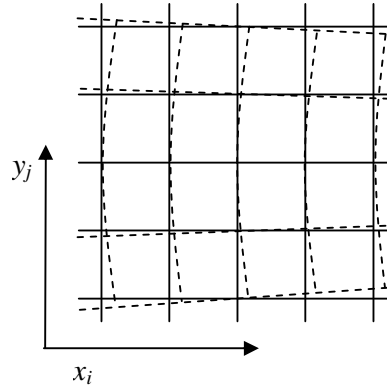


Figure 6.8. Schematic representation of the influence of yaw on the sampling grid. The solid lines indicate the nominal scan grid; the dashed lines indicate the grid when distorted by yaw of the translation axis. In the figure, we assume that yaw changes continuously during translation.

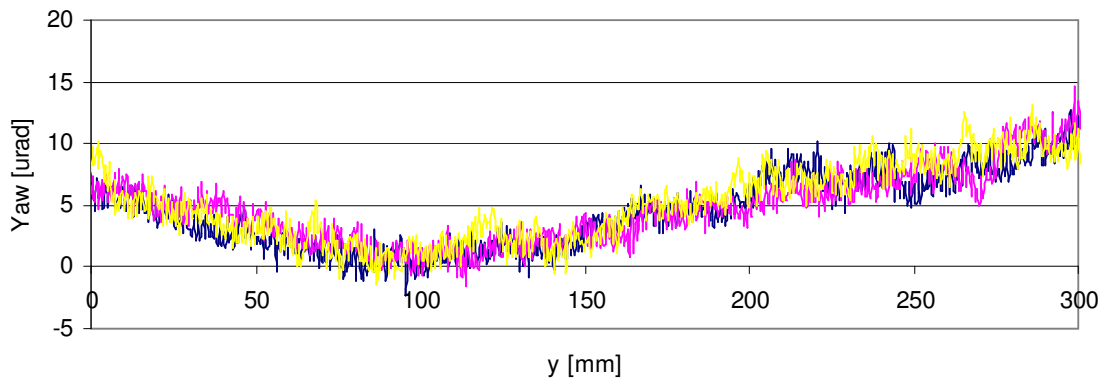


Figure 6.9. The yaw of the translation stage used in the 3D-deflectometer (three independent measurements).

Lens aberrations

Because of the spherical aberration of the scan lens, the optical scan deviates from telecentricity. As a result, the scanning beam falls at a wrong location on the surface-under-test as compared to the nominal position. The resulting pixel position error can be calculated as:

$$\delta x_i = z_{FWD} \sin \delta\theta \quad (\text{eq. 6.12})$$

where z_{FWD} is the free-working-distance of the deflectometer and $\delta\theta$ the angular error introduced by the lens aberration.

To estimate pixel position errors due to the lens signature, we refer to Appendix F5, where the deflectometer's lens signature is presented. We assume that the amplitude of the beam-angle error on the surface-under-test is half of that presented in the appendix. This is because the signature measured at the PSD (as in the appendix) is the result of a double pass through the lens system, while the position error is caused by a single-pass.

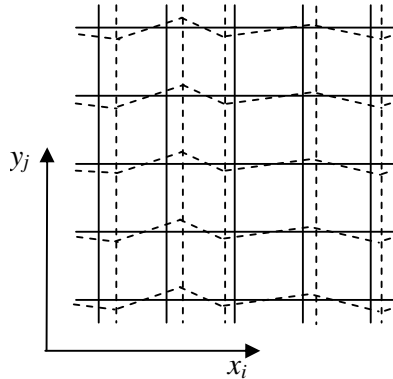


Figure 6.10. Schematic interpretation representation of the influence of the high-frequency lens aberrations on the sampling grid.

The spherical aberration [2] of the scan lens has a similar effect on the pixel position and pixel size errors as the scan a-linearity, but with smaller order of magnitude (table 6.3). Therefore, the error is corrected during calibration of the scan a-linearity as discussed previously in this section (“grid compression”)

The position error due to the high frequency aberrations is more difficult to calibrate since it influences individual pixels. The effective correction can be disabled – e.g., by the jitter in the scan line. The error can be reduced, however, by using a scan lens with higher surface quality and longer free-working-distance (to produce a larger beam diameter at the lens surface). We can estimate that by a combination of both we can gain a factor of three in the reduction of the pixel position error.

Table 6.3. The influence of the scan lens aberrations on the pixel position error δx_i and δy_i . In the calculations we assume a free-working-distance of the deflectometer of $z_{FWD} = 100$ mm.

Signature component	δx_i or δy_i (μm)
Low frequency (spherical aberration)	< 1
High frequency (local lens imperfections)	< 1

Environmental influence

As one can expect, a certain level of pixel position uncertainty will be introduced by the airborne disturbances of the optical scan path. Thanks to the relatively short free-working-distance, the anti-vibration isolation, and randomness in nature, the influence of the environment should be of no concern in our deflectometer. In our design, no further precautions are taken for decreasing the influence of the environmental noise.

Summary

In table 6.4 we give an estimate of the influence of various error sources on the accuracy of the lateral sampling for the 3D-deflectometer. The table shows the absolute position error for the complete scan area. We present both the current status and estimated error values after suggested improvements.

Following the table, the lateral accuracy of the deflectometer can be increased significantly by a combination of hardware and software corrections of the measured data. We can estimate that after the suggested additional calibrations and set-up improvements, the pixel position errors for the complete scan area would not exceed 15-20 μm . As we showed in this section, we are also able to achieve a very low pixel size error of about 0.1 % of the mean value, negligible for the errors in the reconstructed topography.

Table 6.4 Summary of significant error sources of the pixel position δx_i and estimated improvement after further calibration.

Error source	Axis	δx_i (μm)		Applied calibration and/or suggested improvements
		Current status	After suggested improvements	
Scan a-linearity	x			
Lens aberrations (spherical)	x	11	1	6 th order polynomial correction (SW)
Lens aberrations (high frequency)	x,y	1	0.3	Better lens manufacturing, longer polishing
Deflector misalignment	y	1200	1	Better mechanical assembly of the deflector (HW), software correction (SW)
Jitter	x	9	1	Improvement of ADC trigger (HW/SW)
Continuous translation	y	1.5	-	Mechanical correction
Translation axis un-straightness	x	1	1	-
Translation axis yaw	y	0.5	< 0.1	SW correction

6.4. Detector alignment

A small rotation of the PSD coordinate system (ξ, η) with respect to the coordinate system (x,y) of the surface-under-test will cause cross-talk between the measured slope components and thus result in an erroneous reconstruction of the surface. Next, the detector must be positioned very carefully in the optical plane of the scan lens. Looking at figure 6.11, we easily see that when the focal point of the fan of the scan beam does not coincide with the PSD plane, a zero slope of the surface-under-test results in an $S_\xi(x(t))$ value that goes from negative through zero to positive, depending on the position $x(t)$. This signal reflects an artificial curvature of the surface-under-test and results in an erroneous surface reconstruction. Finally, finding the origin of the (ξ, η) coordinate system helps to define the orientation of the support of the surface under test.

Rotation

To correct the deflectometer for detector rotation, the PSD is shifted away from the focal plane, along the optical axis (using the Z-drive, see in figure 5.2) and the S_ξ and S_η signals are observed (e.g. by an oscilloscope connected to the PSD). By such a de-focusing, the probing beam reflected from the surface scans the detector instead of being incident onto a single

(ξ, η) -location on the detector. The detector is scanned along the ξ -axis only; in the η -direction the fan of beams remains focused in the scan plane and the S_η signal remains flat. As the detector moves from the focal plane, the S_ξ signal spreads out to a line focus. However, if the detector axes are misaligned, the tilt will be observed also in the S_η signal. Therefore, we can align the detector by adjusting its orientation until the S_η signal at the oscilloscope becomes flat. Such a procedure is explained schematically in figure 6.11.

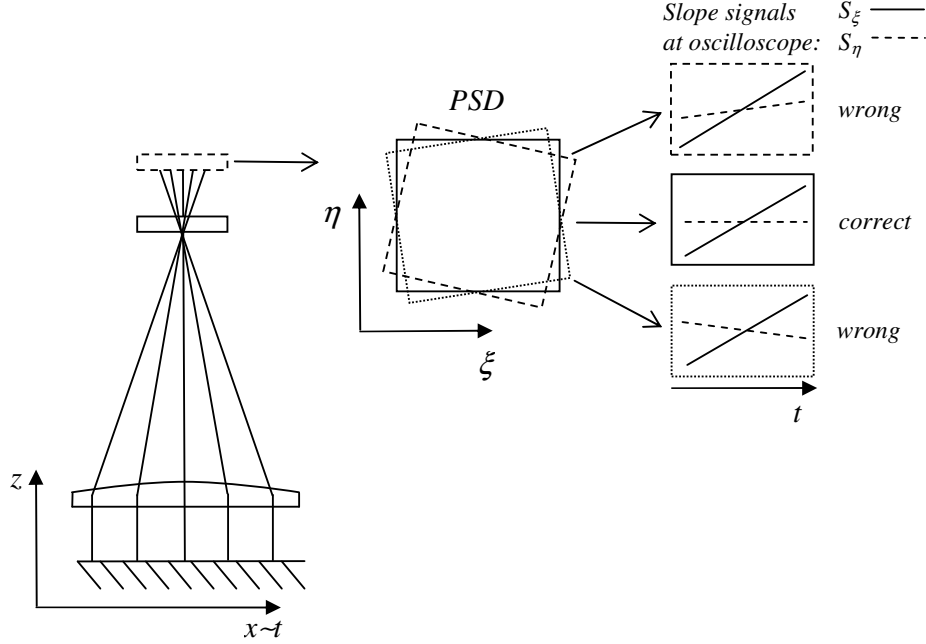


Figure 6.11. Hardware correction procedure for aligning the detector's orientation. The aligning is done using a flat surface-under-test and the detector shifted away from the focal plane of the scan lens in the z -direction.

Using the rotation matrix (eq.6.3) we can approximate the influence of a PSD rotation error $\delta\varphi_{PSD}$ on the measured slope components as:

$$\tilde{\sigma}_x = \sigma_x \cos \delta\varphi_{PSD} + \sigma_y \sin \delta\varphi_{PSD} \approx \sigma_x \quad (\text{eq. 6.13a})$$

$$\tilde{\sigma}_y = \sigma_x \sin \delta\varphi_{PSD} - \sigma_y \cos \delta\varphi_{PSD} \approx \sigma_x \delta\varphi_{PSD} \quad (\text{eq. 6.13b})$$

Hence, we estimate the correction limit using the S_η signal as:

$$\delta\varphi_{PSD} \approx \frac{\delta\sigma_y}{2} / \sigma_x (\Delta z) \quad (\text{eq. 6.14})$$

where $\delta\sigma_y$ is the cross-scan slope error due to high frequency lens aberration and $\sigma_x(\Delta z)$ the maximum scan-slope spread due to defocus Δz (given by equation 6.15). Using a numerical value of $\delta\sigma_y = 20 \mu\text{rad}$ (Appendix F5) and $\sigma_x = 430 \mu\text{rad}$ for $\Delta z = 10 \text{ mm}$ we obtain $\delta\varphi_{PSD} \approx 23 \text{ mrad}$, which results in a slope uncertainty of $\delta\sigma = 46 \mu\text{rad}$ (assuming slope range of $\sigma_{\text{max}} = 2 \text{ mrad}$).

The introduced error is not a fundamental limit, as it could be easily decreased by a calibration using a larger z -shift of the PSD. Unfortunately, with the current set-up, a value of Δz larger than 10 mm is impossible due to compact design and large dimensions of the PSD front-end electronics.

Detector focus alignment

Aligning the PSD detector in the focal plane of the scan lens is done in a similar way as rotationally aligning it. Again, we use an optical flat, an oscilloscope, and the Z-drive of the deflectometer as tools. The procedure is explained schematically in figure 6.12. In this approach the detector is moved along the optical z -axis until the S_ξ signal shows a flat response as a function of $x(t)$.

The sensitivity of the slope error for a misalignment Δz depends on the numerical aperture $L/2f$ of the scan lens and the slope sensitivity C'' of the PSD, as given by:

$$\Delta\sigma_x(\Delta z) = C'' \Delta\xi(\Delta z) = C'' \Delta z \left(\frac{L}{2f} \right) \quad (\text{eq. 6.15})$$

Inserting the numerical value of $C'' = 0.625 \mu\text{rad}/\mu\text{m}$ into equation 6.14 we find $\Delta\sigma/\Delta z = 43 \mu\text{rad}/\text{mm}$. This implies accuracy better than 0.1 mm in the alignment of the detector to achieve errors less than $4 \mu\text{rad}$ in the slope.

Similarly as for the rotation-alignment, one can think of more fundamental limits for the focusing accuracy, since it is limited by the quality of the reference flat and the aberrations of the scan lens. The spherical aberration of the lens, by definition, disables ideal focusing of the whole fan of the reflected beams along the scan line. This is because the effective z -location of the focal plane is a function of the beam position x along the scan line (see section 6.5). With the current setup, the aberration in the scan direction is about $20 \mu\text{rad}$ for the complete scan line, which is also the limit in slope of the accuracy of the focus alignment. This remaining error can be corrected by the signature subtraction procedure (see section 6.6).

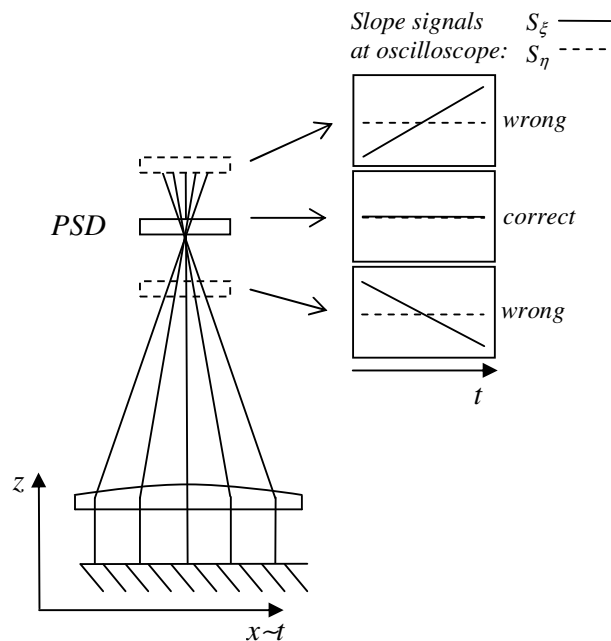


Figure 6.12. Slope error due to out of focus PSD position.

6.5. Slope response

Polynomial slope calibration

A calibration of the slope sensor is used to provide a relation between the PSD slope signals S_ξ and S_η and the corresponding slope of the surface. In the traditional configuration with a small beam on the detector, the PSD is assumed to have a highly linear position-to-signal response. Therefore, the calibration is about a single geometrical factor providing a linear relation between the detector response and the measured slope. In our deflectometer we use the Large Beam Detection mode with D/B ratio of about 0.6, which means that the detector response is strongly a-linear (see section 4.5.1). Therefore, we must consider an alternative calibration procedure than a simple linear approximation. As we showed in section 4.5.1, already using a 3rd order polynomial approximation of the detector response gives promising results for calibration of a PSD in the LBD mode.

In order to choose the best calibration procedure, we measure the deflectometer's response to the slope with an autocollimator setup (figure 3.3) and approximate the calibration curve using a polynomial fit with different polynomial orders. To estimate the slope error introduced by the approximation, we calculate the residue of the polynomial fits. The result of such verification for the S_ξ -signal is shown in figure 6.13. In the figure we compare the residues for four different orders of the polynomial fit, including a linear approximation.

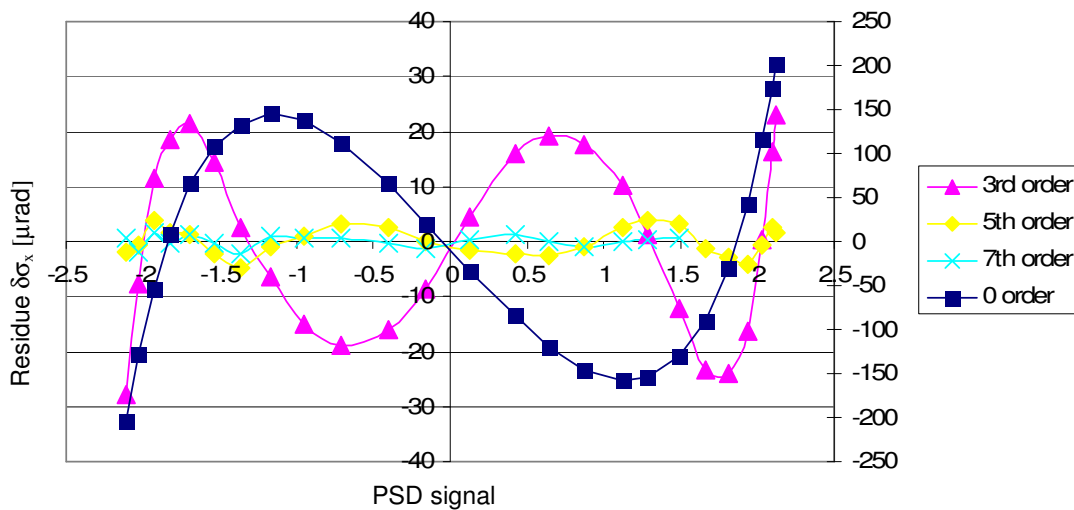


Figure 6.13. The residue of the calibration curve for different orders of the polynomial fit (scan slope axis). The values of the “linear” fit refer to the secondary vertical axis.

Clearly, due to a large error in the linear approximation a calibration with a simple geometrical factor is not suitable for calibrating a PSD in the LBD mode. The higher order polynomial approximations lead to a strong increase of the calibration accuracy. To give a numerical comparison of the considered approximations, we estimate the RMS error for each residue curve. The results are given in table 6.5.

Table 6.5. The RMS slope error $\delta\sigma$ for different modes of the slope calibration, estimated from the residue of the calibration curves.

Calibration mode	$\delta\sigma$ (μrad)
linear	120
3 rd order	16
5 th order	2.5
7 th order	1

As we can conclude from table 6.1, using the 5th or the 7th order polynomial calibration seems to be a perfect solution for the 3D-deflectometer, as the corresponding RMS errors are well within the required specification.

Calibration repeatability

Although the slope calibration with a polynomial fit gives a highly accurate result, the question is how repeatable is the measurement of the calibration curve itself. In order to verify the repeatability, we repeat the calibration procedure five times for the same ξ -line at the PSD. We then approximate one of these curves by using a 7th order polynomial fit and calculate the residue of the four other response curves, using the former as reference. The result is given in Table 6.6.

For the 3rd order polynomial approximation of the reference curve, the residue of the fit (table 6.5) and the comparison (table 6.6.) are of equal magnitude. For the 5th and 7th order polynomial approximation, the residue of the different calibration measurements is larger by a factor 2 to 5 than the residue of the original fit.

We conclude that the measurement error of the polynomial calibration decreases again with the order of the polynomial approximation. However, for higher order polynomials, the repeatability of the calibration is below the accuracy of the fit. We conclude that the accuracy of the calibration is limited by errors in the measurement itself, most likely caused by the airborne noise and mechanical drift. Though, the accuracy of the 5th- and 7th-order polynomial approximations is still high as compared to the system requirements, therefore either can be applied for the calibration of the deflectometer. We choose to apply to 7th order calibration curve.

Table 6.6. Repeatability of the slope calibration. RMS error $\delta\sigma$ of the polynomial fit residue, for multiple measurement of the same calibration curve.

Calibration mode	$\delta\sigma$ (μrad)
linear	116
3 rd order	16
5 th order	5.5
7 th order	4.8

Cross-talk between the slope components

An inaccurate PSD position and/or rotation introduce cross-talk between the measured slope components (section 6.2.1). Cross talk can also be caused by a deviation of the beam shape from the ideal Gaussian profile. For a non-linear behaviour of the PSD near the edges, this effect will be even more pronounced, as it is the case in our choice of using the detector in the Large Beam Detection mode. To check on the cross dependence of the slope components in this situation, we have measured the scan slope response curves for the ξ -axis for five different values of η ranging from $\eta = -1.5$ mm to $+1.5$ mm (figure 6.14). The same procedure was repeated for the cross scan slope. To compare the calibration results, we use the response curve at $\eta = 0$ and $\xi = 0$ as a reference, respectively. The results are given in Table 6.7.

From our experiment, we can conclude that the largest error of the slope calibration is due to the cross-talk between the measured slope components. The residue of the polynomial fit (appendix F) suggests that this measurement error is due to the inaccurate rotational alignment of the PSD. However, the small difference between the results for both PSD axes may suggest that the cross-talk is influenced also by the non-ideal nature of the beam profile itself. For our system, this is difficult to avoid, due to a relatively low quality of the laser used in the deflectometer (causing beam astigmatism and beam-shape deviations).

The calibration procedure enables us to estimate the uncertainty of the measured slope to $\delta\sigma \leq 15$ μ rad, when the 5th order polynomial calibration is applied. Further increase of the polynomial order does not lead to an increase of the calibration accuracy. The obtained uncertainty level can be accepted for the design of our system, since it is better than the required specification. The measurement, however, must be combined with an advanced topography reconstruction. Probably even higher calibration accuracy could be reached if a better quality laser and scan lens are used, which would increase the beam shape quality and enable a more accurate adjustment of the PSD.

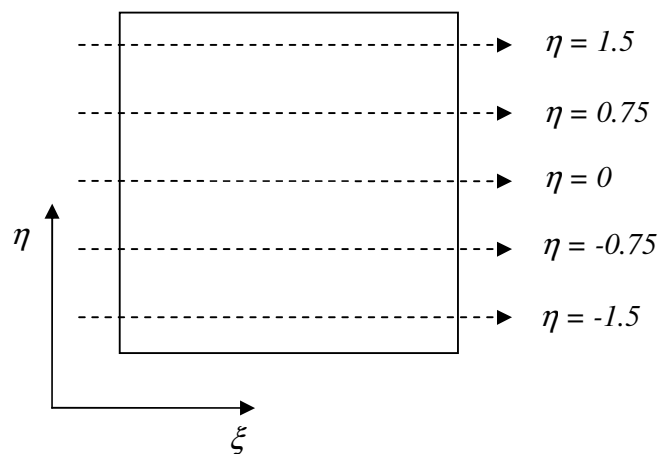


Figure 6.14. Paths of the beam on PSD for the verification of the cross-talk between the slope components. The dashed lines indicate positions on the η -axis at which the slope calibration for the S_{ξ} signal is done.

Table 6.7. The RMS error $\delta\sigma$ of the polynomial calibration for five different positions across the second PSD-axis.

Calibration mode	$\delta\sigma$ (μrad)	
	Scan axis	Cross-scan axis
linear	115	102
3 rd order	19.8	19
5 th order	12.8	14.9
7 th order	12.7	15

6.6. System signature

In this section we discuss the calibration of the 3D-deflectometer for the system signatures. The signatures have been measured using a reference flat. To measure the signatures we assume that they are the only systematic components in the slope data; therefore, they can be extracted by averaging the measured slope arrays in the scan- and cross-scan direction, for the lens- and the stage signature, respectively (see section 3.3).

Next, we present examples of correcting measurements for the signatures.

Lens signature

In figure 6.15 we show the lens signature of the deflectometer (section 3.3), i.e., the systematic errors due to imperfections of the lens and spherical aberration. The data have been taken with the reference flat described in Appendix F4. The most pronounced feature in figure 6.15 is the 200 μrad PV sharp structure in the cross-scan data at $i = 2650$. We assign this peak as the result of the ‘‘cat’s-eye effect’’, which occurs when the detector ‘‘sees’’ a direct reflection of the scan beam by the scan lens. This effect is not related to the lens signature: for this reason, the data between $i = 2250$ and $i = 2750$ are not taken into account in our analysis.

The lens signature consists of a low spatial-frequency component ($k < 70 \text{ m}^{-1}$) and a high spatial-frequency component ($k > 70 \text{ m}^{-1}$). The former is caused by spherical aberration and low frequency form errors in the manufacturing of the lens. The latter are due to local imperfections (scratches, dust, local in-homogeneity) of the lens surface and body. These components can be separated by Fourier analysis or by using a polynomial fit and inspecting the residue. Here we follow the polynomial fit approach (see Appendix F4), since we apply it further for the signature correction. The results are given in Table 6.8, in terms of peak-to-valley and RMS error.

As we expected, the scan-slope lens signature is influenced strongly by the low-frequency component, with a PV value of $\delta\sigma_{x,y} = 20 \mu\text{rad}$. However, the characteristic of this component deviates significantly from a pure 3rd order curve, as would be expected from the spherical aberration only. Therefore, we assume manufacturing errors as the secondary source of low-frequency aberration. We use a 20th-order polynomial fit to approximate this component which corresponds to a cut-off spatial frequency of $k = 91 \text{ m}^{-1}$.

As expected, the low-frequency signature component in the cross-scan direction is weak and has almost no influence on the system performance. We use a 2nd order polynomial fit to describe the low frequency part of the cross-scan lens signature, corresponding to cut-off spatial frequency of $k = 9 \text{ m}^{-1}$.

Table 6.8. Slope error of the 3D-deflectometer due to the lens aberration. The low and high frequency components are separated by using a polynomial fit and its residue (20th and 2nd-order polynomial for the scan- and the cross-scan slope components, respectively).

Signature component	Scan slope (μrad)		Cross-scan slope (μrad)	
	PV	RMS	PV	RMS
Complete	53.3	7.5	55.6	9.6
Low frequency (fit)	20.4	5.9	0.81	0.2
High frequency (residue)	43.3	6	55.6	9.6

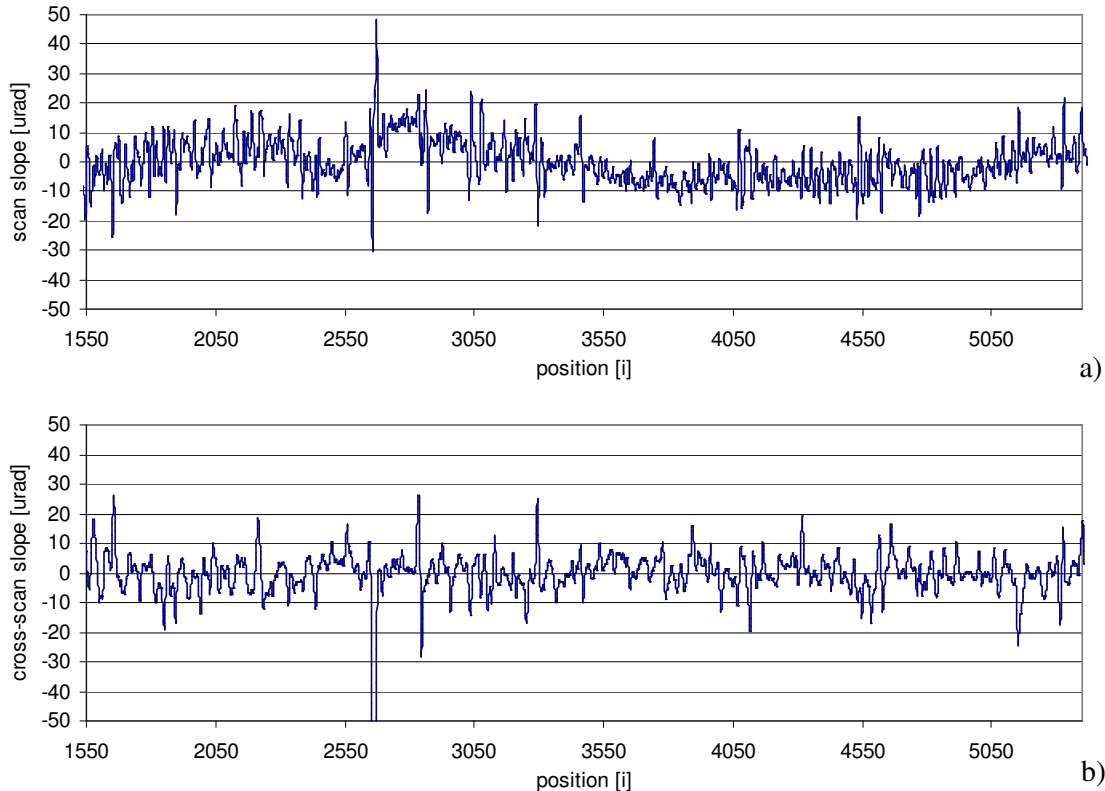


Figure 6.15. Lens signature of the 3D-deflectometer measured by using a $\lambda/10$ -flat reference surface: a) scan-slope, b) cross-scan slope. The horizontal scale represents a scan length of about $L = 110$ mm. The peak due to the “cat’s-eye” effect ($\sigma_{y_{\min}} = -163 \mu\text{rad}$ at $i \approx 2650$) is clipped.

Stage signature

The mechanical imperfections of the translation stage that travels in the y-direction are captured in the stage signature of the deflectometer (section 3.3). The pitch and roll (figure 3.4) introduce systematic errors in the measurement of both the scan and the cross-scan slope. We have again used the reference optical flat to measure the stage signature. The data are given in figure 6.16 (full measurement report in Appendix F5). Again we have used a polynomial fit and its residue to characterize the low frequency and the high frequency region of the spatial frequency spectrum. Using a 20th order polynomial fit, the corresponding cross-over spatial frequency is $k = 90 \text{ m}^{-1}$. The resulting peak-to-valley deviations and the corresponding RMS values are given in Table 6.9.

The flat behaviour of the scan slope signature (fig. 6.16) shows that the roll of the translational stage is small, with an RMS value $\delta\sigma_x = 3.1 \mu\text{rad}$, stemming mainly from the high spatial frequency band. We conclude that we do not have to apply a correction for the scan slope signature.

The pitch of the translational stage results in a cross-scan slope error with a peak-to-valley range of $18 \mu\text{rad}$, mostly due to the low spatial-frequency band. Correction for the stage signature of the cross scan slope is essential for obtaining the required specification for the long range consistency of the surface reconstruction.

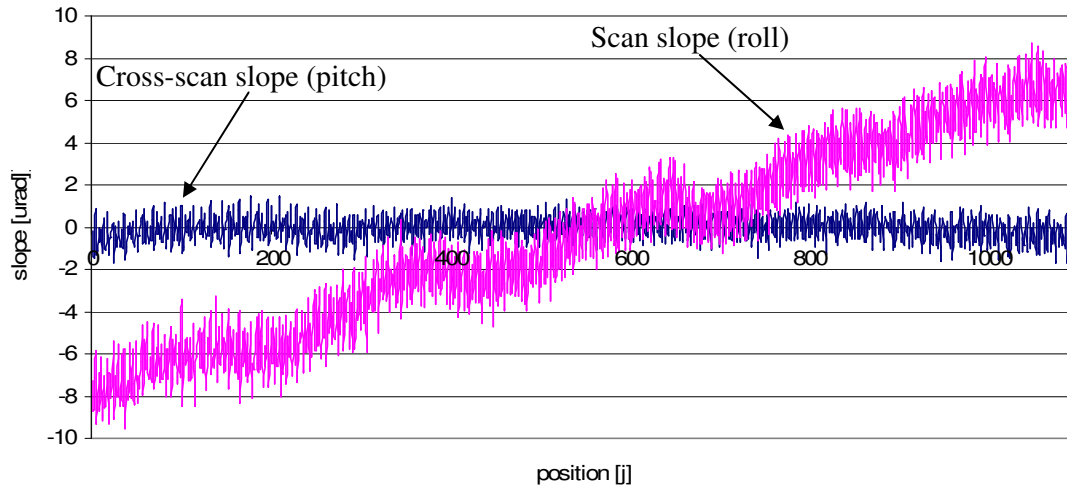


Figure 6.16. Stage signature of the 3D-deflectometer measured with a reference flat; scan distance $L_y = 110 \text{ mm}$.

Table 6.9. Slope error of the 3D-deflectometer introduced by the stage signature. The high-/low-frequency components are separated by using a 20th order polynomial and its residue

Signature component	Scan slope (μrad)		Cross-scan slope (μrad)	
	PV	RMS	PV	RMS
Complete	3.1	0.6	18.3	4.4
Low frequency	0.7	0.1	15	4.3
High frequency	2.8	0.6	5.5	1.1

6.7. Optical flat reconstruction

No signature correction

To investigate the accuracy in surface topography measured by the 3D-deflectometer, we use a $110 \times 110 \text{ mm}^2$ area of the reference flat. As we see in the figure 6.17, the structure of the measured surface differs a lot from the calibration report of the flat (Appendix F1): the surface topography given in the report exhibits a quasi-polar symmetry, with peaks and valleys distributed along a donut-like structures with a PV value of 79 nm . In the reconstructed topography, a strong bend in the scan direction is apparent, as well as a weaker bend in the translation direction. Also, the reconstructed surface amplitude is 450 nm , much larger than expected.

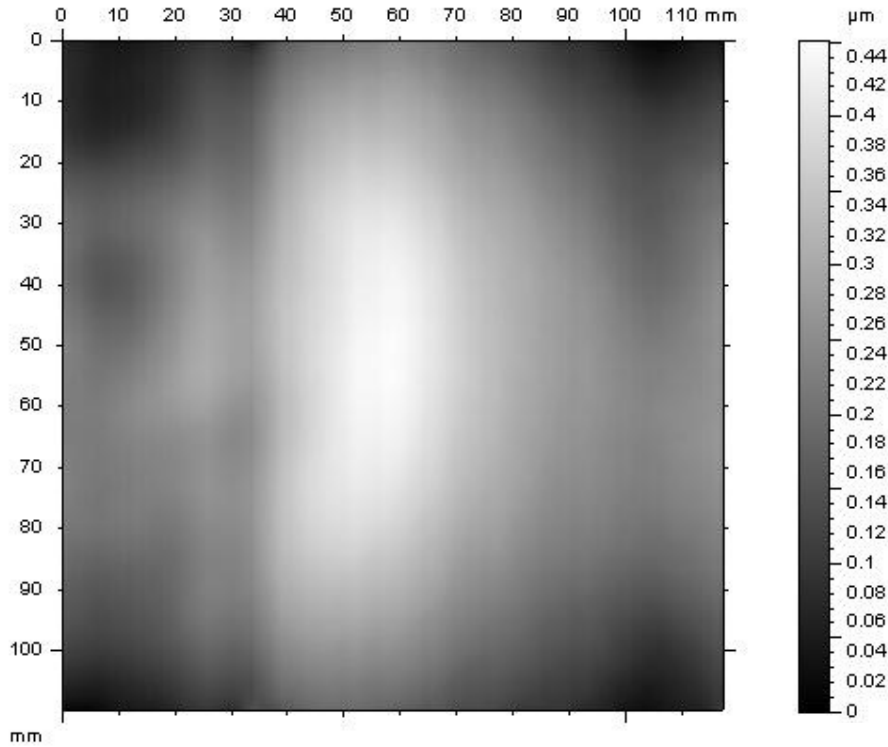


Figure 6.17. Raw topography of the reference flat ($110 \times 110 \text{ mm}^2$ area) as measured by the 3D-deflectometer.

Since both major components of the erroneous surface distortion seem to have a highly systematic nature, we point out the system signatures as the primary source for the surface error. Using the signatures given in section 6.6 we can estimate the error in the corresponding topography using simple line integration. In figure 6.18 we present the height error in the scan direction calculated from the scan slope lens signature. This height error can clearly be assigned as the primary source of the erroneous bending in the scan direction in figure 6.17. In figure 6.19 the height error due to pitch of the translation axis is depicted, which we associate with the cross-scan bending in figure 6.17.

The total height deviation from the calculated errors of about 450 nm, i.e. the sum of the errors in the scan and the cross-scan direction, closely matches the difference between the measured and the expected PV height range of the reference flat.

Other components of the system signature will have a minor influence on the global shape accuracy, mostly in the high spatial frequency band. For example, the high-frequency component of the lens signature will appear as groves and lines in the cross-scan direction, characterized by a typical value $k = 10^3 \text{ m}^{-1}$ and with a PV height range of about:

$$\Sigma_{HFS} = \frac{\sigma_x}{4\pi k_x} \approx 4nm \quad (\text{eq. 6.16})$$

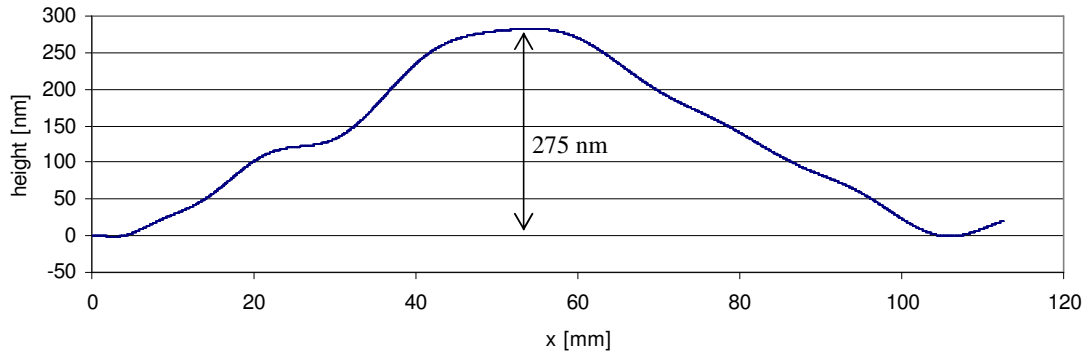


Figure 6.18. Height profile reconstructed from the low-frequency part of the lens signature of the scan slope component.

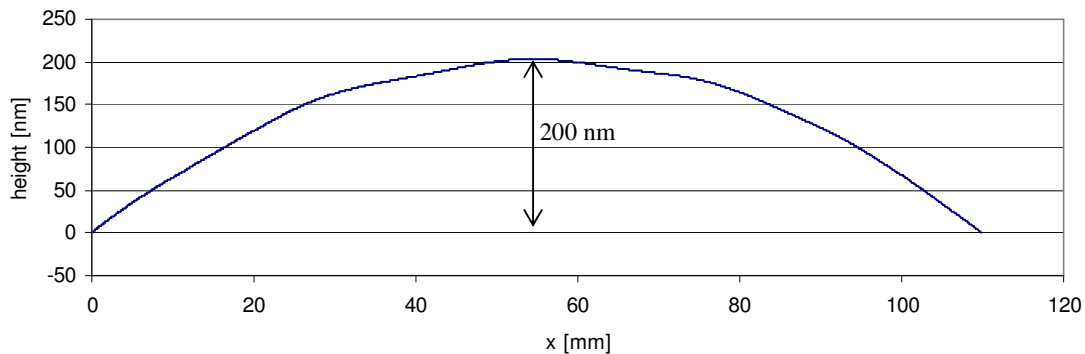


Figure 6.19. Height reconstructed from the low-frequency part of the stage signature of the cross-scan slope component.

Including signature correction

Following the procedure for the signature correction as described in chapter 3.3, we should be able to reconstruct the surface of the reference flat with much higher accuracy than just given by the raw measurement. In figure 6.20 we show the surface of the reference flat from figure 6.18 after correcting for system signature (detailed description can be found in appendix F6). In addition to the signature subtraction, we use low-pass spatial filtering with cut-off spatial frequency $k_{\max} = 125 \text{ m}^{-1}$ ($\Lambda_{\min} = 8 \text{ mm}$). The filtering has been used in order to remove the remaining influence of the high frequency signature, apparent after the raw signature correction. Although the filtering can produce additional errors by removing real topology, it seems to be a safe solution for measuring the optical flat, which has a smooth surface with only long spatial-wavelength structures (see calibration report in Appendix F1). The removed high frequency structure (figure F6.2) represents very well the topography errors from the high-frequency lens signature including, though one can notice some surface features “leaking” through the filtering

By comparing the corrected surface with the calibration report, we conclude that the measured topography is close to what has been measured during calibration of the flat by the supplier using interferometry. The general structure with polar-symmetry is apparent in both images. We can clearly recognize the area of the surface – a donut-like structure with the

deepest valley near the left edge of the image – being the origin of the surface. Also the vertical scales match well, with a PV range of about 72 nm in the measured surface, and about 78 nm in the calibration report for the complete surface.

Finally, we can conclude that removing the system signatures leads to high long-range accuracy in the measured topography. Even without full numerical verification, we can give a safe estimate of the height error of no more than $\delta\Sigma = 35$ nm per 110×110 mm² (about half of the PV height given in the calibration report of the reference flat).

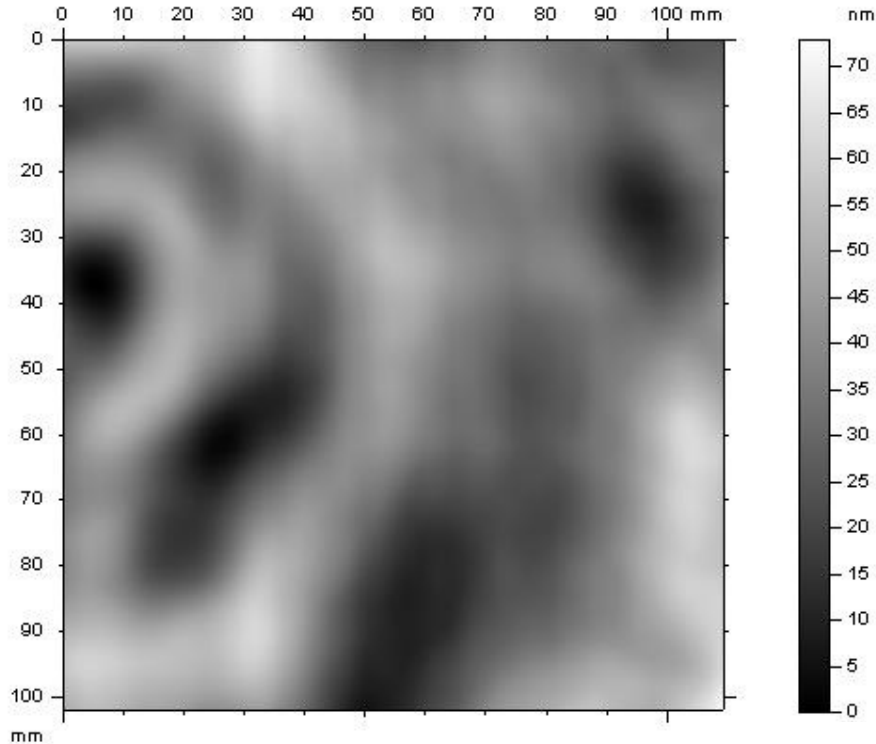


Figure 6.20. Topography of the reference flat (110×110 mm² area) measured by the 3D-deflectometer corrected for the system signature.

6.8. Surface reconstruction errors

The surface reconstruction will introduce an error $\delta\Sigma$ that depends both on the random errors in slope σ as well on the random errors of the Cartesian grid position. The influence of both these errors in the reconstructed topography is investigated in this section.

Slope error

For easy reference we repeat the result of equation for the error propagation of random errors in the slope in the surface reconstruction (section 1.4), as given by:

$$\delta\Sigma = 0.7\delta\sigma * \Delta x$$

The summary of slope errors in table 6.10 shows us that the random error is on the order of $19 \mu\text{rad}$ in both $\delta\sigma_x$ and $\delta\sigma_y$. Using a typical value of $\Delta x = 30 \mu\text{m}$ for our deflectometer, we find a negligible reconstruction error $\delta\Sigma = 0.6$ nm.

Table 6.10 Summary of RMS error in the measured slope

Error source	$\delta\sigma$ (μrad)
Calibration non-repeatability	5
Cross-talk	15
High frequency lens signature	10
High frequency stage signature	1

Step size error

A simple dimensional analysis shows that the RMS error $\delta\Sigma$, as given by:

$$\delta\Sigma = C \delta x * \Delta x * \delta(d\sigma/dx) \quad (\text{eq. 6.17})$$

Where:

$$\delta(d\sigma/dx) = \sqrt{\left\langle \left(\frac{d\sigma}{dx} \right)^2 \right\rangle} \quad (\text{eq. 6.18})$$

is proportional to the RMS error δx in the step size, the step size Δx , and the RMS value of the derivative of the slope. In this equation we again assume the suppression of error propagation due to the multi-path nature of the integration process, as is the case for errors due to noise $\delta\sigma$ in the measurement of σ .

The parameter C in Eq. 6.17 is on the order of unity and has to be determined by comparison to numerical simulations. Using the work of Potze [1] we find:

$$0.65 < C < 1.08 \rightarrow \langle C \rangle = 0.86$$

depending on which derivative we consider, i.e., $d\sigma_x/dx$ or $d\sigma_x/dy$. The comparison also confirms the correctness of the structure of Eq. 6.17, e.g., the scaling with $(\Delta x)^2$ for a constant value of $\delta x/\Delta x$.

As expected, the magnitude of the reconstruction error depends on the spatial wavelength $\Lambda = 1/k$ of the surface-under-test. Assuming a surface $\Sigma = A_k \sin(2\pi kx)$ represented by a single term of a Fourier series, we calculate the RMS value of $d\sigma/dx$ and substitute it in Eq.6.16, resulting in

$$\delta\Sigma = 0.6(2\pi k \Delta x)^2 |A_k| \varepsilon \quad (\text{eq. 6.19})$$

where:

$$\varepsilon = \delta x / \Delta x \quad (\text{eq. 6.20})$$

From this equation we directly see that the product $(k^2 A_k)$ determines which spatial frequencies will contribute most heavily to the RMS error in the reconstructed surface $\tilde{\Sigma}$.

Another error we have to investigate is the discretization error, due to the input of slope values on a discrete grid with spacing Δx . A dimensional analysis results in an RMS error $\delta\Sigma$ equal to:

$$\delta\Sigma = C' \delta(d\sigma/dx) (\Delta x)^2 \quad (\text{eq. 6.21})$$

where:

$$\delta(d\sigma/dx) = \sqrt{\left\langle \left(\frac{d\sigma}{dx} \right)^2 \right\rangle} \quad (\text{eq. 6.22})$$

A comparison with the numerical simulation of Potze results in $C' = 0.1$. For a surface with a single Fourier component we then find

$$\delta\Sigma = 0.07(2\pi k\Delta x)^2 |A_k| \quad (\text{eq. 6.23})$$

showing the same dependency on the surface structure as in the previous case.

Based on this analysis, we can now check the influence of the errors in our 3D-deflectometer on the surface reconstruction. Table 6.3 shows the total contributions to the RMS error to be $\delta x_{total} \leq 15 \mu\text{m}$. The same order of magnitude can be assigned to the cross-scan component δy_{total} .

Assuming a step size of $\Delta x = 30 \mu\text{m}$, as relevant for our 3D-deflectometer, and using $\varepsilon = 0.5$, we can write Eqs.6.19 and 6.23 as:

$$\text{Random:} \quad \delta\Sigma / A_k = 1.0 * 10^{-4} \delta\Sigma / A_k = 3.6 * 10^{-4} (k/100 \text{ m}^{-1})^2 \quad (\text{eq. 6.24})$$

$$\text{Discretization:} \quad \delta\Sigma / A_k = 0.3 * 10^{-4} (k/100 \text{ m}^{-1})^2 \quad (\text{eq. 6.25})$$

For $k = 100 \text{ m}^{-1}$ (wavelength 10 mm) and $A_k = 10 \mu\text{m}$ we find errors equal to $\delta\Sigma = 1.0 \text{ nm}$ and 0.3 nm , respectively, combined into a total error of 1.1 nm . For $k = 1000 \text{ m}^{-1}$ (wavelength 1 mm) we find the same errors for $A_k = 100 \text{ nm}$. These figures are very satisfactory and show that the calibration of the grid spacing and localization is accurate enough for reconstructing the surface with the desired precision of a few nm.

These equations also help us to define a “well behaved” surface for our deflectometer by the relation

$$A_k k^2 < 10^{-1} \text{ m}^{-1} \quad (\text{eq. 6.26})$$

which guarantees a total error – random and discretization– of less than 1 nm.

6.9. Calibration procedure

The calibration of the 3D-deflectometer as applied currently for the instrument consists of two major steps. First, there is a set of procedures that must be applied before the surface-under-test is measured. These are applied in the following order:

- PSD adjustment
- PSD focusing
- Slope calibration (a-linear (5th order) using an autocollimator as the calibration device)
- Pixel size calibration (a-linear (6th order) using the reference grid as the calibration device)
- Measurement of the lens signature (using the flat reference as the calibration device)
- Measurement of the stage signature (using the flat reference as the calibration device)

In principle, the first three procedures can be applied frequently (e.g. three-four times a year), since the mechanical stiffness of the instrument should prevent significant changes in the system configuration. The latter three can be applied more often, say once a day, since they are more dependent on the mechanical and temperature drift and do not require much effort anyway.

After the object is measured, the following procedures are applied:

- Subtraction of the lens signature
- Subtraction of the stage signature
- Re-mapping the measured slope arrays into an equidistant array (currently applied to the scan axis only)

The re-mapping of the slope arrays is done using spline interpolation. Therefore, we evaluate a spline interpolant for each scan-line of the arrays; afterwards we assign slope values to the new, equidistant grid, with the step size equal to the mean pixel Δx size measured along the scan line.

6.10. References

- [1] W. Poetze, *Method to reconstruct surface topography from measured slopes*, Philips Applied Technologies internal report CTB56-02-0000, (2002)
- [2] E. Hecht, *Optics*, Addison Wesley; 4th edition, (2001)

Chapter 7

Validation by industrial applications

In this chapter we present several examples of measurements done with the 3D-deflectometer on various industrial surfaces. First, we show examples of measurements on silicon wafers, including wafer substrates, structured test wafers for investigation of the polishing (CMP) quality, and a patterned wafer for commercial applications. Then we present measurements of other industrial objects, which show specific features of the 3D-deflectometer. All the examples are used for verifying the measurement accuracy for various independent measurements.

7.1. Introduction

The goal of this chapter is to show the potential of 3D-deflectometry as a surface metrology tool. At the moment of writing this thesis, the 3D-deflectometer at Philips Applied Technologies was considered as a research tool; therefore the results of the measurements could not be officially certified. Nevertheless, since the device was shown to produce reliable and accurate measurements, the instrument was often used for preliminary tests and feasibility studies of various industrial objects during the project time.

In this chapter we have chosen five examples of different objects measured with the deflectometer. These are:

- 4" silicon-wafer substrate (section 7.2)
- 12" silicon wafer substrate (section 7.3)
- 8" patterned wafer for CMP testing (section 7.4)
- 8" patterned wafer for LCoS panels (section 7.5)
- 380 x 30 x 30 mm³ Aluminium mirror (section 7.6)

With each example, we try to point out some characteristic and unique features of the 3D-deflectometer, e.g., high accuracy at the nanometre scale in section 7.3, or large dynamic range of the measurement in section 7.5. Finally, each measurement was verified with an independent metrology tool. Therefore, we could show a direct comparison between the 3D-deflectometer and standard tools used in surface metrology, like stylus and white light or phase-shift interferometry.

In order to make the chapter easier to read, we put the full metrology reports on each measurement into separate appendices, including the parameters and results of the measurement and post-processing. This way, the main text contains mainly highlights, specs and conclusions on the measurement.

The measurements were compared to the each other by plotting corresponding height profiles into a single graph and estimating the peak-to-valley (PV) height difference between the profiles. We decided not to compare the 3D topography images since the interpretation of the result would be much more complex (e.g. lateral errors, different orientations, or different image resolution would influence height, etc.).

Finally, it is often that additional post-processing is needed for getting the correct answer to a specific question. E.g., in some cases, a strong form distortion disables identification or comparison of the surface feature at the nanometre scale. In this case we use a high-pass spatial filtering to access different regions of spatial frequency. We use a standard single Gaussian filter, with a cut-off defined at 50 % response.

Measurement configuration

Each measurement has been done using the same configuration of the 3D-deflectometry set-up and calibration procedures. The configuration is summarized in table 7.1. Unfortunately, at the time of doing the measurements, the calibration flat had not been delivered yet. Therefore, the measurements have been done without subtraction of the system signatures (see section 6.6).

Table 7.1 Summary of the calibration procedures applied for validation of the 3D-deflectometer.

Calibration parameter	Status
Pixel size calibrations	6 th order polynomial
Slope sensor calibration	separate calibration for each PSD axis, with a 5 th order polynomial (single polynomial for each axis)
Lens signature calibration	no
Stage signature calibration	no

7.2. Flatness of a 4” Si-wafer

In the first example we present the most straightforward application of the 3D-deflectometer, which is an inspection of a silicon wafer substrate. In figure 7.1 we present the result of a measurement of the topography of a 100 mm silicon wafer substrate manufactured by Siltronic Inc (Appendix G1). As we show in the figure, due to characteristics of the 3D-deflectometer, multi-scale information of the measured surface can be obtained directly by software manipulation of the measured data. Already the general figure, shown in figure 7.1a, carries important information concerning the stress level in the material introduced during the manufacturing process. By using a high-pass filter we can access directly the nanotopography information (figure 7.1b,c). Striking feature in figure 7.1.b is the steep edges of the wafer, with the height values strongly exceeding the overall flatness. This is a typical problem of edge polishing, since the polishing pads do not cross the wafer’s edge. The edge control of wafer substrates recently became an important issue, since a lot of effort is being spent on optimizing the polishing processes such that the polished area extends as close to the edge as

possible. This way the production cost can be decreased, since more ICs can be produced on a single wafer. Clearly the edge control is fully supported by the 3D-deflectometer. Finally, a high resolution nanopography map can be accessed (figure 7.1c), from which the quality of the wafer product can be compared directly with the requirements.

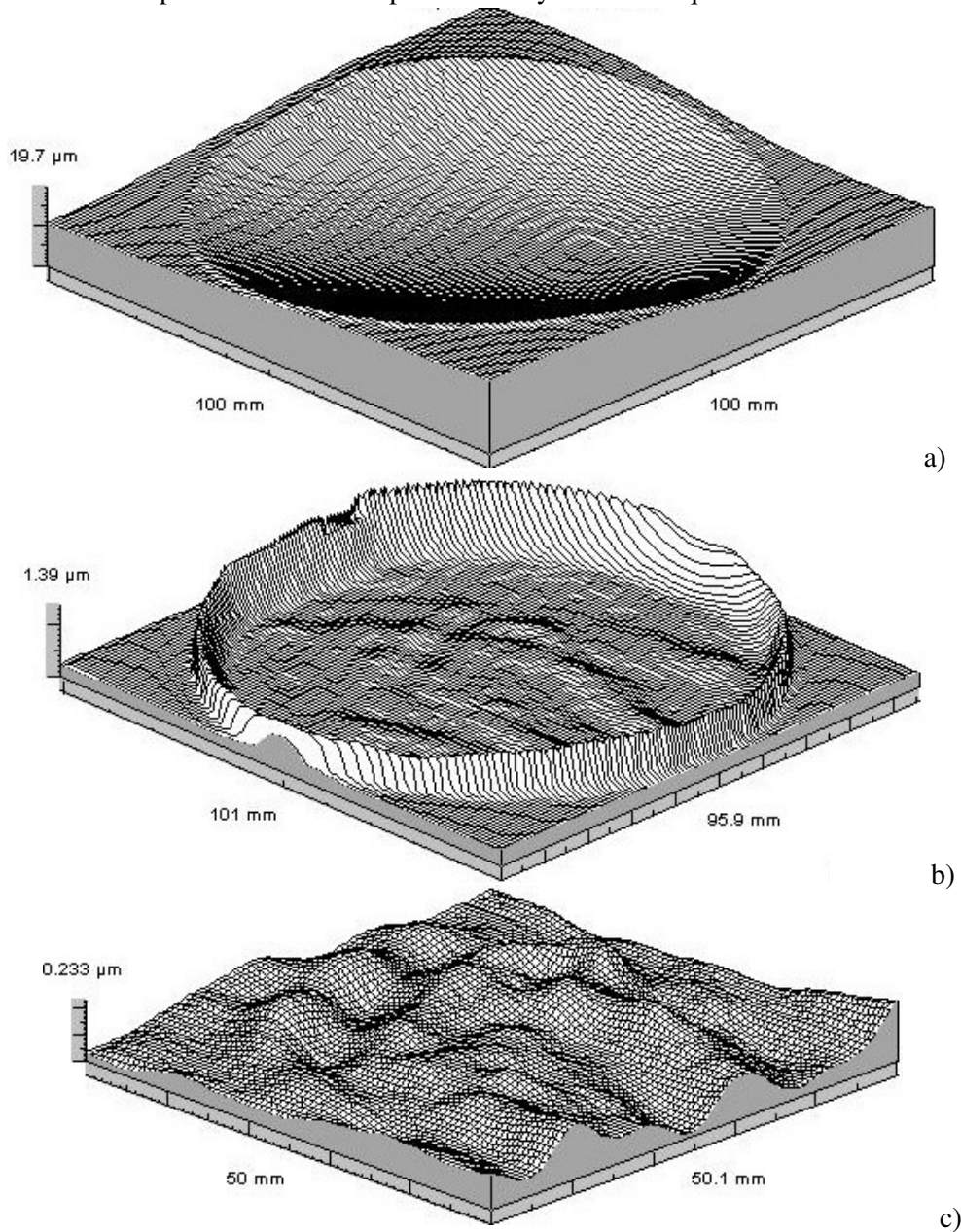


Figure 7.1. Free form topography of a 4" wafer substrate (a) and the corresponding nanopography (filtered with a 20 mm-cut-off high-pass filter) (a,b – full area and sub-field in the middle, respectively), measured with the 3D-deflectometer.

As we showed in this example, a single measurement with the 3D-deflectometer enables a fast and fully quantitative analysis of the wafer's flatness, with the vertical and spatial range ranging from general form analysis down to nanopography and partially to the roughness level.

7.3. Epi-pinmark profile

In this section we will concentrate on a high resolution and accuracy of the measurement. Therefore we will show a measurement of the epi-pinmark, an artifact present on a surface of silicon wafer substrates (Appendix G2). The epi-pinmarks are surface structures introduced during the production of an epitaxial layer. During that process, the wafers are supported by 3 pins, touching the back-side surface. As the result of diffusion and local temperature gradient, doughnut-like structures are produced on the bottom surface.

In figure 7.2a we show a height map of an epi-pinmark measured with the 3D-deflectometer on a 12" silicon wafer substrate manufactured by Siltronic Inc. The diameter of the measured structure is about 7 mm and the measured height deviation is less than 70 nm. However, the resolving power of the instrument in both the lateral and the vertical coordinate is much better than these values. Clearly, structures with only a couple of nm in height can be identified easily, like a small ring at the top of large one, which has a width of about 0.5 mm and height of 5-10 nm.

To verify the accuracy of the measurement, we measured the same epi-pinmark with an independent reference device, a white light interferometric microscope from Zygo Corporation (Appendix G3). Both measurements produce a qualitatively very similar topography. With a pixel size of about 23 μm , the interferometer represents about 8 times higher lateral resolution; therefore much higher spatial frequencies are present in the interferometric measurement. However, since the field of view of the objective used is only $7.3 \times 5.5 \text{ mm}^2$, already such a relatively small area of $10 \times 10 \text{ mm}^2$ has to be stitched from many measured sub-fields. As a result, the total measurement time with the interferometer was about 50 minutes.

In order to compare the measurements quantitatively, we tried to find the same profile across the epi-pinmark in both data-sets and plot them together in the same graph. Afterwards, we estimated the peak-valley height difference between the plots. The profiles were chosen by finding two characteristic surface features in the 3D-plots as reference points, and leading the profiles through them. By following such a procedure we estimate the error in the lateral position of the profiles to be less than 0.5 mm. The result of this comparison is given in figure 7.3. Once again the comparison shows a very high similarity in lateral and vertical coordinates, with a PV difference between the profiles of about 5 nm. A more detailed comparison of the profiles would be more difficult since it is limited by the profiles exact location and the difference in the lateral resolution between the images. Finally, it is difficult to judge or even verify at such a small height level which method gives a more accurate result (e.g., some stitching errors can be recognized in the interferometric image, the measurement by deflectometry is influenced by the high frequency lens signature, etc). Nevertheless, we can conclude that the 3D-deflectometer is capable of producing topography images with accuracy on the order of a few nanometres.

The measurement of the epi-pinmark is a good example of the capabilities of 3D-deflectometry, where a small feature is localized and quantified directly from the topography map of the complete surface after the measurement. This is different from the usual procedure for other profilers, where a small feature must first be localized and only then can be measured.

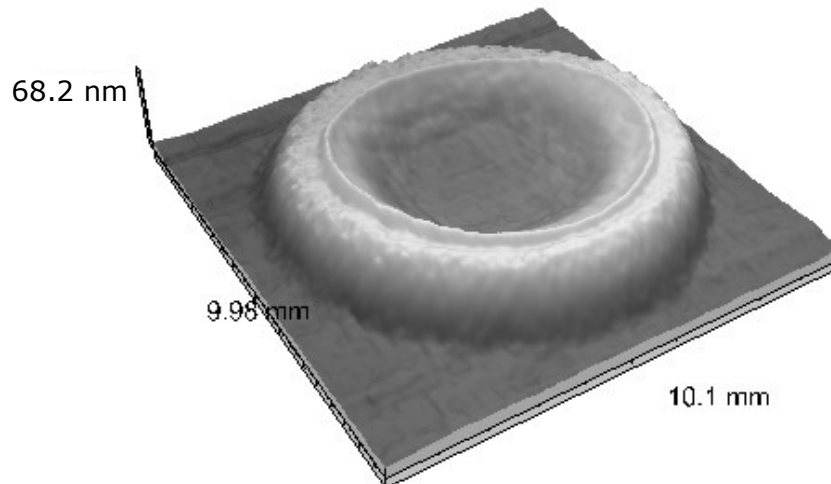


Figure 7.2. An epi-pinmark on a silicon wafer substrate measured with the 3D-deflectometer.

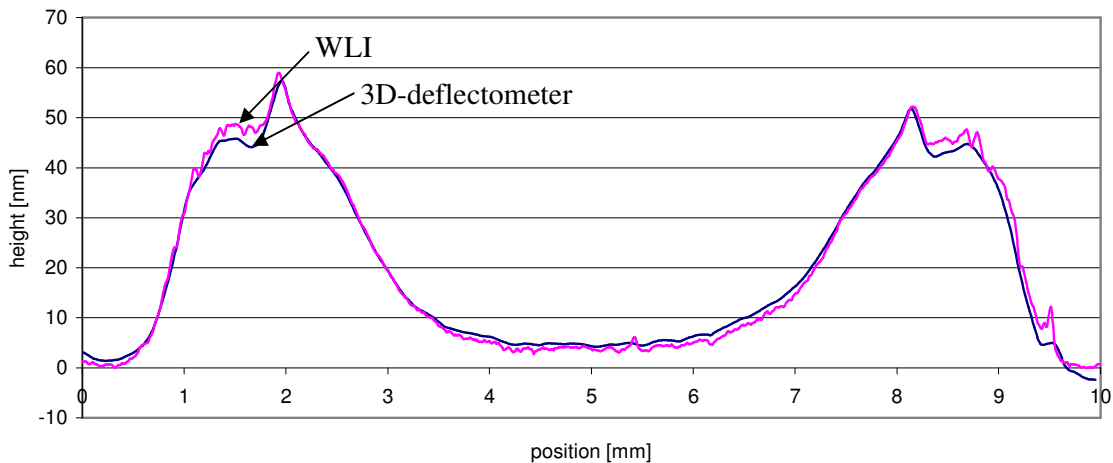


Figure 7.3. Comparison of the height profile measured across the epi-pinmark with the 3D-deflectometer and a white light interferometer (WLI).

7.4. Polishing control

As mentioned in section 2.2, the physical influence of the polishing processes on the surface is still not fully understood. It is often studied empirically by using special test wafers and observing the topography changes at different stages of the polishing process. In this section we will show a possible application of 3D-deflectometry for the nano-topography measurement of structured wafers for testing the CMP process. In the measurement we used four 200 mm wafers produced by Philips Semiconductors Nijmegen (Appendix G4). The samples include one non-polished wafer and three wafers at different stages of polishing (polishing time: 30 s, 90 s and 120 s, respectively). To show the influence of the polishing we measured a single die ($22 \times 22 \text{ mm}^2$) at the same location on each wafer.

In the metrology reports in appendix G4 we also show the slope maps of these measurements, i.e., an image where the amplitude of the two components of the slope vector are shown as a function of position. These slope maps illustrate the high sensitivity of deflectometry to very

small height variations: even for the fully polished sample the slope map still shows the original surface features before polishing.

The measured height maps in figure 7.5 give direct qualitative information on the influence of the polishing process on the surface evolution. For example, we can clearly see that the first effect on the surface after a short polishing time is the strong attenuation of the high spatial frequency structures. With increased polishing time the amplitude of low spatial frequencies is also being reduced. The process can be characterized by calculating the RMS height deviations per die for all four measurements; the result is given in table 7.2.

Table 7.2. The RMS height deviation per die for various stages of the CMP process of the test wafer.

CMP time (s)	RMS height (nm)
0	79
30	68
90	65
120	48

The quality of our measurement was verified with a Stylus instrument, which, due to its high vertical and horizontal dynamic range is still considered the “golden standard” for wafer testing. The verification was done by measuring profiles on two test wafers: the non-polished and the fully-polished wafer after 120 s. Afterward, we tried to localize the corresponding profile in a data-set from deflectometer and compare the profiles by plotting the in the same graph. Similar to the previous section, the 3D-deflectometer’s profiles was chosen by looking for similar surface features. Since the exact location of the profiles measured by Stylus is unknown, we claim a position uncertainty of 2-3 mm.

First, we compare the wafer after polishing, since we can predict that such a smooth surface produces much less measurement artifacts. The profiles are plotted in figure 7.4.

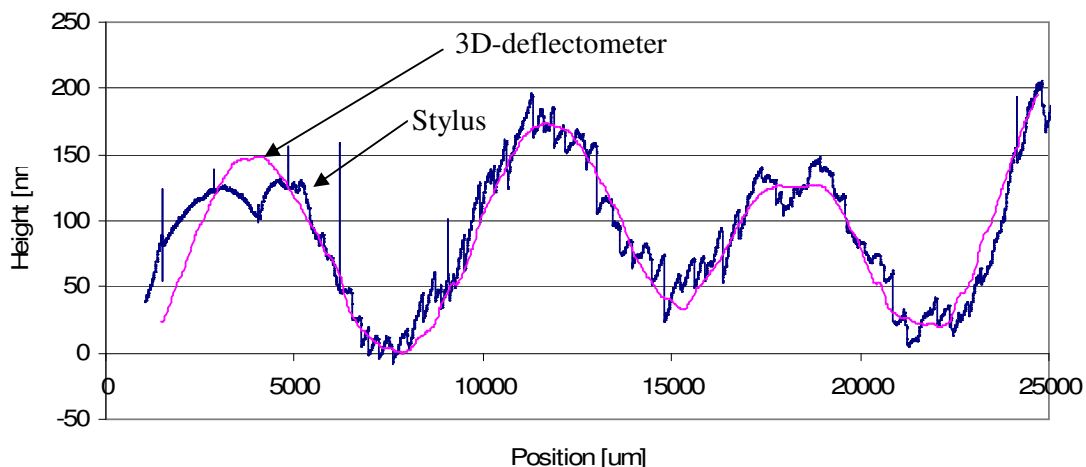


Figure 7.4. Single profile measured on the fully-polished wafer after 120s. Comparison with a Stylus instrument (HRP 220 from KLA-Tencor).

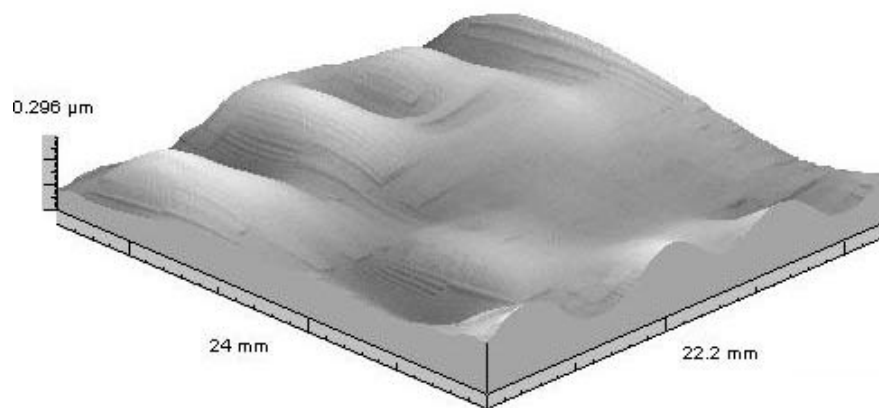
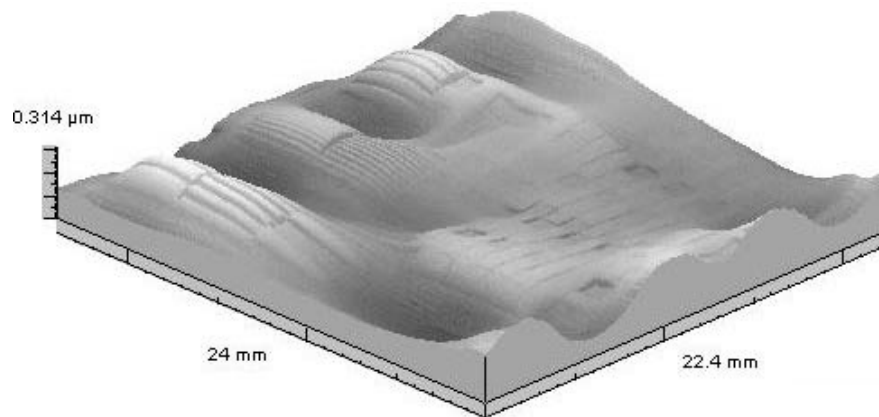
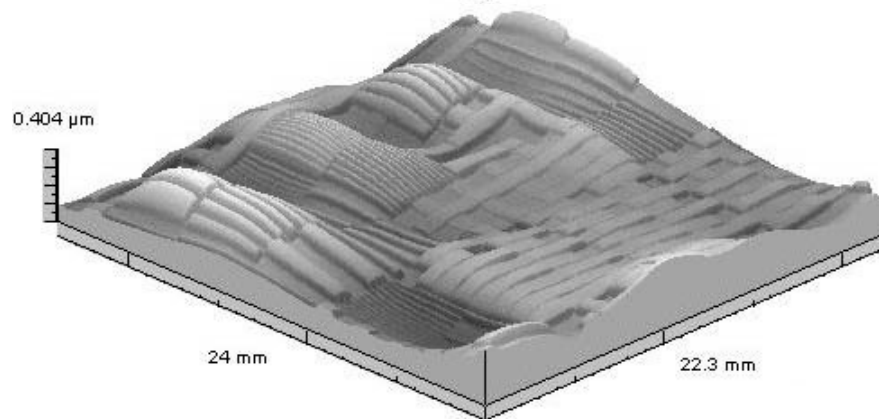
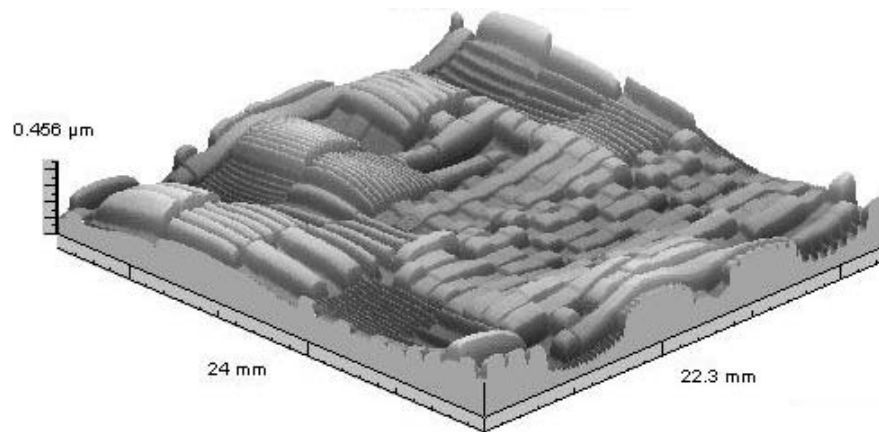


Figure 7.5. (previous page). A single die on a patterned silicon wafer measured by the 3D-deflectometer, showing changes in the nanopography for various stages of the CMP process. The images correspond to 0, 30, 90 and 120 seconds of polishing time. A parabolic bend has been removed in software from all the images.

Both profiles show a similar envelope for the low spatial frequencies. The stylus measurement is characterized by a higher lateral resolution (about 2 μm); therefore the corresponding curve exhibits more high-spatial-frequency structures than the curve measured by the deflectometer. Most of those structures, however, are measurement artifacts due to vibrations, mechanical drift, and instrument instability during the long measurement time (about 20 min for the complete profile). Clearly, the deflectometer seems to be characterized by much higher stability against vertical noise. This is due to shorter measurement time (scan time less than 1 ms for a scanning velocity of 33 m/s) and the strong suppression of noise in the surface reconstruction algorithm. The difference around 3000-5000 μm position on the horizontal scale between the graphs was recognized as an artifact of the measurement with the Stylus. We estimate the difference in the measured profiles to be about 30 nm PV. A more accurate comparison would be rather difficult due to difference in the lateral resolution and uncertainty of the position of the profiles.

Next, we compare the profiles measured on the non-polished wafer (figure 7.6). Just by looking at the plot we can recognize the drawback of an optical measurement of sharp and/or repetitive structures on a surface, as compared to the mechanical probing. Two main distortions of the measured surface are apparent in the measurement by deflectometry.

First, we recognize a general deviation in the long spatial wavelengths, particularly at the locations where high-spatial frequency structures are present. We presume that the main source of such image distortion is the result of diffraction at the surface. Just to give an idea of possible levels of errors introduced, we refer to image D3.1 in appendix D3, which shows the very strong distortion of the reflected beam on the deflectometer's detector, measured from the same wafer.

Second, we recognize also a strong damping of the steep and high spatial-frequency structures. We assume that the damping is mainly the result of attenuation of the slope signal at spatial wavelengths comparable to, or shorter than the lateral resolution of the deflectometer. Therefore, the damping of the structures with higher spatial density is stronger than that for less dense structures. Beside of the natural response limit, probably other factors may be causing the damping effect: the mentioned erroneous measurement due to the diffraction, the numerical integration (which acts like a low-pass filter) and the slope at the etched edges that are larger than the slope range of the instrument.

However, a positive conclusion from the patterned wafer is that even for such a "difficult" surface, a long-range consistency of the topography is conserved. This is due to a strong error reduction by the surface integration procedure, which uses many integration paths to reach the valley floor.

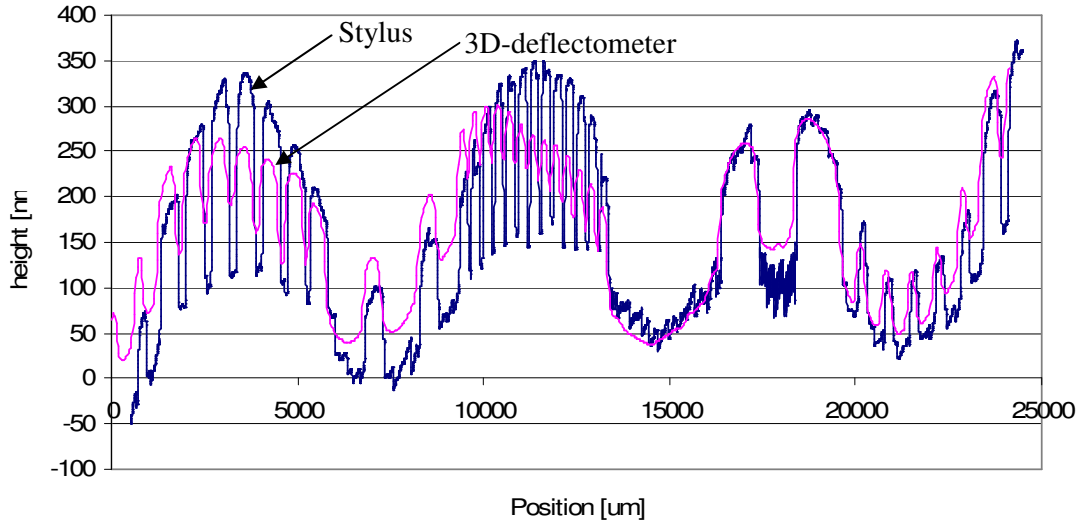


Figure 7.6. A single profile measured with the 3D-deflectometer and a Stylus (HRP 220) on a non-polished wafer.

From the examples presented, we can conclude that the 3D-deflectometer produces an accurate measurement of the nanotopography of polished silicon wafers, comparable with the accuracy of the standard instruments used in the semiconductor industry. Furthermore, although the 3D-deflectometer cannot compare with the Stylus at high lateral resolutions, for the nanotopography measurements with spatial wavelengths on the order of $200\ \mu\text{m}$ and more, the deflectometer shows a clear advantage upon the Stylus because of the measurement stability and short length of time. We also recognized topography errors when non-polished structured wafers are measured. In this case, the measurement can be strongly distorted locally, but the long range consistency is conserved.

7.5. Patterned wafer: LCoS panels

As we explained in section 1.2, one of the advantages of measuring a surface in the slope domain is the large dynamic range of the measurement. This feature is important when the measured surface contains a large form deviation at long spatial wavelengths, and at the same time, small height deviation, characterized by short spatial wavelengths. The dynamic range, as well as the field of view, can be extended by applying a slope stitching procedure (see section 4.5.3). In this case, the dynamic range is increased by re-adjusting the object's tilt between the sub-measurements.

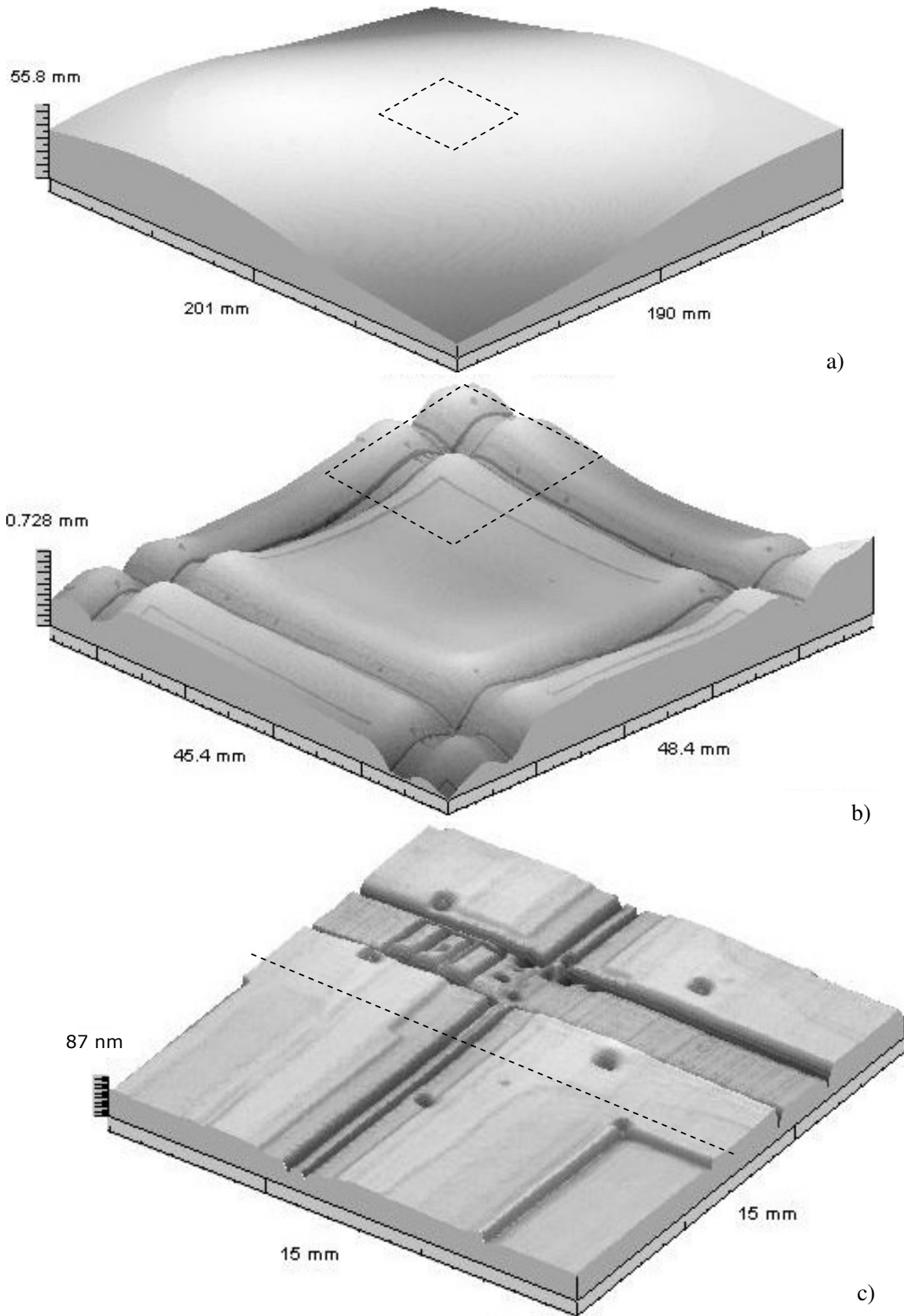
To show an application where this extended dynamic range is used in both spatial and height coordinates, we present a measurement example of a patterned and metalized wafer for Liquid-Crystal-on-Silicon (LCoS) panels (Appendix G4a). The wafer has been manufactured at Philips Semiconductors Boeblingen for high-resolution projection TV. Due to stress during processing, the wafer's form exhibits a strong bending. In order to capture the complete surface map of this 8" wafer, we measured four overlapping sub-fields of the wafer and stitched them together in the slope domain. The result is given in figure 7.7.

As we show in figure 7.7, the combination of the high vertical and lateral ranges enables a “virtual microscopy” by zooming-in from the global figure of the complete surface into small details on the surface. This zooming feature is accomplished purely in software, by applying spatial filtering (for the vertical zoom) and area extraction (for the lateral zoom) on the same data set. In this very example we show a dynamic range above $1:10^4$ in height and $1:10^3$ in spatial coordinates. This, however, is not the limit of the deflectometer; by applying more stitches and efficient numerical integration routine, much larger and more curved surfaces could be easily measured.

To verify the accuracy of the measurement at the nanometre scale, we did an independent reference measurement on the same wafer by white light interferometric microscopy (Appendix G4b). As we show in the Appendices G4a and G4b, both measured surfaces present qualitatively similar results (figures G4a.3 and G4b.1). In order to compare the measurements quantitatively, we plotted the corresponding height profiles measured by both instruments into a common graph. The result is shown in figure 7.8.

From the figure we can estimate a PV difference between the measured profiles of about 5 nm throughout most part of the profiles. The measured height difference is much higher in the narrow trenches, where the interferometer measures about 60 nm-deep valley, but the deflectometer indicates only about 30 nm PV (figure 7.8 b). This damping can be explained by the response limit of the deflectometer at such a short spatial wavelength – the width of the trench of about $150\ \mu\text{m}$ is already below the lateral resolution of the deflectometer. However, as we see in figure 7.8.a, the long-range consistency in the deflectometer measurement is not influenced by the erroneous measured at the trenches. Once again, this indicates robustness of the multi-path integration routine.

Figure 7.7. (next page). A silicon wafer for LCoS panels measured with the 3D-deflectometer and viewed at different lateral and vertical scales. The dashed squares (figures a,b) show the area zoomed at the following image, the dashed line in figure (c) indicates the location the profile shown in figure 7.8.



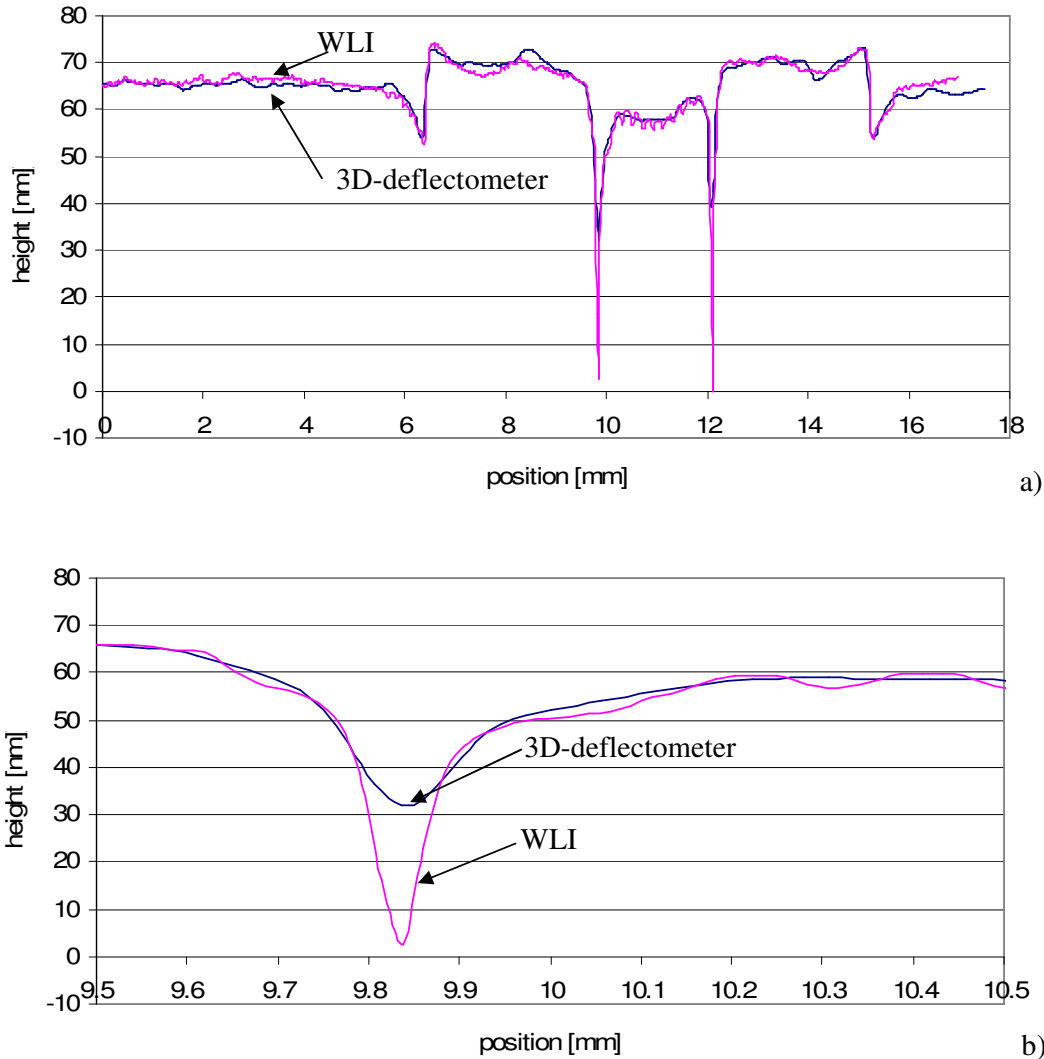


Figure 7.8. A height profile on the LCoS panel, measured with a white light interferometer and the 3D-deflectometer; a) the complete profile, b) zoom on the trench.

7.6. Long aluminium mirror

One of the important challenges in surface metrology, where the 3D-deflectometry shows its potential, is high-resolution profiling of surfaces characterized by large lateral dimensions. An excellent example is given by an aluminium mirror, which has been studied as a possible solution for a precise, interferometry-based positioning system. The mirror has been produced by diamond-turning, which is a cost-effective process as compared to precise polishing. Both the global shape and the microstructure information are interesting for the customer. Since the total length of the mirror is 380 mm, it was difficult for the customer to find an instrument which could measure the complete surface with sufficient lateral resolution. The available stitching interferometers suffer from deviations of the mechanical translation and error propagation of the stitching procedure for such large lateral dimensions. On the other hand without stitching, the lateral resolution of large interferometers is

insufficient, as it is limited by the resolution of the CCD camera: the larger the field of view, the lower the absolute value of the spatial resolution

A direct solution for such a metrology problem is found in the 3D-deflectometer, which could measure the complete surface in a couple of minutes. The measurement result is given in figure 7.10 (Appendix G5a).

Very poor quality of the manufacturing process related to the global form of the mirror can be recognized immediately from the measurement. The surface exhibits a strong form distortion with a PV height deviation of $\Sigma = 10.3 \mu\text{m}$ (figure 7.10a). Since the absolute lateral resolution of the 3D-deflectometer is not decreased by the large field of view, high resolution profiling can be realized across the complete surface of the mirror. The result of the profiling is shown in figure 7.10b, where the high-pass spatial filter was applied to the data set in order to remove the global shape. This nanotopography image shows a strong signature of the diamond turning machine, which results in characteristic waviness with a PV height deviation of $\Sigma=350 \text{ nm}$ and a high spatial frequency roughness of $\Sigma = 30 \text{ nm}$ (PV). As a consequence of the measurement, the mirror was rejected, and the manufacturing process deemed not suitable as a production alternative.

To verify our measurement results with an independent measurement, we inspected a part of the surface with a 4" phase-shifting interferometer from Zygo (Appendix G5b). Since the interferometer could not capture the complete surface, we compared only the first 90 mm of the mirror (in figure 7.10, 90 mm from the top). As shown in Appendices G5a and G5b, both measurements gave qualitatively the same topography. In figure 7.9 we present a plot of the corresponding height profile measured with both methods. Although the general characteristics are similar, clearly the high spatial frequency structures – the high-frequency signature of the diamond turning – are damped in measurement by the interferometer. This is due to a relatively low lateral resolution of the interferometer that acts as a low-pass filter for the high frequency structure, as compared to the measurement with the deflectometer. The PV height difference between the profiles is about 30-40 nm. The difference in topography is mostly due to much higher amplitude at high spatial frequencies, as measured by the deflectometer. Due to this unique multi-scale feature of the deflectometer it is difficult to verify its performance for such a large object with a single instrument.

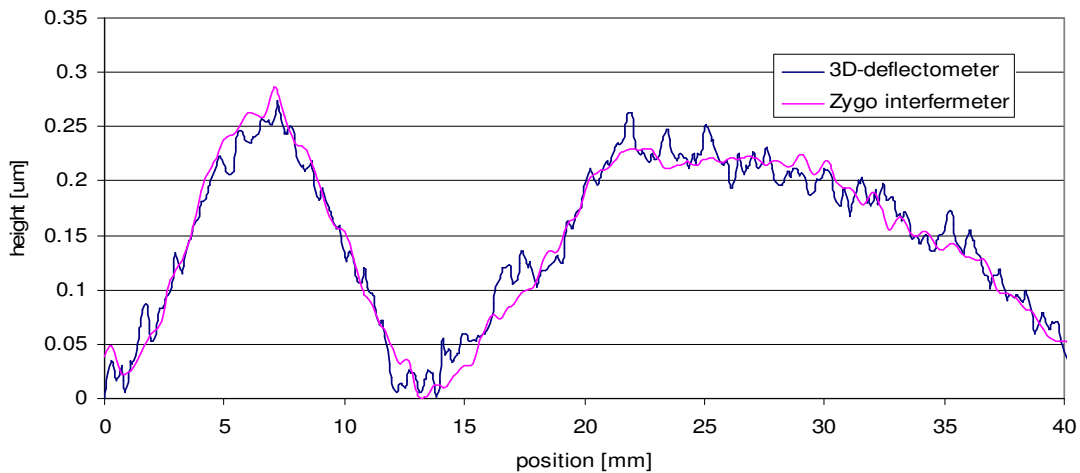


Figure 7.9. Comparison of the same profile extracted from a surface-measurement by the 3D-deflectometer and the GPI XP/HR Zygo interferometer.

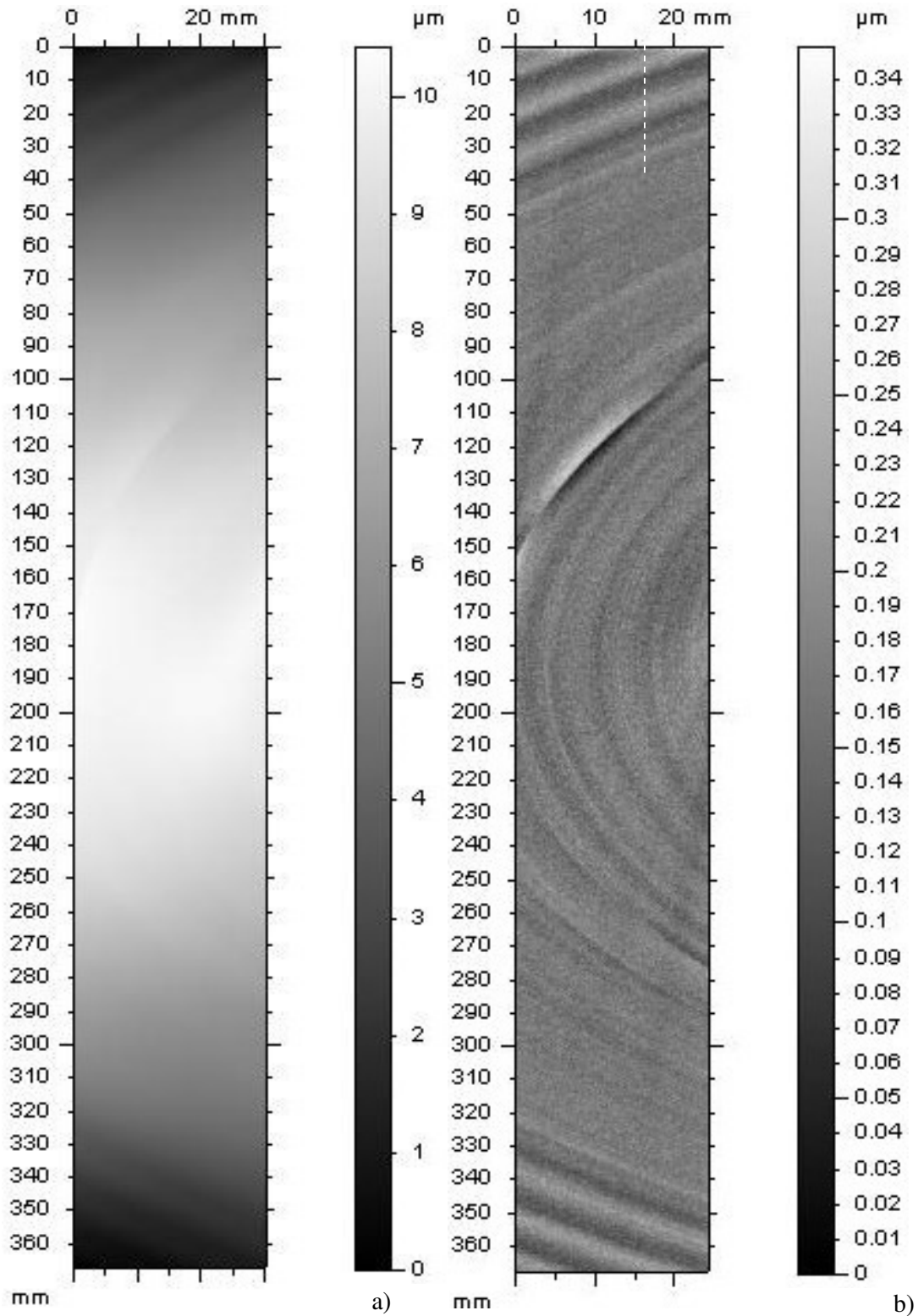


Figure 7.10 A long aluminium mirror measured with the 3D-deflectometer: a) the global form; b) filtered microstructure (single Gaussian filter, 8mm cut-off). The dashed line in figure (b) indicates location of the height profile shown in figure 7.9.

7.7. Final performance estimation for the 3D-deflectometer

From the measurements presented in this chapter we can give a fair estimation of the performance of the 3D-deflectometer. The main system parameters are summarized in table 7.2. Furthermore, in figure 7.12 we depict a Stedman diagram for the instrument. In the table as well as in the figure we present the AW-space for the set-up with a single scan mode, as well as for the slope stitching mode. The latter results in an increased dynamic range in slope, and consequently in height. We assume a minimum stroke-width for stitching of $L_S = 10$ mm; therefore maximum height Σ'_{\max} for stroke L is increased as $\Sigma'_{\max} = \Sigma_{\max} * L/L_S$.

Table 7.3. Current performance parameters of the 3D-deflectometer at Philips Applied Technologies.

Parameter	Value
Lateral range	optical $L = 110$ mm ($L' = 190$ mm by stitching) translation $L_y = 500$ mm
Lateral resolution	$\Lambda_{\min} = 200$ μm
Sampling distance	$\Delta x = 30$ μm
Maximum number of data points for surface reconstruction algorithm	$N^2 = 6.25 * 10^6$
Height range	$\Sigma_{\max} = 1$ mm / 500 mm $\Sigma'_{\max} = 50$ mm / 500 by stitching
Height resolution	$\Sigma_{\min} < 1$ nm
Height accuracy	$\delta\Sigma \leq 5$ nm in nanotopography $\delta\Sigma \leq 35$ nm global (for 110×110 mm ² area)
Measurement time	$T = 73$ s / 110×110 mm ² area

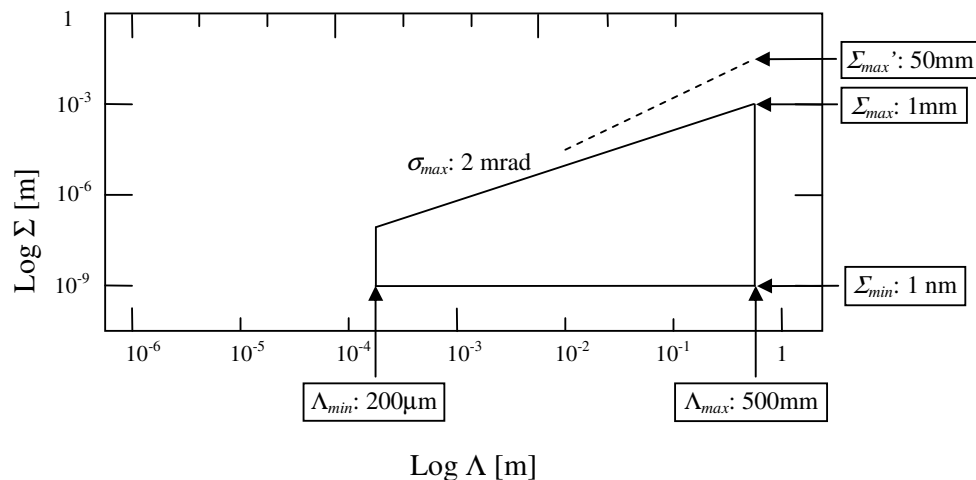


Figure 7.11. Stedman diagram for the 3D-deflectometer. The dashed line indicates the maximum height/slope range when stitching is applied to extend the dynamic range of the measurement.

Chapter 8

Concluding remarks

The major achievement of this thesis is the evolution of the promising but unproven concept of 3D deflectometry as a device for rapidly characterizing surface topology to a full scale metrology tool with a proven performance and solid calibration procedures. The new instrument has been carefully compared to other metrology tools like the White-Light Interferometer and meets the accuracy of this Golden Standard. The major advantage of the new instrument is its superior lateral resolution and its ability to handle large surfaces without sacrificing the off-line possibility of zooming in on small features.

Careful calibration of the prototype has shown that a simple reference surface-under-test can be used to eliminate the influence of systematic errors in the lens and the translation stage, by applying simple software corrections on the slope data arrays of actual measurements. Using an external reference is an easy means of frequent check-ups on the calibration by the end users.

Underlying this achievement is the availability of advanced integration procedures that take into account the large number of paths that connect the different positions on the surface-under-test. This least-squares type of optimization of the surface reconstruction leads to a rigorous surface topology that fully avoids the build up of uncertainty over increasingly distant points. This also leads to very relaxed demands on the accuracy of the slope measurement and thus on the required resolution of the A/D converter, a feature that was not recognized at the start of this project.

Concerning the throughput, surprisingly, the major limitation at this moment is the computational power and speed necessary to reconstruct the surface topology by advanced integration procedures. The 1 min scanning time of a 12'' wafer that can be achieved with an upgrade of the current prototype of a 3D deflectometer is in strong contrast to the 30 minutes processing time of a 1000 x 1000 array of slope vector information on a Pentium IV system. The limitation in the field of mechatronics is the necessary scanning speed, which translates into galvo-mirrors with a resonance frequency larger than 1 kHz or high speed polygon-based deflectors.

Very-high resolution applications of 3D-deflectometry lead to a large beam size at both the detector and the beam deflector, due to the wavelength determined phase space area of a (Gaussian) beam of light. This results in a loss of accuracy of the slope measurement and to a decrease of the slope range dynamics of the instrument. This conflict in design specifications can be sweetened by switching to a laser with a shorter wavelength, e.g., a blue laser at 405 nm as used in the new generation of DVD players. Switching to a Large Beam Detection mode for slope detection can also help in this respect.

We believe that the performance of the 3D deflectometer can still be improved by a thorough theoretical analysis of the correlation between the sampling step size and the desired consistency in form of the surface-under-test. The very good results that have already been achieved with the prototype fully support such an effort.

Recently, we have learned that a leading semiconductors equipment supplier – the ADE Company – has also designed a deflectometer that is commercially available [1,2]. This is good news, because it proves that 3D deflectometry is coming off age as a mature member of the field of metrology.

References:

- [1] Method and apparatus for mapping surface topography of a substrate, ADE corporation patent, publication info: WO0023794, (2000)
- [2] ADE corporation, Web Site: www.ade.com

3D-deflectometry

Fast nanotopography measurement for the
semiconductor industry

APPENDICES

Introduction to appendices

The appendices have a very special role in this thesis. They not only support the main text with additional background information but also help to make the text “cleaner” and easier to read. Therefore, they are often a part of the text that is simply taken out and put into an appendix, like the derivation of formulas, a detailed description of topics, which are beyond the main scope of this thesis, detailed measurement reports, etc. This section is much larger than usually met in a regular PhD thesis, but correlates well with a design-based PhD project. Second, some cross references between the main text and the appendix may happen, particularly in case of deriving formulas.

The appendixes are numbered with letters, adequately to the number of the corresponding chapter; thus the appendixes referring to chapter 1 are marked as A1, A2, A3, ..., the appendixes corresponding to chapter 4 are marked as D1, D2, D3, ..., etc. One can notice for example, that as a consequence there is no appendix B at all (as no appendix refers to chapter 2), which may lead to some confusion. Nevertheless, the author believes that with a large number of appendixes that is present in this thesis, such notation is helpful and sufficiently transparent for the reader.

Appendix A1 Definition of the Gaussian beam size

One of the key parameters in design of deflectometry systems is the beam size, which describes the intensity distribution (or more properly irradiance) in the plane x-y perpendicular to the direction of the laser radiation propagation. Deflectometry applies typically a single mode laser beam for slope detection. Such a beam is characterized by the transversal intensity distribution described by a Gaussian function. Since the Gaussian distribution has no natural boundaries, various definitions of the beam size are used commonly in the literature [1-3]. One of the most popular definition concerns half width or radius of the beam where the one-dimensional transversal irradiance distribution is described as:

$$I(x) = I_0 \exp(-2x^2 / w^2) \quad (\text{eq. A1.1})$$

with I_0 the maximum intensity and w the half-width e^{-2} maximum (HWe⁻²M) – the position of the beam radius where intensity drops down to $1/e^2$ of the maximum intensity (~13.5 %).

In design of optical scanning system it is more practical to use a full-width or a diameter criterion rather than a radius. Thus, in this thesis, the beam will be described by its full-width e^{-2} maximum (FWe⁻²M) and the beam size (diameter) will be marked as $d(e^{-2})$ or simply d . Using the FWe⁻²M the irradiance distribution in a one-dimensional space can be written as:

$$I(x) = I_0 \exp(-8x^2 / d^2) \quad (\text{eq. A1.2})$$

or a normalized irradiance distribution:

$$I_N(x) = \frac{4}{d\sqrt{2\pi}} \exp(-8x^2 / d^2) \quad (\text{eq. A1.3})$$

Finally, in a two-dimensional space a Gaussian irradiance pattern is described as:

$$I(x, y) = I_0 \left[-8(x^2 + y^2) / d^2 \right] \quad (\text{eq. A1.4})$$

Another popular definition of the beam size, which will be occasionally referred to in this thesis, is full-width half maximum (FWHM) marked as d_{50} , which is the beam diameter where the intensity drops down to 50 %. The relation between d and d_{50} is:

$$d_{50} = 0.5884d \quad (\text{eq. A1.5})$$

The meaning of various definitions of the beam size parameters is explained schematically in figure A1.1.

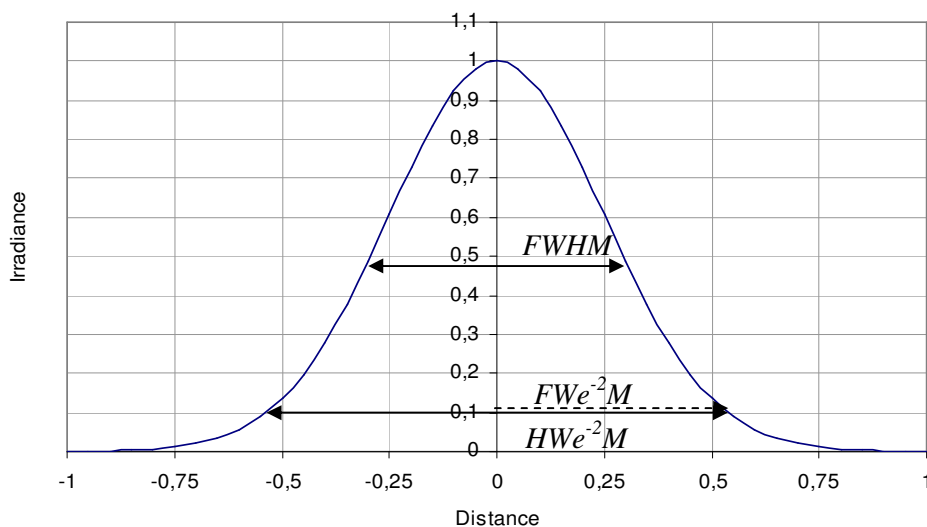


Figure A1.1. Profile of a Gaussian beam and various beam size parameters.

References:

- [1] E.Hecht, *Optics*, Addison Wesley; 4th edition (2001)
- [2] G.H.Seward, *Two-dimensional space-angle product of a Gaussian beam*, Opt. Eng. **40**, 1959-1962, (2001)
- [3] G.Marshall, *Laser Beam Scanning: opto-mechanical devices, systems, and data storage optics*, Marcel Dekker, New York (1985)

Appendix C1. Position Sensitive Diode

To measure position of a reflected beam, the deflectometer incorporates a Position Sensitive Diode (PSD) as the detector. A PSD is a three-layer silicon structure, closely resembling a conventional photodiode. It is operated in the reverse biased mode. As a result of the multiple connected resistive top and/or bottom layers this photodiode has a position sensing capability. When a light beam hits the surface of a PSD the photocurrent generated in the resistive layer is distributed to the contacts according to Ohm's law. When the resistive layer is homogenous, this distribution is related linearly to the distance between the incident beam and the contacts. Figure C1.1 shows the operation of one-dimensional PSD with two connections on the top layer.

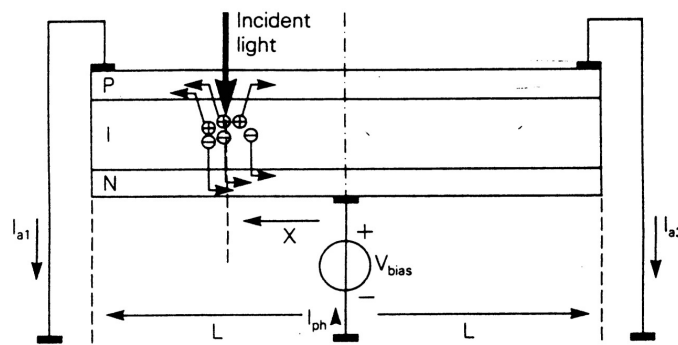


Figure C1.1. Cross-section of a one dimensional Positional Sensitive Diode [1].

A position x and light intensity I_{ph} of the incident beam are calculated as:

$$x = \frac{I_{a1} - I_{a2}}{I_{a1} + I_{a2}} \quad (\text{eq. C1.1})$$

$$I_{ph} = I_{a1} + I_{a2} \quad (\text{eq. C1.2})$$

with I_{a1} and I_{a2} currents at the electrodes.

The same principle can be applied to calculate position of an incident light for a two-dimensional detector. A schematic view of two-dimensional PSD is shown in figure C1.2. In this case, the second contact pair is connected to the bottom layer of the PSD. Using equation C1.1 for the second axis, the position of the incident light can be calculated for two axes simultaneously. Typically for PSDs, both measurement axes are perpendicular to each other so that the beam position on the surface is measured in Cartesian coordinates.

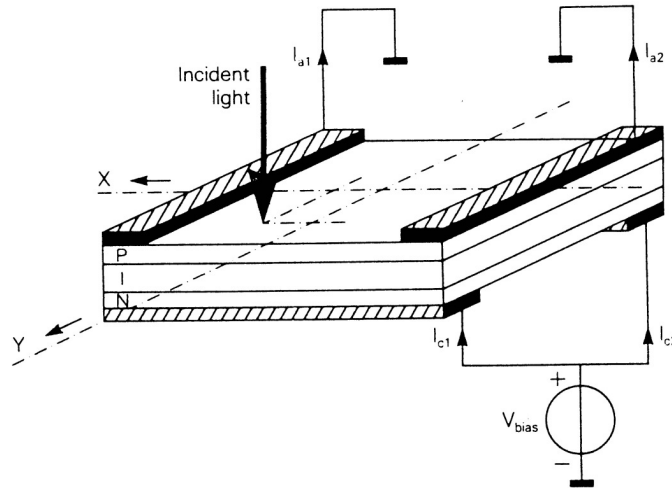


Figure C1.2. Schematic view of a two-dimensional Position Sensitive Diode [1].

The most meaningful PSD parameters for deflectometry-like systems are the measurement accuracy and the bandwidth. In principle, PSDs are very accurate and fast. Typically, both parameters are limited rather by sampling speed and noise of the driving electronics than by the PSD itself.

A high accuracy of a PSD is the result of high linearity (about 0.1 % over 80-90 % of the area [1]) and low signal-to-noise ratio, mostly limited by shot noise and thermal (Johnson) noise. Position accuracy of one part per million is claimed by manufacturers [2,3]. For well-designed circuits, PSD resolution of $1:10^4$ can be achieved easily.

Also the bandwidth of PSDs is high. Assuming a simple RC model, one could find the response time of a PSD (decribed as $1/\text{Bandwidth}$):

$$\tau = 2\pi C_j R_{\text{det}} \quad (\text{eq. C1.3})$$

With C_j the junction capacitance and R_{det} the sheet resistance.

More complex model of PSD operation exists - a so-called distributed RC-network [1, 4-6]. As stated by C.S. Kooijmans [1], by the rule of thumb, the bandwidth of a PSD is 10-times higher than as given by the RC model. In result, the PSD response time can be expressed by:

$$\tau = \frac{2\pi C_j R_{\text{det}}}{10} \quad (\text{eq. C1.4})$$

Since the junction capacitance is roughly proportional to the detector area, the response time can be defined more general as:

$$\tau = \Xi * A_{\text{PSD}} \quad (\text{eq. C1.5})$$

with Ξ the unite response time, expressed in s/m^2 and A_{PSD} the detector area. Substituting a typical values of $C_j = 1 \text{ pF/mm}^2$ and $R_{\text{det}} = 10 \text{ k}\Omega$ [2,3], one can find that $\Xi \approx 6 \cdot 10^{-3} \text{ s/m}^2$ and the unit bandwidth $B_{\Xi} = 160 \text{ Hz/m}^2$.

In practice, the response time is limited also by the PSD preamplifier. Including that factor, the response time of the complete PSD detection unit can be defined as:

$$\tau = \gamma_{\text{PSD}} * \Xi * A_{\text{PSD}} \quad (\text{eq. C1.6})$$

where $\gamma_{\text{PSD}} \geq 1$ defines the preamplifier quality.

References:

- [1] C.S. Kooijman, Position sensitive detectors, Philips Production Means, **5**, 12-17, (1989)
- [2] Pacific sensors, Web site: www.pacific-sensors.com
- [3] Sitek, Web site: www.sitek.se
- [4] M. de Bakker, *The PSD chip. High speed acquisition of range images*, PhD thesis, Technical University Delft, 2000
- [5] M. de Bakker, P. Verbeek, G. Steenvoorden, I. Young, *The PSD transfer function*, IEEE Transactions on Electron Devices, 49, 202-206, (2002)
- [6] C. Narayanan, A Buckman, I. Busch-Vishniac, W. Wang, *Position dependence of the transient response of a Position-Sensitive detector under periodic pulse light modulation*, IEEE Transactions on Electron Devices, 40, 1688-1694, (1993)

Appendix C2. Parabolic approximation of a sphere

Equation of the circular cross section of a sphere:

$$x^2 + (\Sigma - R)^2 = R^2 \quad (\text{eq. C2.1})$$

where the centre of the sphere C is shifted from the origin O by one radius R in the Σ direction (figure C2.1). After rewriting this as:

$$\Sigma^2 - 2\Sigma R + x^2 = 0 \quad (\text{eq. C2.2})$$

we can solve for Σ :

$$\Sigma = R \pm \sqrt{R^2 - x^2} \quad (\text{eq. C2.3})$$

After expansion in a binomial series:

$$\Sigma = \frac{x^2}{2R} + \frac{1x^4}{2^2 2! R^3} + \frac{1 \cdot 3x^6}{2^3 3! R^5} + \dots \quad (\text{eq. C2.4})$$

The corresponding deviation $\delta\Sigma$ is:

$$\delta\Sigma = \frac{x^4}{8R^3} + \frac{y^6}{16R^5} + \dots \quad (\text{eq. C2.5})$$

When R is relatively large in comparison to x , $\Sigma(x)$ can be approximated by the first contribution in the series in equation C2.4, which describes a parabolic function:

$$\Sigma \approx \frac{x^2}{2R} \quad (\text{eq. C2.6})$$

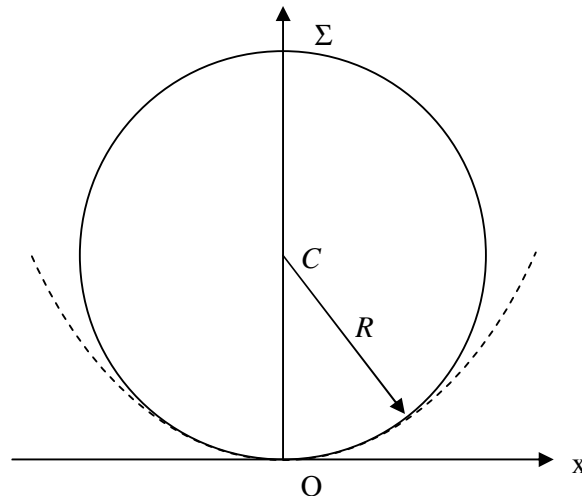


Figure C2.1. Comparison of spherical and paraboloidal surfaces.

Appendix C3. Estimation of scan lens quality from its high frequency aberrations

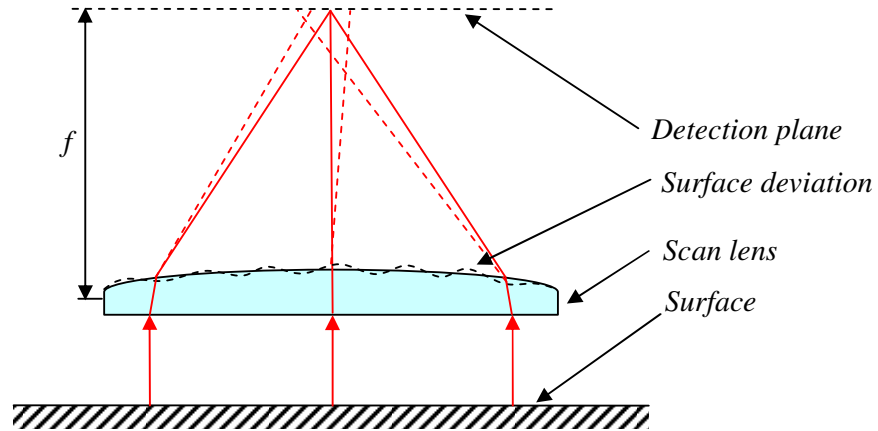


Figure C1. Simple model of lens imperfections introducing error into the slope information acquired by the deflectometer.

Snell's law for the tilted lens surface:

$$\frac{\sin(\theta_{glass} - A_i / \Lambda_i)}{\sin(\theta_{Air} - \Delta\sigma / 2)} = \frac{n_{Air}}{n_{Glass}} = 0.66 \quad (\text{eq. C1})$$

where A_i / Λ_i is the local slope on the lens surface and $\Delta\sigma$ the resulting error in the slope measurement (see figure 3.11).

Applying the small angle approximation ($\sin \theta = \theta$) we obtain:

$$A_i / \Lambda_i = 0.66\sigma_i \quad (\text{eq. C2})$$

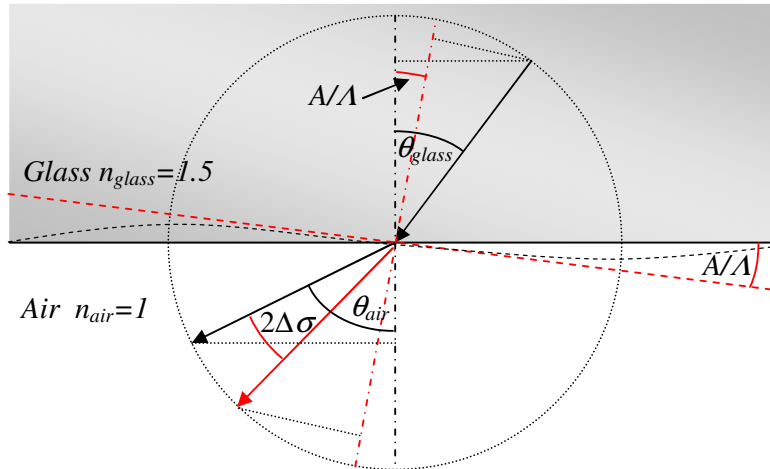


Figure C2. Refraction of a laser beam through a glass-to-air interface for varying angles of the glass surface. The solid black line indicates the nominal surface, the dashed red line indicates a local surface slope A/Λ introduced by surface waviness (dashed black curve) due to non-ideal polishing process. θ_G and θ_A indicate the incidence and the refraction angles for the nominal surface, and $2\Delta\sigma$ indicates the slope deviation from the nominal slope of the refracted beam.

Appendix D1. General consideration on the surface-scan strategy

In table D1.1 we compare some basic system parameters for the three systems. For the calculation, we assume a circular surface-under-test (wafer-like), the sampling distance is equal for both axes and the required measurement time T . The resulting scan efficiency is defined as the minimum number of samples used for reconstructing the surface over the total number of samples, which are acquired with a particular system.

Table D1.1 Comparison of the 3D-deflectometry performance for three different system configurations, with N_x , N_y number of samples in scan- and cross-scan axis respectively (in polar system, N_y corresponds to the rotational axis), $1/\tau_{\text{ADC}}$ data acquisition rate, ν optical scan frequency.

System type	N_x	N_y	Total # of samples	$1/\tau_{\text{ADC}}$	ν	Scan efficiency
Single stroke	N	N	N^2	N^2/T	N/T	78.5 %
Two strokes	$1.1N$	N	$1.1N^2$	$1.1N^2/T$	$2N/T$	~65 %
Polar	$0.5N$	πN	$\sim 1.6N^2$	$\sim 1.6N^2/T$	$\pi N/T$	50 %

Single-stroke Cartesian system

The most efficient 3D-deflectometry system (from the point of throughput) is represented by a single-stroke Cartesian scanning. In this approach the scan line must be at least as long as the object's width. The complete surface, thus, can be scanned in one go. This scan strategy is presented schematically in figure D1.1.

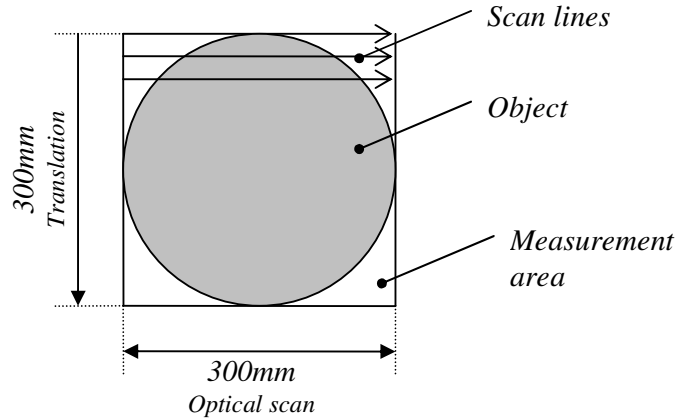


Figure D1.1. Scan strategy for the single-stroke Cartesian scan

The scan efficiency of the single-stroke Cartesian scan of a wafer-like area can be calculated as a ratio between the circular- and the square area:

$$\text{Efficiency} = \frac{\pi r^2}{(2r)^2} = \frac{\pi}{4} \approx 78.5\% \quad (\text{eq. D1.1})$$

Multiple-stroke Cartesian system

The multiple-stroke scan is similar to the single-stroke scan, but the complete surface is measured with at least two overlapping strokes (figure D1.2). In result, the obtained data must be stitched together during the post-processing. The focal length of such a system can be shorter than for a single-stroke system (when it is limited by aberrations level). In result a smaller and faster PSD can be used, and in result the measurement time can decrease (two times shorter focal length will lead to 4 times faster PSD!). Nevertheless, the complete system design is more complicated since an additional translation axis is needed to translate the object between the strokes and additional processing is required.

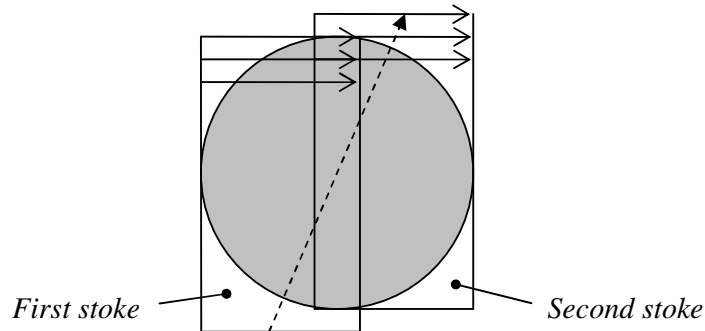


Figure D1.2. Scan strategy for the multiple-strokes Cartesian scan. In the figure two-strokes system is presented (offset between the strokes added for presentation reason).

The efficiency of the multiple-strokes scanning comparing to the single-stroke scanning will be decreased by the overlapping measurements. The overlap area will certainly depend on the required accuracy of the stitching algorithm. For example in interferometry, where the lateral stitching is commonly applied, about 20 % of overlap is assumed to give a satisfactory trade-off between stitching accuracy and measurement speed. However, the measured sub-fields in stitching interferometers are usually very small, with the number of samples per field limited by the CCD resolution. In deflectometry the measurement sub-fields and the number of samples are much larger; therefore much smaller overlap is required to achieve high stitching accuracy. We can safely estimate that performance of a stitching deflectometer would decrease by no more than 5 % in comparison to the single stroke system which leads to the scan efficiency of about 75 %.

Polar system

In contrast to the Cartesian systems, in polar scanning for a silicon wafer testing, only the area of interest is measured (discarding same additional over-scan for alignment). The optical scan is performed along the radius, and the complete surface is measured by rotating the object around its origin (figure D1.3). At first sight, such an approach seems to have higher efficiency as compared to the Cartesian systems. One can realize, however, that the tangential sampling distance will be a function of position across the scan line. In result the density of samples around the origin will be much higher than required, which will decrease the overall scan efficiency.

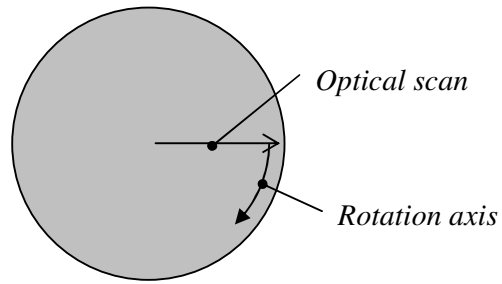


Figure D1.3. Polar scanning system

To calculate the scan efficiency we compare the real wafer area to the virtual rectangular area, which is virtually scanned during the polar scan:

$$Efficiency = \frac{\pi R^2}{2\pi R^2} = 50\% \quad (\text{eq. 4.2})$$

The benefit of a polar system is a small footprint of the instrument since no object translation is required. A polar system might be characterized by a shorter measurement time than a single-stroke Cartesian system (because a two-times smaller focal length is possible) but longer than for a stitching system (because of lower scan efficiency).

Appendix D2 Model of the surface response for an optical slope measurement

To find the correct spot size for the required measurement resolution, one should know the transfer function of the slope measurement by deflectometry. To find the transfer function we propose a first approximation model of the optical slope response. In the model we will approximate the beam by a bunch of parallel rays, weighted by intensity distribution. The intensity distribution is assumed to be Gaussian. The slope response will be calculated from the centre of gravity of all the reflected rays, incident on the detector. One can notice that the model is an extension of equation 3.1, where the finite dimension of the probing beam is included. As the result of the model, the slope response of a deflectometer is approximated by a convolution of the beam with the surface derivative.

We introduce the following assumptions:

1. The optical slope measurement represents a linear, time-invariant system (LTI) and can be considered separately for each coordinate of the measured slope. Hence, the model is simplified to the one-dimensional case.
2. The scanning spot on a surface has a normalized Gaussian intensity profile, described by:

$$\bar{G}(x) = \frac{4}{\sqrt{2\pi}d_0} e^{-8x^2/d_0^2} \quad (\text{eq. D2.1})$$

3. The diffraction effects, like the diffraction on the surface-under-test or the diffractive beam divergence, are neglected
4. The detector is ideal, with no restrictions on its accuracy, lateral range and bandwidth.
5. The measurement system is aberration free (paraxial approximation)

The basic formula describing a one-dimensional slope response of a deflectometer is given by equation 3.1. To extend the equation by a finite dimension of the beam, we substitute position of the reflected beam on the detector ξ by its centre of gravity ξ_{CGL} . The centre of gravity of intensity pattern is defined as the first moment M_1 divided by the total light intensity I_{total} . Using the fact that the total intensity of a normalized beam equals unity, the system's slope response can be written as:

$$\tilde{\sigma}(x) = \frac{\xi_{CGL}}{2f} = \frac{1}{2f} \frac{M_1(x, \xi)}{I_{total}(\xi)} = \frac{1}{2f} M_1(x, \xi) \quad (\text{eq. D2.2})$$

As we mentioned, in our model the beam is approximated rays, which are laterally displaced and intensity-weighted, accordingly to the beam shape and intensity pattern. Collectively, the reflected rays will produce a new intensity pattern on the detector, from which the first moment can be indicated as follows:

$$M_1 = \int_{-\infty}^{+\infty} \xi(x - x') \bar{G}(x') dx' \quad (\text{eq. D2.3})$$

Substituting the last equation into equation D.2.2, we obtain the response function of the deflectometer:

$$\tilde{\sigma}(x) = \frac{1}{2f} \int_{-\infty}^{\infty} \xi(x-x') \bar{G}(x') dx' \quad (\text{eq. D2.4})$$

where $\xi(x)$ is the deflectometers response for a single ray. The transition from the first moment M_1 to a convolution integral needs a bit deeper explanation. In the equation, we assumed a simple ray-tracing operation; the incident beam is approximated by a bunch of infinitely narrow rays. The intensity of each ray is weighted by the corresponding irradiation distribution of the beam $\bar{G}(x-x')$ with x' the running variable across the surface-under-test. Therefore, position of each ray ξ in the detector plane is a function of its position on the object $x-x'$.

Due to infinitely small diameter of a ray, the system response for a single ray $\xi(x)/2f$ is equal the exact surface-derivative; therefore $\xi(x)$ in equation D2.2 can be substituted by $\sigma(x)$. Hence the deflectometer response is:

$$\tilde{\sigma}(x) = \frac{1}{2f} \int_{-\infty}^{\infty} \sigma(x-x') \bar{G}(x') dx' = \frac{1}{2f} \sigma(x) \otimes \bar{G}(x) \quad (\text{eq. D2.3})$$

As one could expected, in first approximation, the deflectometer's response is a convolution of the beam profile with the surface, multiplied by the deflectometer's scaling factor $1/2f$. From the theoretical response $\tilde{\sigma}(x)$, we can derive the frequency transfer function of the deflectometer. A system transfer function $H(k)$ is defined as the Fourier transform of a system impulse response $h(x)$, which is the response of the system for the Dirac delta function $\delta(x)$:

$$H(k) = F[h(x)] \quad (\text{eq. D2.4})$$

Since we are investigating the slope response, δ describes the impulse slope. In result, the transfer function of the slope measurement is the convolution of the beam with the delta function:

$$h(x) = \frac{1}{2f} \bar{G}(x) \otimes \delta(x) = \frac{1}{2f} \bar{G}(x) \quad (\text{eq D2.5})$$

The last equation gives an interesting result, implying that the deflectometer's response for the impulse slope (which approximates the slope of an infinitely steep surface) is equal to the intensity profile of the beam itself. In result, the transfer function is also represented by a Gaussian distribution.

Appendix D3. Surface finish considerations for deflectometry

In deflectometry a flatness deviation is measured by applying the law of reflection to a laser beam, incident on a surface. With this approach the beam is approximated by a single ray, since the angular deviations of the deflected beam are measured from the centre of gravity of its intensity pattern.

One must realize, however, that the law of reflection is only a specific case of interaction between a light beam (electromagnetic radiation) and a surface. The reflected beam is the summation of a huge number of scatter components that are similar in direction, phase, and frequency. Hence, the law of reflection is merely a statistical result that is true only in an average sense, and depends heavily on the material and the surface preparation. A fluctuation of surface homogeneity will result in a scatter, viewed out of a specular beam; in extreme case (which is actually the most common in nature) the reflected beam practically cannot be detected since the intensity pattern of the scattered light is diffused over a large angle. Such surfaces cannot be inspected with metrology tools, like deflectometry. Therefore, to make use of the law of reflection, a special finishing of a surface is required, which must lead to a so-called smooth surface. In general, a surface can be considered as optically smooth, when the height variations are small as compared to the wavelength of light. This assumption is almost always true for optical, well polished surfaces, particularly of polished silicon wafers.

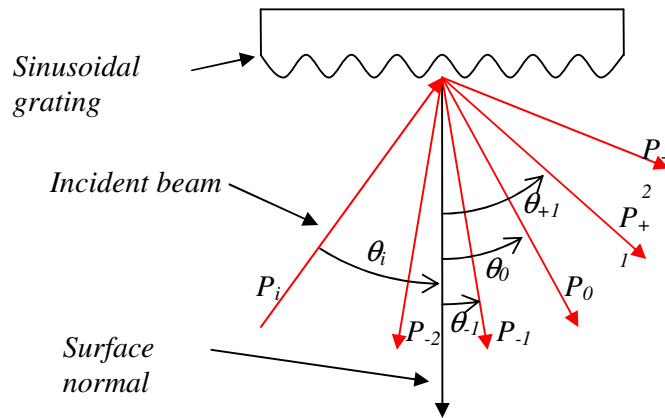


Figure D3.1. Diffraction from a sinusoidal grating.

A special case of surface scattering from a smooth, reflective surface is when the surface has a periodic structure. In result, a diffraction pattern containing multiple beams, deflected at various angles is observed in the scattered light, instead of a single-reflected beam. Some of those surfaces, however, could still be inspected with deflectometry. For a simple explanation of the last statement, we will consider diffraction on a smooth surface with a single-frequency, sinusoidal pattern; the sinusoidal grating. The grating is described by the height variation:

$$\Sigma(x) = A \sin(2\pi k_g x + \alpha) \quad (\text{eq. D3.1})$$

where A is the height amplitude, $k_g=1/\Lambda_g$ is the grating wavenumber, with Λ_g the distance between peaks on the grating, and α is an arbitrary constant that describes the location of the grating, relative to $x = 0$. Hence, locations of the diffracted orders are given by:

$$\sin \theta_n = \sin \theta_i + nk_g \lambda \quad (\text{eq. D3.2})$$

with θ_i the of incidence and θ_n deflection angles. The meaning of the last equation is explained schematically in figure D3.1.

The location of the diffracted beams is independent on the grating amplitude or the light power. The diffraction pattern however, does depend on the angle of incidence (or grating tilt θ_i) and on the grating period, which properties have an important consequence for deflectometry. Firstly, they imply that the slope information from a surface can be retrieved, even if there is a grating-like structure superimposed on the general topography. The surface slope can be measured just as for a single beam, but choosing one of the diffraction orders. To perform such a measurement, however, some additional requirements must be met. Namely, the slope can be measured properly only if either all detectable diffraction orders giving contribution to the centre of gravity of the diffraction pattern lie on the detector, for the full angular range of the slope measurement, or if the first-order diffracted beams fall outside the detector for the full slope range. In other words, the diffraction orders must have much lower- or much larger angular spread as compared to the detector-size limited slope range of the deflectometer. Hence, in practice, there is a certain surface-frequency window for surfaces containing periodic structures, for which surface topography can/cannot be measured by deflectometry. It is a very important conclusion since periodic structures are often introduced by producing various IC structures on a silicon wafer.

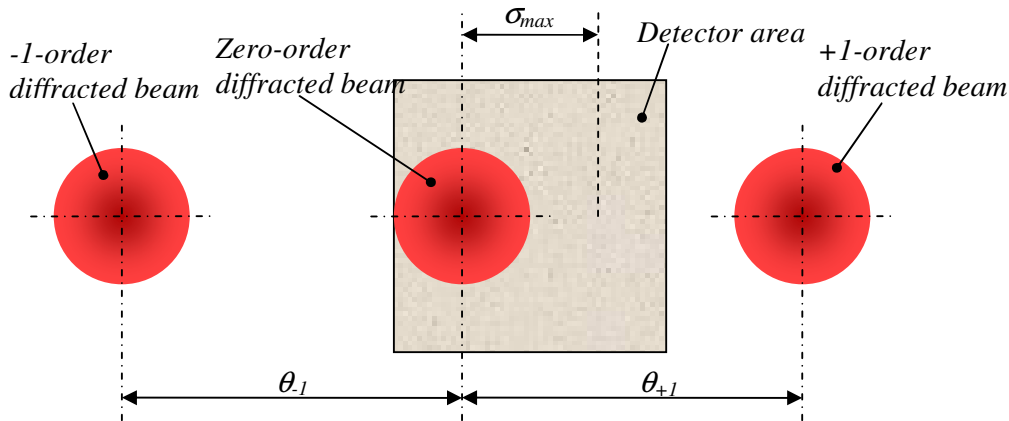


Figure D3.2. A boundary condition for a deflectometrical slope measurement of diffractive surface structures, with σ_{\max} the detector size limited slope range of the deflectometer and $\theta_{\pm 1}$ the diffraction angle of the first order diffracted beams.

To give an insight into a practical application of those criteria, we will calculate the boundary condition for the grating-period, where the first-order diffracted beams fall outside the detector. Thus we will assume the incident beam normal to the surface, 2 mrad of the deflectometer's slope range, and a $\lambda = 670$ nm laser. By a rule of thumb we will define the boundary condition for the diffraction, such that the $\theta_{\pm 1}$ is 2.5 times larger that the slope range. Such configuration should guarantee that the first the location of the zero-order beam

is measured precisely by the detector. This is explained schematically in figure D3.2. Following equation D3.2 one would find that the diffraction-spread criterion is met when the grating has period of $\Lambda_g \leq 100 \mu\text{m}$. In the example we assumed that the beam size is d_0 is half of the detector size, which is in agreement with the discussion about the fundamental limits for deflectometry in chapter 1.5.

On our example, however, one must be aware that the spot size is an important parameter, which we did not include so far. In order to have diffraction from a grating, the spot size must be larger than the grating period. By a rule of thumb, in order to have a well defined diffraction from a grating, the spot size must be three to five times larger than Λ_g . Otherwise, the diffraction pattern will not be present, or the beam truncation on the grating will give rather strange diffraction patterns. This is not a problem, when the beam on the detector is very small, thus the centre of gravity is well defined even for strongly distorted intensity pattern. When the beam is relatively large, however, its shape distortion can introduce significant errors to the measured centre of gravity. In figure 4.7 we show several examples with an influence of the surface structure on the scattered beam. In the example we used a patterned silicon wafer as test surface, and a 670 nm wavelength laser beam, with spot size on the surface of about $d_0 = 150 \mu\text{m}$.

References:

- [1] J. Schmit, J. Wyant, *Large field of view, high spatial resolution surface measurement*, Application Note AN504, Veeco Instruments, Inc, www.veeco.com
- [2] E. Hecht, *Optics*, Addison Wesley; 4th edition (2001)
- [3] J.C. Stover, *Optical scattering: measurement and analysis*, SPIE; 2nd edition (1995)

Appendix D4 Derivation of the basic scan requirement formula

To derive a basic scan requirement in Fast Optical Scanning deflectometer, we assume that the measurement speed should be limited rather by the slope measurement than the scanning system. Therefore, we will compare the velocity of the scanning beam due the scanning and slope measuring.

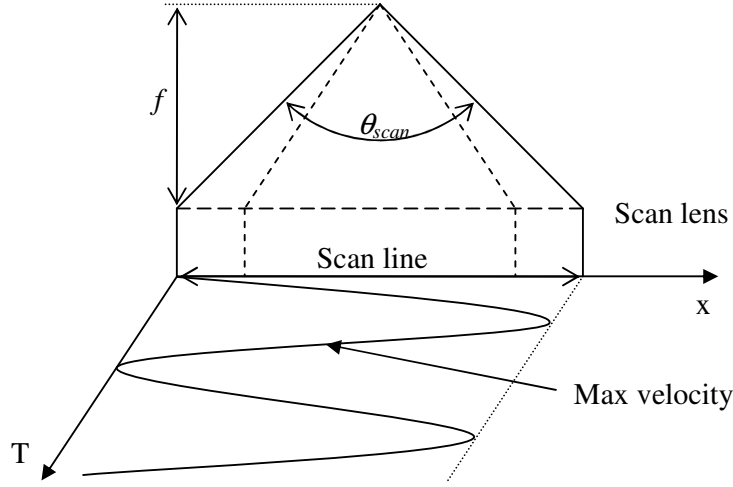


Figure D4.1. Schematic explanation of the optical scan velocity distribution in 3D-deflectometry.

Velocity of the scan beam due to the slope measurement is simply:

$$V_{scan} = \frac{\Delta x}{\tau_{ADC}} \quad (\text{eq. D4.1})$$

with Δx step size (sampling distance) and τ_{ADC} step time of the A/D converter. The equation can be also written in more elegant form:

$$V_{scan} \approx 1.4 \frac{d_0}{\tau} \quad (\text{eq. D4.2})$$

with d_0 the spot size of the scanning beam and τ the response time of the detector. In the equation we assumed the sampling distance $\Delta x = 1/4 * d_0$ and $\tau_{ADC} = 1/5.5 * \tau$, which results from equation 4.5.

To calculate the scan velocity due to the optical scanning we define the formula for spot position of the beam on the surface-under-test:

$$x = f \frac{\theta_{scan}}{2} \sin(2\pi \nu t) \quad (\text{eq. D4.3})$$

with x position of the spot along the scan line, f the focal length of the objective, θ_{scan} full scan angle of the deflector, and ν the scan frequency in Hertz. In the equation, we assume a sinusoidal scan of the scanning mirror. Hence:

$$V_{scan} = \frac{dx}{dt} = 2\pi \nu_{scan} f \frac{\theta_{scan}}{2} \cos(2\pi \nu t) \quad (\text{eq. D4.4})$$

Since for the maximum scan beam velocity corresponds to $\cos(2\pi\nu t) = 1$, thus:

$$\max V_{scan} = \pi v_{scan} f \theta_{scan} \quad (\text{eq. D4.5})$$

Finally, the basic requirement for the scanning system:

$$\pi v_{scan} f \theta_{scan} \geq 1.4 d_0 / \tau \quad (\text{eq. D4.6})$$

Appendix D5 Translation speed of the 3D-deflectometer

Translation speed can be calculated using from the step size in the cross-scan direction and the optical scan time for a single line:

$$V = \frac{\Delta x}{\tau_{line}} \quad (\text{eq. D5.1})$$

with

$$\tau_{line} = N\tau_{ADC} = \frac{L}{\Delta x}\tau_{ADC} \quad (\text{eq. D5.2})$$

Substituting the last equation into D5.1:

$$V = \frac{\Delta x^2}{L\tau_{ADC}} \quad (\text{eq. D5.3})$$

The equation D5.3 can be expressed with the basic parameters. Following the general sampling-rule (eq. 4.5):

$$V = \frac{0.34d_0^2}{L\tau} \quad (\text{eq. D5.4})$$

Appendix D6 Measurement time of the 3D-deflectometer

In most general, the measurement time of a 3D-deflectometer is:

$$T = \frac{1}{\chi} N \tau_{ADC} \quad (\text{eq. D6.1})$$

with χ the duty cycle, N the number of samples, τ_{ADC} step time of the A/D converter. Solving the parameters in the equation:

$$\tau_{ADC} = \frac{\tau}{5.5} \approx 0.18 \gamma \Xi A_{PSD} \quad (\text{eq. D6.2a})$$

where γ is the electronics-quality factor and Ξ is a unit response time of the detector, expressed in [s/m²] (Appendix C1). Following equation 4.5 we have assumed the 5.5-fold over-sampling upon the lateral resolution.

The detector area:

$$A_{PSD} = (d_f + 2\xi_{\max})^2 = \left(\frac{4\lambda f}{\pi d_0} + 4f\sigma_{\max} \right)^2 = 16f^2 \left(\frac{\lambda}{\pi d_0} + \sigma_{\max} \right)^2 \quad (\text{eq. D6.3a})$$

with d_f beam size on the detector; ξ_{\max} maximum displacement amplitude on the detector; σ_{\max} the maximum amplitude of the measured slope.

The number of samples:

$$N = \frac{A}{(d_0/4)^2} = 16 \frac{A}{d_0^2} \quad (\text{eq. D6.4a})$$

with A the area of the surface-under-test, and where four-times over-sampling upon the spot size $\Delta x = d_0/4$ has been assumed.

Substituting equations 6.2a-6.4a into equation 6.1, one obtains the measurement time formula:

$$T = 46 \frac{A}{d_0^2} \left(\frac{\lambda}{\pi d_0} + \sigma_{\max} \right)^2 \frac{\gamma}{\chi} \Xi f^2 \quad (\text{eq. D6.5a})$$

In table D1 we give the result to calculate the measurement time for a 3D-deflectometer with the following specification:

$$A = 0.09 \text{ [m}^2\text{]} \text{ (300mm Si wafer)}$$

$$f = 0.5 \text{ [m]}$$

$$\lambda = 405 \cdot 10^{-9} \text{ [m]}$$

$$d_0 = 75 \cdot 10^{-6} \text{ [m]}$$

$$\Xi = 6 \cdot 10^{-3} \text{ [s/m}^2\text{]}$$

The measurement time for an idealized system, ($\gamma_{PSD} = 1$ and $\chi = 1$) and a realistic system ($\chi = 0.5$, $\gamma_{PSD} = 2$), for various spot sizes is shown in figure D1.

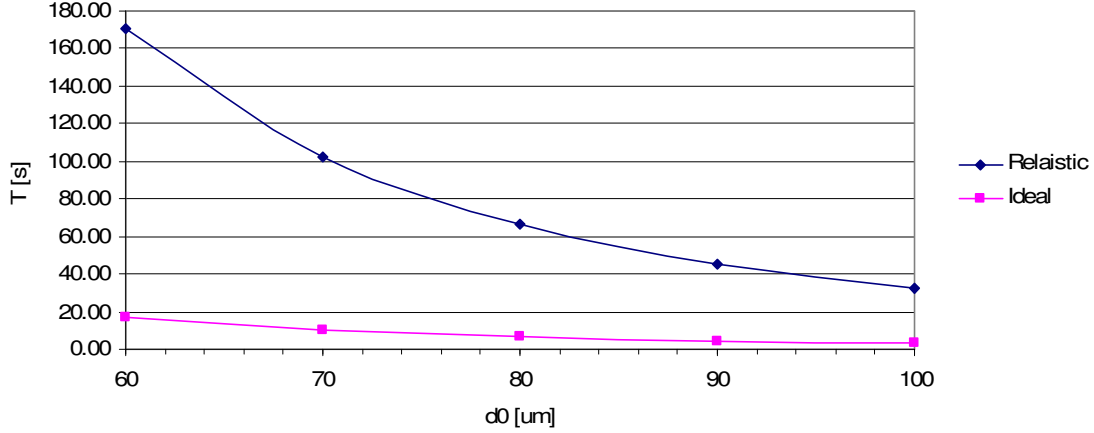


Figure D1. Measurement time of the 3D deflectometer for an ideal and realistic performance of the deflector and PSD electronics.

In chapter 4.5 we discuss an alternative design of the deflectometer, which we call the technology tuning. In result of this improved design we define a new set of equations. Hence, the new equation for the A/D conversion step size becomes:

$$\tau_{ADC} = \frac{1}{4} \tau = \frac{1}{4} \gamma \Xi A_{PSD} \quad (\text{eq. D6.2b})$$

with:

$$A_{PSD} = (2\xi_{\max})^2 = 16f^2\sigma_{\max}^2 \quad (\text{eq. Db6.3})$$

The new equation for the number of samples:

$$N = \frac{A}{(d_0/4)(d_0/2.3)} = \frac{9.2A}{d_0^2} \quad (\text{eq. D6.4b})$$

Finally, the measurement time:

$$T = 37 \frac{A}{d_0^2} \frac{\gamma}{\chi} f^2 \sigma_{\max}^2 \Xi \quad (\text{eq. D6.5b})$$

Table D2 The measurement time of the 3D-deflectometer for different system parameters

A_{SUT} (mm)	d_0 (μm)	λ (μm)	γ_{PSD}	χ	Ξ (s/m ²)	f (m)	T (s)
0.09	75	0.405	1	1	0.06	0.5	9
0.09	75	0.405	2	0.2	0.06	0.5	86
0.09	100	0.405	2	0.2	0.06	0.5	48
0.09	140	0.405	2	0.2	0.06	0.5	25
0.09	180	0.405	2	0.2	0.06	0.5	15

Appendix D7 Model of the large-beam detection

The model is based on measuring the centre of gravity of light incident on a position sensitive detector. It is based on the following assumptions:

- The detector response is constant across its aperture
- The beam has an ideal Gaussian profile with constant shape and size

The centre of gravity is defined as the first moment divided by the total area. Figure D7.1 presents schematically the location of the centre of gravity of an arbitrary intensity pattern (irradiance), which we call the centre of gravity of light (CGL), described by spatial coordinates ξ_c, η_c in the detection plane.

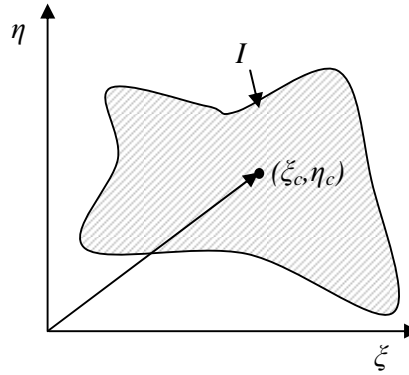


Figure D7.1. Centre of gravity of intensity pattern

Solving the x- and y-coordinate of the centre of gravity:

$$\xi_c = \frac{\int_{-\infty}^{\infty} \xi' I(\xi - \xi') d\xi'}{\int_{-\infty}^{\infty} I(\xi - \xi') d\xi'}, \quad \eta_c = \frac{\int_{-\infty}^{\infty} \eta' I(\eta - \eta') d\eta'}{\int_{-\infty}^{\infty} I(\eta - \eta') d\eta'} \quad (\text{eq. D7.1})$$

Figure D7.2 shows one-dimensional intensity distribution of a “large” Gaussian beam, incident on a finite-dimension detector. In the figure we indicate the location of CGL of the beam and centre of gravity of light on the detector (CGD). One can notice that CGL and CGD are at different locations.

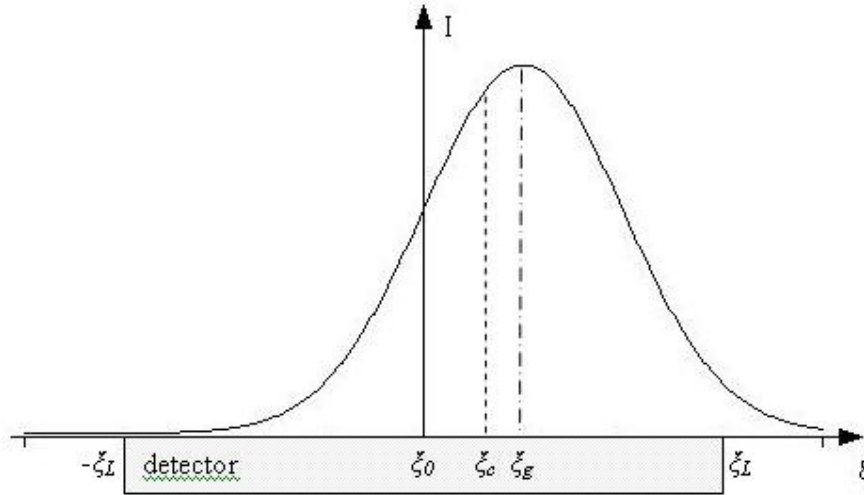


Figure D7.2. Large Gaussian beam incident on a position sensitive detector (one dimensional model): $(-\zeta_L, \zeta_L)$ detector length ; ζ_g centre of gravity of the beam; ζ_c the centre of gravity of the light incident on the detector.

Knowing the location of CGD, the detector aperture $[-\zeta_L, \zeta_L]$ and the beams size D , the location of CGL can be calculated as:

$$\xi_c = \frac{\int_L \xi G(\xi - \xi_g) d\xi}{\int_L G(\xi - \xi_g) d\xi} \quad (\text{eq. D7.2})$$

with G Gaussian intensity distribution and with simplified notation of the integrals

$$\int_L d\xi \equiv \int_{-\zeta_L}^{\zeta_L} d\xi$$

Analogically, to the one-dimensional case, figure D7.3 shows a two-dimensional model of a “large” Gaussian beam, incident on a 2D finite-dimension detector.

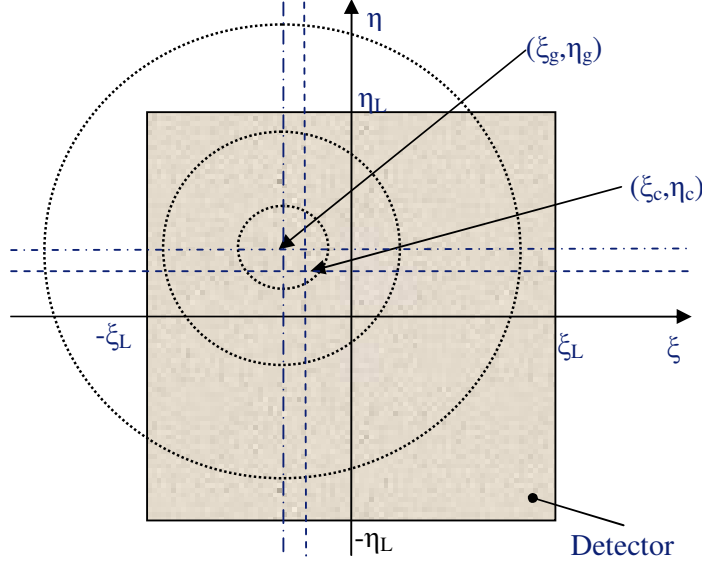


Figure D7.3. Two-dimensional intensity distribution of a Gaussian beam. Position of the beam's centroid is represented by (ξ_g, η_g) coordinates, position of centre of gravity of the light incident on the detector is given by (ξ_c, η_c) coordinates.

For two-dimensional case, location of CGL can be calculated as:

$$\begin{pmatrix} \xi_c \\ \eta_c \end{pmatrix} = \frac{\int_L \int_M \begin{pmatrix} \xi \\ \eta \end{pmatrix} G \begin{pmatrix} \xi - \xi_g \\ \eta - \eta_g \end{pmatrix} d\xi d\eta}{\int_L \int_M G \begin{pmatrix} \xi - \xi_g \\ \eta - \eta_g \end{pmatrix} d\xi d\eta} \quad (\text{eq.D7.3})$$

Applying the last equation to a single axis ξ , one can find:

$$\xi_c = \frac{\int_L \int_M \xi G \begin{pmatrix} \xi - \xi_g \\ \eta - \eta_g \end{pmatrix} d\xi d\eta}{\int_L \int_M G \begin{pmatrix} \xi - \xi_g \\ \eta - \eta_g \end{pmatrix} d\xi d\eta} = \frac{\int_L \xi G(\xi - \xi_g) d\xi \int_M G(\eta - \eta_g) d\eta}{\int_L G(\xi - \xi_g) d\xi \int_M G(\eta - \eta_g) d\eta} = \frac{\int_L \xi G(\xi - \xi_g) d\xi}{\int_L G(\xi - \xi_g) d\xi} \quad (\text{eq. D7.4})$$

The last equation shows that the location of CGD of a Gaussian beam for a single axis is independent on the beam displacement along the second axis. This linear property of the position detection system is very important for any real application, since it implies that the detector axes can be calibrated independently. Furthermore, the single-axis coordinate ξ_c , calculated from the two-dimensional model (eq. D7.4) is identical to ξ_c calculated from the one-dimensional model (eq. D7.2). Hence, we can use a simple one-dimensional model for further modelling of the LBD response.

Appendix D8 Experimental set-up for investigation of the large beam detection (LBD)

To evaluate the PSD displacement response for LBD, we move a “large” laser beam across the PSDs surface and we measured its position response signal. We choose a 4x4mm PSD for test, since it is very well suited for FOS application because high bandwidth and very high displacement resolution.

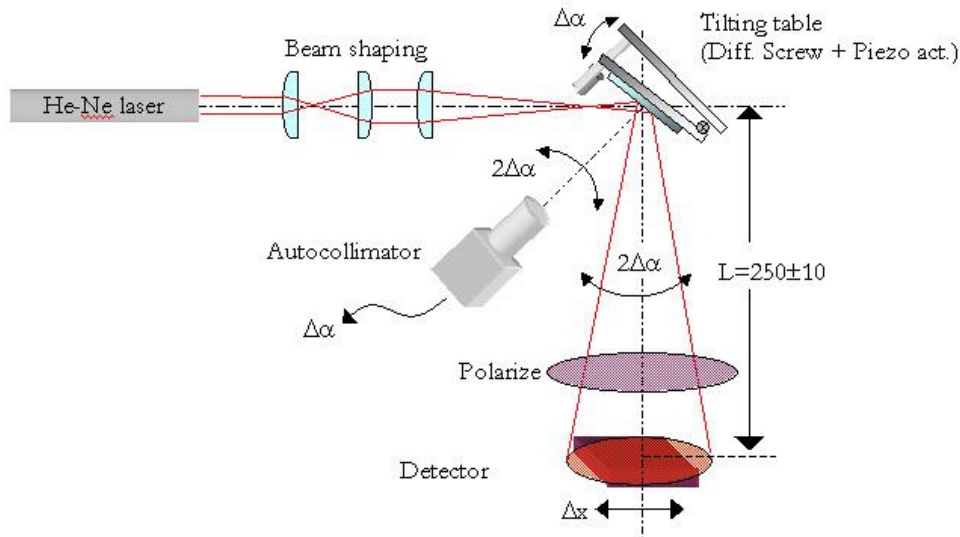


Figure D8.1. Experimental set-up. The angle variation $\Delta\alpha$ of the tilting mirror produces a beam displacement Δx at the object.

In the experiment we use the set-up shown schematically in fig 4.12. In the set-up the beam displacement on the detector is produced by changing the angle α of the tilting mirror. To change the angle of the mirror, we fix it to the tilting table. The tilt of the table can be changed by a differential screw or a piezo-actuator. Using the piezo-element gives much higher angle resolution than with the differential screw, but much lower angle range. Thus, our set-up can reach a tilt range of the mirror of $\Delta\alpha_{\max} > \pm 5$ mrad (using the differential screw) and the tilt resolution of $\Delta\alpha_{\min} < 1$ μ rad (using the piezo element). To measure tilt of the mirror we use an autocollimator. Our autocollimator measures angle in arc sec, thus we will use this dimension for further discussion (1 arc sec ≈ 0.2 μ rad). For adjusting the light intensity level at the detector, we use a polarizer, located a few centimetres from the detector surface.

We used two different beam sizes on the PSD: $d_0 = 4.3$ mm and $d_0 = 6.8$ mm.

Displacement sensitivity of the set-up was measured using an autocollimator and the PSD itself. For this reference measurement the beam size on the detector was only $d_{\text{det}} = 94$ μ m. The result of the measurement is given in figure 8.2, from which we estimate the sensitivity of $s_{\text{setup}} = 11.3$ mV/arc sec (2.26 μ m/arc sec).

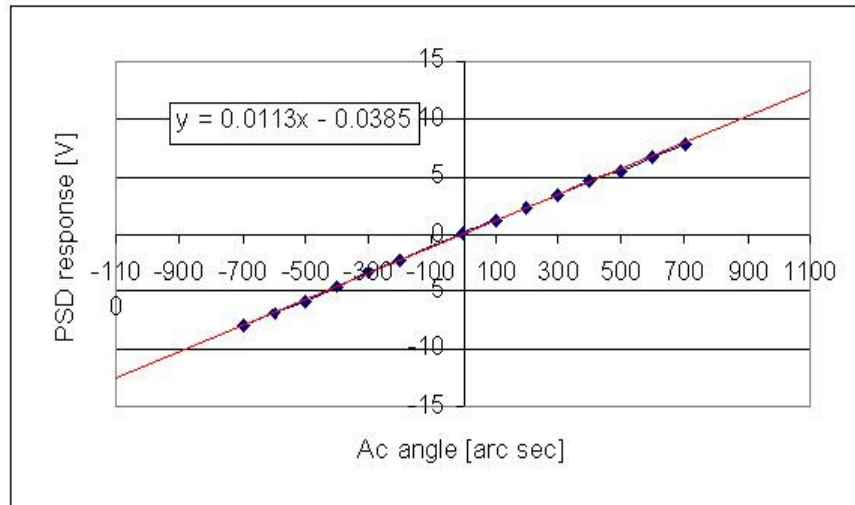


Figure D8.25. 4 x 4 mm PSD response for change of the tilting mirror's angle, with the spot on PSD $d_0 = 94 \mu\text{m}$.

Appendix D9 Experimental evaluation of the displacement response for LBD

The purpose of the displacement response experiment is to measure a real signal-to-slope sensitivity of a PSD, used in a “large beam detection” configuration (figure D9.2) as compared to theoretical predictions (figure D9.1). This should enable us to make a proper choice for detector type (size) for the high-resolution deflectometer.

In the experiment we use a 4 x 4 mm PSD with two “large” beams with $d_{\text{det}} = 4.3$ mm and $d_{\text{det}} = 6.8$ mm, where d_{det} is the beam size on the detector. The theoretical sensitivity at zero are 0.73 and 0.38 of the “small beam” sensitivity, for $d_{\text{det}} = 4.3$ mm and $d_{\text{det}} = 6.8$ mm, respectively.

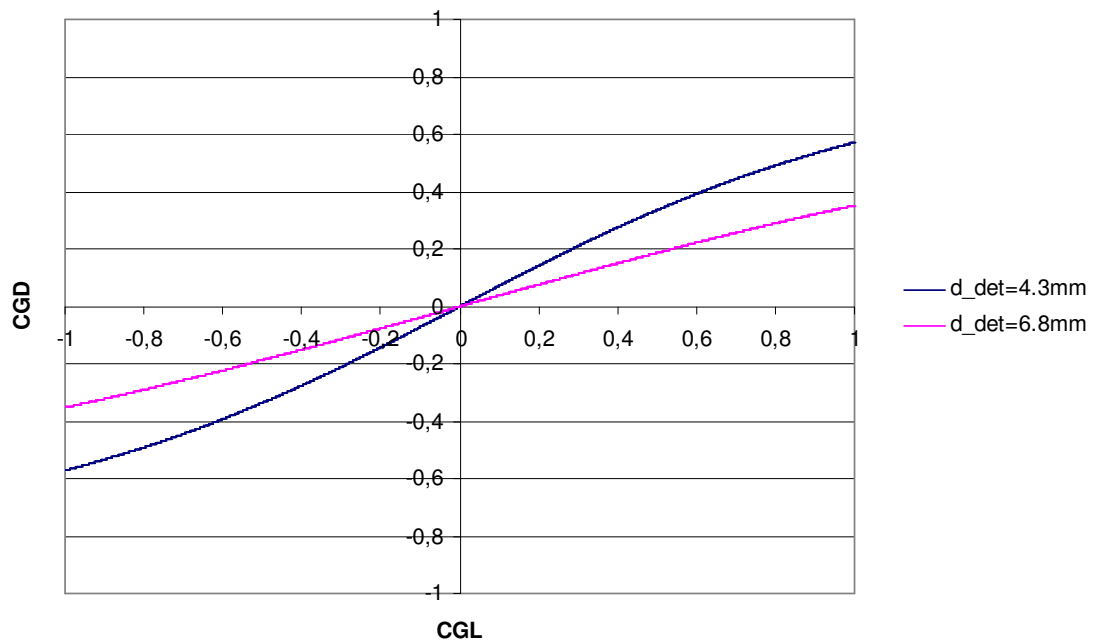


Figure D9.1. Theoretical displacement response of 4 x 4 mm PSD for $d = 4.3$ mm and $d = 6.8$ mm beams.

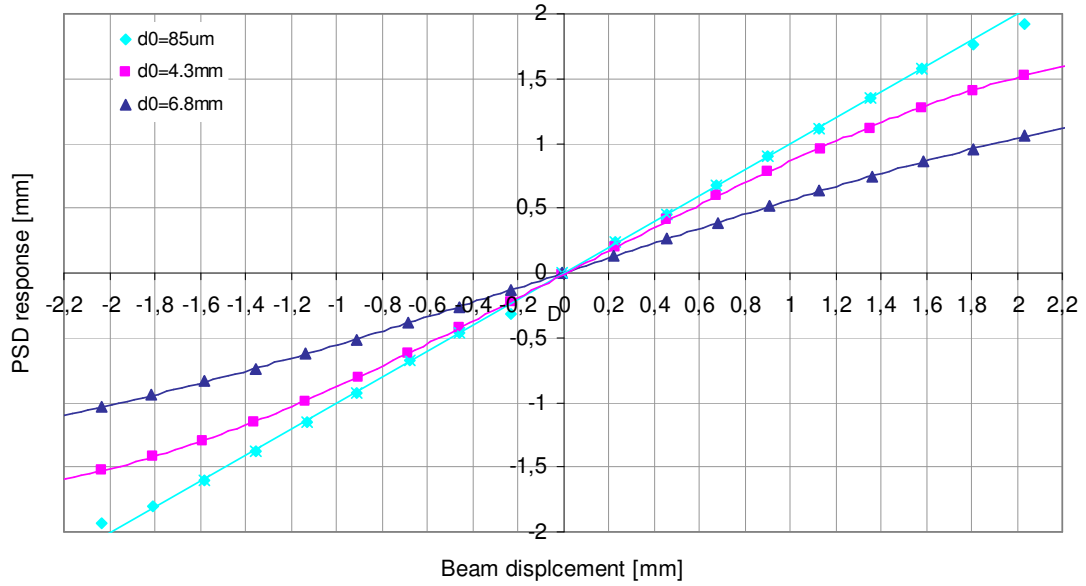


Figure D9.2. 4 x 4 mm PSD displacement response

In figure D9.3 we show the difference between the 3rd order polynomial fit and the measured values. This gives a very good approximation of the response by the fit, with the RMS residue of only 6.6 μm and 2.2 μm for 4.3 mm and 6.8 mm beams, respectively. The sensitivity at zero is calculated from the derivative of the polynomial fit. The measured responses are 0.909 and 0.573 for 4.3 mm and 6.8 mm beams, respectively.

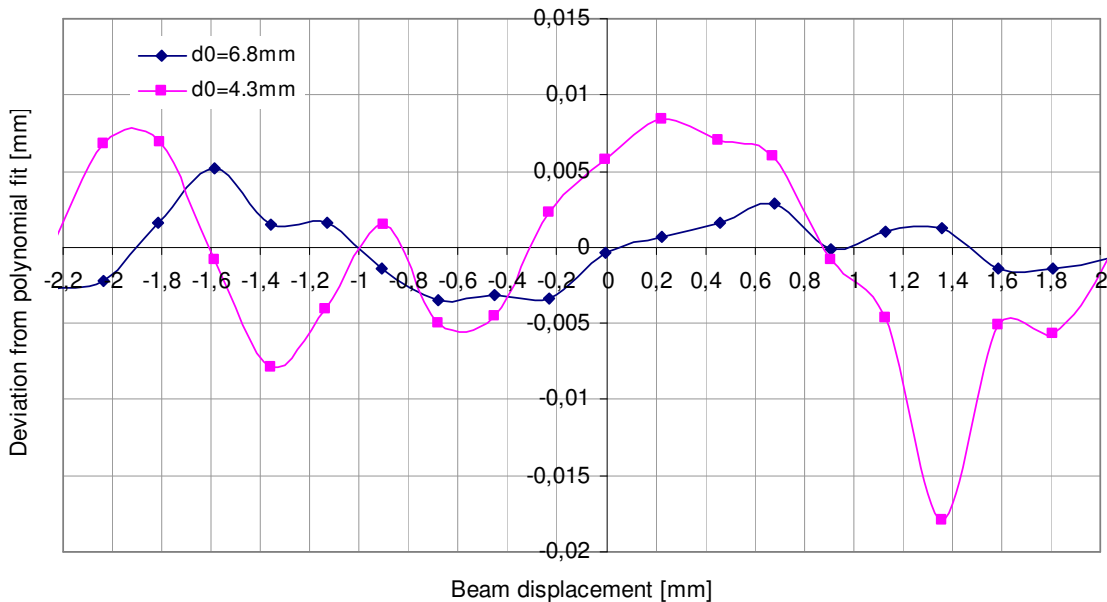


Figure D9.3. Residue of the 3rd order polynomial fit on the LBD response measurement points

Appendix D10 Experimental evaluation of the displacement resolution for LBD

In this experiment we check the resolution of PSD in LBD mode, using a very small beam displacement. In the experiment we use the set-up described in appendix D8. Using a piezo-actuator we can produce beam displacement on the PSD of about $0.5\ \mu\text{m}$, which for $4 \times 4\ \text{mm}$ PSD corresponds to the resolution of 1:8000. A total displacement range is about $22\ \mu\text{m}$, consisting of 50 steps. The time interval between steps is 1 second, and the number of samples acquired for each step is 50. Figure D10.1 shows the mechanical tilt variation of the mirror, which we use to produce a beam displacement on PSD. The angle was measured using an autocollimator.

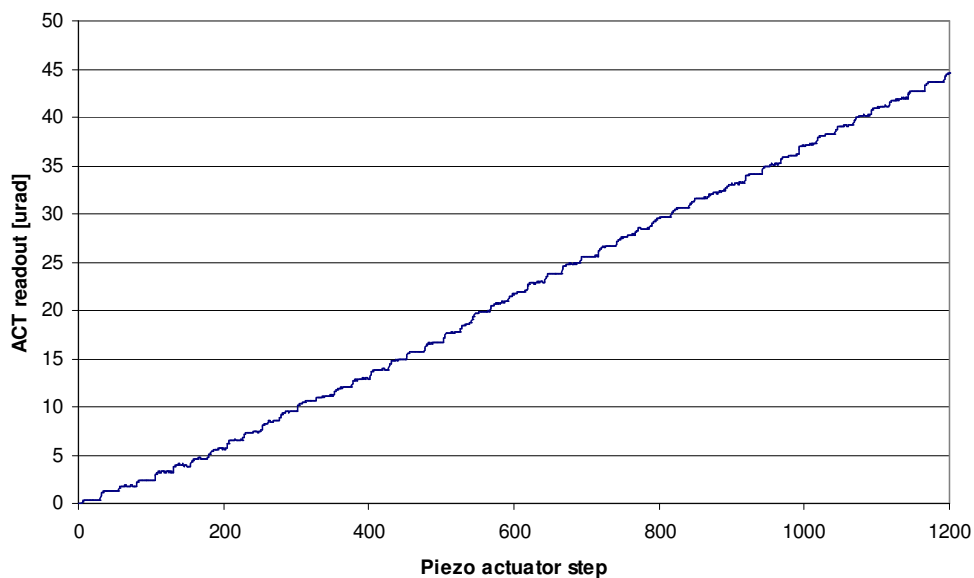


Figure D10.1. Autocollimator's response. Horizontal axis represents number of acquired samples; vertical axis represents angle variation.

Result of the resolution experiment is presented in figure D10.2. To reduce the influence of the environmental noise the PSD response for each step has been averaged.

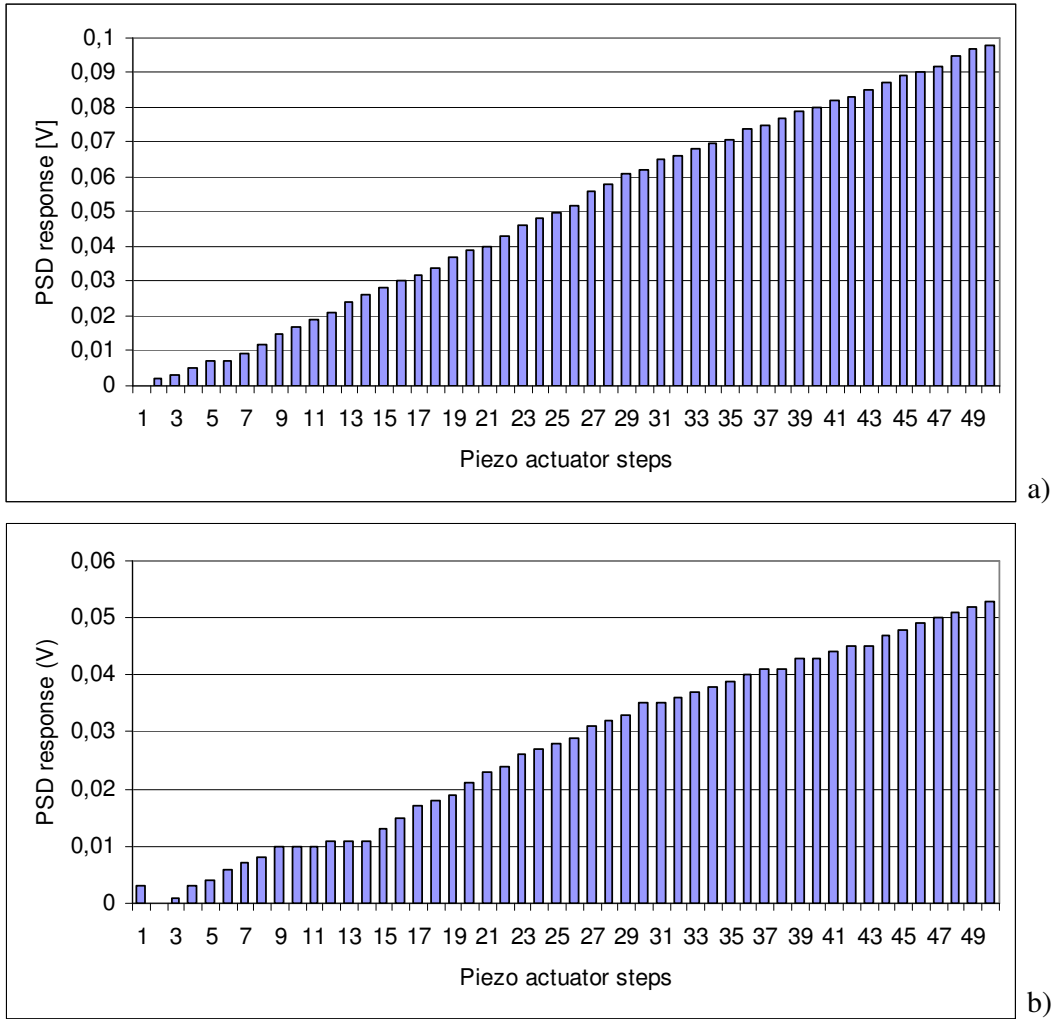


Figure D10.2. Averaged displacement response of 4 x 4 mm PSD for the $d_{det} = 6.8$ mm beam (a) and $d_{det} = 4.3$ mm beam (b). The upper graphs show the direct response; the lower graphs show the averaged response. The beam displacement for each step is less than $0.5 \mu\text{m}$; number of samples per step: 50; time interval between steps: 1 sec.; total number of steps: 50.

The response curves exhibit strong deviations from linearity, which is due the mechanical drift, and air turbulence in the lab room, which was checked by repeating the measurement and comparing the results.

Appendix D11 Derivation of the deflectometer resolution formula

Lateral resolution of a scanner described by the number of pixels N per scan line is:

$$N = L / \Delta \bar{x} d_0 \quad (\text{eq. D11.1})$$

with L scan length and $\Delta \bar{x}$ sampling distance normalized to the spot size d_0 on the surface-under-test.

Through the diffraction theory, the spot size d_0 can be linked with the aperture of the deflector:

$$d_f = f\theta = f \frac{4\lambda}{\pi d_0} \quad (\text{eq. D11.2})$$

where we applied formula:

$$d_0 = \frac{4\lambda}{\pi\theta} \quad (\text{eq. D11.3})$$

On the other hand d_f can be described by the detector aperture D_{defl} :

$$d_f = D_{defl} a^{-1} \quad (\text{eq. D11.4})$$

with a truncation factor a of the deflector.

Combining E11.2-E11.4:

$$d_0 = \frac{4\lambda f a}{\pi D_{defl}} \quad (\text{eq. D11.5})$$

Typically $a = 1.7-2$ in order to obtain a Gaussian distribution of a beam (truncation criterion [1]). Combining eq. D11.1 with D11.5, and taking $a = 2$ for more flexibility for the detector adjustment, we obtain a scan resolution formula:

$$N = \frac{\pi L}{4 f} D_{defl} \frac{1}{\lambda a \Delta \bar{x}} \quad (\text{eq. D11.6})$$

Another useful forms of this equation:

$$N = \theta_{scan} D_{defl} \frac{0.4}{\lambda \Delta \bar{x}} \quad (\text{eg. D11.7})$$

or

$$\frac{L}{d_0} = \theta_{scan} D_{defl} \frac{0.4}{\lambda} \quad (\text{eq. D11.8})$$

with θ_{scan} the scan angle of the deflector

Reference:

[1] Melles-Griot optical guide: www.mellesgriot.com

Appendix D12 Derivation of formula for the resolution of a slope measurement

Lateral resolution of the scanner (number of pixels per scan line):

$$N = L / \Delta \bar{x} d_0 \quad (\text{eq. D12.1})$$

with L scan length, $\Delta \bar{x}$ sampling distance, normalized to the spot size, d_0 spot size on the surface-under-test. The following consideration is based on the diffraction theory, analogically as in derivation of the scan resolution formula in appendix D11. In this case, the detector size is can be bounded with the spot size as:

$$d_f = D_{\text{det}} b^{-1} \quad (\text{eq. D12.2})$$

with b ratio between the detector aperture size and the beam size on the detector. Typically, to guarantee high accuracy of the measurement $b = 10-100$, when using PSD for a beam displacement detection.

Hence, the spot size can be written as:

$$d_0 = \frac{4 \lambda f b}{\pi D_{\text{det}}} \quad (\text{eq. D12.3})$$

Combining E12.1 and E12.3 we obtain a formula for the resolution of the slope detection:

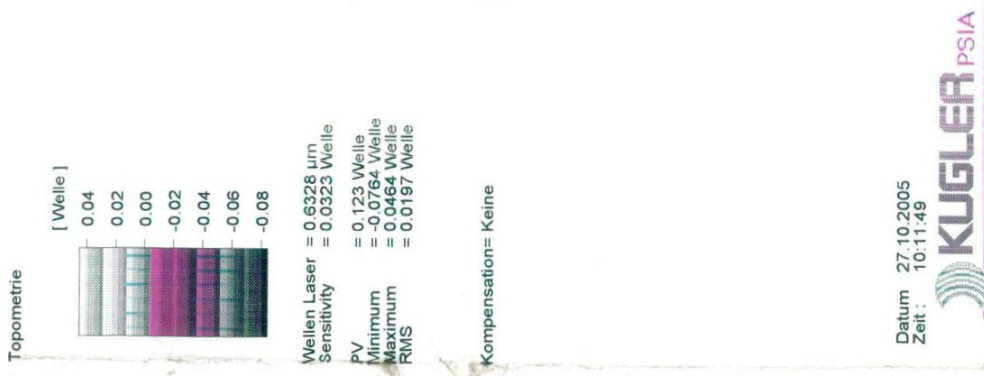
$$N = \frac{\pi L}{4 f} D_{\text{det}} \frac{1}{\lambda b \Delta_s} \quad (\text{eq. D12.4})$$

By rewriting the last equation we can obtain a design formula, which bounds the detector size with some basic parameters of a deflectometer:

$$D_{\text{det}} = 1.27 \frac{f}{d_0} b \lambda \quad (\text{eq. D12.5})$$

Appendix F1 Calibration report of the reference flat

Manufacturer: PlanOptik
Calibration device: Phase-shift interferometer
Manufacturer: Kugler
Type: -
Specification: field of view 300mm, reference flat $\lambda/20$



PlanOptik GmbH
Ludwig-Erhard-Str. 1
50733 Essen



Appendix F2 Calibration of the scan non-linearity

Calibration device:	Cartesian reference grid
Manufacturer:	Philips
Type:	-
Specification:	chromium on glass, pitch 5 mm, line width 1 mm, substrate thickness 3 mm

Procedure:

1. Intensity signal from the reference grid is measured in (i,j) coordinates (figure 1)
2. Position of each grid line is estimated in (i,j) coordinates. It is measured from the middle at the half maximum of the intensity peaks
3. The mean pixel size value Δx is calculated as:

$$\Delta x = x_{\max} / n_{\max} \quad (\text{eq. F2.1})$$

with x_{\max} and n_{\max} distance and the corresponding number of pixels between the first and the last grid line, measured at the scan line

4. Local deviation function $f(i)$ of the pixel size is calculated as:

$$f(i) = (x_{adj} / n_{adj}) / \Delta x \quad (\text{eq. F2.2})$$

with x_{adj} and n_{adj} distance and the corresponding number of pixels for each adjacent pair of the grid lines, respectively. These discrete values of the $f(i)$ function are assigned to the middle pixels between the grid lines (figure 1)

5. The continuous $f(i)$ -function is approximated by a polynomial fit of its discrete values
6. A lookup table for the pixel positions is calculated using the algorithm:

$$x_{i+1} = x_i + f(i) \Delta x \quad (\text{eq. F2.3})$$

Measurement results:

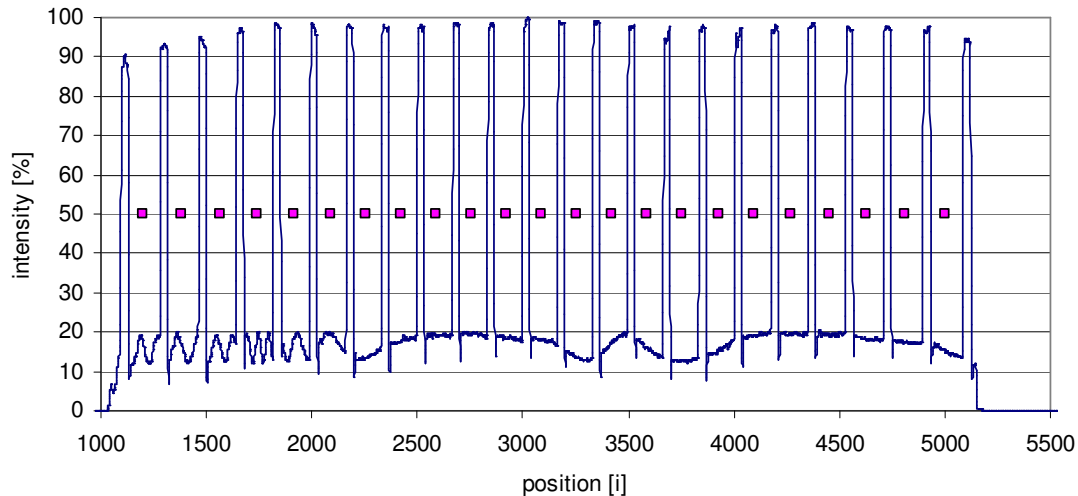


Figure F2.1. Intensity plot of a single line on the reference grid, scanned with the 3D-deflectometer. The points between the lines indicate location of the pixels, where to calculated discrete values of the $f(i)$ -function are assigned.

To verify accuracy of the calibration, we measure the grid again and calculate the pixel position error δx_i as the difference between the nominal and calculated position of the grid lines. The result is shown in figure F2.2.



Figure F2.2. Position error δx_i along the scan line, estimated from the reference grid for different calibration orders. Values of the “linear” plot refer to the secondary vertical axis.

Table F2.1. Pixel position errors δx_i calculated for different orders of the calibration.

Calibration type (polynomial order)	δx_i (μm)	
	PV	RMS
0	1331	749.9
2	37	16.6
4	13	4.1
6	11	3.8
8	11	3.5

In order to verify the influence of the position error δx_i on the pixel size error Δx , we calculate the residue of the polynomial fit of the $f(i)$ -function. The result is given in figure F2.3.

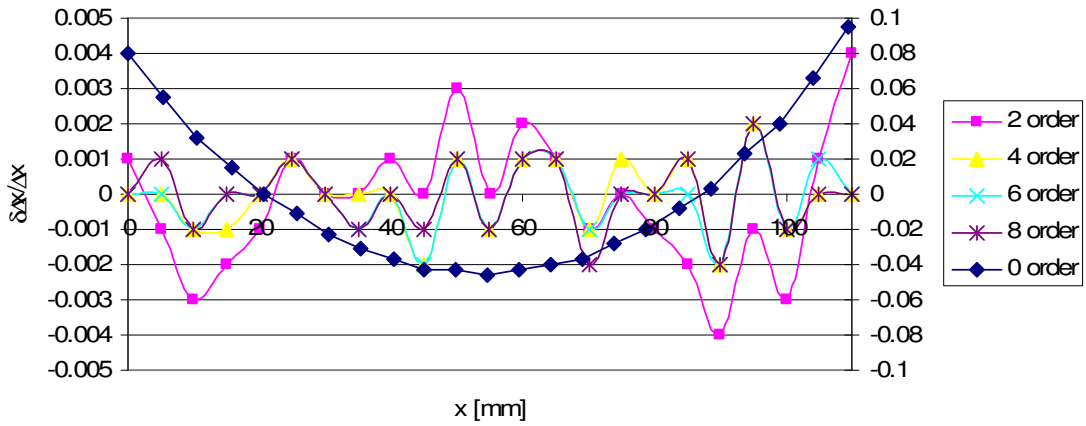


Figure F2.3 Deviation of the pixel size $\delta \Delta x_i/\Delta x$, measured by aid of the reference grid and normalized to the mean pixel size Δx . Values of the “linear” plot refer to the secondary vertical axis.

Table F2.2. Pixel size errors $\delta \Delta x$ calculated for different orders of the calibration.

Calibration type (polynomial order)	$\delta \Delta x$ (%)	
	max/min deviation	RMS
0	+9.48/-4.56	4.32
2	+0.45/-0.41	0.19
4	+0.17/-0.15	0.10
6	+0.17/-0.17	0.09
8	+0.19/-0.15	0.09

Calculated parameters:

Mean pixel size Δx : 28.83 μm

Appendix F3 Measurement report of the yaw of the translation stage

Object-under-test: Translation stage
Type: -
Manufacturer: Pasim GmbH
Specification: Air-bearings, 500mm stroke

Measurement device: Autocollimator
Manufacturer: Moeller-Wedel
Type: Elcomat 2000
Specification: nominal angle accuracy 0.5 μrad

Investigated parameters: Yaw along the effective stroke (300 mm)

Set-up:

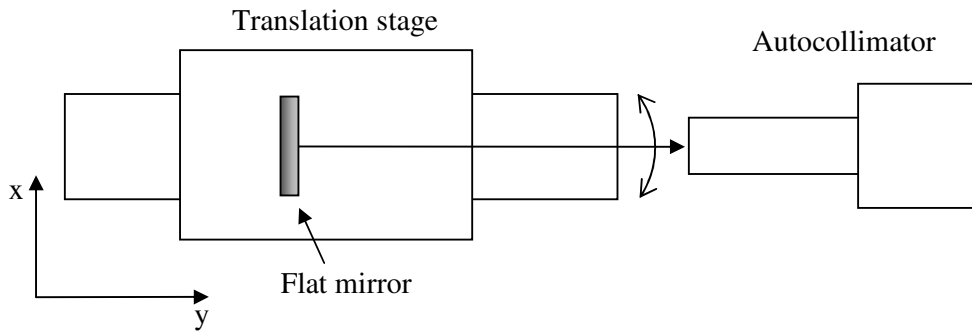


Figure F3.1 Calibration set-up for measurement of yaw of the translation stage.

Measurement results:

Measured yaw

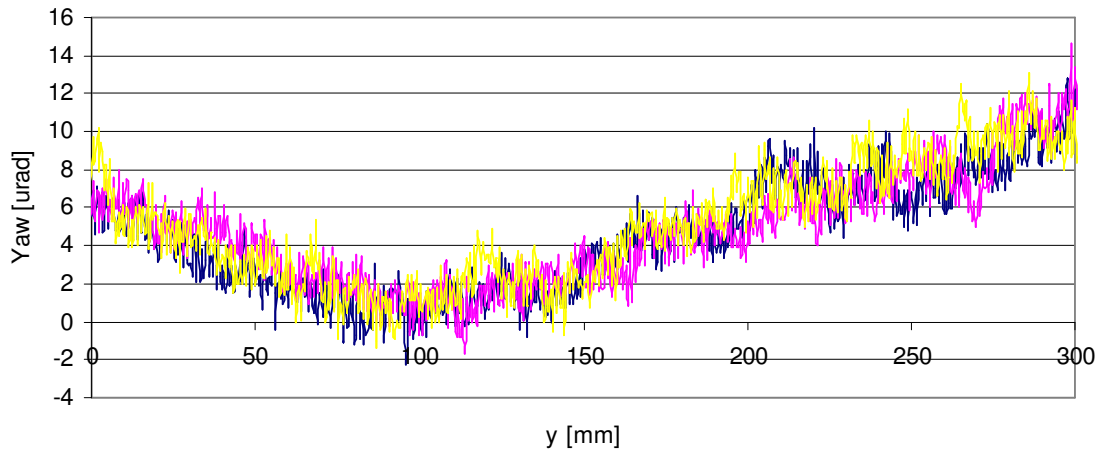


Figure F3.2. Measured yaw: three measurements.

The multiple measurements indicate a systematic character of low frequency yaw and random character of high frequency yaw. Therefore, the systematic component can be estimated from a polynomial fit. The result of such estimation is given in figure F3.3.

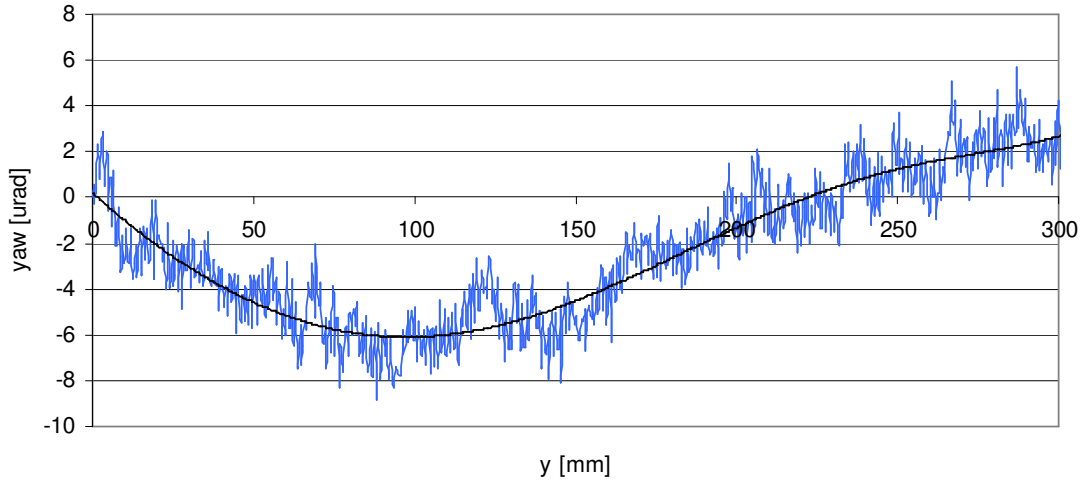


Figure F3.3 Yaw of the translation stage and its systematic component (6th order polynomial fit).

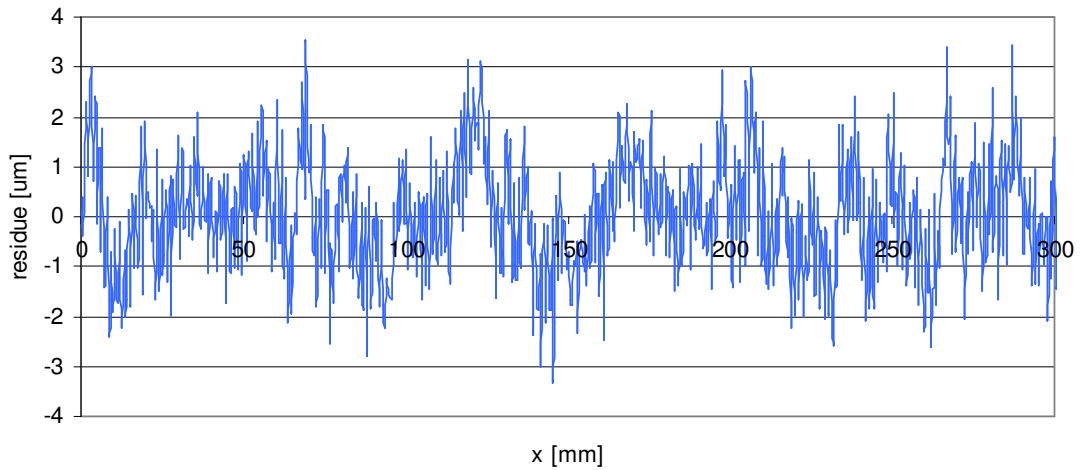


Figure F3.4. Random part of the yaw (residue of the polynomial fit).

Calculated parameters:

Total deviation (PV/RMS):	14.5 / 3.13	μrad
Systematic deviation (PV/RMS):	9 / 2.90	μrad
Random deviation(PV/RMS):	6.8 / 1.17	μrad

Appendix F4 Calibration of the slope response

Calibration device: Autocollimator
Manufacturer: Moeller-Wedel
Type: Elcomat 2000
Specification: nominal angle accuracy 0.5 μrad

Calibration setup:

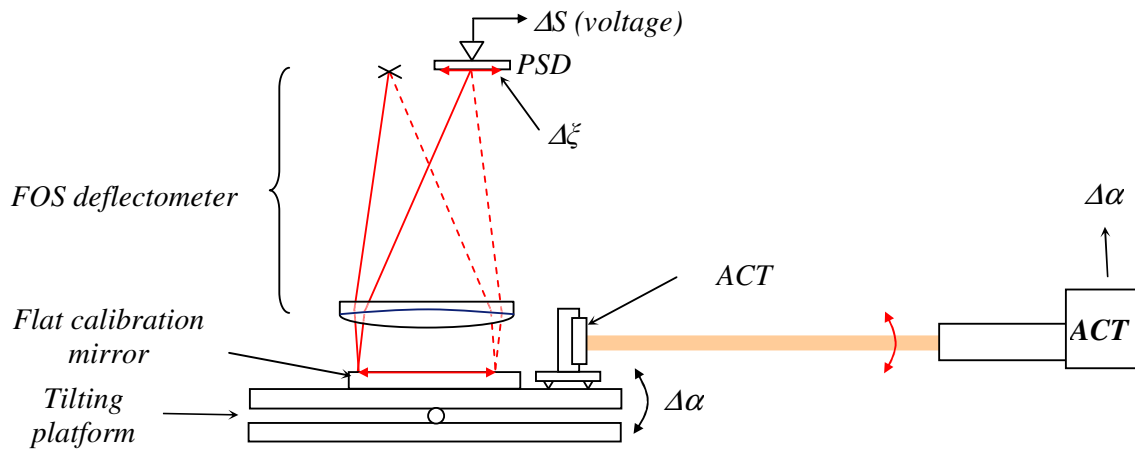


Figure F4.1. Set-up for calibrating the slope response of the 3D-deflectometer.

Calibration results:

A) ξ -axis – multiple measurement across the centre of the PSD:

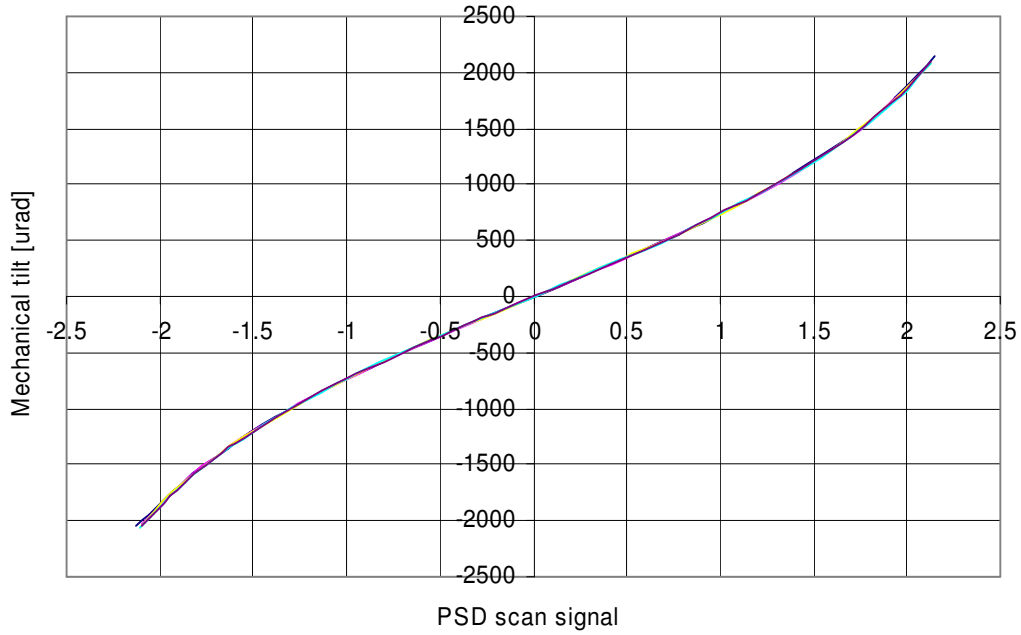


Figure F4.1. Calibration curve: multiple measurement at the middle of the PSD.

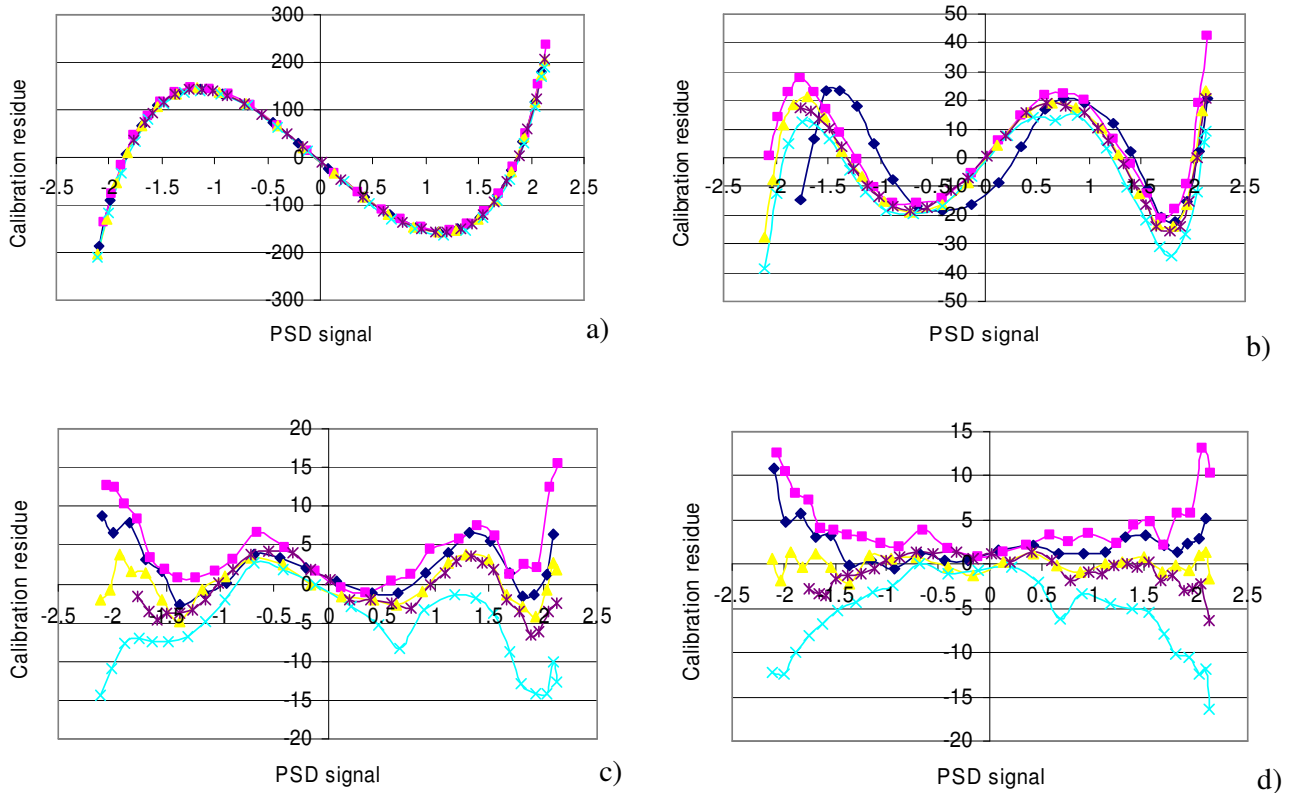


Figure F4.2 Residue of the polynomial fit of the calibration curve: a) linear fit; b) 3rd order fit; c) 5th order fit, d) 7th order fit.

B) ξ -axis – multiple measurement at 5 different positions at η -axis:

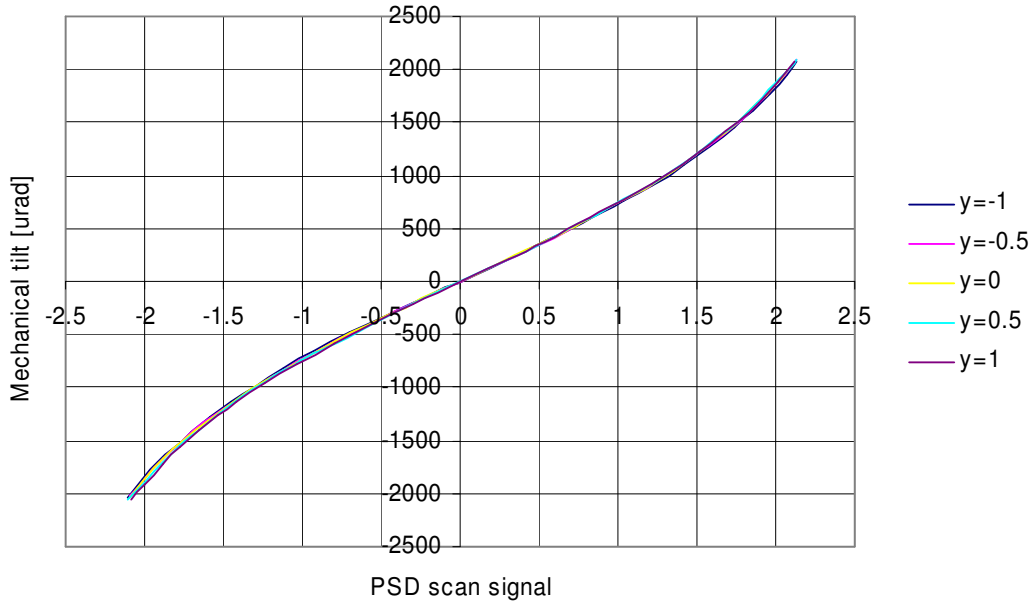


Figure F4.3. Calibration curve: multiple measurement at at five different positions at the PSD.

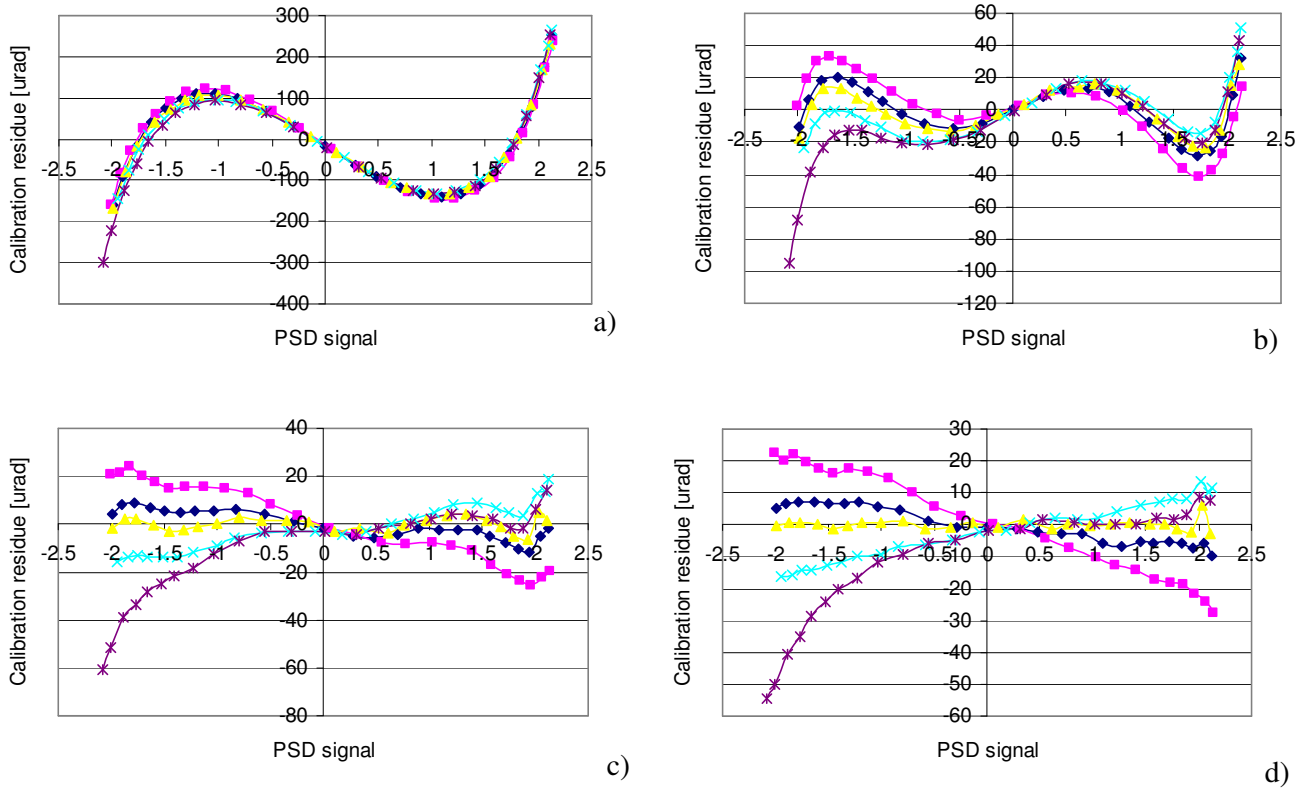


Figure F4.4 Residue of the polynomial fit of the calibration curve: a) linear fit; b) 3rd order fit; c) 5th order fit, d) 7th order fit.

B) η -axis – multiple measurement at 5 different positions at ξ -axis:

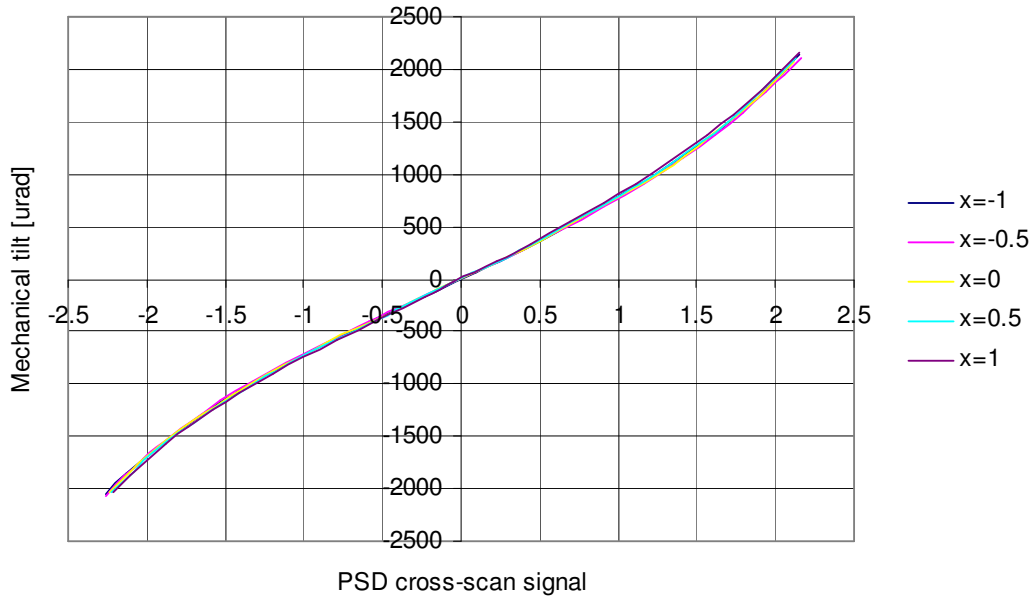


Figure F4.5. Calibration curve: multiple measurements at five different positions at the PSD.

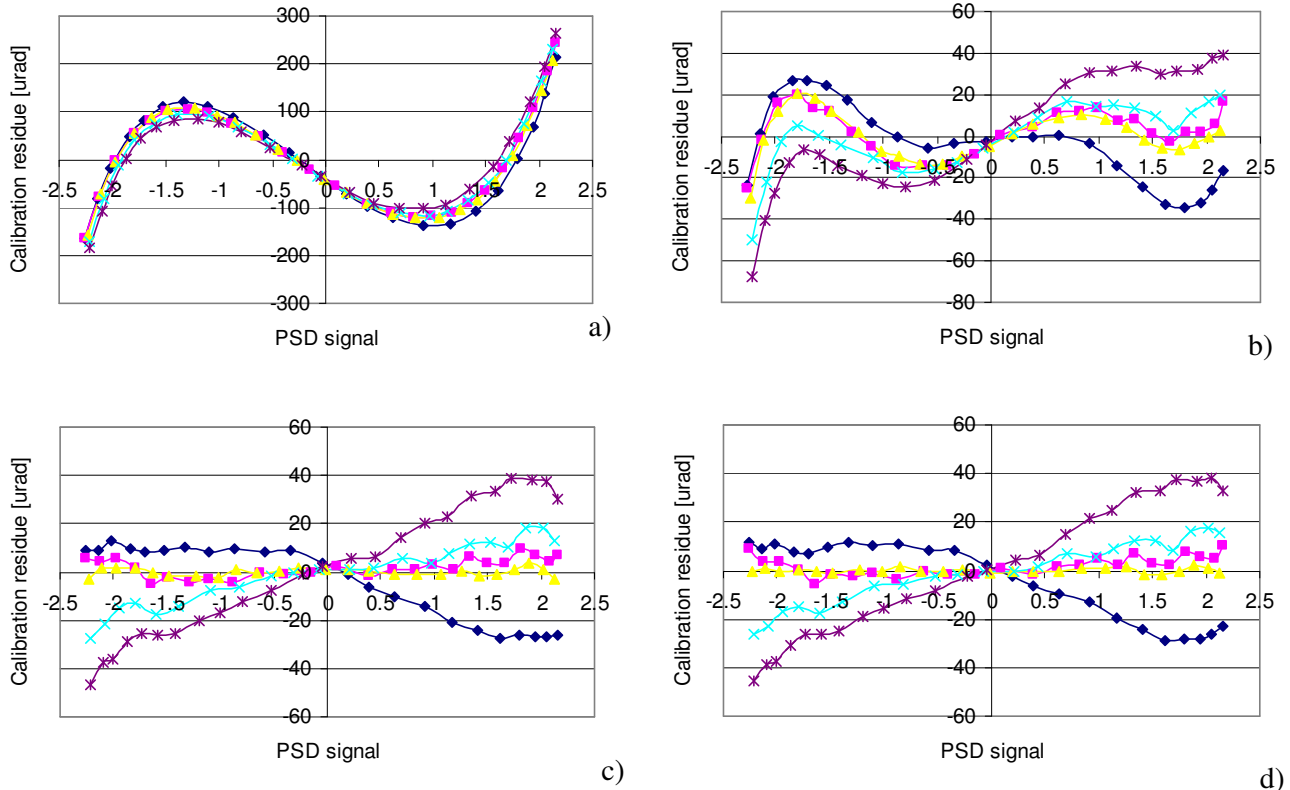


Figure F4.6 Residue of the polynomial fit of the calibration curve: a) linear fit; b) 3rd order fit; c) 5th order fit, d) 7th order fit.

Calculated parameters:

ξ -axis: polynomial fit errors for a single measurement (middle of the PSD):

linear:	120 μrad
3 rd order:	16 μrad
5 th order:	2.5 μrad
7 th order:	1 μrad

ξ -axis: polynomial fit errors for multiple measurements at the same position at PSD (middle of the PSD):

linear:	116 μrad
3 rd order:	16 μrad
5 th order:	5.5 μrad
7 th order:	4.8 μrad

ξ -axis: polynomial fit errors for multiple measurements at five different positions at PSD:

linear:	115 μrad
3 rd order:	19.8 μrad
5 th order:	12.8 μrad
7 th order:	12.7 μrad

η -axis: polynomial fit errors for multiple measurements at five different positions at PSD:

linear:	102 μrad
3 rd order:	19 μrad
5 th order:	14.9 μrad
7 th order:	15 μrad

Appendix F5 Calibration of the system signature

Calibration device: Optical flat
 Manufacturer: PlanOptik
 Type: \varnothing 300 mm
 Specification: nominal flatness: $\lambda/10$ (wavelength $\lambda=632.7$ nm)

Measurement date: 17-11-2005

Investigated parameters: Scan lens signature (A); translation stage signature (B)

Procedure:

- 1) Measurement of the reference surface (110×110 mm² area, mean step size $\Delta x=29$ μ m, $\Delta y=100$ μ m)
- 2) Lens signature extracted by averaging all the rows of the measured slope arrays
- 3) Stage signature extracted by averaging all the columns of the measured slope arrays

A) Lens signature

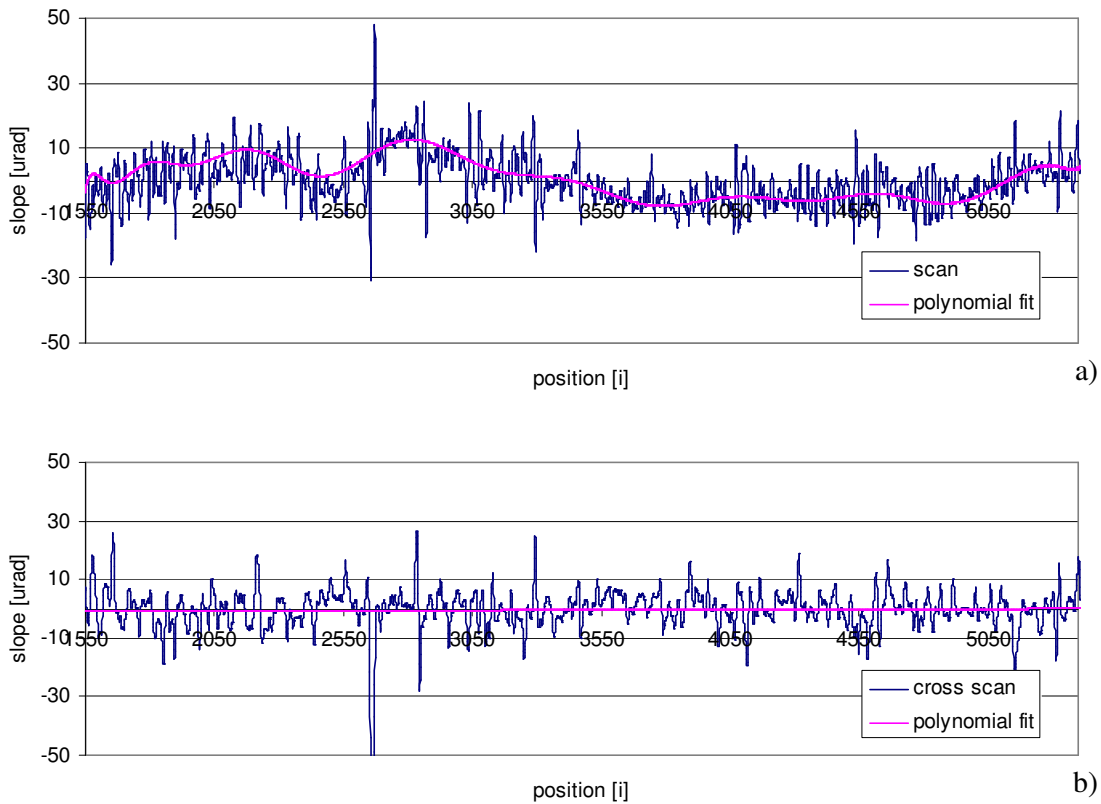


Figure F5.1 Lens signature of the 3D deflectometer and the corresponding polynomial fit (scan slope: 20th order; cross-scan slope: 2nd order): a) scan slope component; b) cross-scan slope component

Parameters calculated for all data (values in parentheses include the “cats-eye” peak):

Scan slope:
PV: 53.3 (78) μrad
RMS: 7.5 μrad

Cross scan slope:
PV: 55.6 (189.7) μrad
RMS 9.6 μrad

Parameters calculated from the polynomial fit:

Scan slope:
PV: 20.4 μrad
RMS: 5.9 μrad

Cross scan slope:
PV: 0.8 μrad
RMS 0.2 μrad

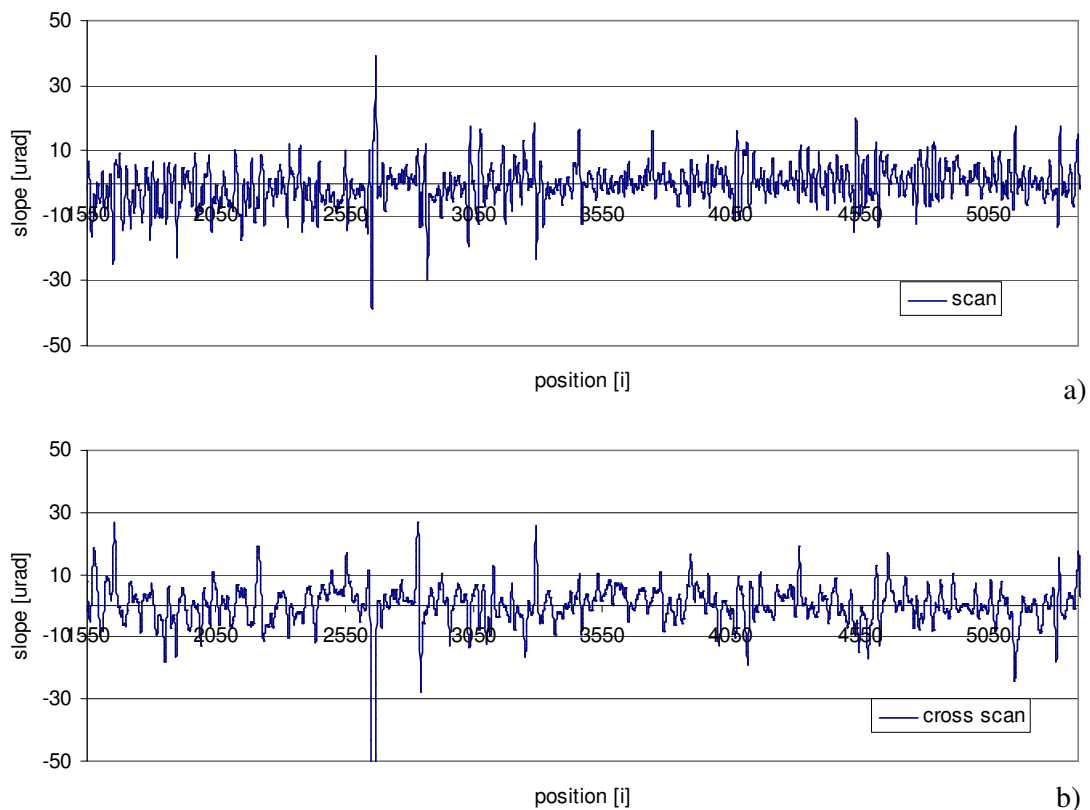


Figure F5.2. Lens signatures: residue of the polynomial fit.

Calculated parameters:

Scan slope:
 PV: 78 (53.3) μrad
 RMS: 7.5 μrad

Cross scan slope:
 PV: 189.7 (55.6) μrad
 RMS 9.6 μrad

B) Stage signature

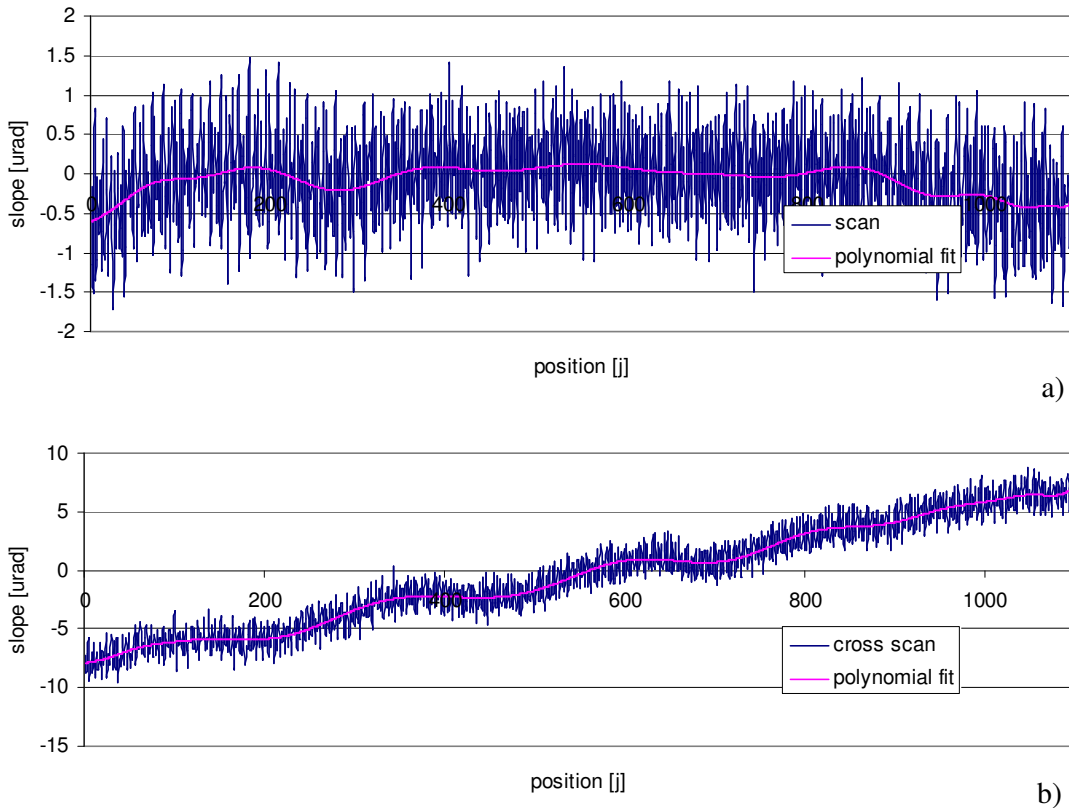


Figure F5.3 Stage signature of the 3D deflectometer and the corresponding polynomial fit (20th order): a) scan slope component; b) cross-scan slope component

Calculated parameters (all data):

Scan slope:
 PV: 3.11 μrad
 RMS: 0.63 μrad

Cross scan slope:
 PV: 18.33 μrad
 RMS: 4.42 μrad

Calculated parameters (polynomial fit):

Scan slope:

PV: $0.7 \mu\text{rad}$

RMS: $0.1 \mu\text{rad}$

Cross scan slope:

PV: $15 \mu\text{rad}$

RMS: $4.3 \mu\text{rad}$

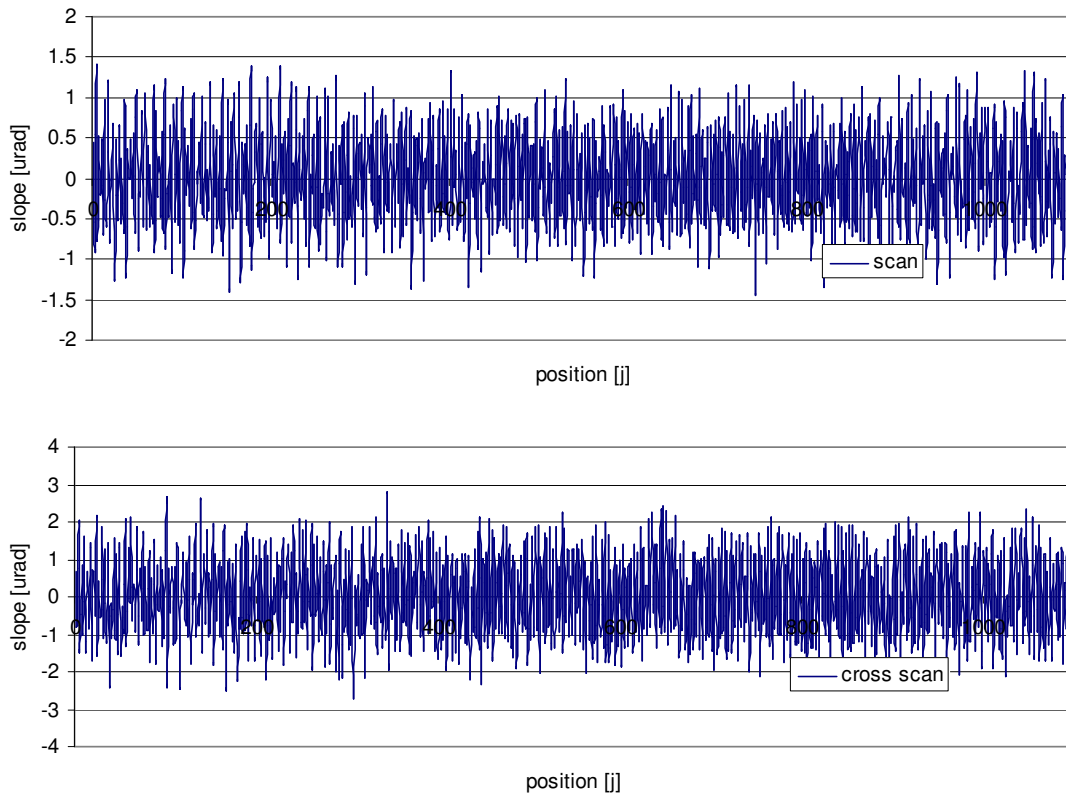


Figure F5.4. Lens signatures: residue of the polynomial fit.

Calculated parameters:

Scan slope:

PV: $2.8 \mu\text{rad}$

RMS: $0.6 \mu\text{rad}$

Cross scan slope:

PV: $5.5 \mu\text{rad}$

RMS: $1.1 \mu\text{rad}$

Appendix F6 Measurement report of the reference flat

Surface-under-test:	Optical flat
Manufacturer:	PlanOptik
Geometrical parameters:	Ø 300 mm
Finishing:	reflective coating
Top-layer:	Al
Device:	3D-deflectometer
Manufacturer:	Philips Applied Technologies
Type:	-
Specification:	mean step size $\Delta x = 29 \mu\text{m}$, $\Delta y = 100 \mu\text{m}$, surface reconstruction by Iterative Fourier Integration
Post-processing and display software:	MountainMap 3.1
Measurement date:	17-11-2005
Investigated parameters:	Un-corrected topography (A); Topography with stage and lens signatures corrected (B); Corrected topography after low (C) and high spatial filtering (D)

A) Non-corrected topography

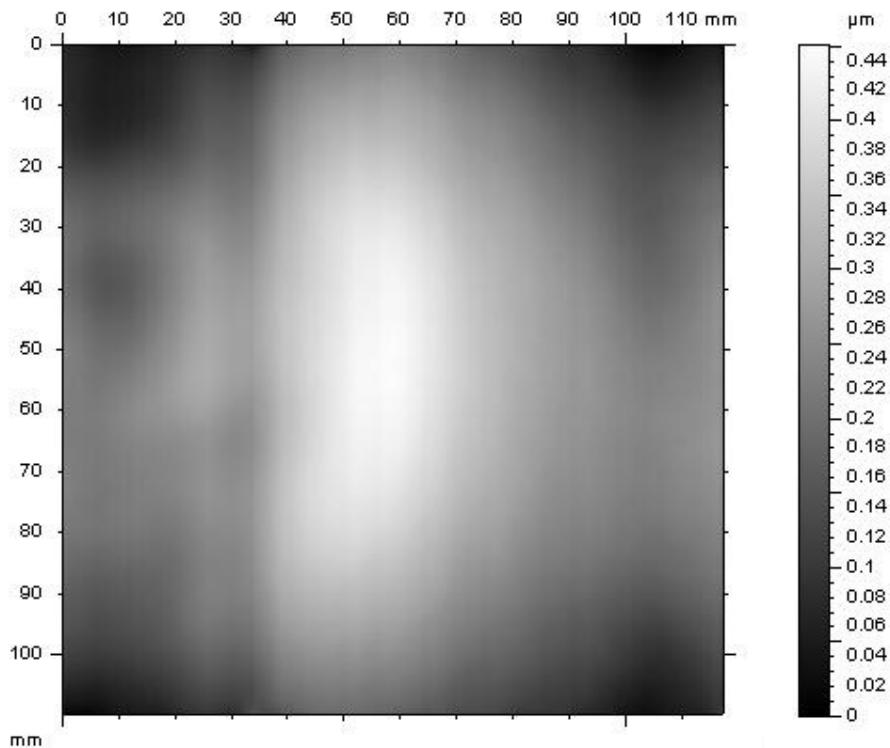


Figure F6.1. Raw topography data (no signature subtraction applied)

Calculated parameters:

PV: 451 nm
RMS: 93.6 nm

B) Correction for lens and stage signature

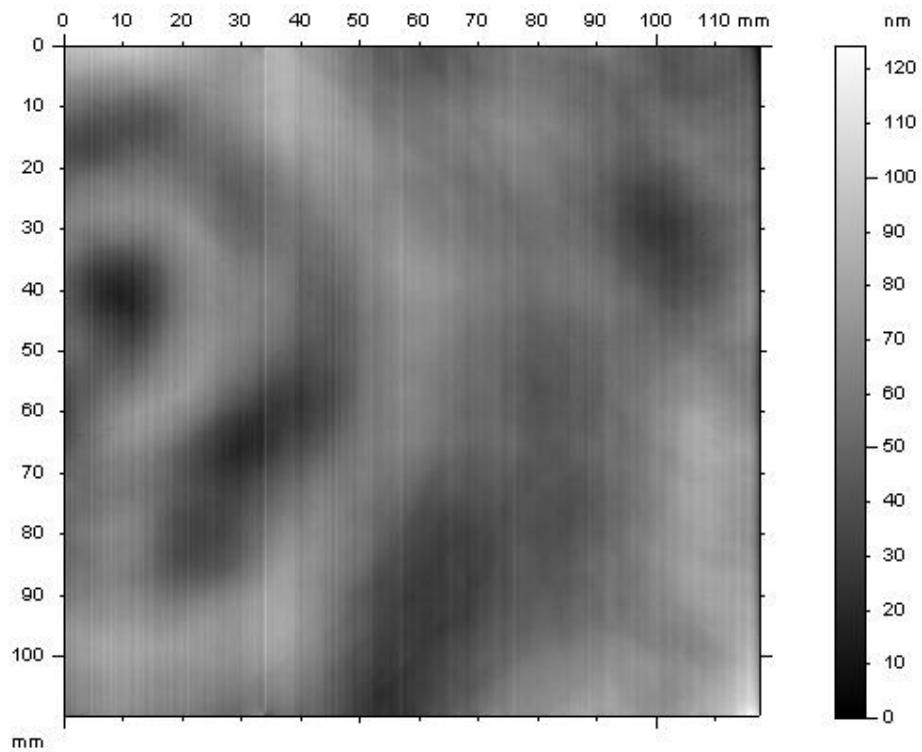


Figure F6.2. Topography image with after subtraction of lens and stage signatures.

Calculated parameters:

PV: 124 nm
RMS: 14 nm

D) Correction for lens and stage signatures + spatial filtering (high-pass)

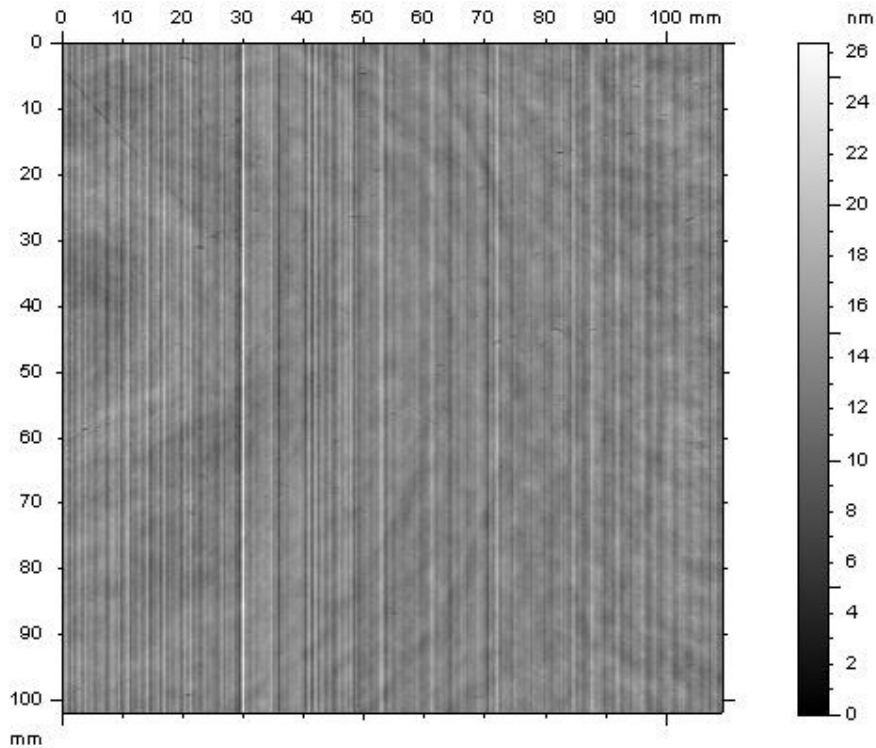


Figure F6.2. Topography image with after subtraction of lens and stage signatures. To show the high-spatial-frequency structure we applied high-pass spatial filtering with single Gaussian filter (8 mm cut-off)

Calculated parameters:

PV: 26.4 nm

RMS: 1.74 nm

D) Correction for lens and stage signatures + spatial filtering (low-pass)

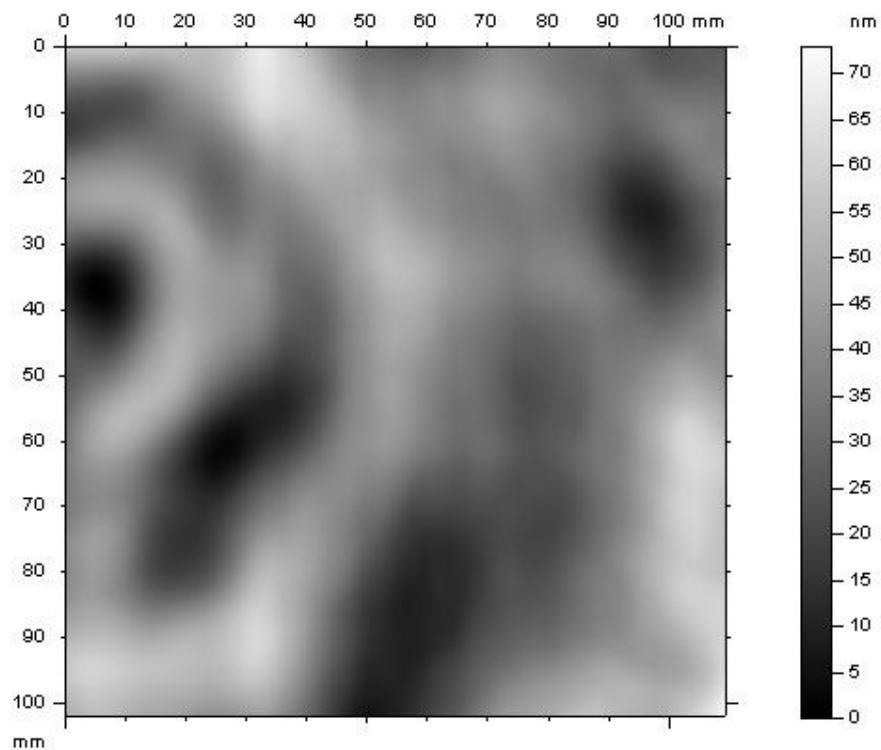


Figure F6.2. Topography image with after subtraction of lens and stage signatures. To show the low-spatial-frequency structure we applied low-pass spatial filtering with single Gaussian filter (8mm cut-off)

Calculated parameters:

PV: 72.9 nm

RMS: 13 nm

Appendix G1 Measurement report of 100mm silicon wafer substrate (3D-deflectometer)

Surface-under-test:	Silicon substrate wafer
Manufacturer:	Wacker-Siltronic
Geometrical parameters:	Ø 100 mm
Finishing:	CMP-polishing
Top-layer:	Si
Device:	3D-deflectometer
Manufacturer:	Philips Applied Technologies
Type:	-
Specification:	mean step size 60 µm, surface reconstruction by Iterative Fourier Integration
Post-processing and display software:	MountainMap 3.1
Measurement date:	13.09.2005
Investigated parameters:	Global shape (A); Influence of polishing on edges (B); Nanotopography excluding edges (C)

(A) Global shape

Support:	flat metal plate, no vacuum chuck
Post-processing:	none

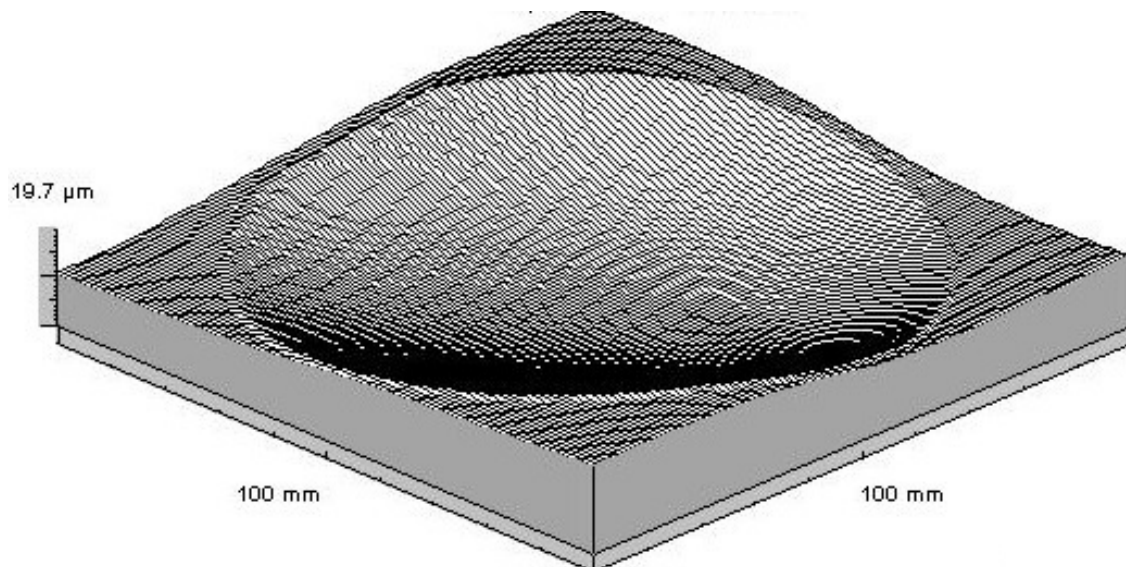


Figure G1.2. 3D plot

Parameters: PV height: 19.7 μm
 RMS height: 5.26 μm

(B) Influence of the CMP-process on edge structure

Support: flat metal plate, no vacuum chuck
Post-processing: high-pass, single-Gaussian filter with 20 mm cut-off

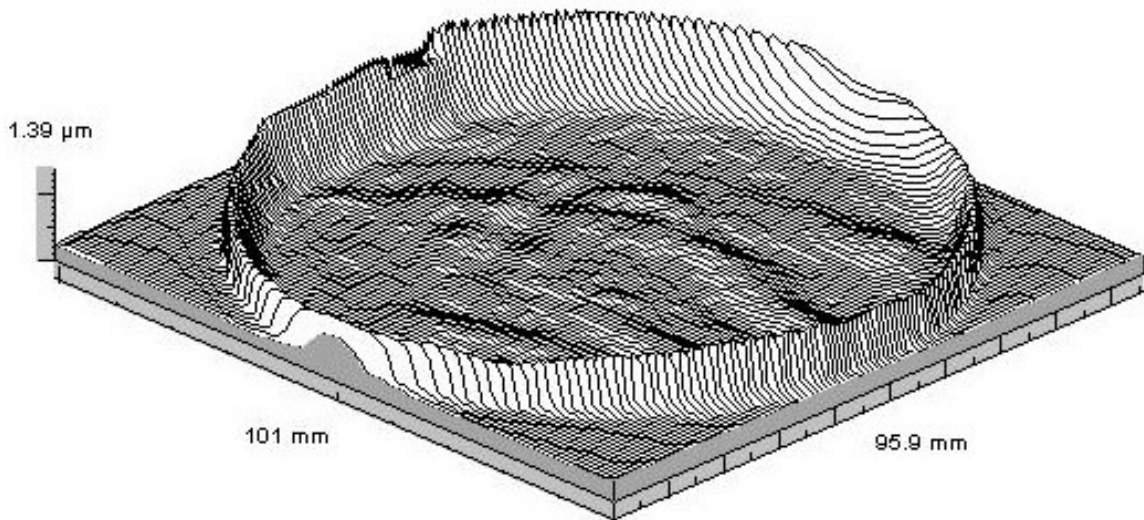


Figure G1.3. Filtered topography (nanotopography)

Parameters: PV height: 1.39 μm
 RMS height: 0.222 μm

(C) Nanotopography

Support: flat metal plate, no vacuum chuck
Post-processing: high-pass, single-Gaussian filter with 20 nm cut-off; area extraction (50 x 50 mm², middle part)

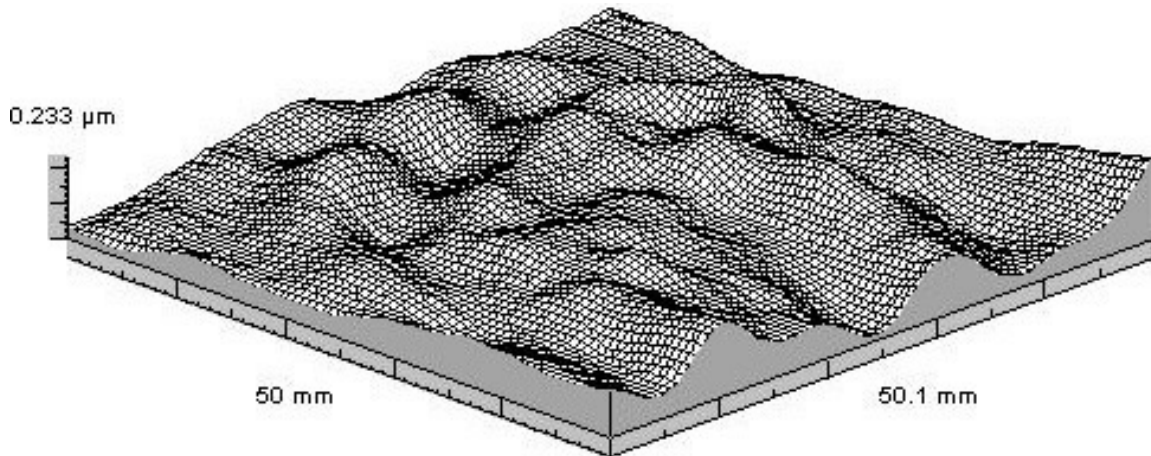


Figure G1.4. Filtered topography (nanotopography), extracted from the middle-part of the wafer

Parameters: PV height: 233 nm
RMS height: 56 nm

Appendix G2a Measurement report of epi-pin marks on 300mm wafer substrate (3D-deflectometer)

Surface-under-test:	Silicon substrate wafer
Manufacturer:	Wacker-Siltronic
Geometrical parameters:	Ø 300 mm
Finishing:	CMP-polishing + epitaxial layer
Top-layer:	Si
Device:	3D-deflectometer
Manufacturer:	Philips Applied Technologies
Type:	-
Specification:	mean step size 30 µm, surface reconstruction by Iterative Fourier Integration
Post-processing and display software:	MountainMap 3.1
Measurement date:	03.10.2005
Investigated parameters:	PV height of epi-pinmark structure
Support:	flat metal plate, no vacuum chuck
Post-processing:	form removal by 3 rd order polynomial fit, epi-pinmark excluded during the polynomial correction

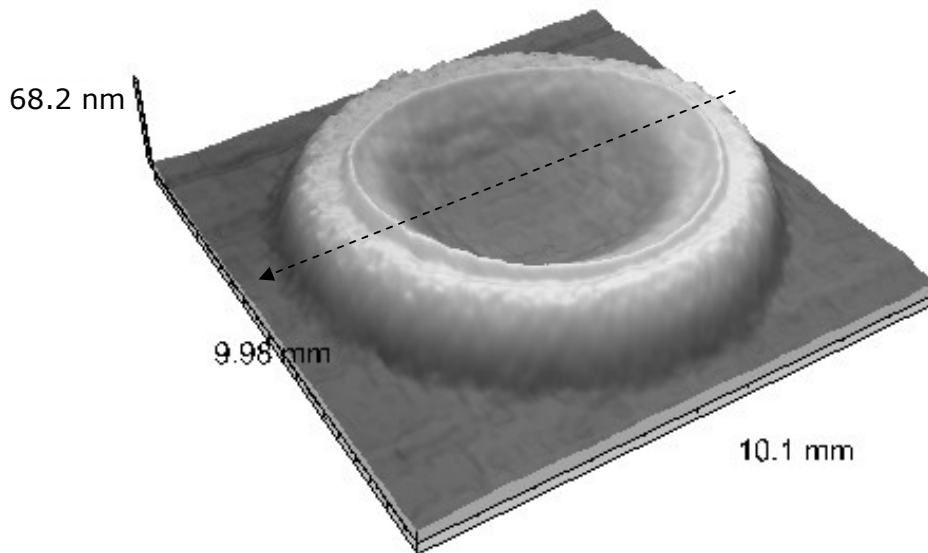


Figure G2a.1 3rd order polynomial shape removed. Black arrow indicates position and orientation of the height profile shown in figure G2a.3.

Parameters: PV height: 68.2 nm
 RMS height: 18.4 nm

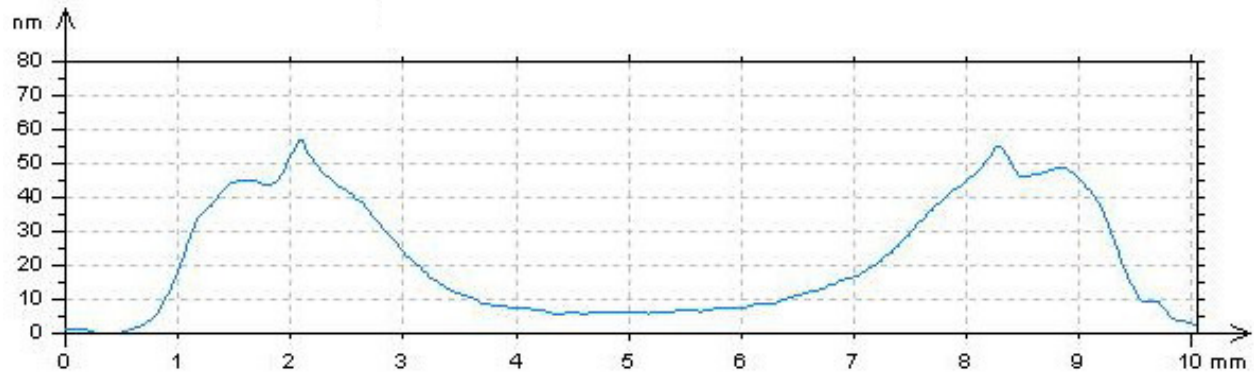


Figure G2a.2. Height profile

Appendix G2b Measurement report of epi-pin marks of 300mm wafer substrate (white light interferometer)

Surface-under-test:	Silicon substrate wafer
Manufacturer:	Wacker-Siltronic
Geometrical parameters:	Ø 300 mm
Finishing:	CMP-polishing + epitaxial layer
Top-layer:	Si
Device:	white light interferometric microscope with lateral stitching
Manufacturer:	Zygo
Type:	NewView 5032
Specification:	Pixel size: 22.92 µm µm, field of view: 7.33 x 5.50 mm
Post-processing and display software:	MountainMap 3.1
Measurement date:	13.10.2005
Investigated parameters:	Height of epi-pinmarks
Support:	flat metal plate, no vacuum chuck
Post-processing:	form removal by 3 rd order polynomial, epi-pinmark excluded during polynomial correction

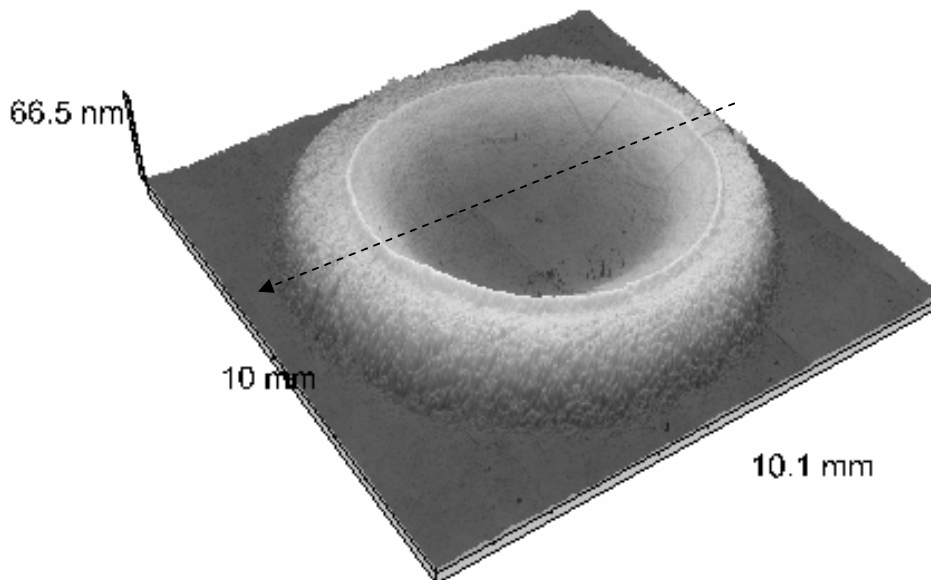


Figure G2b.1. 3rd order polynomial shape removed. Black arrow indicates position and orientation of the height profile shown in figure G2b.2

Parameters: PV height: 66.5
 RMS height: 18.5

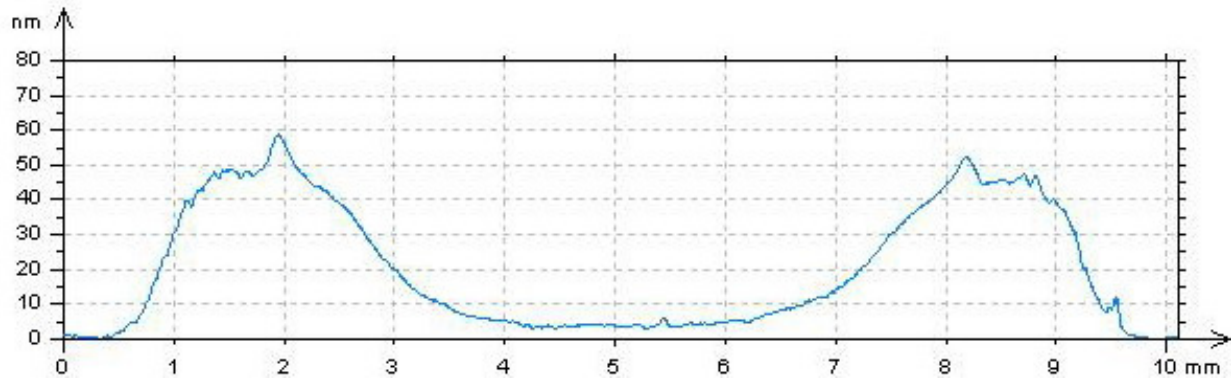


Figure G2a.3. Height profile

Appendix G3a Measurement report of patterned test-wafer (3D-deflectometer)

Surface-under-test:	patterned silicon wafer for testing of the CMP process, four samples with different finishing parameters
Manufacturer:	Philips Semiconductors Nijmegen
Geometrical parameters:	Ø 200 mm
Finishing:	metallization, 30 s CMP + metalization, 90 s CMP + metalization, 120 s CMP + metalization
Top-layer:	TiN coating (200 nm)
Device:	3D-deflectometer
Manufacturer:	Philips Applied Technologies
Type:	-
Specification:	mean step size 30 µm, surface reconstruction by Iterative Fourier Integration
Post-processing and display software:	MountainMap 3.1
Measurement date:	14.06.2005
Investigated parameters:	Influence of the CMP-polishing on nanotopography and PV/RMS height deviation

(A) Wafer W15E1 (no polishing)

Support: flat metal plate, no vacuum chuck
 Post-processing: parabolic bend removal by 2rd order polynomial

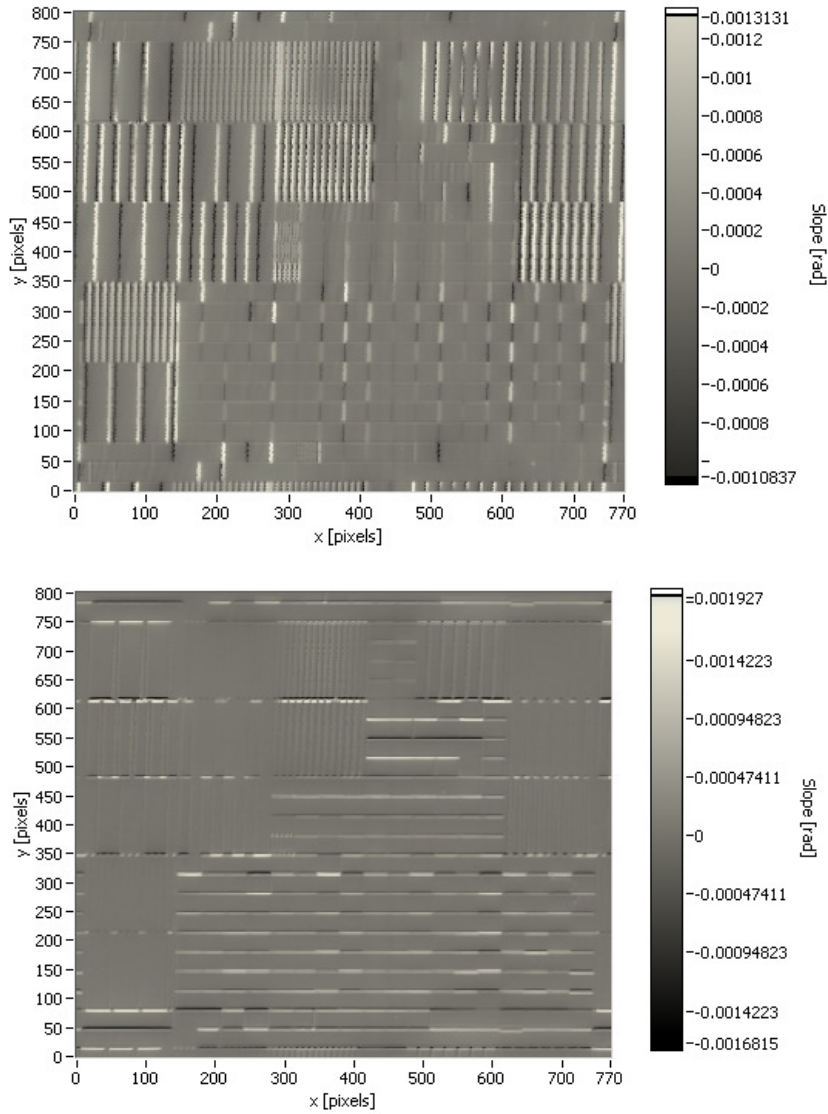


Figure G3a.1 Slope maps

Parameters: PV slope x: 2.397 mrad PV slope y: 3.609 mrad
 RMS slope x: 0.211 mrad RMS slope y: 0.192 mrad

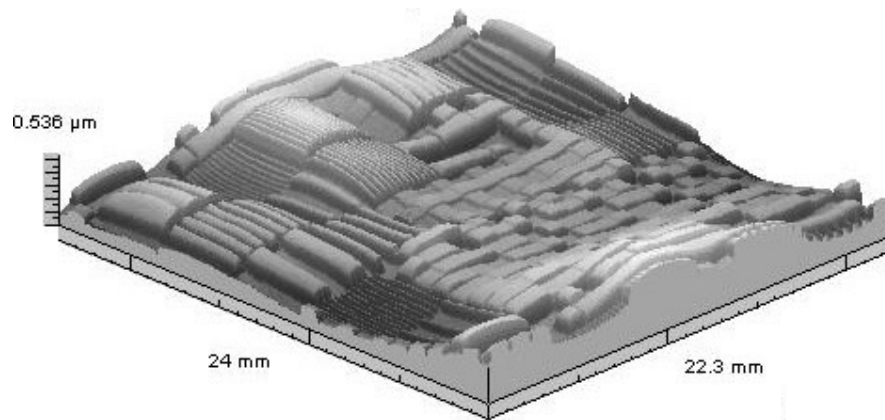


Figure G3a.2 Free-form

Parameters: PV height: 536 nm
 RMS height: 99 nm

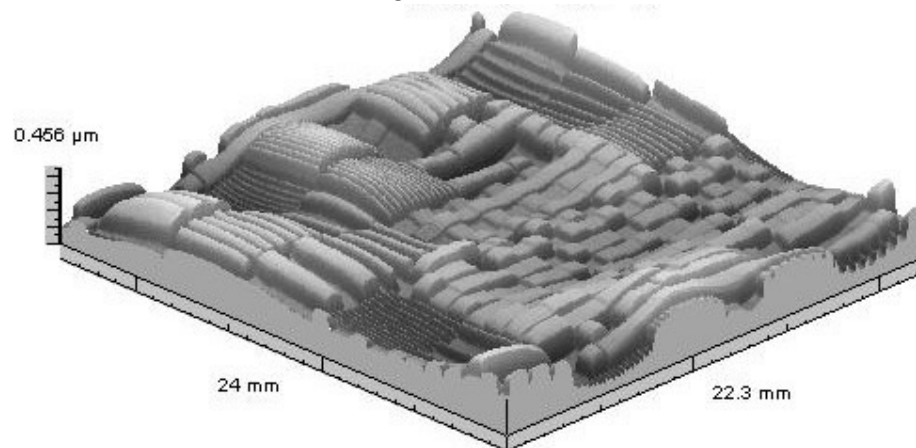


Figure G3a.3 Parabolic bend removed

Parameters: PV height: 456 nm
 RMS height: 79 nm

(B) Wafer W12G0 (30s polishing)

Support: flat metal plate, no vacuum chuck
 Post-processing: parabolic bend removal by 2rd order polynomial

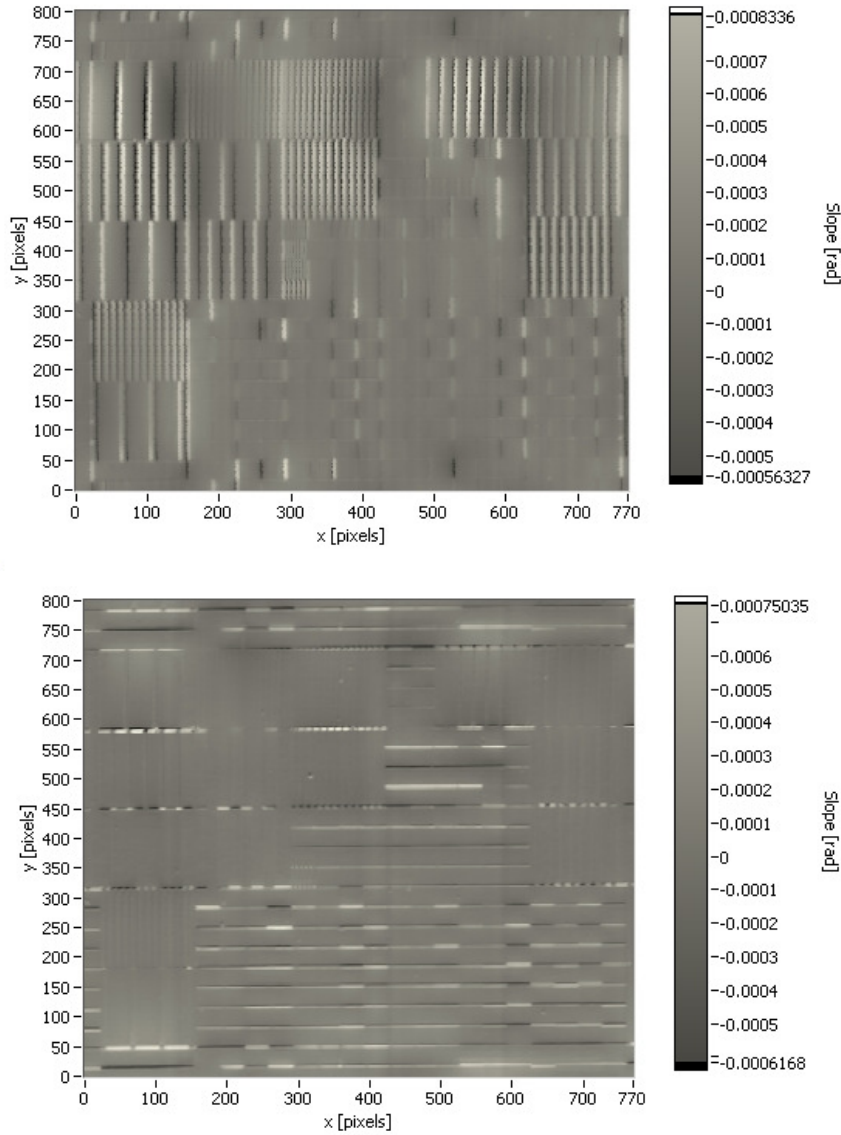


Figure G3a.4 Slope maps

Parameters: PV slope x: 1.397 mrad PV slope y: 1.367 mrad
 RMS slope x: 0.094 mrad RMS slope y: 0.073 mrad

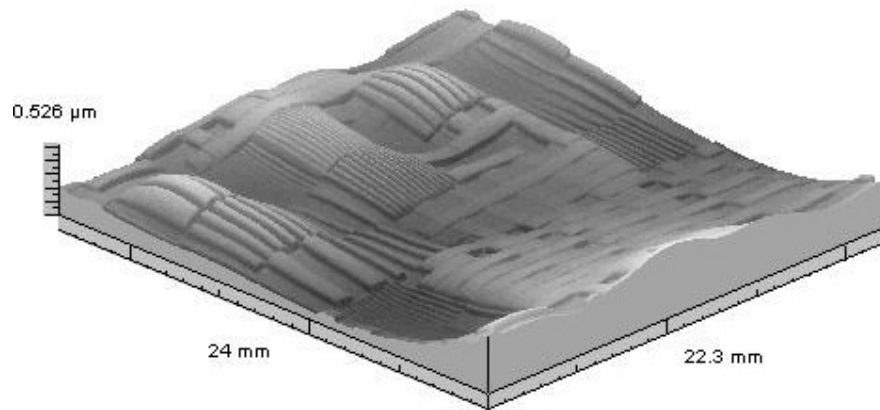


Figure G3a.5 Free-form

Parameters: PV height: 526 nm
 RMS height: 92 nm

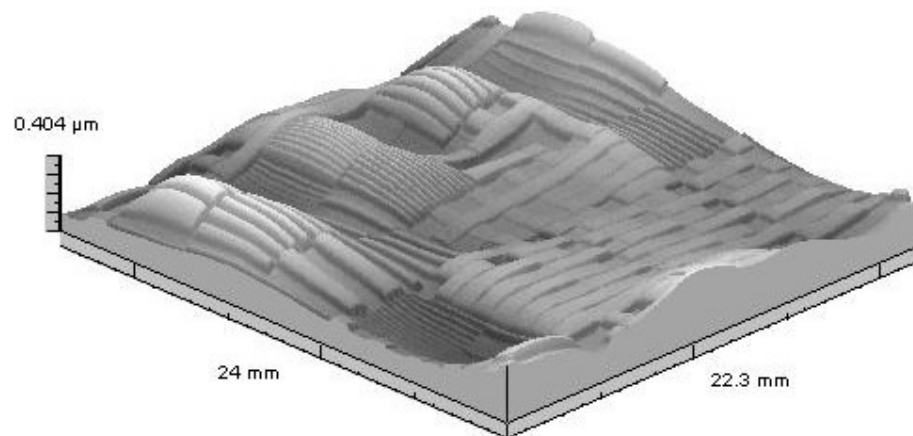


Figure G3a.6 Parabolic bend removed

Parameters: PV height: 404 nm
 RMS height: 68 nm

(C) Wafer W08H2 (90s polishing)

Support: flat metal plate, no vacuum chuck
 Post-processing: parabolic bend removal by 2nd order polynomial

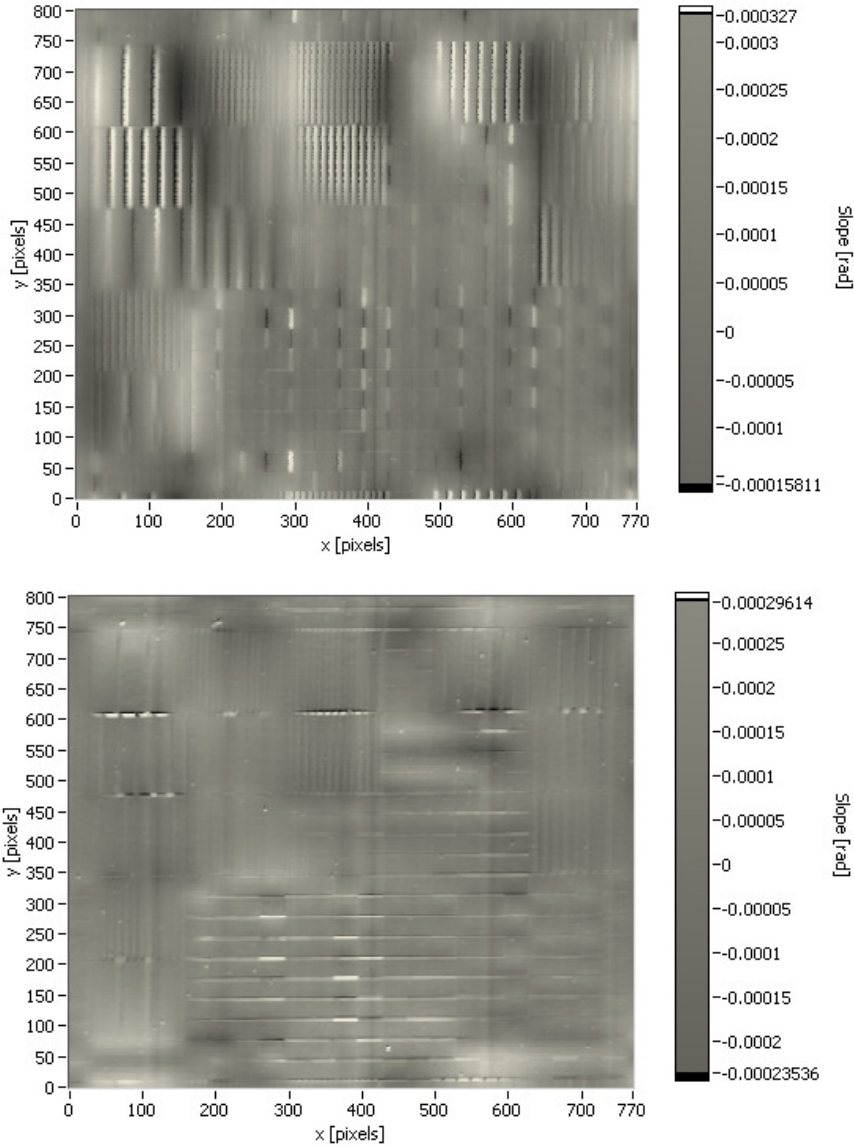


Figure G3a.7. Slope maps

Parameters: PV slope x: 0.485 mrad PV slope y: 0.532 mrad
 RMS slope x: 0.045 mrad RMS slope y: 0.033 mrad

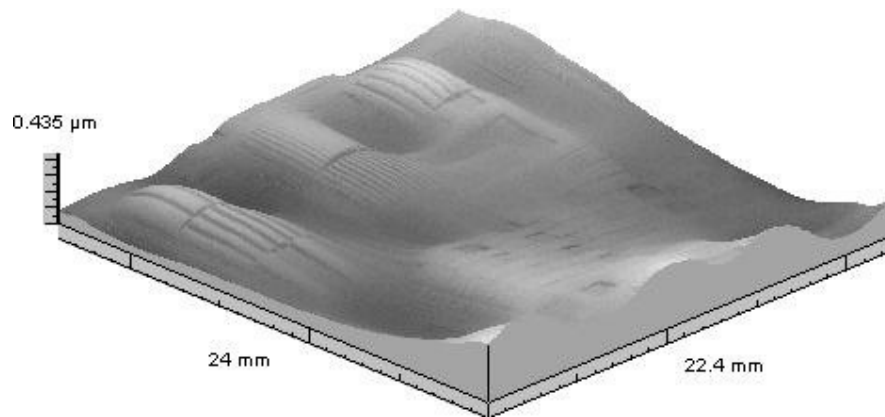


Figure G3a.8 Free-form

Parameters: PV height: 435 nm
 RMS height: 74 nm

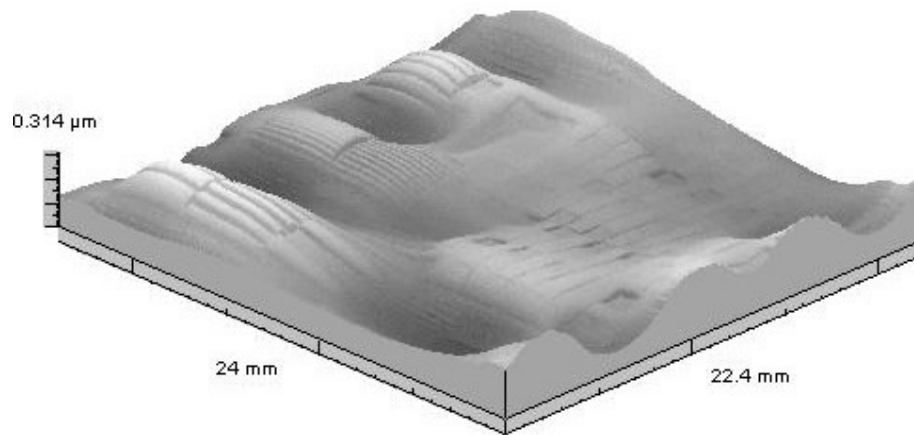


Figure G3a.9 Parabolic bend removed

Parameters: PV height: 314 nm
 RMS height: 65 nm

(D) Wafer W03D0 (120s polishing)

Support: flat metal plate, no vacuum chuck
 Post-processing: parabolic bend removal by 2rd order polynomial

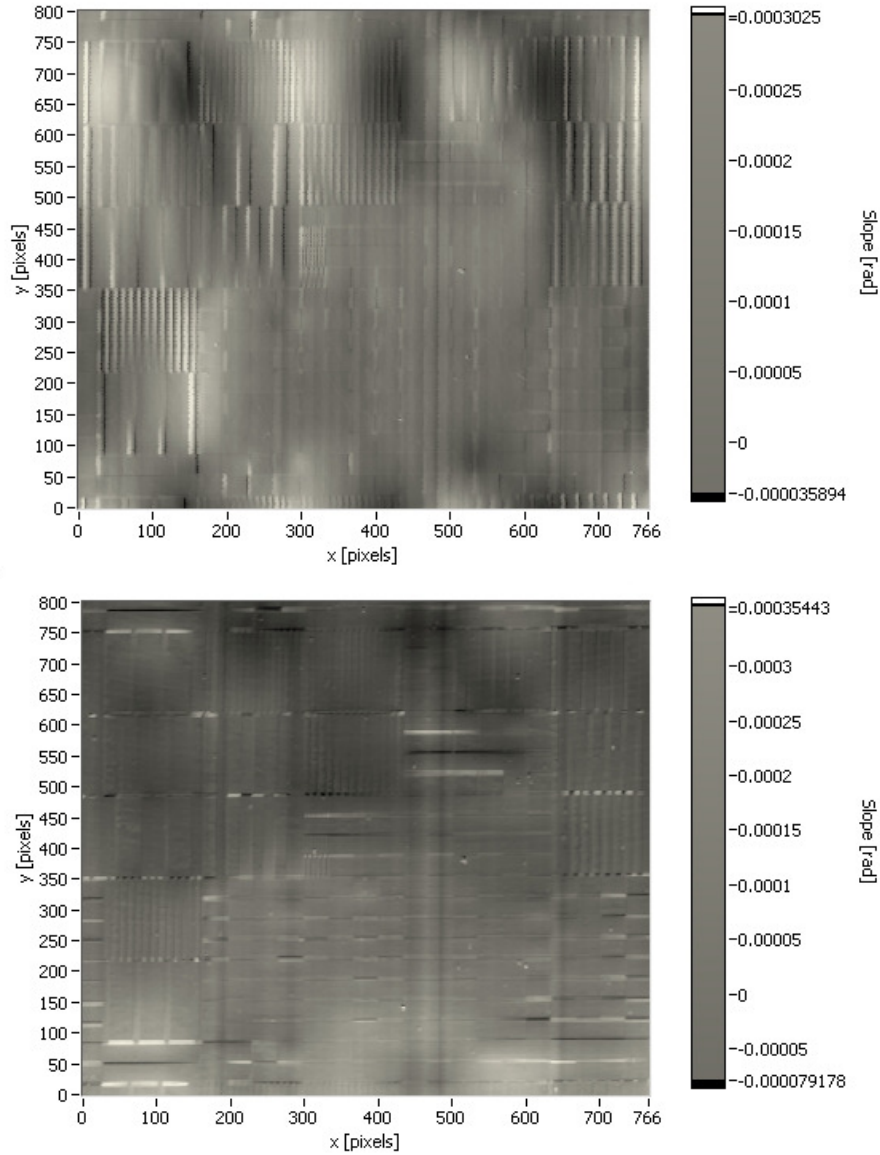


Figure G3a.10. Slope maps

Parameters: PV slope x: 0.338 mrad PV slope y: 0.434 mrad
 RMS slope x: 0.033 mrad RMS slope y: 0.048 mrad

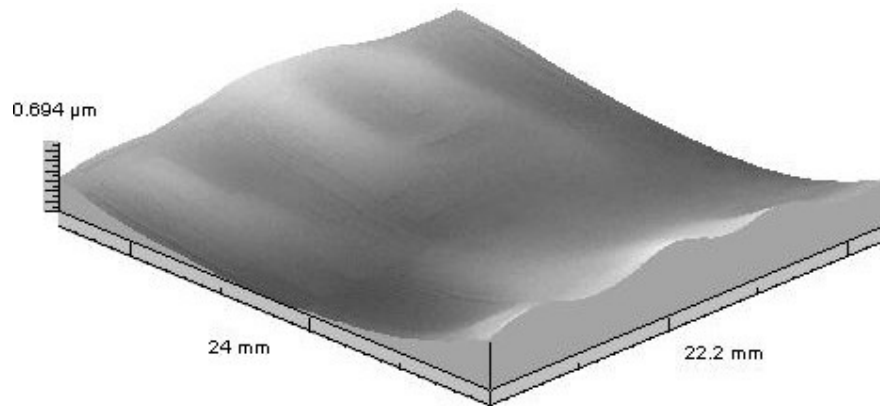


Figure G3a.11 Free-form

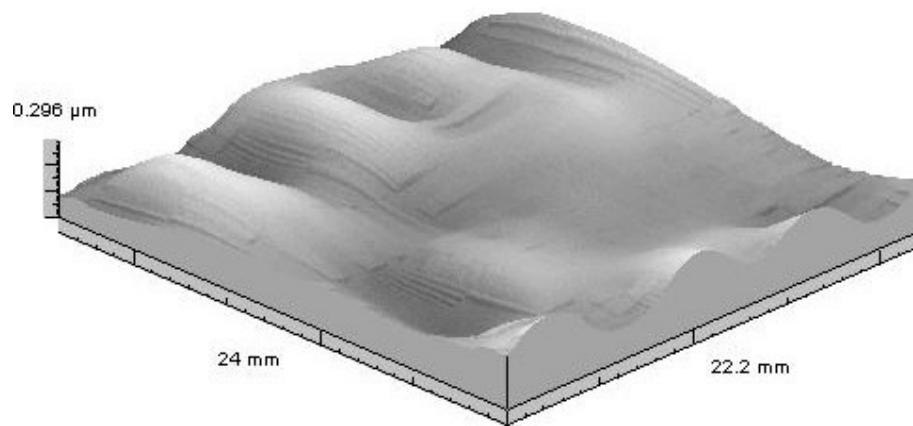


Figure G3a.12 Parabolic bend removed

Parameters: PV heigh: 296 nm
 RMS height: 48 nm

Appendix G3b Measurement report of patterned test-wafer (Stylus)

Surface-under-test:	patterned silicon wafer for testing of the CMP process, two samples with different finishing parameters
Manufacturer:	Philips Semiconductors Nijmegen
Geometrical parameters:	Ø 200 mm
Finishing:	metallization, 120 s CMP + metalization
Top-layer:	TiN coating (200 nm)
Device:	Stylus
Manufacturer:	KLA-Tencor
Type:	HRP 220
Parameters:	step size 2 µm
Post-processing and display software:	MountainMap 3.1
Measurement date:	13.04.2004
Investigated parameters:	Influence of the CMP-polishing on nanotopography

(A) Wafer W15E1 (no polishing)

Support:	3-point
Post-processing:	off-set correction, parabolic bend removed by 2 nd order polynomial

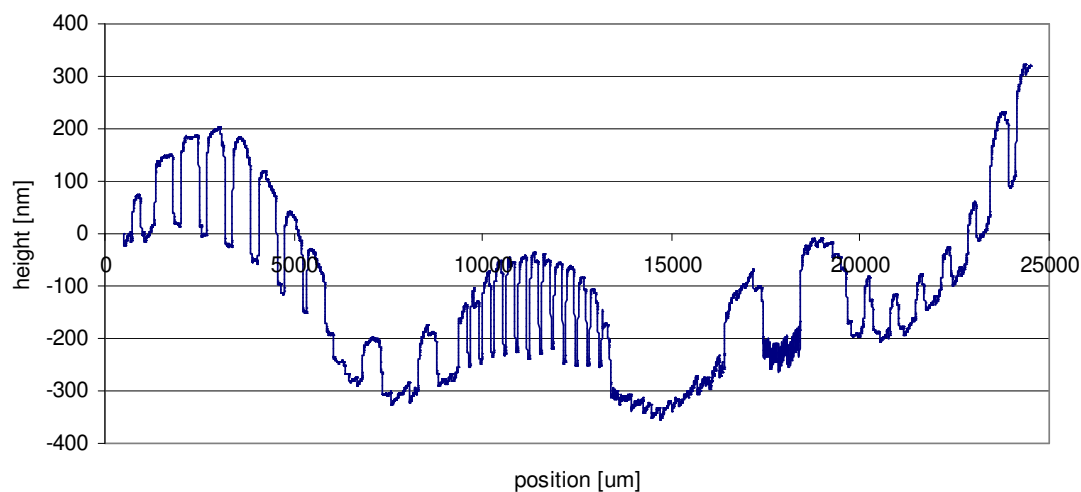


Figure G3b.1. Original profile

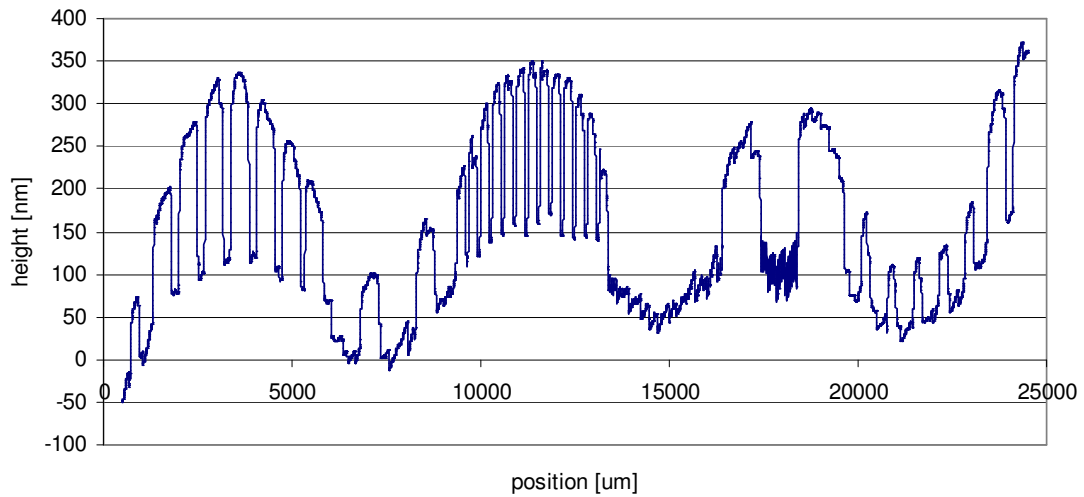


Figure G3b.2. Parabolic bend removed

(B) Wafer W03D0 (120s polishing)

Support: 3-point
Post-processing: off-set correction, parabolic bend removed by 2nd order polynomial

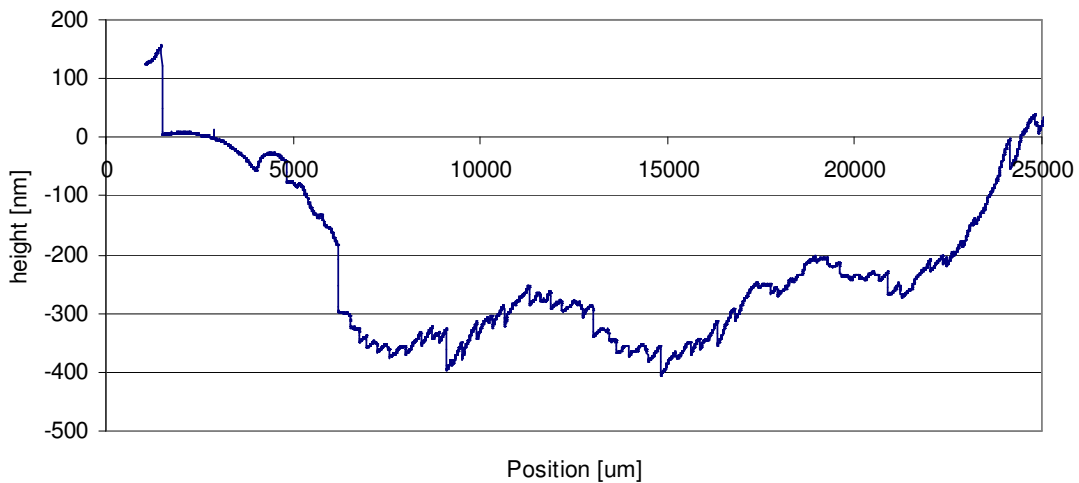


Figure G3b.3. Original profile

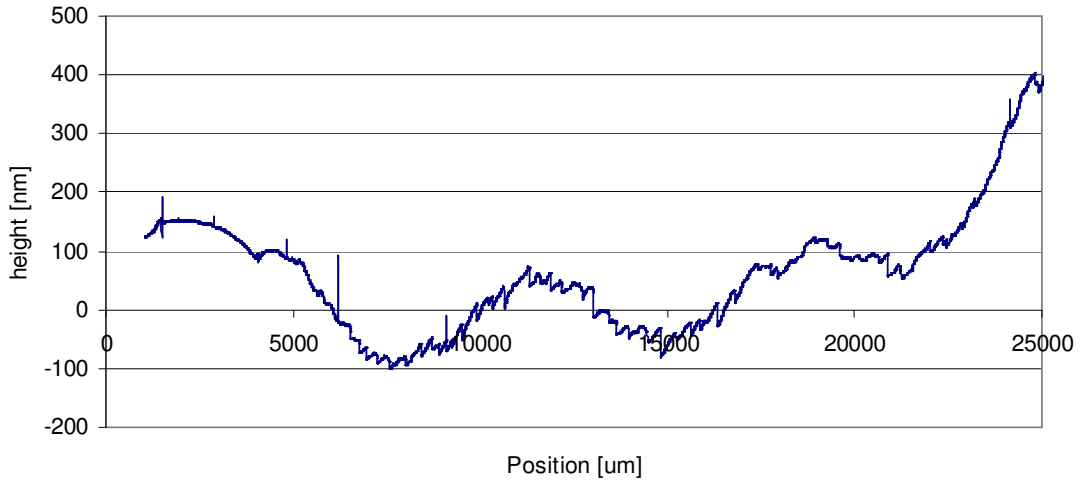


Figure G3b.4. Offset correction

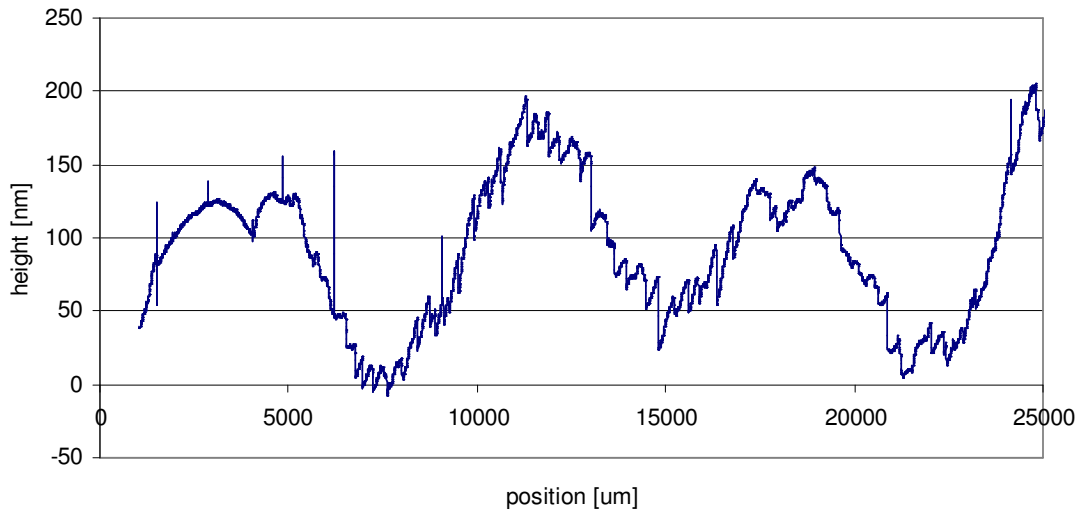


Figure G3b.5. Parabolic bend removed

Appendix G4a Measurement report of patterned wafer for LCoS panels (3D-deflectometer)

Surface-under-test:	patterned silicon wafer for LCoS panels
Manufacturer:	Philips Semiconductors Boeblingen
Geometrical parameters:	Ø 200 mm
Finishing:	metallization
Top-layer:	Al coating (200 nm)
Device:	3D-deflectometer
Manufacturer:	Philips Applied Technologies
Type:	-
Parameters:	mean step size 90 µm (low res), 30 µm (high res), surface reconstruction by Iterative Fourier Integration
Post-processing and display software:	MountainMap 3.1
Measurement date:	22.09.2005
Investigated parameters:	Global shape (A); die structure (B); local nanotopography (C)

(A) Global shape

Support:	flat metal plate, no-vacuum chuck
Post-processing:	stitching in the slope domain prior to surface reconstruction (correction for lateral position and vertical off-set in the slope arrays), the complete image stitched from four overlapping subfields

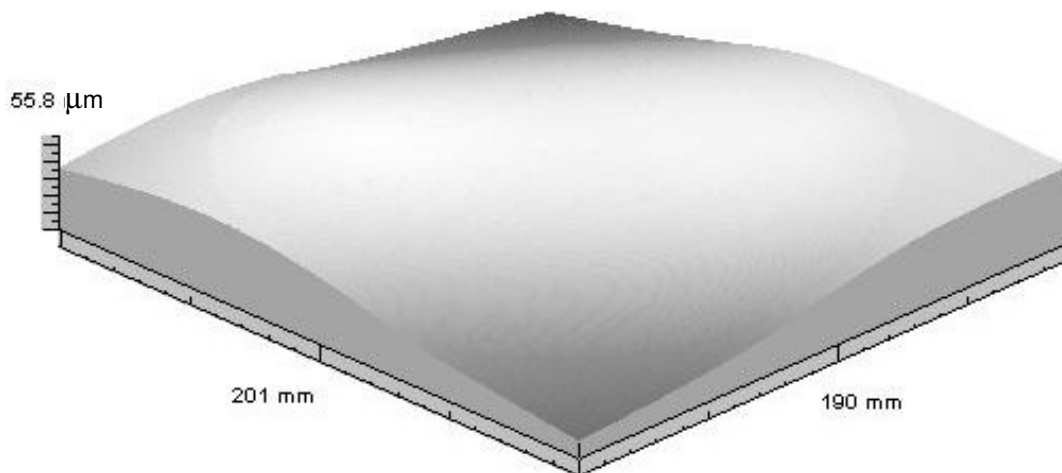


Figure G4a.1 Free-form

Parameters: PV height: 55.8 μm
 RMS height: 12 μm

(B) Die-structure

Support: flat metal plate, no-vacuum chuck

Post-processing: parabolic bend removed by a 2nd order polynomial

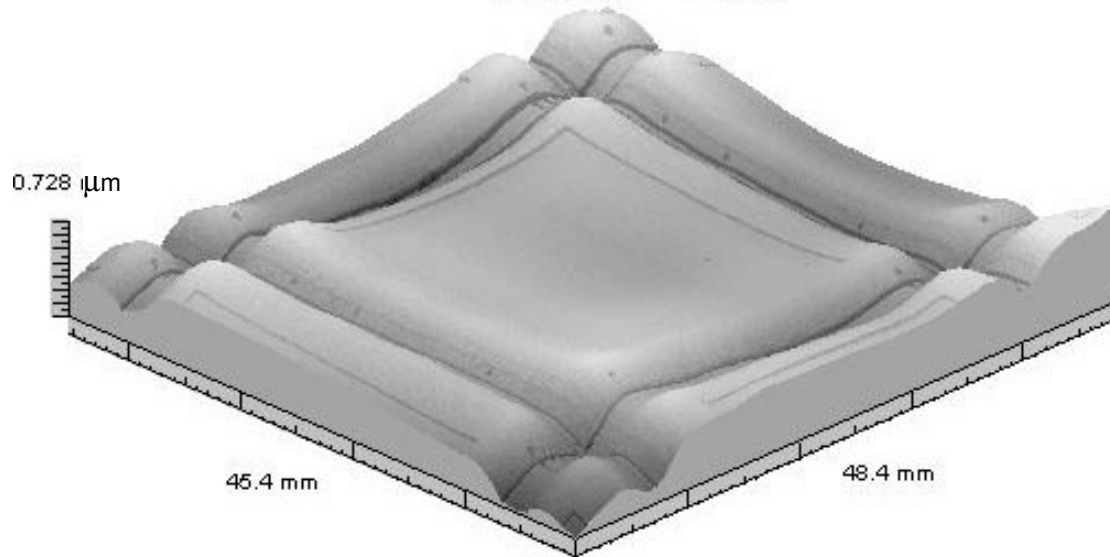


Figure G4a.2. Parabolic shape removed

(C) Local nano-structure

Support: flat metal plate, no-vacuum chuck

Post-processing: high-pass single-Gaussian filter with 2.5 mm cut-off

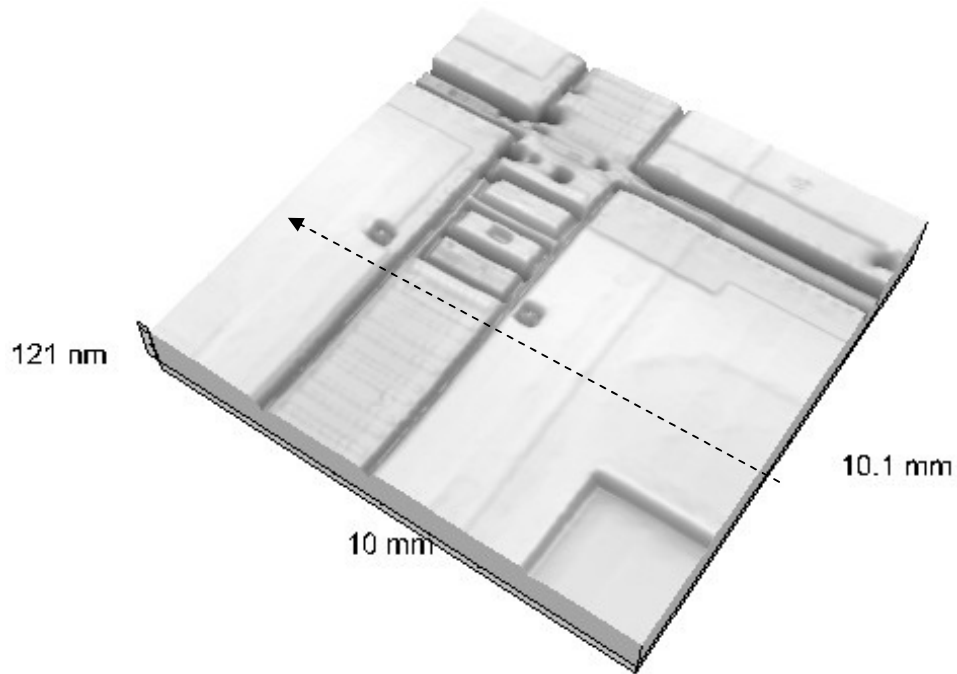


Figure G4a.3. Filtered nano-structure. Black arrow indicated position and orientation of the height profile shown in figure G4a.4.

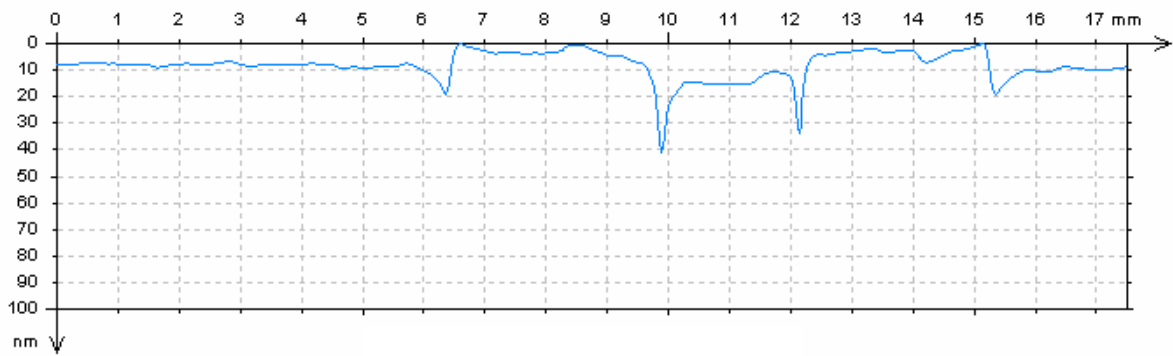


Figure G4a.4. Height profile

Appendix G4b Measurement report of patterned wafer for LCoS panels (white light interferometer)

Surface-under-test:	patterned silicon wafer for LCoS panels
Manufacturer:	Philips Semiconductors Boeblingen
Geometrical parameters:	Ø 200 mm
Finishing:	metallization
Top-layer:	Al coating (200 nm)
Device:	white light interferometric microscope with lateral stitching
Manufacturer:	Zygo
Type:	NewView 5032
Parameters:	Pixel size: 22.92 µm, field of view: 7.33 x 5.50 mm
Post-processing and display software:	MountainMap 3.1
Measurement date:	29.09.2005
Investigated parameters:	Local nanotopography
Support:	flat metal plate, no-vacuum chuck
Post-processing:	High-pass single-Gaussian filter with 2.5 mm cut-off

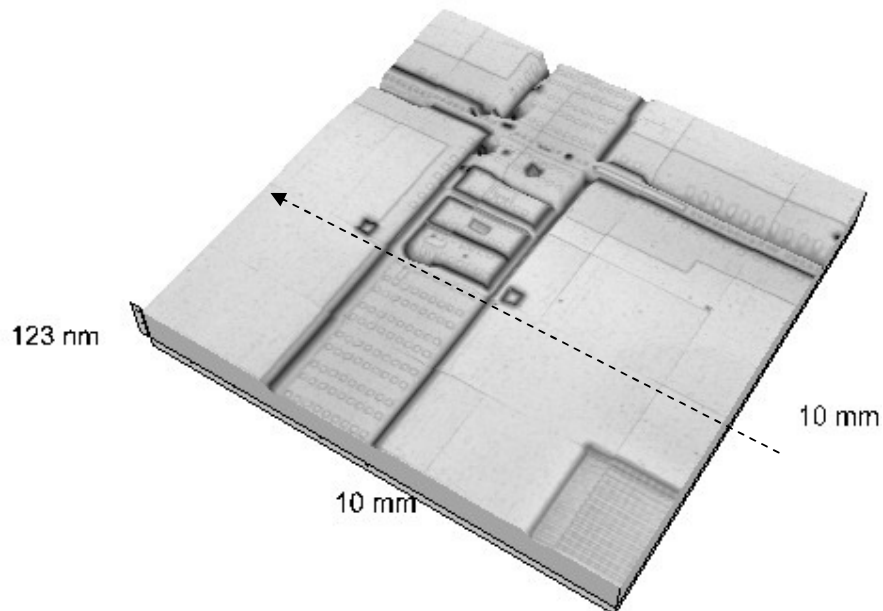


Figure G4b.1. nano-structure. Black arrow indicates position and orientation of the height profile shown in figure G4b.2.

Parameters: PV height: 123 nm

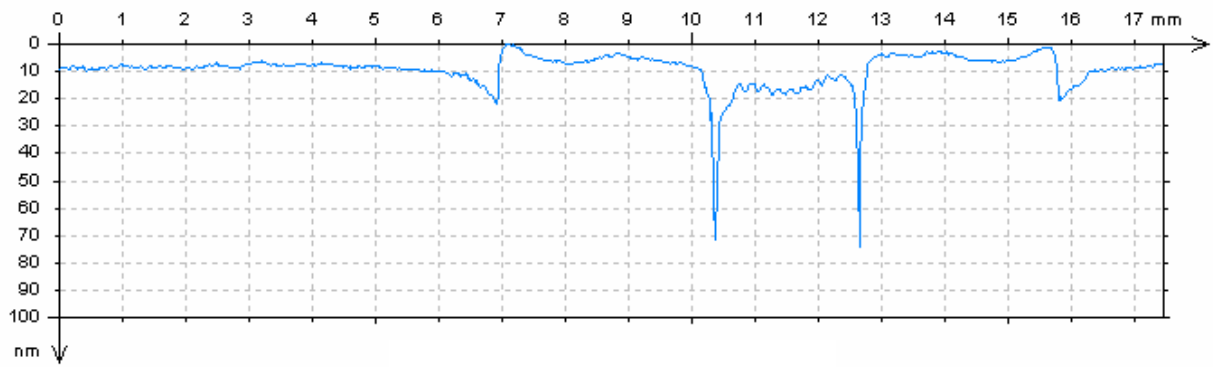


Figure G4b.2. Height profile

Appendix G5a Measurement report on long aluminium mirror (3D-deflectometer)

Surface-under-test:	Aluminium mirror for a interferometry-based positioning system
Manufacturer:	Philips
Geometrical parameters:	length 350 mm, width 35, thickness: 40 mm
Finishing:	diamond turning
Top-layer:	Al
Device:	3D-deflectometer
Manufacturer:	Philips Applied Technologies
Type:	-
Parameters:	mean step size 90 μm (low res), 30 μm (high res), surface reconstruction by Iterative Fourier Integration
Measurement date:	12.10.2005
Investigated parameters:	Global shape (A); local structure (B)
(A) Global shape	
Support:	flat metal plate, no-vacuum chuck
Post-processing:	High-pass single-Gaussian filter with 20 mm cut-off

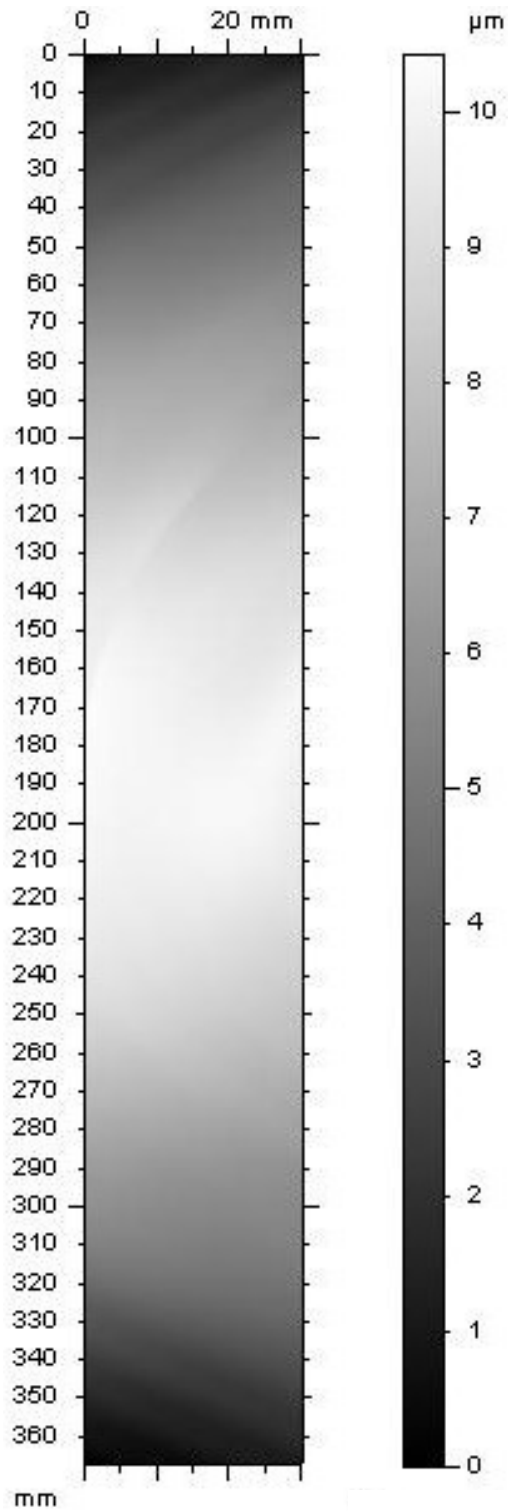


Figure G5a.1. Free form

Parameters: PV height: 10.2 μm
 RMS height: 2.72 μm

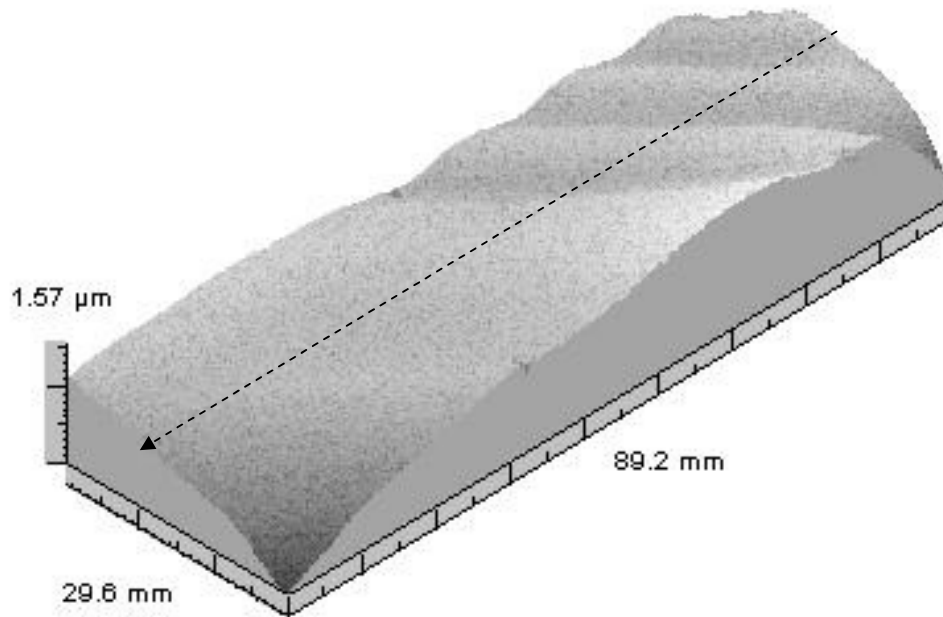


Figure G5a.2. Free-form, zoon on first 40 mm. The dashed arrow indicates location and orientation of the height profile shown in figure G5b.2

Parameters: PV height: 1.57 μm
 RMS height: 0.167 μm

(B) Local structure

Support: flat metal plate, no-vacuum chuck

Post-processing: High-pass single-Gaussian filter with 20 mm cut-off

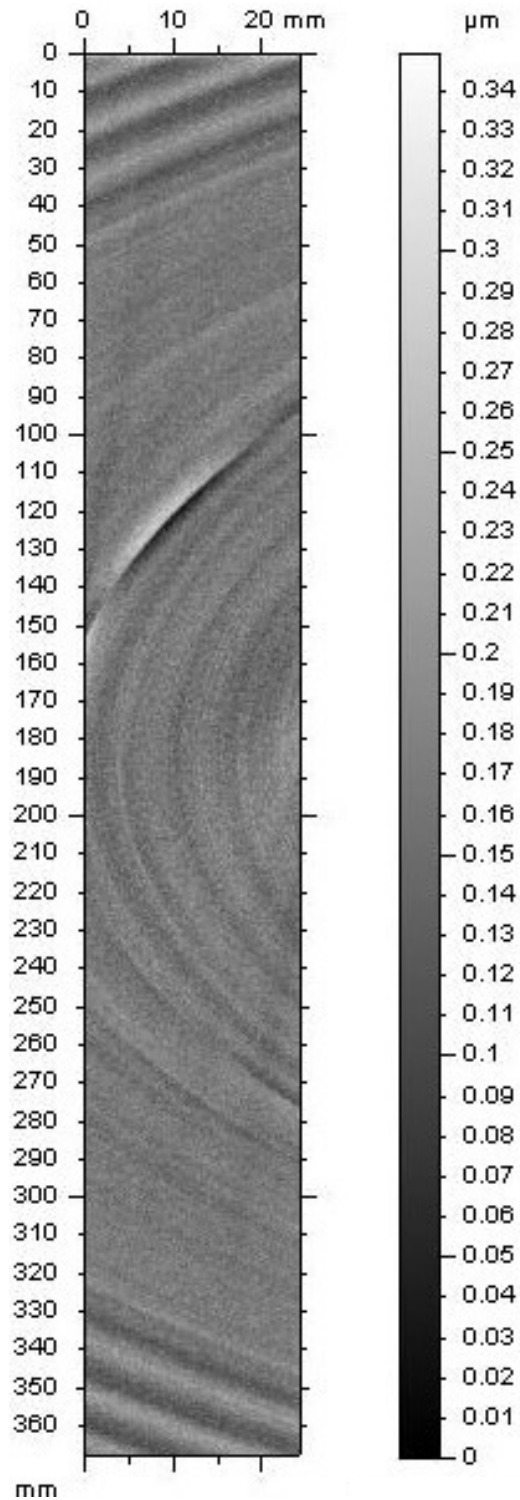


Figure G5a.4 Filtered surface (nanotopography)

Parameters: PV height: 349 μm
RMS height: 22.8 μm

Appendix G5b Measurement report on long aluminium mirror (4" Phase-shift interferometer)

Surface-under-test:	Aluminium mirror for a interferometry-based positioning system
Manufacturer:	Philips
Geometrical parameters:	length 350 mm, width 35, thickness: 40 mm
Finishing:	diamond turning
Top-layer:	Al
Device:	4" interferometer
Manufacturer:	Zygo
Type:	GPI XP/HR
Parameters:	CCD camera resolution 640 x 480 pixels, reference quality $\lambda/10$
Measurement date:	13.10.2005
Investigated parameters:	Global shape

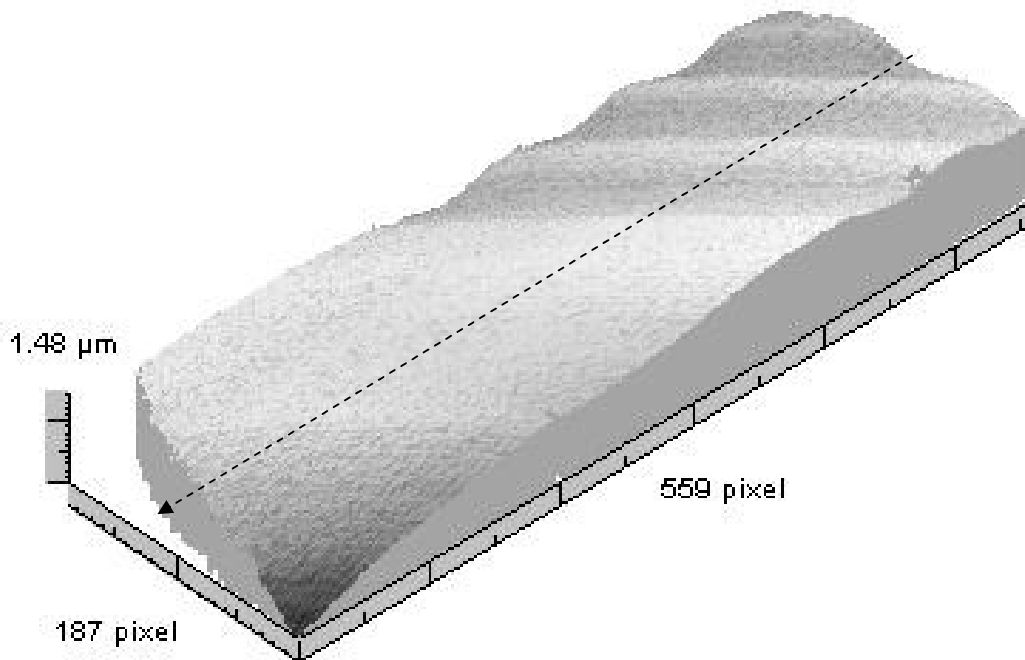


Figure G5b.1 Free-form. The dashed arrow indicates location and orientation of the height profile shown in figure G5b.2

Parameters:	PV height:	1.482 μm
	RMS height:	0.188 μm

Samenvatting

Het hier beschreven onderzoek had ten doel om de mogelijkheden en beperkingen van 3D-deflectometrie te onderzoeken en op basis van deze bevindingen een instrument – 3D-deflectometer – te ontwerpen dat voldoet aan de eisen van de halfgeleiderindustrie. Deze eisen komen neer op een karakterisering van de topografie van een 12” siliciumplak binnen een tijdsbestek van 60 s, met een plaatsoplossend vermogen van 100 micron en een precisie in hoogte van 5 nm. De beschikbare topografische meetmethoden kunnen hier niet aan voldoen. Wij onderzoeken een nieuwe wijze van oppervlakte karakterisering - 3D-deflectometrie – die is gebaseerd op een optische meting van de afgeleide of helling van het oppervlak. Hierbij wordt het gehele oppervlak lijn na lijn afgetast met een gefocuste laserbundel. De verplaatsing van de gereflecteerde bundel, die wordt gemeten met een optische detector, is een maat voor de locale helling van het oppervlak. Deze aanpak is vergelijkbaar met die van een auto-collimator. Op deze manier worden de twee componenten van de locale afgeleide van het oppervlak in kaart gebracht. Door een geavanceerde numerieke integratieprocedure wordt het oppervlakprofiel weer gereconstrueerd.

Deze meetmethode heeft, door de combinatie van een optische- en een mechanische aftasting samen met een snelle optische detector, de krachtige eigenschap dat grote oppervlakken – zoals 12” siliciumplakken – in korte tijd bemeten kunnen worden met nog een hoog plaatsoplossend vermogen. Bovendien kan het hoogteoplossende vermogen zeer groot worden gemaakt door voor het meetsysteem een lens te kiezen met een lange brandpuntsafstand. Het meetprincipe van een deflectometer is bovendien ongevoelig voor hoogtevariaties als gevolg van verticale trillingen of drift van het testobject, die juist bij systemen met een directe hoogtemeting op nanometer schaal de primaire foutenbron vormen.

Om een optimaal ontwerp van het instrument te kunnen realiseren, werd een theoretisch model van de hellingsmeting en de oppervlaktereconstructie afgeleid. Voor dit laatste aspect is aangetoond dat we een sterke afname van de invloed van willekeurige meetfouten kunnen bereiken door het toepassen van een geavanceerd oppervlakte-integratie algoritme. Het inzicht in deze unieke eigenschap van 3D-deflectometrie bleek van essentieel belang, omdat hierdoor minder strenge eisen aan de systeemcomponenten kunnen worden gesteld onder behoud van een zeer goed oplossend vermogen in de hoogte (beter dan 1 nm).

Om de beperking voor het plaatsoplossende vermogen te omzeilen, werd een nieuwe aanpak van optische hellingsmeting geïntroduceerd, de zogenoemde ‘Large Beam Detection’ (LBD) modus. Door toepassing van deze aanpak konden wij het plaatsoplossende vermogen met een factor twee verbeteren zonder afbreuk te doen aan de andere kernparameters zoals de meettijd en het bereik van hellingen dat het instrument aan kan. Toepassing van de LBD modus vereist geen veranderingen aan de hellingssensor maar slechts een aanpassing van de software die het instrument uitleest.

De opstelling die in dit proefschrift wordt besproken, is gebaseerd op een aangepaste ‘Fast Optical Scanner’ (FOS) van Philips Applied Technologies. Deze is geschikt voor het meten van de topografie van vlakke of zwak gekromde oppervlakken met laterale afmetingen tot 110 mm bij 500 mm. Het maximum aantal meetpunten bedraagt 6.5 miljoen. Met toepassing van de LBD modus bereikten we met deze opstelling een plaatsoplossend vermogen van 200 micron bij een meettijd van ongeveer 1 minuut voor een oppervlak van 100 mm x 100 mm.

Voor de ijking van de huidige 3D-deflectometer zijn nieuwe methoden en technieken ontwikkeld, waardoor de positie van meetpunten op het oppervlak en de meting van de helling in absolute zin zijn geborgd. Verder werd een correctiemethode ontwikkeld waarmee de invloed van systematische fouten kan worden geëlimineerd en de hoogte nauwkeurigheid over grotere afstanden sterk wordt verbeterd. Deze systematische fouten, die in hoofdzaak worden veroorzaakt door aberraties van het optische systeem en (kleine) mechanische uitlijnfouten en onvolmaaktheden van het instrument, kunnen geijkt worden met behulp van metingen aan een referentie oppervlak van hoge kwaliteit. Hieruit kan een correctie worden afgeleid die softwarematig wordt toegepast bij metingen aan voorwerpen met een onbekend hoogteprofiel.

Om aan te tonen dat de huidige 3D-deflectometer als een volwaardig instrument voor de meting van de topografie van een oppervlak beschouwd kan worden, werd een uitgebreide verificatie van het systeem uitgevoerd door de resultaten van de 3D-deflectometer te vergelijken met de meetresultaten van geijkte meetinstrumenten die op een ander principe werken. De gebruikte instrumenten zijn een 'White-Light Interferometer', een interferometrisch instrument met monochromatisch licht en een tastinstrument. Op grond van deze vergelijking mogen wij concluderen dat de huidige 3D-deflectometer een nauwkeurigheid in hoogte van beter dan 5 nm behaalt in het nano-topografie bereik (lengteschaal van ~100 micron tot ~20 mm) en beter dan 35 nm voor wat betreft de globale vorm (over een lengteschaal van 110 mm).

In het proefschrift op proefontwerp tonen wij aan dat met een zorgvuldig doordachte aanpassing van het huidige prototype een 3D-deflectometer geconstrueerd kan worden die ruimschoots voldoet aan de eisen van de halfgeleiderindustrie, zoals die hierboven zijn geformuleerd.

Acknowledgments

I would like to thank all people who have helped during the period of my promotion, most of them at Philips Applied Technologies. First of all, however, I would like to highlight two people who contributed the most to the project, as well as to my professional and personal development during that time:

I would like to thank to my mentor at Philips Applied Technologies and “father of laser deflectometry” – Wim van Amstel, without whom this project could never have been carried out. Wim, I am proud that I had opportunity to work with you. Thanks for all the discussions we had and all the knowledge I got from you. I hope you have had as much excitement and fun during this project as I had.

I would like to thank to my promotor: Herman Beijerinck. Herman, thank you for all your time, patience and support for my work and in my private life. The bottle will stay half full.

I truly stand on shoulders of giants! Thank you.

I also would like to thank to Stefan Bäumer – my co-promotor – for great help during the writing of this thesis. Thank you for your sound remarks and for taking so much time to read carefully all the written materials I have delivered to you.

I want to thank to my second promotor Anton Tjihuis for the effort he took during reviewing this thesis and for all the helpful remarks.

I would like to thank to Theo de Cler for his involvement in creating the main software program and software framework for the calibration algorithms. Theo – it was big fun to work with you. Thanks for your official- and free-time that we have spent together on programming.

I wish to thank Willem Poetze for his involvement in modelling of beam detection and for all other discussions about mathematics and surface reconstruction. I am grateful to Piet van Engen for supporting the project and fruitful discussions about the signal theory. Many thanks to Olaf Vermeulen and Toon Blom for their help with electronics components and considerations about deflectometry transfer function. I want to thank to Mathieu Breukers for his support and help in verification of the measurement results. I also wish to thank to Erik Jan Lous his involvement in defining user requirements from the semiconductor industry and verification of the results.

I also would like to thank to all the people that have been involved in the early stage of the project: Gon Weijers and René Klaver for their time and fruitful discussions, Peter van de Goor for help in the mechanical assembly of the system, Harry Verspaget and Rene Duive for introducing me to the LabView programming language and their help in the first data acquisition system.

I want to thank to all other members of Vision, Optics and Sensors department at Philips Applied Technology, who contributed in many ways to this thesis. I was great time for me to work with you. Especially, I would like to thank to Marten Sikkens, without his help the second phase of the project would not take place.

The project described in this thesis could not have been performed without the financial support of a European Project: “3D deflectometry” (contract No. G6RD-CT-2001-00547,

founded by the European Commission under the Framework program: “Competitive and Sustainable Growth”. I wish to thank all the project partners for the pleasant cooperation and great time that we spend during the consortium meetings. Particularly, I want to thank to Juan Campos and Alfonso Moreno, Universidad Autonoma de Barcelona, whose surface integration software program was used as a crucial part of this thesis.

Finally, I want to take this opportunity to thank to my wife Dorota and my daughter Iga for their unbelievable patience, understanding and support. It was long five years for us and I hope we all grew stronger.

Biography

Konrad Szwedowicz was born on 15 February 1976 in Warsaw, Poland. He attended the Stefan Batory II L.O. in Warsaw, where he received his secondary school diploma in 1995. In the same year he commenced his study in Material Science and Engineering at Warsaw University of Technology, where he received his MSc degree in June 2000. His graduation work concerned modification of mechanical properties of the Ti-6Al-4V titanium alloy by a careful choice of parameters of the plasma nitriding.

In 2000 he moved with his wife and daughter to The Netherlands and started a post-graduate designer course in 'Design and Technology of Instrumentation' at Stan Ackermans Institute. After receiving his PDEng diploma in September 2003, he continued his project in the Industrial Optics group of Philips Applied Technology as a design-based PhD study with an advisor from the Department of Applied Physics at the Eindhoven University of Technology in Eindhoven.

Since January 2006 he works as a system designer and a project leader at VisionDynamics in Eindhoven.